A Study of Internal Oxidation in Carburising Steels

Xiaoxue An

August . 2002

A thesis submitted in part fulfilment of the requirements of Sheffield
Hallam University for the degree of Doctor of Philosophy

ON INSTRUCTION FROM THE UNIVERSITY THE FOLLOWING FIGURES HAVE NOT BEEN SCANNED

(2-1)
(2-2) (2-3) (2-4)
(2-5) (2-7)
(2-8) (2-9) (2-10) (2-11)
(8-1) (8-5) (8-7) (8-8)

TO MY BELOVED PARENTS, MY HUSBAND AND MY DAUGHTER

ABSTRACT

The phenomena known as 'internal oxidation' can play a major detrimental role in the failure of carburised components such as bearings and gears. Internal oxidation leads to a degradation of the surface layer often leading to surface break up and fatigue. This work is concerned with a detailed understanding of the formation of internal oxidation leading to modifications to composition or process parameters to eliminate or reduce internal oxidation.

Experimental steels for the most part have been used in this study with Si content varying from 0.11 to 0.77 mass percent. A commercial carburising process at David Brown Heatch Ltd. consisting of a number of process stages with varying C potential and treatment temperature has been used in the study.

Scanning Electron Microscopy (SEM) , Cross sectional Transmission Electron Microscopy (TEM), Energy Dispereive Spectroscopy (EDS) and Electron Probe Microanalysis (EPMA), Glow Discharge Optical Emission Spectroscopy (GDOES), Quantitative Image Analysis techniques were applied to characterise the specimens.

A model has been proposed that explains the formation of the characteristic morphology observed in internal oxidation and is based upon competitive processes concerning the diffusion rate of alloy species within the bulk material and the differences in the free energy of formation of the various oxides types. The observed morphology of the internal oxidation zone at different carburised exposure time, in range of 0.25-16.6h, related to the penetration depth and density of the internal oxides in the internal oxidation zone, with particular emphasis on the relative importance of oxygen partial pressure at reaction and free energy of formation of oxides have been studied. The research indicated that the internal oxides grew fast in the base process. Three elements Cr, Mn and Si were oxidised at this stage and formed complex oxides within the grains and on the grain boundaries. Further, as carburising time increased, existing oxides grew and new oxides nucleated again along grain boundaries. In the boost process, only Si was oxidised. Si oxides penetrated to a greater depth along the grain boundaries. The generally two-zone morphology characteristic was found in the internal oxidation zone of carburised steel. Outer zone: larger size complex oxides which contain higher concentrations of Cr, Mn and some Si on the grain boundaries or within the grain; Inner zone: intergranular Si oxides on the grain boundaries. Small dispersed oxide paticles were observed in both zones.

Different oxides were formed in the internal oxidation zone as complex oxides, sometime as agglomerated oxide phases, and intergranular oxides. These complex oxides were identified as $Cr_{1.5}Mn_{1.5}O_4$, $CrMnO_4$, Mn_2SiO_4 and $MnSiO_3$. The intergranular oxidation was mainly Si oxides, such as SiO_2. The agglomerated oxide phases were observed usually as the Cr-Mn complex oxides with Si oxides or Mn-Si complex oxides growing around them.

The role of Si is critical in that its solid state diffusion coefficient in Fe is considerably higher than that for Mn and Cr whilst the free energy of formation of Si oxide is lower than that for Mn and Cr. It affects internal oxidation, not only on the morphology but also the rate of penetration. For the specimen with low Si bulk content, the internal oxidation zone consisted of larger complex oxides elongation close to the surface, with intergranular oxidation remote from surface. The penetration depth of the internal oxides increased with increasing bulk Si content. In this case, oxygen diffused not only through the metal lattice but also at an enhance rate along the internal oxides/metal matrix interface. There was a peak value, after which as Si increased in the bulk metal, more intergranular oxidation was formed instead of the larger oxides. A continuous layer was formed parallel to the surface that reduced further diffusion of oxygen. The penetration depth of the internal oxides decreased with further increases of bulk Si content. The higher the carbon potential, the lower was the penetration depth of the internal oxides and the less dense the internal oxidation zone.

ACKNOWLEDGEMENTS

I am deeply indebted to my director of studies Dr. Jess Cawley for initially giving me opportunity to undertake a PhD studying in Materials Research Institute (MRI), Sheffield Hallam University and for his kindness support, supervisor throughout my studies during three and half years and help for this thesis.

My special appreciation to my supervisor Prof. Mark Rainforth for his guidance through my studies and help for this thesis. Thanks to Prof. John Aktinson for his supervision for my studies.

I would like to express my gratitude and thanks to Dr. Bill Cook, Mr. Philiph Cleark, Dr. Mike Cristance and Dr. Richeal Williams as my external industrial supervisor to their advice, valuable suggestion for my studies.

I extend my appreciation to all technical staff of the MRI, in particular Dr. Q. Lu and Mr. P. Slingsby, for training the facilities in MRI.

Final, I would like to thank my husband and my daughter for them kindness patience and support all the way through my study.

Thanks must also be given to my sister and brother for them support all the way through my study.

CONTENTS

CHAPTER 3 EXPERIMENTAL PROCEDURE 48

CHAPTER 4 PRECIPITATE MORPHOLOGY AND ELEMENTAL DISTRIBUTION 66

CHAPTER 1
INTRODUCTION

Internal oxidation is the process by which oxygen diffuses into a dilute alloy and causes subsurface precipitation of oxides of one or more alloying elements. Such reactions occur when carbon, nitrogen and other elements are diffused into steel when undergoing carburising and carbonitriding. Therefore, in the gas carburised process become the carburising atmosphere contains oxygen and commercial carburising steels contain alloy elements, such as Si, Cr and Mn which have a higher affinities for oxygen (Kozlovskii 1967) than the bulk metal, internal oxidation occurs.

The presence of internal oxidation at the surface of components that are case hardened by conventional gas carburising has been known for fifty years or more (Parrish 1999). These components are used for structural and engineering applications and certain uses such as bearing applications impart severe dynamic surface loading leading to fatigue conditions. The internal oxidation in carburised steel causes a surface defect to occur by the oxidation of certain elements in the steel (mainly Si, Mn and Cr) during the gas carburising process. The presence of sub-surface defects is very deleterious in terms of surface fatigue and is considered to be undesirable and unavoidable in carburised steel. Internal oxides precipitate both within grains and on grain boundaries close to the surface region of the carburised layer. The different oxide species being distributed at different depths from the surface. At the near surface region complex oxides of Mn and Cr dominate and are observed in globular form both intra and intergranularly. At a greater depths, oxides of Si form as a grain-boundary network that is not observed in the near surface region. Another important microstructure feature associated with internal oxidation in carburised steel is that of non-matensitic transformation products, that can form as a direct consequence of internal oxidation, that have subsequently been found to have an adverse effect on certain properties of the affected parts. The internal oxide and oxidised grain boundaries may act as fatigue crack initiation sites and generate low residual compressive stresses near the surface and develop a microstructure with low hardness and low strength that will decrease the lifetime of components.

The use of an oxygen free gas carburising atmosphere or vacuum carburising process is known to eliminate the oxidation process. However, conventional gas carburising using the endothermic carrier gas is still the most popular and effective method of case hardening and is used widely in industry. Thus, the problems related to the internal oxidation in carburised steel will persist as long as the conventional process is in use. Therefore, it is important to understand how the internal oxidation forms, what its effects are on materials properties, and what can be done to eliminate it. Considerable work has been done in this area accompany the development of new steels, however, the internal oxidation of carburised steel still remains a problem in commercial components and the mechanism of internal oxidation is still not understood in commercial low alloy steels.

It is therefore the object of this work to focus on a study of the mechanism of internal oxidation during the carburisation of a Cr-Mn-Ni base carburising steel grade V2525-70 with different silicon content in range of (0.11-0.77) mass % as studied in this work. The materials were carburised at different carbursing processing that had different atmosphere conditions. The morphology of the internal oxidation and elemental distribution was examined by Scanning Electron Microscopy (SEM) and Energy Dispersive Spectrometry (EDS), more detailed examination of the internal oxide phase, its structure, shape, dimension and composition was studied by Transmission Electron Microscopy (TEM) equipped with an EDS system in cross sectional specimens. Quantitative evolution of the internal oxidation zone as a parameter of penetration depth of the internal oxides and population density of the internal oxides in the internal oxidation zone (area fraction of the internal oxides) was performed by quantitative image analysis techniques. Elemental depth profile in the internal oxidation zone and depletion of alloy elements in the matrix below the internal oxidation region was examined by Electron Probe Microanalysis (EPMA) and Glow Discharge Optical Emission Spectrometer (GDOES). The research was concentrated on the following aspects:

- To understand the formation condition and process of internal oxidation.
- To investigate on the effect of variable carburising process on the internal oxidation, especial for atmosphere condition.
- To study the internal oxide phase, its morphology, structure, dimension and composition.
- To study the influence of the base chemical composition of steel on the internal oxidation, especially of the influence of Si content.
- To develop a model that describes the internal oxidation process during gas carbursing process in terms of differential element partitioning and differing and competitive free energies of oxide formation.
- Proposed method for reduced or eliminated the internal oxidation in carburised steel.

This research project was submitted by a consortium of industrial and is sponsored by the Materials Forum, UK. The project is collaboration between the Material Research Institute, Sheffield Hallam University and the Department of Engineering Materials, the University of Sheffield. The research work is associated with several partners, Swinden Technology Centre, Corus and David Brown Heatech. Ltd. It has concentrated on morphological study and microanalysis of internal oxides and the influence of variable carburising process parameters on internal oxidation.

CHAPTER 2
LITERATURE SURVEY

2.1 Generally Theoretical Aspects of Internal Oxidation

2.1.1 Introduction

Internal oxidation is observed in dilute solid solution alloys composed of a base metal, such as Ag, Cu, Fe, Ni and Co and a small amount of less noble alloying element, such as In, Be, Vr, Al, Mn, Si, W, V and Zr. When such an alloy is exposed to an oxidising atmosphere at high temperature, it is observed that oxide particles of the alloying element precipitate at an advancing reaction front within the base metal.

The necessary conditions for the occurrence of the internal oxidation (Birks and Meier 1984) were:

a). Free energy (ΔG) of formation (for mole O_2) for the solute metal oxide, BO_v, must be more negative than ΔG of formation (per mole O_2) for the base metal oxide.

b). Free energy (ΔG) for the reaction

$$B + v\underline{O} = BO_v$$

must be negative. Therefore, the base metal must have a solubility and diffusivity for oxygen which is sufficient to establish the required activity of dissolved oxygen $\underline{O}$ at the reaction front.

c). The solute concentration of the alloy must be lower than that required for the transition from internal to external oxidation.

d). No surface layer must prevent the dissolution of oxygen into the alloy at the start of oxidation.

Two distinct of internal oxidation condition are distinguishable:

- Internal oxidation in the absence of an external scale
- Internal oxidation in the presence of an external scale.

2.1.2 Internal Oxidation in the Absence of an External Scale

The internal oxidation in the absence of an external scale is the simplest case for theoretical consideration. The early systematic investigations concerning this phenomenon were carried out by Rhines et al (1942), Meijering and Druyvesteyn (1947). Later, numerous experimental and theoretical work has been carried out on this subject and the theory of internal oxidation has been widely developed by Wagner (1959), Rapp (1965) and resulting in a series of general postulates of considerable theoretical and practical importance. According to Wagner's classical model of internal oxidation in a binary alloy A-B in which B was a dilute solute element which forms a very stable oxide, if diffusion control was maintained, the growth of an internal oxidation zone will be a parabolic function with time. Wagner defined a parabolic rate constant as follows:

$$\gamma = \xi / 2(D_o t)^{1/2} \text{ -- } (2\text{-}1)$$

He then sought a solution to the diffusion equations in terms of this rate constant.

The diffusion of oxygen through the subscale is an application of Fick's second law:

$$\frac{\partial N_o}{\partial t} = Do\frac{\partial^2 N_o}{\partial x^2} \text{ -- } (2\text{-}2)$$

The boundary conditions are:

$N_o = N_o^{(S)}$ for $\chi = 0$, $t > 0$ --- (2-3)

$N_o = 0$ for $\chi = \xi$, $t > 0$ --(2-4)

The solution to Eq. 2-2. Subject to the above boundary condition is

$$N_o = N_o^{(s)}\left(1 - \frac{erf\left[x/2(D_o t)^{1/2}\right]}{erf\gamma}\right) \tag{2-5}$$

In addition to oxygen diffusion inward from the external surface to the precipitation front, the oxidising alloying element diffuses outward from the centre of the specimen to the same precipitation front. Wagner showed that the solution to Fick's second law for counterdiffusion of the alloying element is

$$N_b = N_b^{(s)}\left(1 - \frac{erfc\left[x/2(D_b\, t)^{1/2}\right]}{erfc\gamma\phi^{1/2}}\right) \tag{2-6}$$

Where, ν: The stoichiometric ratio of oxygen to metal atoms in the oxide precipitate.

D_o: The diffusion coefficient of oxygen in the metal matrix.

D_b: The diffusion coefficient of B in the bulk alloy

t: The reaction time.

ξ: The penetration depth of internal oxides

χ: Distance from the external surface.

γ: Oxidation rate constant.

N_o: The concentration of dissolved oxygen in the subscale expressed as atom fraction.

$N_o^{(s)}$: The atom fraction of oxygen at surface.

$N_b^{(o)}$:The atom fraction of solute B in the bulk alloy.

N_b: The atom fraction of the alloying element, B

ϕ: The diffusion coefficient ratio, D_o/D_b

The schematic concentration profiles for oxygen and alloying element is shown in Fig. 2-1.

Fig. 2-1 Schematic concentration profiles of dissolved oxygen and alloying element during internal oxidation (ref: Swisher J.H 1970)

Two limiting cases were considered in the above equation.

Limiting case 1: oxygen diffusion predominates ($D_b/D_o \le N_o^{(s)}/N_b^{(o)} \le 1$), γ is given as

$$\gamma \approx (N_o^{(s)}/2\nu N_b^{(o)})^{1/2} \text{ ---------------------------------------(2-7)}$$

Limiting case 2: counterdiffusion of the alloying element is significant and $N_o^{(s)}/N_b^{(o)} \le D_b/D_o \le 1$,

$$\gamma \approx \pi^{1/2}\,\phi^{1/2}\, No^{(s)}/2\nu N_b^{(o)} \text{ -------------------------------------(2-8)}$$

Here, an appreciable enrichment of the alloying element in form of the oxide, BO_ν, in the subscale occurs. Based on Fick's first law, the flux of oxygen through the subscale is

$$J=dm/dt=Do\ N_o^{(s)}/\xi V_M \text{-------------------------------------- (2-9)}$$

Where J=dm/dt is the instantaneous flux of oxygen into the specimen, V_M is the molar volume of the solvent metal or alloy. If enrichment of B in the subscale is assumed to be small, the amount of oxygen accumulated in the subscale per unit area of reaction front will be given by the stoichiometric equation:

$$M=N_B^{(o)}\nu\xi/V_M \text{ -- } (2\text{-}10)$$

And by differentiation,

$$Dm/dt = N_B^{(o)}\nu/ V_M *d\xi/dt \text{ ------------------------------ } (2\text{-}11)$$

Combining by above Eq. (2-9) and (2-11), the penetration depth of the internal oxidation can be described by follows:

$$\xi=\left(2\frac{No^{(S)}Do}{\nu Nb^{(o)}}t\right)^{1/2} \text{ -- } (2\text{-}12)$$

Equation 2-12 points out that the penetration depth for a fixed time is inversely proportional to the square root of the atom fraction of solute in the bulk. And careful measurement of the penetration as a function of time for an alloy of known solute concentration can yield a value for the solubility-diffusion product, $N_o^{(s)}D_o$ (permeability) for oxygen in the matrix metal.

2.1.3 Internal Oxidation in the Presence of an External Scale

In most of the practical applications of alloys at high temperature, the internal oxidation zone is formed below an external oxide scale. The kinetics of simultaneous internal oxidation and external scale formation has been treated by Rhines (1942), Maak (1961), Rapp (1966) and recently by Gesmundo (1997).

If the thickness of the metal layer that has been completely oxidised is equal to

$$x' =(2k_ct)^{1/2} \text{ -- } (2\text{-}13)$$

Where x' is the distance from original surface to the scale/metal interface. k_c is the parabolic corrosion rate of metal.

Makk solved the diffusion equation following boundary condition:

$$N_o = 0 \qquad \text{for } x \geq \xi,\ t>0 \qquad \text{----------------------------- } (2\text{-}14)$$

$N_o = N_o^{(s)}$ for $x=x'$, $t>0$ ----------------------------- (2-15)

$N_b = 0$ for $x \leq \xi$, $t > 0$ ----------------------------- (2-16)

$N_b = N_b^{(o)}$ for $x \geq 0$, $t > 0$ ----------------------------- (2-17)

The solution for the diffusion equation were given by

$$N_o = N_o^{(s)} \left\{ \frac{erf\gamma - erf\left[x/2(D_o t)^{1/2}\right]}{erf\gamma - erf(k_c/2D_o)^{1/2}} \right\} \quad \text{---------------------- (2-18)}$$

$$N_b = N_b^{(0)} \left\{ 1 - \frac{erfc\left[x/2(D_b t)^{1/2}\right]}{erfc(\gamma\phi)^{1/2}} \right\} \quad \text{---------------------- (2-19)}$$

2.1.4. Oxide Morphology

The formation of oxide particles by internal oxidation is a nucleation and growth process for which classical nucleation and growth theories apply. If a very stable oxide precipitates, then the driving force for the process is high. In contrast, for less stable oxides, the driving force is lower, nucleation is more difficult than growth. Bohm and Kahlweit (1964) considered nucleation of a particle from an isothermally supersaturated solution and growth under diffusion controlled model. They indicated that the number of oxide precipitates formed per unit volume, Z(x), should be directly proportional to the surface concentration of oxygen, $N_o^{(s)}$, and inversely proportional to the cube of the distance from the external surface, X.

$Z(X) = \beta(N_o^{(s)}/X)^3$ --- (2-20)

If the particles are spherical, it is possible to determine the mean radius of the particle, r.

$r(X) = (3\alpha V_{BOv} N_b^{(0)})^{1/3}(X/N_o^{(s)})$ ---------------------------- (2-21)

The prediction was confirmed experimentally by the same author for the Ag-Cd system. Qualitative agreement with these predictions was obtained by Wood (1959), Williams and Smith (1968).

Further, Birks and Meier (1984) built up the theory model. They considered that if the nucleation of precipitates was assumed to be controlled by the velocity of the oxidation front (i.e. the rate at which a critical supersaturation was built up) and the growth was controlled by the length of time available for growth of a precipitate, the size should be inversely proportional to the forward velocity.

$$v = d\xi/dt = N_0^{(s)}D_o/\nu N_b^{(o)}\xi \quad \text{------------------------------} \quad (2\text{-}22)$$

The effect of the particle-matrix interfacial free energy was often overlooked but was particularly important in the nucleation and coarsening of internal oxides. The free energy change for the formation of a nucleus of radius r is:

$$\Delta G = 4\pi\sigma r^2 + 4/3\pi r^3\Delta G_v \quad \text{------------------------------------} \quad (2\text{-}23)$$

Where, σ is the interfacial free energy and ΔG_v is the free energy change per unit volume of precipitate or particles formed during the reaction. The surface and volume terms along with ΔG are plotted as a function of r in Fig. 2-2. Nuclei with a radii greater than

Fig. 2-2 Schematic plot of free energy versus radius of nucleating particle (Ref. Birks and Meier 1984)

r^* will tend to grow spontaneously.

$d\Delta G / dr = 8\pi r^{*} + 4\pi r^{*2}\Delta G_v = 0$ ---------------------------- (2-24)

$r^{*} = -2\sigma/\Delta G_v$ --- (2-25)

According to this theory, more stable oxide particles in a matrix of an oxidised specimen are more resistant to growth than particles of an intermetallic or other less stable phase. Swisher (1970) confirmed that MnO and SiO_2 particles were generally larger than Al_2O_3 particles formed under the same oxidation conditions. However, as Williams and Smiths (1968) pointed out if the particles were coherent with the matrix, the interfacial free energy would be low. Williams and Smiths showed that coherent particles of TiO_2 in copper grew more slowly than larger, incoherent particles of SiO_2. After losing coherence with the matrix, the particles of TiO grew faster.

Williams and Smiths (1968) observed that particle size increased lineally with temperature. He also observed that Cr_2O_3 precipitates were initially of a lath like morphology in copper alloys containing Cr_2O_3, MgO and TiO_2, then change to hexagonal plates with further growth. Birks and Meier (1984) believed that the nucleation rate was affected much less by increasing temperature than was the growth rate so that particle size increases with increasing temperature of treatment. As the front penetration increased, the velocity eventually decreased to a point where diffusion of solute to a growing particle occurred rapidly enough to prevent nucleation of a new particle, he considered this resulted in the growth of elongated or needle-like particles.

Internal oxide particles observed in binary alloys had different orientation relationship with the matrix according to different alloys and internal oxidation processes. Williams and Smiths (1968) reported that MgO particles were tetrahedral in shape and had the same crystallographic relationship with the copper matrix in a Cu-0.3% Mg alloy. TiO_2 particles, however, were randomly oriented and were roughly spherical in a Cu-0.3%Ti alloy. Some of the TiO_2 particles observed were intergranular and lenticular in shape and made a fixed dihedral angle with the boundary. Finer particles of MgO and TiO_2 were believed to be coherent with the matrix. Woolhouse and Brown (1970) found that particles of TiO_2 and Al_2O_3 in a high purity copper matrix were incoherent with the matrix down to a particle diameter of 18 Å. SiO_2 particles in copper were observed to be amorphous and spherical in a Cu-0.1%Si alloy (Ebeling and Ashby 1966). Further, Wood and Stott (1987) considered amorphous Si oxide formed as fine-gained or even amorphous, inward transport of O_2 or H_2O was rate determining for amorphous SiO_2 growth. Lanteri et al (1997) reported that larger SiO_2 particles in an internal oxidation zone these were previously precipitated as amorphous SiO_2 particles and had coarsened to a more equiaxed shape in internal oxidised Fe-Si alloy. Stott and Wood (1988) found that size and shape of the internal oxide precipitates developed in the Ni-Al system were considerably different from those in the Ni-V and Ni-Cr alloy system. In the Ni-Al system, the precipitates were rod-like and continuous from the surface to the internal oxidation front. In the Ni-V and Ni-Cr system, the precipitates were not continuous under any conditions. They were discrete, usually being small and granular near the surface, but larger and more irregular in shape near the internal oxide/alloy interface. Tatlock et al (1990) examined individual particles and showed both spinel and alumina particles were often found in close proximity over a greater depth through the internal oxide region than previously reported. The internal structure of the particles was very complex with twins and other linear and non-linear faults present in the spinel oxides.

In classical theory, one alloy element only was considered. The real situation, of course, is more complex when more than one alloying element is present. Internal oxidation with several elements was studied by Huin et al (1997), in which a model was proposed. Huin et al considered for most of the practical cases encountered in the annealing of steels, the oxidation front and enrichment of each element will be modified by the presence of other elements. For example, for a Fe-Mn-Al alloy, the first internal oxidation front corresponded to the formation of the oxides with the lowest solubility product (Al_2O_3) at this front (ξ_{Al}). The oxygen potential was fixed by the Al/Al_2O_3 equilibrium; the second internal oxidation front (ξ_{Mn}) corresponded to the formation of the oxide with highest solubility product (Mn/MnO equilibrium); Between these two fronts , Mn can diffuse without reacting with oxygen since the oxygen potential was too low for the formation of MnO. The model was based on the competitive consumption of the available oxygen assuming that the diffusion coefficients were not affected by the presence of other elements or by the presence of previously precipitated particles and limited to the formation of single oxides. However, this situation was complicated due to the transformation of previously precipitated Al_2O_3 to $MnAl_2O_3$. An alloy containing 1.57%Mn and 0.27%Si produces transparent SiO_2 rich oxides at the subscale advancing front and more opaque (Mn,Fe)/O oxides within the deeper zone examined by electron microscopy was reported by Van Vlack in his review paper (1977). Studies have no been made which reveal the effects of varying Mn/Si ratios. The $MnCr_2O_4$ at the not surface side of the internally oxidised zone in Fe-Mn-Cr alloys when both alloy elements were present in the 1-2% range was reported by the same author. The formation of complex oxides during internal oxidation resulted in the coarsening of precipitates, the particles were larger than the finest simple oxide. The situation of different oxide phases was dependent on the oxygen partial pressure in the atmosphere and free energy for formation of an oxide phase. Another example of internal oxidation of a three component alloy was given by Daneliya and Kanduba (1987) who studied Cu-Al-Ni, Cu-Al-Sn and Cu-Al-Cd alloys and found that near the specimen's surface, simple stable Al_2O_3 oxide formed instantly as a complex oxide, at greater distance, the stable oxides (such as $NiAl_2O_4$, $SnAl_2O_3$, $CdAl_2O_4$) were formed.

Transformation of Mn-oxide precipitates in copper was observed by Kool and Hosson (1998) who reported that internal oxidation resulted in mainly MnO precipitates with a minor fraction of Mn_3O_4. The Mn_3O_4 developed in Cu by transformation of MnO. Thermodynamically Mn_3O_4 was, for small coherent or semi-coherent precipitates, more stable than MnO and the presence of MnO in Cu was a consequence of growth kinetics. The orientation between Mn_3O_4 and Cu was mainly determined by the orientation between MnO and Mn_3O_4 developed during transformation.

In summary, the size of internal oxides will be determined by a number of factors with larger particles forming for

a) Deeper front penetrations,ξ

b) Higher solute concentrations, $N_b^{(o)}$

c) Lower oxygen solubilities and lower po_2,

d) Higher temperature,

e) Higher particle-matrix interfacial free energies,

f) Less stable oxides

(Birks and Meier 1984)

2.1.5 Transition from Internal to External Oxidation

According on equation (2-22), the penetration velocity of the internal oxidation zone decreases with increasing $N_B^{(o)}$ and decreasing $N_O^{(s)}$. When the concentration of solute in the alloy is increased to exceed a critical composition, a continuous layer of solute element oxides BO_v form as the external surface and blocks oxygen diffusion, further retarding internal oxidation. The analysis of this problem has been carried out by Wagner (1959) and further Birks and Meier (1984) gave a critical value for external oxidation as

$$N_B^{(o)} > \left[\frac{\pi g}{2\nu} N_O^{(s)} \frac{D_O V_m}{D_B V_{ox}} \right] \text{ --(2-26)}$$

Where g= f(V_{ox}/V_m): critical value of volume fraction of oxides. At this point, the transition from internal to external scale formation will occur. V_{ox} is molar volume of solute oxides. V_m is molar volume of alloy.

Rapp (1961) tested the Wagner theory for Ag-In alloys. It was found that at P_{O2}=1 atm and T = 550°C, the transition occurred for g=0.3. Wood and Stott (1987) considered that at least 10% alloy solute (B) was required to give a surface layer of BO in 1 atm oxygen. Birks and Meier (1984) considered that influence on the transition was the presence of a second solute whose oxide had a stability intermediate between that of A and B. If Po_2 was high enough to form the oxide of the second solute, this would decrease the inward flux of oxygen and allow external formation of BO_v at lower solute concentrations.

2.1.6 Oxygen Diffusion Path in Matrix Materials

Oxygen diffusion path in matrix can be considered as:

- Through the lattice (interstitial)
- Along the grain boundary.
- Along the incoherent internal precipitate/metal interface.
- Through existing precipitates materials.

As in other precipitation processes, particles formed by internal oxidation were more highly concentrated at grain boundaries than within grains. In an average metallic specimen, the total grain boundary area is much greater than the surface area so that grain boundary diffusion is usually most important. Porter and Easterling (1989) described the grain boundary diffusion by welding together metal A and B. An atom diffusion along the boundary will be able to penetrate much deeper than atoms which only diffuse through the lattice. In addition, as the concentration of solute built up on the boundary these atoms will also diffuse from the boundary into the lattice. The relative numbers of atoms that diffused along grain boundaries and by direct lattice diffusion will be a function of the grain size. The smaller the grain sizes, the greater the total grain boundary area available for boundary diffusion and therefore, the greater the importance of boundaries in the diffusion process.

The importance of grain boundary phenomenon in diffusion measurement is also a function of temperature. Reed-Hill (1973) demonstrated this using silver. For grain boundary self-diffusion, D_b:

$$D_b = 0.025 e^{-20,200/RT} \quad \text{------------------------------------} \quad (2\text{-}27)$$

For volume or lattice self diffusion, D_l:

$$D_l = 0.895 e^{-45,950/RT} \quad \text{------------------------------------} \quad (2\text{-}28)$$

It emphasised the fact that first, diffusion was easier along grain boundaries, and second, it showed that grain boundary and volume diffusions had different temperature dependence. As the temperature was raised, the rate of diffusion through the lattice increased more rapidly than the rate of diffusion along the boundaries. Conversely, as the temperature was lowered, the rate of diffusion along the boundaries decreased less rapidly. The net effect was that at very high temperature diffusion through the lattice exceeds the grain boundary component, but at low temperature grain boundary diffusion became more and more important in determining the total diffusion.

In the situation where internal oxidation can occur, the alloy grain boundary is a preferential site for nucleation of internal oxides due to the smaller degree of supersaturation required. Consequently, the population density of oxides is usually higher in the boundaries than in the grains. Early research by Ashby and Centamore (1968) found that amorphous oxides could be dragged by a migrating boundary, accumulating oxides at the boundary and leaving a depleted zone in its wake. SiO_2 particles in copper behaved this way, but Al_2O_3 did not. Wolf et al and Evans (1962) and Wolf et al (1965) noticed faster intergranular penetration in Ni-Al alloys, at 1000°C but more often at 815°C. Swisher (1970) considered that the major reason for this behaviour was the grain boundaries had preferred nucleation sites and the oxidisable alloying elements may be present in higher concentrations at grain boundaries because of segregation in the alloy. An oxide concentration film was formed that embrittled the alloy. Wood et al (1983) observed rapid penetration of intergranular oxidation in Ni-Cr alloys at relatively low temperature. Villafane (1983) studied a wide range of Ni-alloys and concluded that the intergranular oxide precipitation reflected the easier nucleation of internal oxide particles at the grain boundaries. In the case of dilute alloys, intergranularr oxide appeared to form relatively easily and some oxygen diffused from the grain boundary to the adjacent matrix and nucleated internal oxide particles. In the case of high solute content alloys, more oxygen was consumed in forming intergranular oxide and then the requirements for internal oxides formation in the adjacent grains were not satisfied, allowing the solute element to diffuse to the grain boundary and precipitates formed deeper in the alloy, resulting in a relatively thick intergranular oxide.

Recently research has indicated that some assumptions made within the classical model were not correct. Early, Bohnenkamp and Engell (1964) reported the possible preferential transport of oxygen along the interfaces between oxide particles and the metal takes place. Shida and Stott (1982) studied a wide range of Ni-Al alloys and indicated that precipitates within the internal oxidation zone affected the diffusivity of oxygen in metal. Diffusion along the intergranular oxide/alloy or internal oxide-alloy interface was relatively rapid compared with diffusion through the metal lattice. Presumably diffusion rates of oxygen through the intergranular or internal oxide lattices themselves were so small that oxide did not contribute to the inward transport of oxygen and, in fact, it would block oxygen diffusion if it developed as a continuous, healing layer at the internal oxide or intergranular oxide front. The situation was complicated if voids were present in the precipitate zone which would influence the diffusion process.

Further, Stott and Wood (1984, 1988) summarised several alloy (Ni-Al, Ni-V and Ni-Cr) system and indicated that the precipitates within the internal oxidation zone did influence the diffusivity of oxygen. They found the effective flux of oxygen was influenced by the size, shape and orientation of the internal oxide precipitates, as illustrated schematically in Fig. 2-3. In Fig. 2-3a, the precipitates were continuous rods from the surface to the internal oxidation front and the flux of oxygen through the zone was relatively fast because of substantial contribution of the continuous, incoherent precipitate/metal interface, as occurred in the Ni-Al system. In Fig. 2-3c-f, the precipitates were discrete, here, there was some overall enhancement of the oxygen flux through the internal oxidation zone but less than the configurations in which the precipitates were continuous, as observed in Ni-V and Ni-Cr system. In Fig. 2-3g, there were no precipitates and the flux of oxygen occurred entirely through the metal lattice, as assumed in the classical models. In Fig. 2-3 h-j, the internal precipitates exerted an overall blocking effect to the oxygen flux. This occurred as the concentration of solute metal approached that required for the transition from internal to external oxidation.

Experimental determination of the diffusion coefficient of oxygen in α iron for internal oxidation of a Fe-Si alloy (Takada and Adachi 1986) and γ iron in Fe-Al alloy (Takada et al 1986) also confirmed this point. The internal oxidation was carried out using a mixture of equal amounts of iron and Fe_2O_3 powers at 1123K, 180ks for Fe-Si and 1323K, 345.6ks for Fe-Al alloy. Both experimental and theoretical calculations showed that the diffusion coefficient of oxygen in the internal oxidation zone was increased with the increasing volume fraction of the oxide. The presence of oxide particles accelerated oxygen diffusion. In contrast, Foryst et al (1989) studied on the internal oxidation of Fe-Al and Fe-Al-Si alloy in CO atmosphere at 1223K and reported that during the internal oxidation, the fine precipitates of Si and Al oxides were formed that inhibited the diffusion rate of oxygen. Therefore, they believed that the rate of oxygen diffusion decreased. Later, Yi and Lin (1990) studied internal oxidised 20Cr, 20CrNi carburised steel and also reported that the interface was a high diffusivity path for oxygen. The diffusion coefficient of oxygen within the internal oxidation layer was affected by the diffusion of oxygen, not only in the matrix of the steel, but also at the

Fig. 2-3 Schematic representation of relative path lengths for oxygen flux through internal oxidation zone for various internal oxidation configurations (ref. Stott 1988) interface of the oxide and the matrix. The increase in volume fraction of internal oxides accelerated oxygen diffusion at the interface, agreeing with previous research. Young (2000) believed the classical model of internal precipitation supported by volume diffusion of oxidant through the metal was inapplicable in many cases. For example, he found that internal precipitation of molybdenum sulphide in Ni -20wt% Mo proceeded via the development of lengthy, finely and uniform spaced lamellae oriented parallel to the reaction front. The reaction front advanced according to linear kinetics. At reaction temperature 700°C, a D_s of 10^{-15} m^2s^{-1} was far too low to support the observed reaction front velocity of $6x\ 10^{-9}m\ s^{-1}$, as was the diffusion coefficient in molybdenum sulphides. It was concluded that sulphur transport occurred along the numerous sulphide-matrix interfaces and was so rapid as not to control the rate. Hence, Young believed that the development of precipitate morphologies provided interfaces that could provide rapid diffusion paths, thereby accelerating the internal oxidation process.

2.2 Internal Oxidation of Carburised Steel

2.2.1 Oxidised Alloy Elements

Even when heat treating metals or alloys in atmospheres designed to reduce oxidation of the base metal, it is still possible for oxides of alloying elements to form in the surface zone if the elements have a higher affinity for oxygen than the base metal. Early studies considered the elements commonly found in the composition of carburising steel, such as silicon and aluminium (Kary 1948), had the greatest influence on internal oxidation and the possibility of internal oxidation of chromium, silicon, tungsten and molybdenum has been assumed (Hultgren and Haggeland 1947). The oxidation potentials of the main element used for alloying can be derived from the ratios of partial pressures of the oxidising and reducing constituent in the atmosphere, that is, pH_2O to pH_2 and pCO_2 to pCO. The results of calculation for a carburising temperature of 930°C as reported by Kozloskii et al (1967) are shown in Fig 2-4. The diagram shows that on heating at 930°C in an endothermic atmosphere, elements Ti, Si, Mn, and Cr are oxidised, while Fe W, Mo Ni and Cu are not oxidised, and oxides of these elements are reduced in the endothermic atmosphere.Therefore he concluded that the steel containing Cr, Mn, Si and Ti, and susceptible to internal oxidation when heat treated in an endothermic atmosphere. Parrish in his review paper (1976) further indicated that two possible important omissions from Kozloskii's diagram were Al and V, both of which were common addition to carburising steel. According to the Fig 2-5 (Fairbank and Palethorp 1966), these elements will oxidise in an endothermic atmosphere; thermodynamically, aluminium appears to be slightly more ready to oxidise than titanium, whereas vanadium will have an oxidation potential somewhere between those of silicon and manganese. Chatterijee-Fischer (1978) studied different alloys and further confirmed that Al was oxidised in an endothermic atmosphere, an increase of Al content of approximately 0.11% led to severe internal oxidation. Preston (1989) worked on a carburising steel with different V content. He found that internal oxides at the subsurface contained Cr, Mn and V. Agreeing with Preston, Murai et al (1999) reported

Fig. 2-4 Oxidation potential of alloy elements and iron in steel heated in endothermic gas with an average composition of 40%H_2, 20%CO, 1.5%CH_4,0.5%CO_2, 0.28%H_2O (dew point 10°C) and 37.72%N_2 (ref. Kozloskii 1967) that the V was detected as spherical oxides close to the surface of the steel containing 0.1 mass % V and 0.2 mass % V.

Fig. 2-5 Critical requirements for the oxidation of selected metals with indicated temperatures in atmospheres containing a) water vapour and hydrogen; b) carbon dioxide and carbon monoxide (ref. Fairbank 1966)

2.2.2 Morphology and Elemental Distribution in the Internal Oxidation Zone

In commercial carburising steel, the subsurface internal oxidation zone consists of two oxide morphologies. Kalner and Yurasov (1970) and Arkhipor and Kanunikova (1972) reported that the oxide nearest to the surface (approximately 8μm examined by optical microscopy) appeared as globular particles of approximately 1.5μm in diameter. The second type of oxide resided at depth typically 6-20μm and mainly occupied the prior austenite grain boundaries where it appeared as a continuous 'dark phase'. Kalner and Yursov (1970) analysed the distribution of elements in the internal oxidation zone by Cameca MS-46 microanalyser and found that the concentration of Cr and O decreased at the grain boundaries whilst Mn increased at the grain boundaries. Arkhipor et al (1972) reported that the concentration of Mn and Cr increased only in larger particles in the surface zone at a depth between 6.0-8.0 μm and the Si,O concentration increased at a deeper depth of 20μm in internally oxidised 30KhGT steel. Further, Chatterijee-Fischer (1978) first showed an interesting morphology of the oxide phase by electron probe microanalysis (EPMA) X-Ray mapping in Cr-Mn alloy steel, which was confirmed by later studies (Sun et al 1988, Wang 1991, Verhoeven et al 1992) and that it was a general characteristic of internal oxidation accompanying the carburising process. Verhoeven et al (1992) described this morphology of internal oxidation as two-zone morphology, as shown in Fig. 2-6. In outer zone, the oxide phase was predominantly in the form of small particles. In inner zone, oxides appeared as lie along grain boundaries. According to the EPMA mapping results, Chatterijee-Fischer (1978) concluded that Cr-oxides where only formed in the outer part close to the surface. Mn–oxides extended to a greater depth and Si-oxides appeared at the greatest distance from the surface. Hence, outer zone was rich in elements Cr and Mn, while that in inner zone was rich in element Si. Thyne and Krauss (1989) considered that the formation of globular boundary oxides took place due to a discontinuous, lamellar growth process in 20MnCr5 steel containing boron; that is, rods of the oxide form, each separated from the next by a band of alloy-depleted austenite. These rods tended to grow in the direction of the oxygen gradient. The oxides appeared as rows of spheres when viewed in cross section of rods. At greater depth within the oxidised layer, the oxides appeared to be continuous and at the prior austenite grain boundaries.

Chatterijee-Fischer (1978) did not report oxygen analysis. Verhoeven et al (1992) reported oxygen analysis by Auger mapping on a scanning auger microprobe. The oxygen was concentrated on the grain boundaries with a few particles located near the outer surface. The results confirmed that the morphology of internal oxidation zone produced by endothermic gas carburising for steel containing Cr, Mn and Si consisted

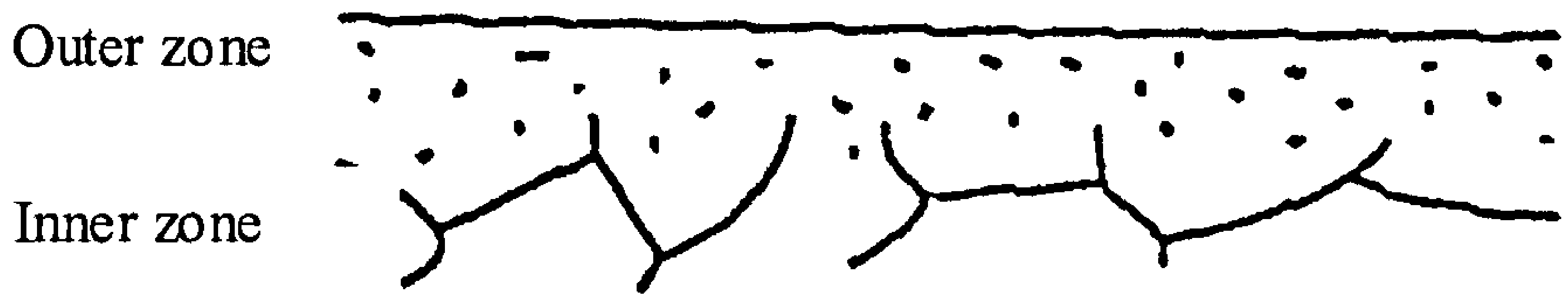

Fig. 2-6 Two-zone morphology of internal oxidation zone of carburised steel

of two zones, in which the outer zone 1 containing discrete particles of Cr and Mn oxide with little Si and a deeper zone 2 consisting of Si oxide on prior austenite grain boundaries. Krauss (1995) agreed with the two-zone morphology of internal oxidation and further indicated that outer zone , about 5μm thick, contained fine, intragranular spherical oxide particles, and inner zone, depth up to a approximately 30μm, contained oxides distributed along prior austenite grain boundaries in a 20Mn Cr_5 carburised steel. EDX analysis showed that intragranular particles were rich in Cr while the grain boundary oxides were of lamella or fibrous morphology and were rich in Mn and Si. Recently, an X- Ray line scan result of a SCM420 steel, as shown in Fig. 2-7, was given by Kanisawa (1997). It showed elemental distribution at different distances from surface. Cr was rich at the near surface between 0-10μm. Mn was rich at the 5.0-10.0 μm range whilst Si was rich at the 10-20μm range. Mo was constant over the measured zone (0-60μm). Oxygen was rich at 0-20μm close to the surface region. Further, analysis was carried out on one grain boundary by Auger Electron Spectroscopy (AES) by the same author. It showed that the Si concentration increased near the grain boundaries, then Mn and followed by Cr. There were no further studies as to why there was an absence of Si near the surface. Verhoeven et al (1992) assumed that in the early stages of the process, Si oxides would have formed only to be replaced later by Cr- Mn oxides. This mechanism is not well understood by current research.

Fig. 2-7 Element distribution from surface to core in Cr-Mn carburised steel (ref. Kanisawa 1997)

The penetration depth of internal oxides is influenced by a number of factors, such as carburising time, temperature and steel composition. In the commercial case hardening steels, the depth at which the oxides were detected by conventional optical microscopy was typical less then 25μm (i.e., for a carburised total case depths of 1 to 2mm). Deeper cases will produce deeper penetrating oxides; for example, a 8mm total case depth in Cr-Ni-Mo steel would likely have an oxide penetration depth of 75 to 100μm (Parrish 1999). The larger oxide layer usually penetrated to a depth of 6-8μm (Arkhipov 1972).

The penetration depth in research Cr-Mn carburised steel at which the oxides were detected by electron microscopy can reach to 30-50μm (Muriai 1999)

2.2.3 Internal Oxide Phases

Early research by Kalner and Yurasov (1970) , who studied Cr-Mn steel and detected oxides to a depth of 30μm, identified that internal oxides were complex oxides that contained at least two metallic elements with a spinel structure $nFeO.M_2O_3$, in which M was Mn or Cr. It was analysed that the total M content of the oxide was up to 15% Cr or 11.3% Mn. It was also found that some part of the M could be replaced by small amounts of titanium and molybdenum in those steels which contained them. The same authors observed that with samples of the same steel, carburised in the same heat, one sample produced the Cr-oxides and other produced Mn-oxides. The same situation was observed by Gunnerson (1963) that Cr and Mn formed independent oxide and the amount present depended upon their respective concentrations in the steel as a whole, or locally due to micro-segregation. However, Parrish (1999) believed that the reason for this difference in behaviour was not established, although it was considered that alloy segregation difference or the presence of varying amounts of carbide might have been responsible. It was interesting that titanium and molybdenum was deteced in the oxides in the steel only containing 0.1% Ti and Mo which were one of those alloying elements regarding as being unlikely to be oxidised. Parrish suggested that perhaps the atomic sizes of titanium and molybdenum compared with that of iron (Ti,+36%; Mo, +10%) made their inward or outward diffusion rates sluggish. A different internal oxide phase was reported in different carburising steel by Sun (1988), who identified an oxide phase determined by X-ray diffraction in 20CrMnTi steel to be FeO, Cr_2O_3 which was larger and denser, and mainly distributed on the grain boundaries and appeared in a network form. There were small oxide particles within the grains that were more homogeneous at the surface layer. The Si_nO and $(Cr_xMn_y)_nO$ as precipitates were also detected in Mn-Cr-B steel (Parrish 1999). In another study (Yi 1991), internal oxides, $(Mn_{0.84}Fe_{0.17})$, $(Al_{1.96}Fe)O_4$, $Fe(AlCr)_2O_4$ and Fe_2SiO_4 were identified in 20Cr, 20CrNi, GCr15 steel by TEM. The former was a spinel type, and latter resembled an olivine type. Intergranular oxides formed further from the surface (typically μm) were reported in the above research as SiO_2. However, Vehoeven et al (1992) found that a Si rich oxidation layer on the grain boundaries consisted primarily of a mixture of SiO_2 and Fe_2SiO_4 plus metallic bond Si throughout the thickness of the layer in Cr-Mn steel. The thicker of the Si oxide layers, which was determined by EDS point analysis on the fracture surface, to be approximately 120nm. Agreeing with the former study, Wang (1991) also reported an internal oxide phase in Cr-Mn steel as $FeCr_2O_4$, $FeSiO_4$ which appeared as a distribution of globules along the grain boundaries. However, Dowling et al (1995) found that Mn_2SiO_4 in a carburised SAE 4615 steel and $Mn_2Cr_3O_4$ as cubic shape in dimension about 1μm in a carburised SAE 8620 steel. The internal oxides were identified by electron diffraction and energy dispersive X-ray analysis (EDS). Semi-quantitative EDS analysis of Cr-Mn oxides showed the Mn/Cr ratio to be closer to 2/3. It was also observed that some prior austenite grain boundaries in 8620 steel exhibited grain boundary oxidation in the form of an amorphous iron-silica phase. The increased propensity of the amorphous silica content of the 4615 alloy compared with 8620 alloy was observed due to the increase silicon content of the 4615 alloy. Recently, Murai et al (1999) studied internal oxides in a Cr-Mn steel with different carburised conditions by combined X-ray diffraction and TEM. Extraction replicas of massive and spherical oxides from surface oxide layer of the specimens identified that oxides were Cr_2MnO_4, a spinel type.

The composition of an oxide phase at any depth from the surface is primarily governed by its free energy of formation. Stephenson and Michael (1988) found that oxide particles in the Si-Al steel were duplex particles in diameter between 0.1-0.2 μm with a core of Al_2O_3 surrounded by a shell of SiO_2. Consequently, the Al_2O_3 core must be precipitated first followed by the SiO_2 shell with some MnO dissolving in the latter becoming somewhat spherical. The sequence was considered with the free energy of precipitate oxides. The free energy of formation for Al_2O_3 was more negative than the free energy of formation for SiO_2, with MnO the less negative. The particles formed initially as Al_2O_3 rectangular plates and became spherical with time as the SiO_2 shell formed. The oxides which were observed at the internal oxidation front appeared to be Al_2O_3 without a shell of SiO_2. The same situation was observed in another oxide that the core of the precipitate was Al rich while shell contained Al and Mn. The atomic ratios O/Si and O/Al in the shell and core of the precipitates were determined by quantitative microanalysis. O/Si ratio was 2.0±3 and O/Al ratio was 1.8±0.5. However, in Mn-P steel, internal oxides were roughly spherical (Mn,Fe)P oxides, and, possible $2(Mn,Fe)O.P_2O_5$. The precipitates usually contained a Cr-rich inclusion, possible, $2(Mn,Fe)\,O.Cr_2O_3$, which may have been created with the (Mn,Fe)P oxide. The degree of internal oxidation of a Mn-P steel was less than a Si-Al steel. Recently, Liu and Chang (1997) explained the formation process of internal oxides of $MnAl_2O_4$ and Al_2O_3 in a carburised and internal oxidised Cr-Mn-Al alloy. They considered that the equilibrium oxygen pressure of Al_2O_3 formation was two orders of magnitude lower than that of $MnAl_2O_4$ in the temperature range studied. Measurements found that the Al content of the internal oxide at the frontier of the internal oxide layer and of the centre of a large oxides were higher than at all other locations. This implied that Al_2O_3 formed first during internal oxidation at the frontier of the internal oxide layer where the concentration of dissolved oxygen was just over equilibrium level of Al_2O_3. The formation of the Al_2O_3 produced an Al depleted zone around Al_2O_3 particle which increased the equilibrium oxygen pressure for the formation of Al_2O_3. As the equilibrium oxygen partial pressure at the Al_2O_3 /matrix interface exceeded that of the $MnAl_2O_4$ phase, this oxide nucleated in the oxidation front to form of a spinel oxide.

2.2.4. Composition Gradient

The metal–oxygen reaction that led to the precipitation of oxides must produce local composition gradients of the participating elements between the oxidised and un-oxidised layers. Such an effect, involving both Cr and Mn, has been reported by a number of researchers (Smith 1975, Hilldenwell and Ericsson 1980) and later, has been summarised by Parrish (1999), as shown in Fig 2-8. It was understood that when an element migrating to the surface to form an oxide, the matrix materials in the vicinity of the oxide remains, if not completely depleted in the alloying element, substantially below the average level for the steel. Asa result of internal oxide formation, alloying elements were depleted within the matrix below the internal oxidation zone. In other words, alloy elements migrated to the oxide layer that was obviously observed in many researchers, typical as shown in Fig. 2-7 (Kansawa 1997). Recently, Li and Marral (2002) reported a local equilibrium model for internal oxidation. They indicated the average concentration of the solute (oxidised solute) in the internal oxidation region will always be less than the initial concentration of solute in the alloy, that the average concentration of solute decreases with increasing solute diffusivity and that the concentration of solute at the moving boundary between the internal oxidation region and unioxidised region approaches the initial alloy concentration as the solubility product and solute diffusivity approach zero.

The carbon content was also affected by the oxidation process. Kozlovskii (1967) related that a sample of a carburised steel 25KhGT exhibited a low carbon content in the internal oxidation layer. Clombo et al (1983) determined that the carbon content within the internal oxidation region (i.e., within the 20μm) was 0.53% C, which was lower than the deeper region (i.e., 0.1mm, 0.95%C). Shcherbedinskii and Shumakov (1979) also suggested that there was a reduced carbon content within the internal oxidation layer,

Fig. 2-8 Composition gradients associated with internal oxidation (ref. Parrish 1999).
a)15Cr4Ni6; b)20MnCrB5; c) SIS 2515

but only where oxides had formed. Recently, Murai et al (1999) studied the effect of alloying elements on equilibrium C content in Cr-Mn steel. He found that as carburising time was increased, the C content in the specimen deviated from the calculated values. The deviation was caused by a oxygen potential in the atmosphere which produced the oxides, thereby decreasing the amount of alloying elements in austenite which changed the activity coefficient of C in austenite. This deviation due to oxygen potential was enhanced by Si, Cr and V that also changed the activity coefficient of carbon. The results indicated that the growth of internal oxide may result in decarburisation which depends upon the total change of the activity coefficient for carbon. Murai et al (1999) considered that Si increased the activity coefficient of carbon in austenite, thus the decrease of the Si content in austenite resulted in an increase in carbon content. In contrast, Cr decreases the activity coefficient of carbon in austenite that resulted in a decrease in carbon content. So, Muriai indicated if reduction of Si and Cr was equal, the total change of activity coefficient for C would be negligible.

2.3 Factors Influencing the Internal Oxidation Zone

2.3.1 Alloy Elements

Namiki et al (1986) found that the depth of the internal oxidation layer increased with increasing alloying element content, and gave a composition parameter as (10Si+Mn+Cr). It indicated that the contribution of Si was almost 10 times as large as that of Mn and Cr. Agreeing with Namiki et al generally, Koyasu et al (1992) reported the composition parameter as (13Si+5Cr+Mn+1). Similarly, in a large study of a wide range of different steel compositions, Lohrmann & Lerche (2000), linearly correlated mean internal oxidation depth with total oxidation potential (= 4.87Si + 3.7Mn + 1.47Cr - 3.24Ni - 1.82Mo). Thus, these specific cases confirmed the widely held view that the Si is the most important factor in determining the internal oxidation kinetics. Further, Murai et al (1993) studied a wide range of steels and found that the penetration depth of internal oxides increased with increasing Si ,Mn and Cr content until it reached a limiting point, where, it decreased with further increases in alloying element. This limiting point was found to be in the range of 0.5-0.6% for Si, Cr about 0.8%, and Mn 2.1%. Meanwhile, the penetration depth of internal oxides decreased with increasing Mo, Ni and Cu content in the range of 1.0-10%. Similar results was give by Sakamoto et al (1995), in his study, the limiting point for Si was approximately 0.35%, below this level, the penetration depth of internal oxides increased with increasing Si content.

The above research indicated that silicon strongly inflenced the internal oxidation in carburised steel. Chatterijee-Fischer (1978) studied various Fe-Cr, Fe-Cr- Mo and Fe-Ni-Mo alloys with different Si contents in the range of 0-0.3%. The results showed that the penetration depth of internal oxides increased with increasing of Si content in the matrix, the observation was also evident for the Fe-Si alloy. It was found that pure iron did not oxidise whilst with a silicon content of 0.09% already led to the formation of the internal oxidation. The conclusion given in this work was that silicon content seemed to be a major factor affecting internal oxidation.

Kanazawa et al (1997) found that when Si<0.9%, Mn<0.7%, Cr<0.5%, the internal oxides precipitated on grain boundaries. When Si>0.9%, Mn<0.7%, Cr<0.5%, internal oxides precipitated within grains as well as on grain boundaries. Meanwhile, surface spall off was observed by Williams (1997 and 1998), who indicated that as the Si content increased from 0.065% to 0.77%, the proportion of globular oxides decreased and became more confined towards the surface. The proportion of the intergranular oxides was at a minimum for the 0.065% Si steel and increased with increasing Si content. The total oxidation depth reached a maximum at 0.1-0.3% Si but decreased for higher or lower silicon levels. Hence, the results confirmed again that Si was a major factor affecting internal oxidation. Although the penetration depth of the internal oxides decreased with further increasing of Si content, the internal oxides was more dense with increasing Si content.

The influence of alloy elements on internal oxidation was studied in conjunction with the development new steel for the significance of the low Si steel, US patent (1990) that was concerned with the avoidance of internal oxidation during the carburising process and specifies a Si level below 0.11%. Agreeing with former work, the US patent which was awarded to Burris (1996) reported that it had been discovered within the present invention, that an even lower Si level, of below 0.05% decreased internal oxidation without decreasing the mechanical properties. Similar work has been done by Murai et al (1993), Kurokawa (1996), Ban (1995), as shown in Table 2-1. A new steel exhibited excellent properties for reducing intergranular oxidation and improving fatigue and impact strength of the tooth root comparing with SCM420. However, another Canadian patent, registered by Sakamoto et al (1995) gave opposing views, who developed a new steel for carburised gears (Table 2-1) base on the research that high Si (exceeding 0.45%Si) decreased the penetration depth of internal oxides. According to this work, when the Si exceed 0.45%, internal oxidation depth was limited to approximately 10μm, therefore, the Si content in the new steel was (0.45-1)%. The new steel exhibited a prolonged pitting fatigue life and cost reduction. The new low Si, low Cr steels was also developed by a number of authors (Hirai 1989 and Tanaka 1993). In those steels, the Si was reduced to 0-0.03 % and Cr was reduced to 0.01% (Hirai 1989). The steels exhibited no internal oxidation layer at the surface and maintained excellent fatigue strength. The steels were a potential heavy-duty gear material that could can meet an ever increasing demand of the automotive industry for weight reduction and increased engine output.

Besides the Si content, other alloy elements were studied. Chatterijee-Fischer (1978) reported that an increase in Al of approximately 0.11% led to severe internal oxidation. The use of Nb for grain size control appeared more suitable than Ti in carburised steel because at the low concentration it hardly formed internal oxides while Ti lead to severe oxidation even at low contents. If V was to be used for this purpose, it should be lower than 0.08%. According to the Okasaki (1973), in a steel with up to 0.1% titanium, the oxygen, carbon, nitrogen and sulphur, that inhibit grain growth, combined with the titanium to reduce the grain boundary oxidation (0.1%Ti having the maximum. effect). Therefore, Ti content in excess of 0.1% would be expected to support the internal oxidation reaction. Molybdenum was an effective element to reduce the internal oxidation, however, Kalner and Yurasov (1970) found the addition of 0.6%Mo in Cr-Mn carburised steel did not eliminate or reduce the internal oxidation. Nakamura et al (1993) believed that 0.8%Mo in steel was effectively in inhibiting internal oxidation, especial for non-martensitic transformation products. The new steel was recommend in this study which contained 0.86%Mo, 0.09%Si , Cr and Mn content maintained at normal levels (Table 2-1).

Fig. 2-4 indicates which elements in steel were likely to oxidise during the carburising process. However, it does not consider how much of any particular element is needed for the oxidation reaction to take place. Chatterijee-Fischer (1978) studied the pure Fe-Si, Fe-Mn and Fe-Cr alloy systems and confirmed that those alloys containing elements with a propensity to oxidise do indeed oxidise, provided that a sufficient amount of that elements was present. Parrish (1999) analysed Chatterijee-Fischer's results and considered the limiting elements content related with its atomic size and atomic number. The elements with larger atomic sizes, or similar atomic number, need only be present in amounts of less than 0.1 by vol. % to promote internal oxidation, whereas significantly more was needed for those elements whose atoms were of a similar size to that of iron.

2.3.2 Variable Gas Carburising Processes

Internal oxidation occurs due to oxygen containing compounds, such as CO, CO_2 and etc that are present in most gas carburising media. To minimise internal oxidation it is necessary to decrease the amount of oxygen compounds. Chatterijee-Fischer (1978) studied the effect of the CO_2 content (0.1-0.45%) on internal oxidation in a given carburising atmosphere and found that the depth of internal oxidation decreased with increasing carbon potential, the higher the carbon potential, and the lower the CO_2 content.

Dawes and Cooksey (1966) estimated that 0.2% would be the maximum value of CO_2 that could be tolerated to prevent internal oxidation of a 1% Cr steel, and that 0.01% CO_2 would be the limit for 1% Mn steel. When carburising a 16MnCr5 steel with the carbon potential and carburising duration each held essentially constant, doubling the carbon monoxide content from 20 to 40% doubles the depth to which the internal oxides penetrated (Edenhofer 1995). A similar result was given by Stratton and Tsujimoto (2000), as shown in Fig. 2-9.

The different atmosphere conditions in the gas carburising process must strongly affect on the degree of internal oxidation. Kim and Lee (1991) reported that with increasing oxygen concentration in organic liquid (e.g. methanol + toluene, methanol + acetone) and decreasing nitrogen addition to the carburising atmosphere, the depth of internal oxidation layer was increased. The control of internal oxidation in drip-free carburising atmospheres was possible by lowering the CO gas content of the carburising atmosphere by the addition of N_2 gas. Although non-cryogenically-generated nitrogen has been employed as the basis of nitrogen/methanol carburising for several years. The effect of the level of oxygen impurity present in the gas was still poorly documented. Stratton and Tsujimoto (2000) studied this phenomenon and found that small amounts of residual oxygen in non-cryogenically-generated nitrogen led to increasing internal oxidation by direct reaction with free oxygen with the steel before it could take part in the slow reactions that buffer it in the carburising atmosphere. When employing 99.9% nitrogen, no evidence of influence on the internal oxidation occurred. However, the use of 99% purity nitrogen required minor adjustments to the carbon potential control parameter in order to obtained similar properties. It was recommended that for most applications, 99.5% purity gas was used. Edenhofer (1999) compared the gas carburising process, employing traditional generated endothermic carrier gas and direct-feed atmospheres, with the use of pure hydrocarbon and reported that direct- feed atmosphere offered the benefits of total suppression of internal oxidation due to the

Fig. 2-9 Internal oxidation of SCR420 and SMC420 steel after heating 5 h at 930°C as function of carbon monoxides content (ref. Stratton 2000) absence of oxygen bearing gases. An industrially proven process that utilised the high carbon transfer rate of hydrocarbon gases in controllable carburising process was given by Gantois et al (1999). It confirmed that the process reduced cycle time significantly and internal oxidation was less (but not eliminated) than in normal carrier gas treatment. In recently research, Lohrmann and Lerche (2000) looked at different atmosphere processes and found that if a low oxygen atmosphere was generated during most of the carburising phase (e.g. by injecting only natural gas), the resulting internal oxidation was reduced quite significantly at the end of the whole cycle. For example, whether carburising was accomplished with natural gas and air, using the direct feed or with endogas and natural gas, using the carrier gas, the average penetration depth of the internal oxides was about 20-25μm at end of whole cycle. By injecting only natural gas, the penetration depth of the internal oxides at the end of whole cycle was reduced to some 5-10μm.

The carburising time and temperature also affected internal oxidation. Chatter-Fischer (1978) stated that for a given temperature, the increase of the penetration depth of the internal oxides was proportional to the square root of the carburising time. The longer the carburising time and the higher the carburising temperature, the depth of the internal oxidation layer was increased. For a given time, the penetration depth of internal oxides will be greater at higher temperatures. Similar results were reported recently by Kizu et al (2002) who studied internal oxidation of ultra-low carbon steel. However, the atmosphere in a furnace will vary with different heating stages in commercial carburising processes. Hence, the degree of the internal oxidation will be different at different time stages. It has been assumed that a large proportion of internal oxidation occurred during the early heat treatment stage (Hoffmann 1984). However, recent studies by Lohrmann and Lerche (2000) reported that internal oxidation during the heat-up phase, was very limited and not affected by the duration of the heat-up time within the normal range of 50-90 minutes. Most of the internal oxidation occurred during the carburising stage. The internal oxidation increased with an increase in case depth, in other words, as carburised time increased.

2.4 Influence of Internal Oxidation on Materials Properties

Internal oxidation may affect the materials properties in the following ways:

1) By its structure, e.g. the presence of the non-martensitic microstructure with low hardness and low strength.
2) By the different distribution of residual stresses (lower compressive stresses or even tensile stress near surface).
3) By cracking or even crumbling of the surface in case of severe grain boundary oxidation.

2.4.1 Microstructure

Due to internal oxide formation, depletion of the alloying elements occurs in the matrix of the near the surface region resulting in a loss of case hardenability. The material locally adjacent to the oxides will have its transformation behaviour modified. Hence, instead of the expected martensite, non-martensitic transformation products can be developed during the quenching process. This non-martensitic microstructure, which occupies the same area affected by internal oxidation, was variously described as pearlite or quenching pearlite, or either or both lower and upper bainites, or mixtures of all of them. Whichever non-martensitic microstructure was formed, it will be comprised of ferrite and carbides. Kalimin (1965) reported this phenomenon early in 1965. Later, Arkhipov (1972) found the radial pealite and bainite appeared in the surface to a depth of approximately 10μm near the particles of non-metallic phase; in a lower layer, 5-10μm thick, a substantial number of grains had a bainitic structure. The non-martensitic transformation products (troosite) were also observed around nonmetallic inclusions to a depth of 0.1mm in Cr-Mn-Ti carburising steel. The influence of depletion of alloying element on hardenabiliy was reported by Parrsh (1999). He indicated that even with a section equivalent to a 50mm diameter bar, some bainite would form if the manganese and chromium were reduced to half of their original amount as a result of internal oxidation. This excluded the likelihood of the internal oxidation providing favourable sites for the nucleation of non-martensitic transformation products. If the carbon content was reduced to 0.5%, then for the 17CrNiMo6 steel, the largest section to avoid bainite formation in the low-carbon surface layer is 100mm. If the low carbon content surface layer was accompanied by a 50% reduction of both Mn and Cr, the limiting section will be approximately 37mm. If, however, the Mn and Cr were completely removed by the formation of internal oxides, even thin sections will have a bainite microstructure in region of internal oxidation.

It considered that no non-martensitic transformation products would be formed when the cooling rate was high or when there were sufficient amounts of nickel and molybdenum in the matrix adjacent to the oxides. Sun (1988) described the non-martensite microstructure in 20CrMn steel to be a very fine pearlite layer in the near the surface and under this layer, pearlite and upper bainite in mixed non-martensitic layer with a non-uniform distribution along the surface carburised layer. An increase in cooling rate was an effective means of controlling or decreasing the depth of the non-martensitic microstructure layer from 100μm to 10μm. Murai et al (1993) studied a wide range of carburising steels and further confirmed that higher cooling rates resulted in a decreased depth of the non-martensitic layer. For the same steel with Si content of 0.1% in different section diameter, the depth of the non-martensitic microstructure layer was about 19μm in section diameter of 40mm but only about 4μm in section diameter of 10mm.

The increase of Mo and Ni content in steel will benefit the reduction the of depth of the non-martensitic microstructure layer. One example was given by Doweling et al (1995). He found that non-martensitic transformation products associated with internal oxidation in a carburised SAE 8620 steel consisted of both pearlite and bainite. Only martensitic was observed in the surface of a carburised SAE4615 steel, which has same carburising process as SAE 8620. The reason for this was that higher Ni and Mo content add in SAE 4615, which maintained adequate hardenability and did not oxidise during the gas carburising. Another example was given by Nakamura et al (1993), who reported that raising the Mo content inhibited the formation of a non-martensitic microstructure layer, which disappeared when Mo content was 0.8%.

2.4.2 Residual Stress

The residual stress through the roots of case-hardened gear has been determined for a number of steels by Arkhipov (1970), and trend towards tensile residual stresses at the surface. Additional work on the same gear showed that the greater the tensile residual stress, the lower the fatigue strength. Similar observations were reported by Naito (1984) for carburised SCM 415 with internal oxidation and non-martensitic transformation products at the surface, the tensile stress was approximately 40MPa. Dowling (1992) compared the residual stresses in two case-hardened surfaces, as shown in Fig 2-10: one steel (8620 steel) that formed pearlite and bainite internal oxidation and another steel (4615 steel) that exhibited no non-martensitic transformation products formed while there was internal oxidation. The surface residual stresses in the 8620 steel were about zero compared to the approximately –210Mpa found in the 4615 steel.

Parrish (1999) considered that the oxides of Cr, Mn and Si that formed in the surface of components during their carburisation, would likely be in compression when the temperature reduces to room temperature because their volume thermal contraction over the temperature range 920 to 20°C will be less than that of the steel in which they resided. The non-martensitic microstructure associated with those oxides was in a residual tensile stress state. This was partly due to the volume mismatch between the non-martensitic transformation products and the underlying high-carbon martensite. He believed that non-martensitic transformation products were probably the first material to transform, while the adjacent martensitic was the last to transform. This different tensile and compression situation determined the residual stresses at the surface of carburised component.

2.4.3 Mechanical Properties

2.4.3.1 Bending Fatigue

Parrish (1976,1985) reviewed earlier studies and believed that the depth of internal oxidation had a significant bearing on the response of the component to fatigue. The internal oxidation to a depth of 6-10μm did not affect the bending fatigue strength when compared with tests where the test pieces were free from oxidation, but when the depth of oxidation was greater than the threshold depth of 13μm, reductions in the fatigue limit were observed. Later Parish (1999) further reported that idea that there was a threshold might not incorrect, though other work has indicated that a presence of less than 13μm of non-martensitic transformation product had led to a reduction of fatigue strength (Ono 1981); Ono reported that 11μm of non-martensitic transformation products caused a 15% reduction in fatigue strength. The summaries of test results on different carburised steels showed that due to internal oxidation, the tensile residual stresses in the surface were increased, and the hardness of the surface and hence fatigue limit were decreased. It indicated that if the internal oxidation was accompanied by non-martensite transformation product, the bending fatigue strength would be significantly reduced. As the depth of the non-martensitic layer increased from 7μm to 17 μm, the bending fatigue limits decrease from 71kg/mm^2 to 49kg/mm^2. It could be that smaller amounts of non-martensitic transformation products did cause reduction of fatigue life, but the amount was sufficiently small to be regarded as insignificant.

Naito et al (1984, 1985) and Kikachi (1987) reported the fatigue behaviour of two carburised steel, Mn-Cr-Ni steel and Cr-Mn steel, in their series of papers during 1984-1987. The former had internal oxidation and the later had internal oxidation with non-martensitic microstructure near to the surface up to 30μm causing residual tensile stress at the surface. Both steels had similar fracture origins, beginning at the oxidised grain boundary sites. Further studies by Kikuchi (1986) found that shot peening was an effective means to improve fatigue durability of carburised steel with surface anomalies and it could increase the fatigue strength of steel by as much as 50%. Therefore, it was concluded in this study that the non-martensitic microstructure was one of the major factors affecting the fatigue behaviour of carburised low alloy steels. Later research by Dowling (1995) further confirmed that fatigue strength of carburised steel was low in the surface non-martensitic layer and internal oxides acted as the defect to the initiate fatigue cracks. Two steels (ASTM 8620 and 4615) had similar internal oxidation layers (5 μm) but had quite different fatigue behaviour because that 8620 steel had a non-martensitic layer at the surface of approximately 10μm but 4615 steel did not, as shown in Fig 2-11. The bending fatigue performance of the 4615 was 20% better than 8620 steel. After removing the surface defect for both steels, the fatigue resistance of 8620 steel was improved substantially, whilst the 4615 steel was unchanged.

Parrish (1999) summarised the existing test data which indicated that in the low-cycle region of the S-N plots, there was a general trend toward a small adverse effect (0 to 12% reduction of strength at 10^4 cycles) due to the presence of the non-martensitc microstructure layer. In the high cycle region, the fatigue life can be reduced by as much as 45% due to the presence of the non-martensitic microstructure layer, though 20-35% was more common. The amount depended upon the depth, microstructure, and the hardness of the non-martensitic microstructure layer.

Fig. 2-11 S-N curve for fatigue test on carbuirsed 4615 and 8620 (ref. Dowling 1995)

Kikuchi et al (1989) showed the influence of internal oxides on the fatigue strength of carburised steels was strongly affected by the amount of retained austenite (γ_R) and the non-martensitic microstructure at the surface. Rotating bending fatigue tests were carried out on the three types of carburised specimen that had the same depth of internal oxides but contains 20% and 46% γ_R (peak value), and 20% γ_R with non-martensitic microstructure. Internal oxides reduced the fatigue strength about 30% on the specimen with 20%γ_R, whereas the specimen with 46% γ_R has a comparable fatigue strength to the specimen without internal oxides which was prepared by electroplating the surface. It was also shown that the specimen with non-martensitic microstructure had higher fatigue strength than those specimens with only internal oxides. The three types of specimens exhibited almost the same fatigue strength when the internal oxides were removed from the surface. The results of this study did not agree with other studies.

It was interesting to note the influence of grain size on bending fatigue. Pacheco and Krauss (1989) compared with plasma carburised sample without internal oxidation and gas carburised sample with a sample that contained internal oxidation to a depth of - 13μm without non-martensitic transformation products. He found the fine grained gas carburised specimen tolerate the presence of intergranular surface oxidation and had better fatigue resistance than coarse grained specimen without surface oxidation. The transformation of a finer parent austenite microstructure led to finer mixtures of tempered martensite and retained austenite. The finer composite mixtures have been shown to have higher elastic limits than coarse distribution of retained austenite and martensite, and were therefore more resistant to low strain plastic deformation mechanisms which led to high cycle fatigue crack initiation and propagation. Further work by Krauss (1999) confirmed the fatigue strength of carburised steel could be improved by reducing prior austenite grain size. Satoshi and Koide (1989) reported that the bend fatigue limit load of the gas carburised gear was smaller than vacuum carburised gear due to the effect of the intergranular oxidation.

2.4.3.2 Contact and Impact Fatigue Strength

There is little data available on the subject, and these tend to conflict. Early studies by Sheehan et al (1972) reported that the presence of internal oxidation in case hardened SAE 8620 was not significant to the contact fatigue resistance, and even beneficial, to contact durability under slide-roll test conditions. The test results showed that there was generally no loss of contact fatigue resistance until the internal oxidation and non-martensitic microstructure had been removed. They considered that plastic deformation within the non-martensitic transformation product layer, which would bring about a more favourable distribution of contact load, could only account for part of the difference shown. However, later studies by Kanisaw (1993) found that pitting strength increased with decreasing internal oxidation because that formation of cracks was decreased. Kimura's (1998) study also confirmed that specimens with non-martensitic microstructure at the surface showed lower pitting resistance. At the surface of the carburised specimens, martensite areas derived from low hardenability due to internal oxidation were worn and detached with increase in the content rolling cycles. It roughened the contact track and accelerated the main propagation.

Namiki et al (1989) reported that impact strength was also proportional to composition parameter (Ni+Mo/10Si+Mn+Cr). The parameter was based upon the concept that oxide formers, especially Si, affected the fatigue strength of carburised steels strength by the promotion of intergranular oxidation, whereas Ni and Mo raised fatigue resistance without forming oxide.

Table 2-1 New Grade Steel Developed In Recently Years

No (Inventor)	Composition mass %							
	C	Si	Mn	Cr	Mo	Ni	Cu	Other
1 (Burris 1996)	0.20-0.22	0-0.05	1.00-1.20	0.50-0.65	0.12-0.15	0.09		
2 (Murai 1993)	0.20	0.07	0.70	0.95	0.39	0.04		
3 (Kurokawa 1996)	0.20	0.10	0.45		0.80	2.00		Nb addition
4 (Ben 1995)	0.15-0.25	0.10-0.15	0.45-0.65	0.50-0.60	0.40-0.80	1.0-2.50		V, Nb addition
5 (Nakamura 1993)	0.20	0.09	0.80	1.06	0.86	0.02		
6 (Sakamoto 1995)	0.18-0.25	0.45-1.00	0.40-0.70	1.0-1.5	0.30-0.70	0.30-0.70	>0.50	
7 (Hirai 1989)	0.20	0-0.02	0.33	0.01	0.80	2.00		Nb: 0.02
8 (Tanaka 1993)	0.18	0-0.03	0.33-0.45	0.08-0.02	0.75-0.85	2.00		Nb: 0.025
9 (Tanaka 1993)	0.20	0.03	0.35-0.45	0.60-0.65	1.00-1.05	0.22		Nb: 0.030
SCM420	0.20	0.20	0.75	1.07	0.17	0.04		

CHAPTER 3

EXPERIMENTAL PROCEDURES

3.1 Materials

A carburising steel is usually selected on the basis of case and core hardenability. Alloy steels are used for the most heavily loaded parts, such as automotive gears. The materials studied in this work were commercial carburised steels with different Si contents and were mainly supplied by Corus, Swinden Technology Centre. The composition of the materials were to one of company grade V2525-70 (Volvo), with silicon contents in the range (0.11- 0.77) % in order to study influence of silicon content on the internal oxidation phenomena. The product chemical analyses are given in Table 3-1, in order of their silicon contents. There were two groups samples, one group were carburised samples, in which the carburising treatment was carried out using a standard commercial cycle in a 'WARST' furnace in VOLVO and delivered to the MRI for further study of the influence of silicon on the internal oxidation phenomena and detailed analysis on the internal oxide phases by Transmission Electron Microscopy (TEM). The second group were uncarburised bars, in which further carburising treatment was carried out by a variable carburising process. First, the steel bars (25mm diameter × 150mm long) were normalised from 850°C and ground to 22 mm diameter at the Swindon Technology Centre. Then, small samples of dimensions 22x30mm were cut from the bar in the MRI laboratory. A fresh surface was then prepared by a conventional grinding process. Grinding was done using progressively finer metallographic grinding papers down to $1200^{\#}$ paper ready for carburising treatment. The surface condition of the prepared specimens is shown in Fig. 3-1.

Table 3-1 Specimens Chemical Composition

Samples	Steel type	Analysis mass %										
		C	Si	Mn	Cr	Mo	Ni	Cu	Al	P	S	Sn
A	commercial	0.20	0.11	1.05	1.06	0.14	1.12	0.16	0.020		0.052	0.007
B	commercial	0.19	0.19	1.02	1.01	0.13	1.14	0.17	0.019	0.010	0.049	0.009
C	commercial	0.19	0.31	1.00	0.96	0.11	1.07	0.21	0.025	0.012	0.047	0.011
D	experimental	0.18	0.56	0.96	1.06	0.12	1.17	0.19	0.017	0.011	0.051	0.011
E	experimental	0.18	0.77	0.81	1.03	0.12	1.18	0.19	0.024	0.011	0.053	0.014

* These elements only are from cast analyses undertaken at STC

3.2 Gas Carburising

3.2.1 Commercial Gas Carburising Process

Carburising is a case hardening process by which carbon is dissolved in the surface layers of a steel-part at a temperature sufficient to render the steel austenitic, followed by quenching and tempering to form a matensitic microstructure. As there is a resulting carbon gradient from surface to core, there will be a higher hardness at the surface and subsurface region that produces a strong, wear- resistant surface layer on the part.

Gas carburising is a recommended method in commercial carburising process. It can be described by two steps: 1) reaction in the gaseous atmosphere and absorption of carbon at the boundary layers at the surface of the steel; 2) diffusion of carbon from the surface to the interior of the steel. The source of carbon is a carbon rich furnace atmosphere produced usually by a carrier gas-endothermic gas, in which is a blend of carbon monoxide, hydrogen and nitrogen producing by reacting a hydrocarbon gas such as methane. The carrier gas performs with reaction (Stickel 1991):

$$2CO = C + CO_2 \text{ ------------------------------ } (3\text{-}1)$$

$CO + H_2 = C + H_2O$ -------------------------- (3-2)

$CO = C + 1/2\ O_2$ ------------------------------ (3-3)

$CH_4 = C + 2H_2$ --------------------------------- (3-4)

to introduce carbon into the surface of a steel. With the equilibrium reaction of the constituents of the atmosphere (water -gas equilibrium)

$CO_2 + H_2 = CO + H_2O$ ---------------------- (3-5)

The carbon dioxide from reaction (3-5) is decomposed again. These reactions have both a carburising and a decarburising effect, which means that after sufficient carburising time an equilibrium between carburisation and decarburisation is established whose carbon content is known as the carbon potential. It is defined as the carbon dissolved in pure iron that is in thermodynamic equilibrium with the atmosphere. The carbon potential of the furnace atmosphere must be higher than the carbon potential of the surface of the workpieces in order for carburising to occur. The different carbon potential provides the driving force for carbon transfer from the atmosphere to the parts.

Three principal variables factors have an effect on the gas carburising process. 1) temperature; 2) time; 3) atmosphere. The temperature most commonly used for carburise is 920 ± 10 °C. This temperature permits a reasonably rapid carburising rate without rapid deterioration of furnace equipment. Carburising is dependent on the case depth required. Carbon potential control is achieved by varying the flow rate of the hydrocarbon –enriching gas, while maintaining a steady flow of endothermic carrier gas. The combined effects of the temperature, time and carbon concentration on the diffusion of carbon in austenite can be expressed by Fick'laws of diffusion. Carbon diffusion determines the rate of carbursing. The carburising time can only be reduced by higher temperature for a required case depth.

3.2.2 Experimental Gas Carburising Procedures

The commercial carburising process develops the carbrising treatment that will produce a specific case hardness, case depth and core hardness required to meet the service loads. Therefore, the combined factors, such as case microstructure, residual stress, alloy selection, operating schedules are considered in setting up the process. Most processes are set up in boost-diffuse mode (Stickel 1991). The boost step is at relatively high temperature and high carbon potential to facilitate the rapid development of a deep case; the diffuse step is at lower carbon potential, allowing the case carbon content to decrease to the desired level. Modern commercial carburising furnaces are equipped with computer control system to control the process parameters.

The samples studied were carburised in a commercial batch furnace at Davie Brown Heatech Ltd. The carbon potential was controlled according equation (3-1) (by using infrared analysis of carbon dioxide content of atmosphere), equation (3-2) (dew point analysis of the water vapour content) and equation (3-3) (measuring of oxygen content with an oxygen probe). The carburising process is shown in Fig.3-2. Usually, the parts were put into the furnace at 800°C, given a certain time to achieve uniform heating at this temperature (2.0h), this process is known as the base process. During this process, the carbon potential is uncontrolled and varied in the range (0.3-0.6) %. Then the furnace temperature is raised to 930°C, the carbon potential is raised to 1.2% and given a certain time to reach thermal equilibrium (3.0-5.0h). Following that, a full carburising atmosphere was introduced to the furnace until required carburised time was reached. The oxygen partial pressure in the different heating stage is shown in Table 3-2. It shown that lowest oxygen partial pressure was in the low temperature base process (800°C, 2.0h). The highest oxygen partial pressure was in the high temperature base process (930 °C, 3h). Finally, the parts were taken out from the furnace and quenched and tempered to obtain the required microstructure.

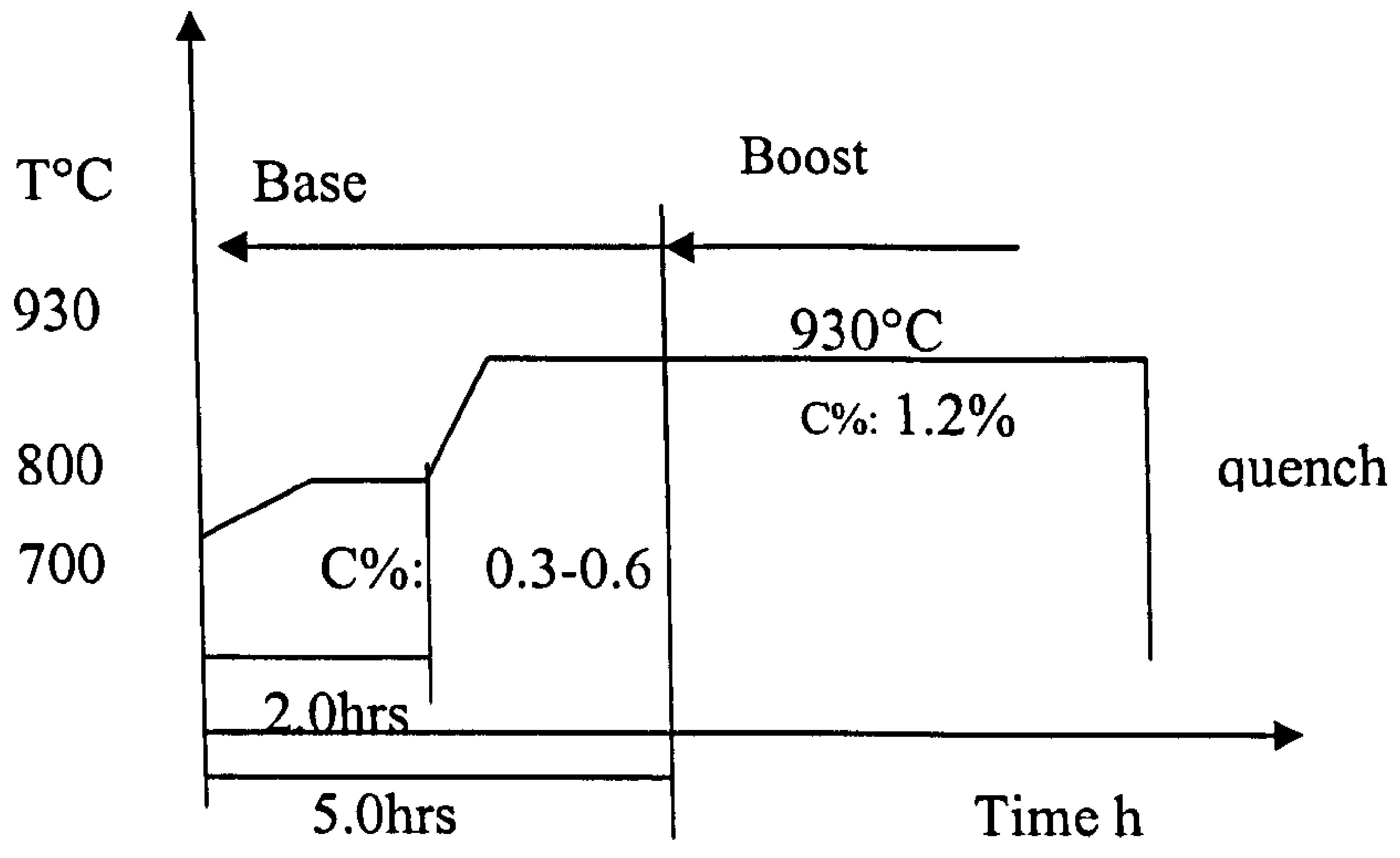

Fig. 3-2 Experimental Gas Carburising Process

Table 3-2 Oxygen Partial Pressure in the Atmosphere

Carbon Potential	**Temp' °C**	**% CO**	**O_2 Probe mV**	**CO_2 %**	**O_2 Partial Pressure**
Base	800	17%	1100	0.70	5.E-21
Base	930	"	1120	0.25	2.E-19
0.40	930	"	1125	0.22	2.E-19
0.68	930	"	1150	0.150	4.E-20
1.00	930	"	1160	0.085	3.E-20
1.20	930	"	1170	0.070	2.E-20

In order to study the internal oxidation growth process and the effect of the carbon potential on the internal oxidation, different kinds of carburising process were chosen in this work, as shown in Table. 3-3.

Table 3-3 **Gas Carburising Procedures**

Carburised procedure	Samples	Samples' I'D	Exposure time h	Carbon potential %	temperature °C
procedure 1	B1, C1, D1	B1-1, C1-1, D1-1	0.25	0.3-0.6	800
	B1, C1, D1	B1-2,C1-2,D1-2	0.5	0.3-0.6	800
	B1, C1, D1	B1-3, C1-3, D1-3	1.0	0.3-0.6	800
	A1, B1, C1, D1, E1	A1-1,B1-4, C1-4, D1-4, E1-1	2.0	0.3-0.6	800
	B1, C1, D1	B1-5, C1-5, D1-5	5.8	0.3-0.6, 1.2	800-930
	B1, C1, D1	B1-6, C1-6, D1-6	8.0	0.3-0.6, 1.2	800-930
	B1, C1, D1	B1-7, C1-7, D1-7	11.0	0.3-0.6,1.2	800-930
	A1, B1, C1, D1, E1	B1-8,C1-8, D1-8	16.6	0.3-0.6, 1.2	800-930
procedure2	B2, C2, D2	B2-1, C2-1, D2-1	0.5	1.2	930
	B2, C2, D2	B2-2, C2-2, D2-2	1.0	1.2	930
	B2, C2, D2	B2-3, C2-3, D2-3	2.0	1.2	930
	B2, C2, D2	B2-4, C2-4, D2-4	2.9	1.2	930
	B2, C2, D2	B2-5, C2-5, D2-5	6.9	1.2	930
	B2, C2, D2	B2-6, C2-6, D2-6	12.5	1.2	930
	A2,B2, C2, D2, E2	A2-7,B2-7, C2-7, D2-7, E2-7	16.5	1.2	930
procedure 3	C3, B3, D3	B3-1, C3-1,D3-1	6.9	0.60	930
	C3, B3, D3	B3-2, C3-2,D3-2	6.9	0.72	930
	C3, B3, D3	B3-3, C3-3,D3-3	6.9	0.90	930
	C3, B3, D3	B3-4, C3-4,D3-4	6.9	1.20	930
Procedure 4	B4	B4-1	2.0	0.3	800
	B4	B4-2		0.4	800
	B4	B4-3		0.6	800
	B4	B4-4		0.3-0.6	800
procedure 5	A5, B5, C5,D5, E5	A5, B5, C5, D5, E5	Carburised at Volve commercial		

The procedure 1: The samples were put into the furnace at 800°C and carburised following the commercial carburising process (Fig. 3-2). The samples were then removed at different exposure times in the range of 0.25-16.6 h to observe the internal oxides growth process. The furnace parameters for this carburising procedure are shown in Fig. 3-3.

The procedure 2: The samples were put into the furnace at 930°C and carburised at the boost process. Then, the samples were removed at different carburising times in the range 0.5-16.5h to observe the internal oxides growth process.

The procedure 3: The samples were put into the furnace at 930°C and carburised for 6.6h at different carbon potentials (%C) in the range 0.6-1.2% to observe the influence of carbon potential on the internal oxidation phenomena.

The procedure 4: The samples were put into the furnace at 800°C and carburised for 2.0 h in controlled and uncontrolled carbon potentials (%C) in the range of 0.3-0.6 % to observe the influence of the base process on the internal oxidation phenomena.

The procedure 5. The samples were carburised at standard commercial cycle carburising process in a 'Warst' furnace of the Volvo company.

3.3 Scanning Electron Microscopy (SEM)

In SEM, a finely focused electron beam (diameter < 10nm) scans the sample point by point and line by line. The incidence of the electron beam at a point on the sample gives rise to emitted electrons, which are of two types: secondary electrons and back-scattered electrons. The secondary electrons are low energy electron (<50ev) and are emitted predominantly from the thin surface layer (of 1-10nm) of the volume irradiated by the primary electron beam. The back-scattered electrons are energetic, scattered primary electrons which can be leaved the sample from a larger area around the primary electron beam. They are emitted from relatively deep within the sample.

Image contrast depends predominantly on the angle of inclination of the specimen to the electron beam. Surfaces which are perpendicular to the beam emit relatively few electrons and appear dark, whereas surfaces which are inclined to the beam emit many electrons and appear bright. Electron emissions were also dependent on the atomic number of the atoms in the surface. Heavy elements emit more back scattered electrons than light elements. Therefore, different phases can be differentiated as a result of the material contrast in the image. The resolution of the SEM is determined by the diameter of the area of emission of secondary electrons on the object being examined. Good SEM secondary electron image permit a resolution < 10nm to be achieved. The resolution in the back scattered electron imaging mode is lower than in the secondary imaging mode.

The morphology of the internal oxidation zone of the specimens was observed by SEM in this current research. The work was completed using a Philips XL 40 which was equipped with an energy dispersive spectrometer (EDS) usually at an operating voltage 20kV (for imaging) or 15kV (for EDS analysis on light elements). EDS was equipped with an ultra-thin window Oxford ISIS system which allowed the detection of light elements, e.g., carbon and oxygen. The secondary electron image (SEI) technique and the backscattered electron image (BEI) technique were used to investigate the morphology of the internal oxidation zone of the specimens. The BEI was frequently used to present the morphology of internal oxidation because the BEI intensity is a function of the average atomic number of the specimens and it gave compositional information from the specimens and carry information about sub-surface inclusions that was not visible using the secondary electron image.

Transverse cross section specimens were cut from the carburised coupons. The specimens were mounted, ground and polished by conventional methods. Grinding was done using progressively less aggressive metallographic grinding papers step by step to 1200# until the surface was ready for polishing. Polishing was done step by step by less aggressive cloths from 6μm to 1μm (diamond polishing) ready for SEM examination. The carburised surface was cut from the carburised samples in order to observe the morphology of the internal oxidation zone in the different oxidation depth layer. In some cases, the specimens were sputtered by Glow Discharge Optical Emission Spectroscopy (GDOES) at different sputtering times, operating at 600V, 25 mA, argon pressure. By using different sputtering times, the sputtering surface at different depth of the internal oxidation zone in the specimens was achieved readily for examined on SEM.

3.4. Transmission Electron Microscopy (TEM)

A Philips CM 20 Transmission Electron Microscopy operating at 200 kV was used to study the detail of sub-microstructureal the internal oxide phases. Microanalysis of the specimens were carried out at 200kV using an Oxford analytical (ISIS) thin window. EDS detector which has capable of doctoring elements with Z>4. Semi-quantitative microanalysis of the internal oxides was performed using window integral of the X-Ray intensity of elements. The bright field image gives detailed information about internal oxide phase and microstructure around the internal oxides. Select area diffraction (SAD) pattern gave structural data of the internal oxides to allow identification of the internal oxide phases.

Cross-sectional TEM specimens were prepared in order to characterise the subsurface internal oxides. The cross-sectional specimens were cut from the carburised coupons. A precision saw was used to section the specimens, using a blade less than 0.5 mm thick and copious lubrication with mechanical oil to minimise mechanical damage. Specimens of 2.5~3.0 mm on the carburised surface side, 2.0-3.5 mm normal to the carburised surface, and 1.0-2.0 mm thick were produced in this manner. The sectioned specimen was mated by wax or super-epoxy glue to a piece of material possessing very similar hardness to the substrate of the specimen. The gap between the two was minimised and filled with glue. The composite was then mounted using wax onto a flat glass for manual grinding. Grinding was carried on abrasive paper step by step from used $240^{\#}$ to $1200^{\#}$. Importantly, the sliding of abrasive particle was only allowed perpendicular and towards the carburised surface, i.e., from mating material to the specimen. When approximately half of the thickness had been removed, it was finished by polishing from 6μm to 1 μm diamond paste. Then the same procedure of grinding and polishing was undertaken on the other side of the specimen, to obtain a foil as thin as 25~40 μm. By the method described above, a specimen virtually free of grinding damage was produced.

Each specimen was initially examined using optical microscopy or SEM, if necessary to make sure the subsurface region under investigation was not damaged. Then specimen was mounted using super glue on to a copper grid containing a slot hole, with the carburised edge perpendicular to the longer axis of the slot hole. Ion beam milling was performed on a precision ion polishing system (PIPS, Gatan model 691). During ion beam thinning, an argon beam eroded the surface from the back (substrate side) towards the carburised surface edge. The ion beam was angled at approximately 8° -7°, 5.5kV initially and gradually down to approximately ± 4°, 4.0kV until a hole appeared on the specimen. Then, the specimen was cleaned by larger angle and lower voltage for a short time. Finally, a hole was completed, which was invariably near a surface region and an area thin enough for electron beam transparency was obtained at the carburised edge.

3.5 Electron Probe Microanalysis

3.5.1 Energy Dispersive Spectrometer (EDS)

When electrons ionise an atom, the emitted characteristic X-ray energy is unique to the ionised atom. Therefore, the energy of the X-ray photon is element-specific and provides information about the chemical composition of the specimen. Energy Dispersive Spectromety (EDS) was designed to measure the energy of the characteristic X-ray energy when the electron strikes the specimen to give information about the chemical composition of the specimen. A Si (Li) detector was used to generate a charge pulse proportional to the energy of the incoming X-Ray. Light elements with few energy levels will show few peaks in their characteristic X-Ray spectra, whereas the heavier elements will show many peaks. A Be detector window is normally used, however, an ultrathin window (UTW) is usually used to detected light elements. The energy resolution of EDS is 135eV.

An Oxford exL and ISIS EDS system was used in the current study to give useful information of the elemental composition on the internal oxidation zone and internal oxide phases. In order to obtain information of oxygen, the UTW window was chosen operating at 15kV, 20kV in SEM and 200kV in TEM. The elemental X-ray mapping was performed in high or medium resolution (pixel size 256x256 or 128x128) which shows the distribution of element within the internal oxidation zone.

3.5.2. Wavelength Dispersive Spectrometer (WDS)

The WDS was conducted by placing a series of diffracting crystal which are on the same focussing circle(Rowland circle) as the source of x-ray (specimen) and the x-ray detector on the circumference. By scanning the sample, a limited range of X-ray wavelengths of about the same values as the d-spacing of the analysing crystal can be detected. Therefore, a typical analysis involves obtaining a strip chart recording of X-ray intensity as a function of crystal angle, converting peak position to wavelengths through Bragg's law ($n\lambda=2d\sin\theta$). Then, relate the detected wavelengths to the presence of specific elements. Compared with EDS, it has a considerably better energy resolution (<10ev) that aids the interpretation of the peak overlap and is more sensitive to detection of light elements ($Z = 4$, Be)

EPMA Cameca SX 50 was used in current research for quantitative analysis, composition gradients to show element depletion in the surface region of the matrix by line scan, and also elemental X-ray mapping on the internal oxidation zone to give clear information about elemental distribution, especial for oxygen. The same specimens prepared for SEM were used here. Line scans were obtained from depth range of 50-100 μm within the specimen to the surface and operated at 15kV and 20mA. 50 measured points were chosen. In order to get information of the depletion of alloy elements in the surface region of the matrix, as much care as possible was taken to avoid the line scan passing through any obvious oxide particles. Elemental X-Ray images were obtained by scanning the electron beam over a subsurface internal oxidation area of interest and recording the intensity of the emitted X-Rays for each point in a 256x256 grid, operating at 15kV,100nA.

3.6 Quantitative Area Analysis

Quantitative evaluation on the internal oxidation zone was performed by measuring the penetration depth and area fraction (A) of the internal oxides in the internal oxidation zone

A= area of the internal oxides / area of the internal oxidation zone

The penetration depth of the internal oxidation was determined using SEM images by measuring the depth of the uniform internal oxidation front from the interface between the surface oxide scale and external surface of the bulk matrix. Approximately 30 measured points were made around the periphery of each sample and mean values determined. It gave information of the oxidation rate for the different oxidation conditions.

The area fraction of the internal oxides in the internal oxidation zone of specimen was determined using SEM images of the cross section specimens (2500x, 5000x), by an image analysis system (Ominimet enterprise software), as shown in Fig. 3-4. It was hypothesised that at same oxidation depth layer, the internal oxides were uniform distribution in the whole depth layer. Therefore, it was considered that the area fraction of the internal oxides in the internal oxidation zone which was calculated on the cross section image can give information about population density of the internal oxidation zone in the specimen at the different experiment condition. Approximately 8 images were analysed in each specimen to obtain its mean value. The measured areas of dimension 50 μm or 25μm (width L) × 4 μm (depth d) was taken in subsurface region on each image. The Omnimet enterprise software was used in this analysis. It provided a full featured colour image analysis system. A routine is developed such that all the images were evaluated using same condition. Each image used for the analysis was calibrated before measurement.

3.7 Glow Discharge Optical Emission Spectroscopy (GDOES)

Glow Discharge optical emission spectroscopy (GDOES) is a powerful technique for the quantitative analysis of elements in the surfaces of materials and coatings. The quantitative methods of GDOES for depth profiling are based on the assumption that the sample surface is uniformly eroded layer by layer. The sample to be analysed is mounted onto an O-ring seal, completed to a vacuum chamber. Then, argon is bled continuously through the anode. A voltage is applied between the anode and the sample. Interaction of electrons and the argon atoms causes positive ionisation of the argon. The argon ions are then driven by the negative bias into the cathode dark space to collide with the sample causing the sputtering of sample surface. These sputtered atoms move away from the surface of the sample and are excited in the negative glow region of the glow discharge source. The emitted photons have a characteristics wavelength of the elements from which they were emitted, pass through a window into a conventional spectrometer. In the spectrometer, the photons with characteristics of different wavelength are converted to intensity signals, the intensity signal for the elements to be analysed can be further converted to the elemental concentrations as the function of sputtered depth.

A Leco GDS 750 was used in the current research. The sample was first sputtered operating at 600V, 25 mA to obtain information of the element depth profile, and then using this information, the carburised surface was sputtered by GDOES at different depths, layer by layer, by controlling the sputtering time, as shown in Fig.3-5. After sputtering, the internal oxidation of different layer depths was obtained for observing the morphology of the internal oxidation zone.

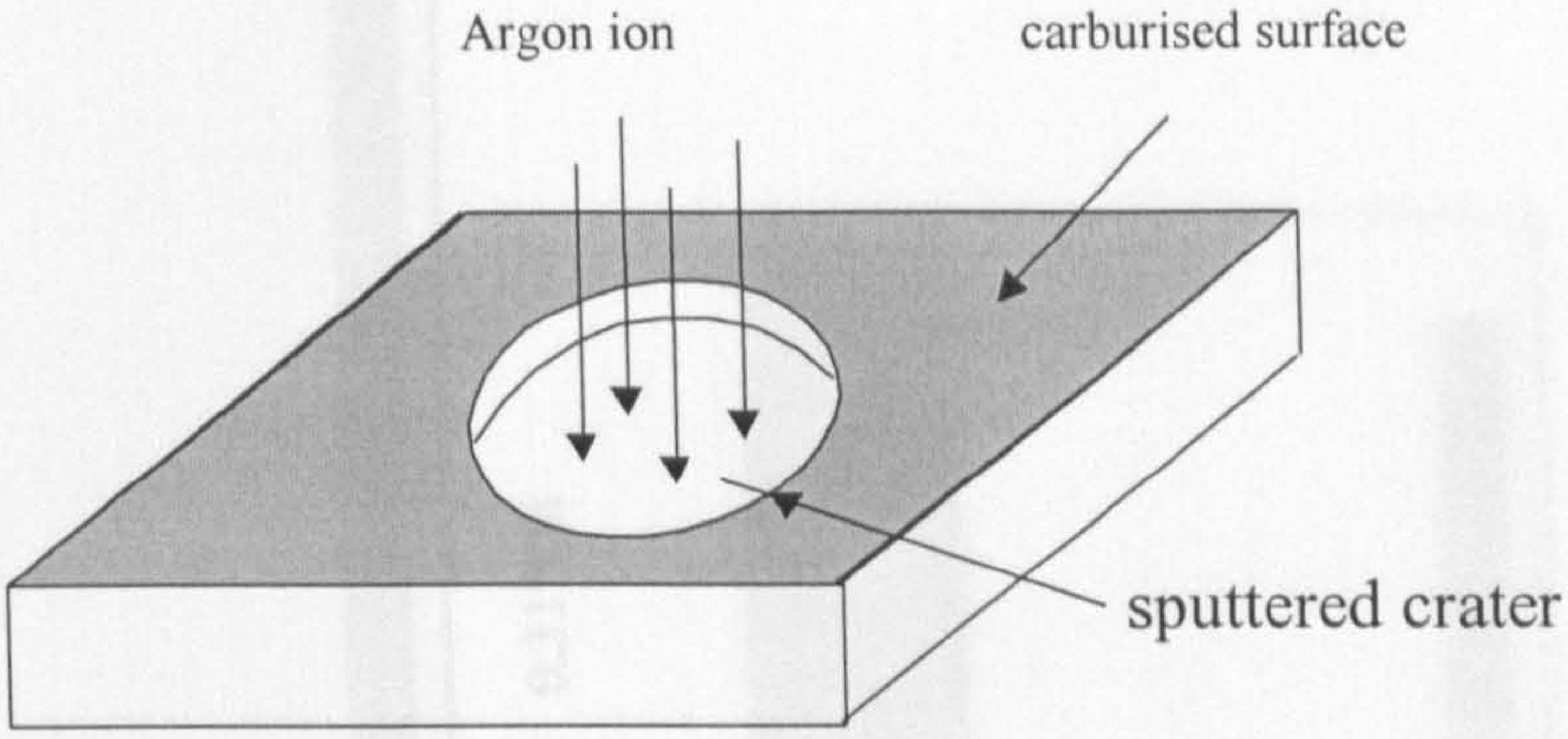

Fig. 3-5 GDOES sputtered on the carburised surface

3.8 Microhardness

Knoop indentation was used in this study to determine the microhardness of the internal oxidation layer and the case layer of the specimens studied. The Knoop test utilises a diamond payramid indentor who strong diametrical axis, of ratio of 30:1 and with this is depth designed to give a long thin impression, the length being seven times greater than the width and about thirty times greater than its depth.

The varying microhardness of the internal oxidation zone from surface to core approximately 100 μm depth was measured with the indenting loads of 50g. The case depth from surface to core depth of approximately 3.0 mm was measured with an indenting load of 100g. The cross section specimens were prepared by polishing to a 1μm finished. The length of the indentations was measured to a precision of ± 1μm with the micrometer fitted to the microhardness tester

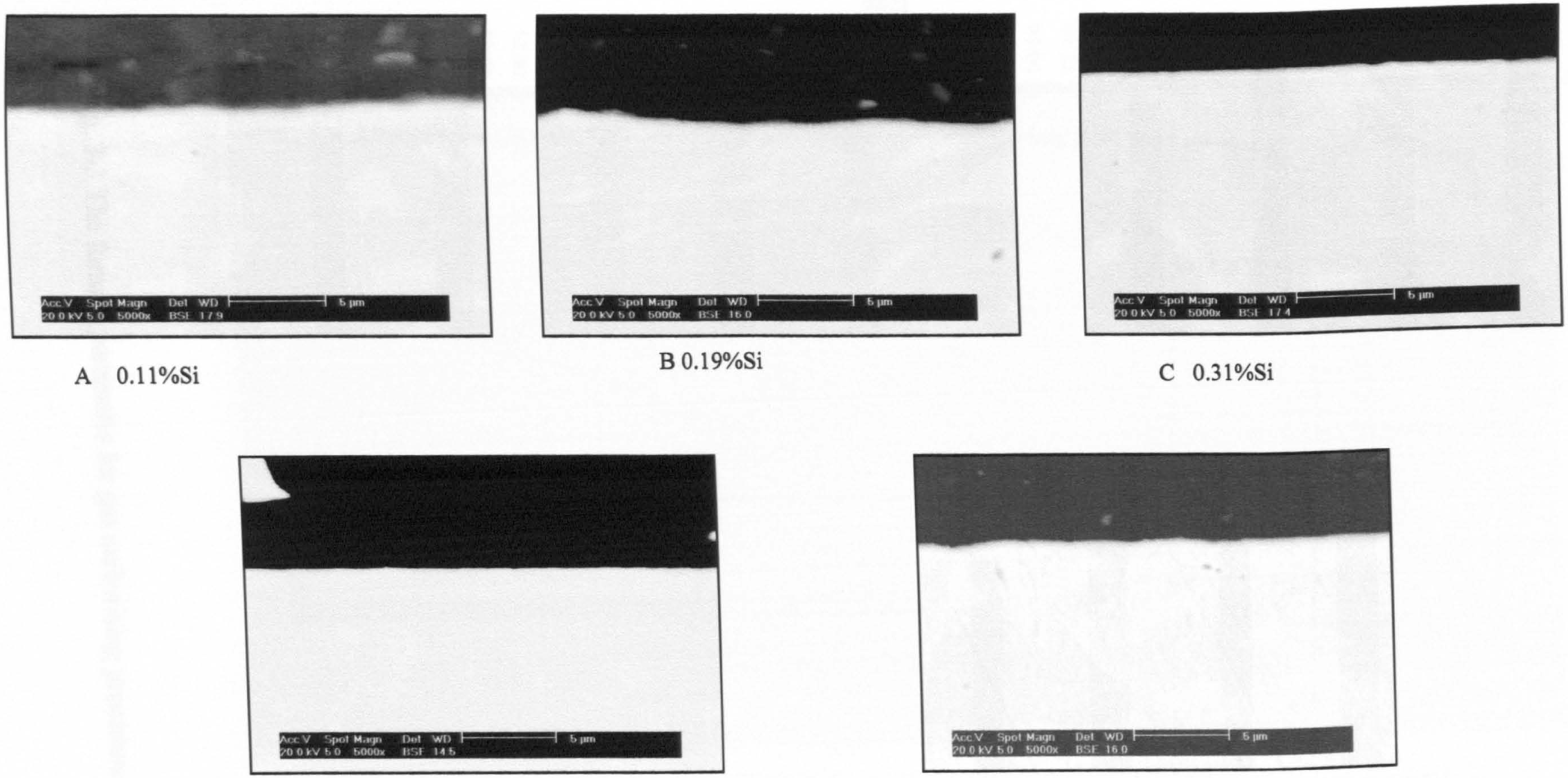

A 0.11%Si

B 0.19%Si

C 0.31%Si

D 0.56%Si

E 0.77%Si

Fig. 3-1 The surface region of the materials as received

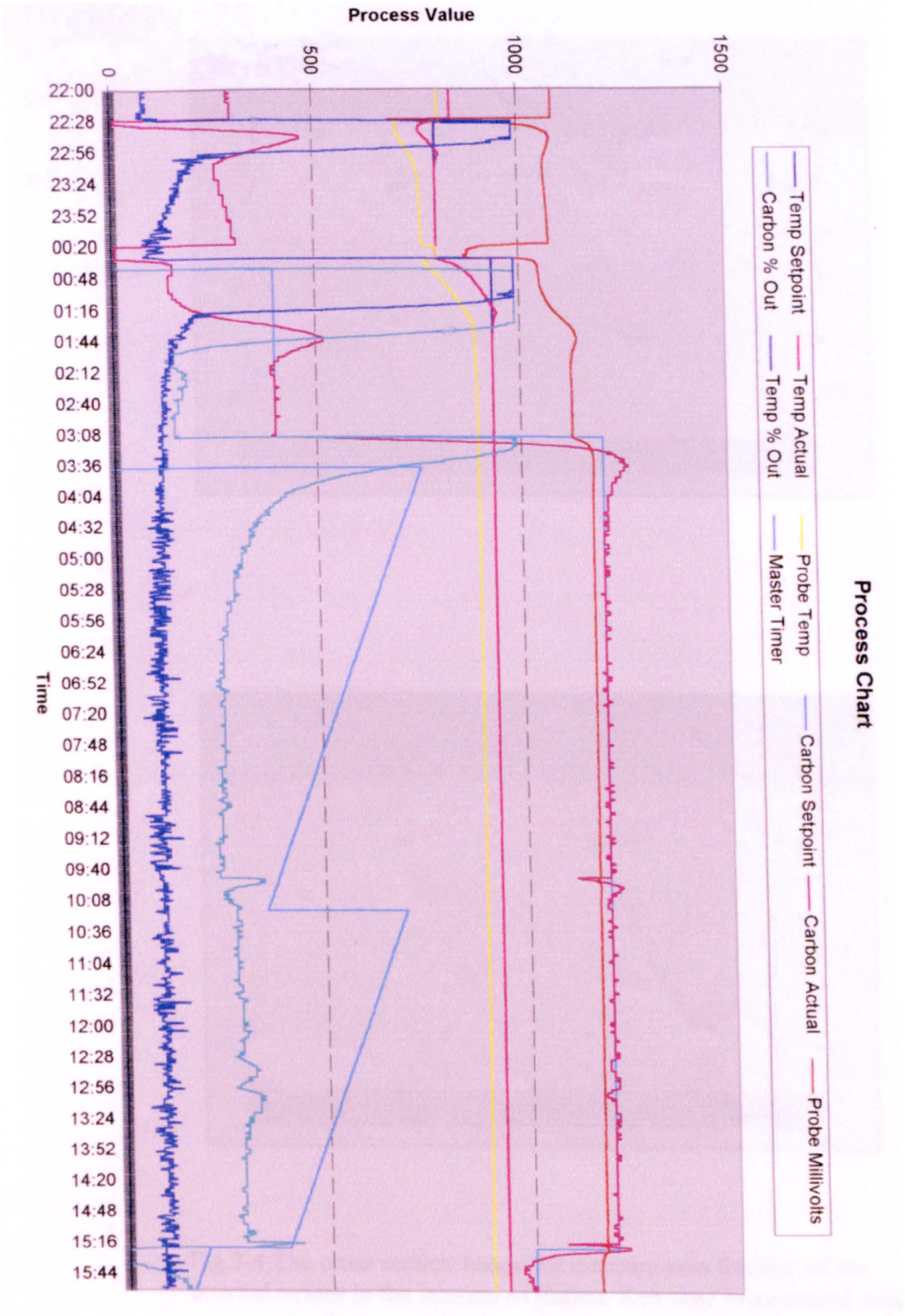

Fig. 3-3 The furnace parameter for gas carburising procedure 1

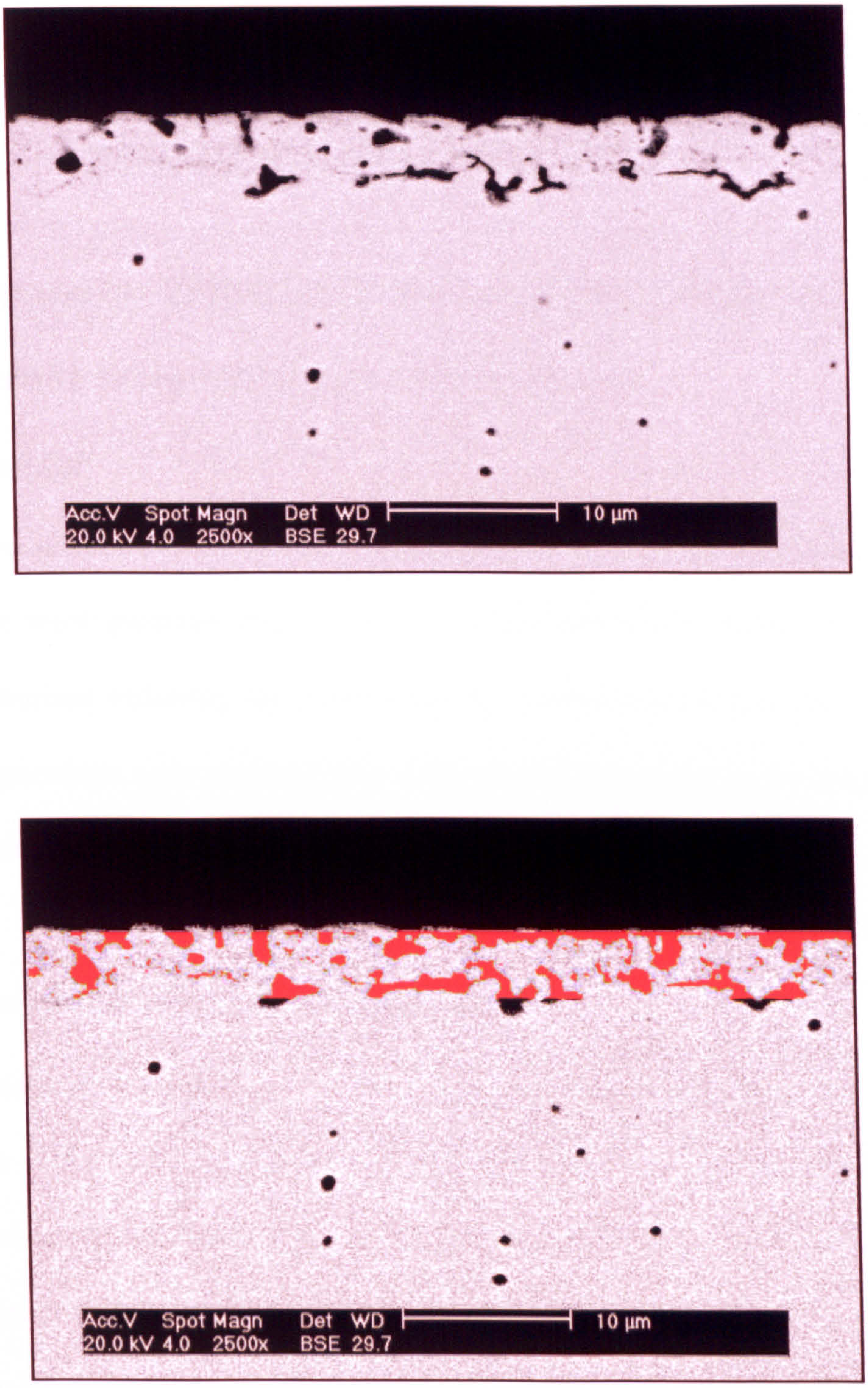

Fig.3-4 The cross section image for measure area fraction of the internal oxides in the internal oxidation. Red zone is measured zone.

CHAPTER 4

PRECIPITATE MORPHOLOGY AND ELEMENTS DISTRIBUTION

4.1 The Specimens Carburised Following Whole Commercial Carburised Process (Carburised Procedure 1)

4.1.1 Introduction

The chemical composition of the carburising steel used in this work is shown in table 3-1. The samples were mounted into a commercial gas carburised furnace initially at 800°C and carburised following the commercial gas carburising process, as shown in Fig. 3-2. The specimens were removed after different exposure times in the range 0.25-16.6h in order to observe the internal oxidation growth process.

4.1.2 Morphology of Internal Oxidation Zone

Typical cross-sectional images Fig. 4-1, 4-2, 4-3 shows the morphology of the internal oxidation zone of the specimens B1, C1, and E1. The internal oxides appeared to be a continuous growth process through the time range up to 16.6h. After short heating times 0.25h, a surface oxide layers was formed to the depth of approximately 1.5μm as block and continuous layer. The very small precipitates just below the metal/ scale interface are shown in Fig. 4-1a, 4-2a, 4-3a. The small precipitates appeared to be elongated and were orientated approximately perpendicular to the specimen surface. After the samples for 0.5h, the precipitates are clearly visible, growing along the grain boundaries and generally normal to the surface (Fig.4-1b, 4-2b, 4-3b). This was evident in all the specimens. Meanwhile, some larger oxides also formed, especial for the specimen with higher bulk Si content. After heating for 1-2h, intergranular oxides were formed within the internal oxidation zone to a depth of approximately 4-5μm, as shown in Fig. 4-1c-d, 4-2c-d, 4-3c-d, in all the specimens studied. The oxides were thin films along the grain boundaries. Upon further heating the samples, subsurface intergranular oxides grew to a larger size close to the metal /scale interface within grains and on grain boundaries. Meanwhile, new intergranular oxides were formed close to the internal oxidation front as thin films, as shown in Fig.4-1e, 4-3e, along a growth direction related to the larger oxides. The larger oxides usually grew perpendicular to the surface and close to the metal/scale interface as either elliptical or rough spherical shapes approximately 1-3μm, as shown in Fig. 4-4. There were some small dispersed internal oxides around the larger oxides and intergranular oxides, as shown at higher magnifications in Fig.4 -4, Fig.4 -5.

With further treatment, the structure developed into clear two zone morphology. For the outer zone (zone 1), close to the surface, showed large oxides within the grains and on the grain boundaries elongated and approximately normal to the surface; the inner zone (zone 2), close to the internal oxidation front, showed a continuous thin oxide film that precipitated along the grain boundaries as intergranual oxides, as shown in Fig. 4-1 f-g to 4-3 f-g. There were small dispersed oxide particles within both zones. As the carburising time increased, the larger elongated oxides became roughly spherical. Some agglomerated oxides were observed in the internal oxidation zone, as shown in Fig. 4-6. Meanwhile, small dispersed precipitate particles (50nm or less) were observed around the larger oxides and grain boundaries. Intergranular oxidation penetrated further than the intragrannlar oxidation with time. After long cycle heating, surface internal oxidation zone was spalled by severe intergranular oxidation, as shown in Fig. 4-7.

At different depths of the internal oxidation of specimens B1, E1 are shown in Fig. 4-8, 4-9. In specimens B1-4 and E1-4, heating for 2.0h, uniform intergranualr oxidation was observed up to depths of 1.56-2.78μm, as measured by GDOES. However, intergranular oxidation was observed clearly reduced at deeper depths of approximately 3.5 μm, as shown in Fig. 4-8b. This work agreed with the observation on the cross section images that at the initial heating stage, the internal oxides precipitated along grain boundaries. In specimen B1-5, heating for 5.8h and B1-8, heating for 16.6h, at a depth of 1.4-2.5 μm, the surface topography was globular particles that were more evidence the grain boundaries for approximately 1.0 -2.5 μm, meanwhile, no continuous oxide particles grew along grain boundaries combined with the globular particles, as shown in Fig. 4-8c,e. This layer was adjacent to the outer zone of the cross section. The internal oxides were distributed especially uniformly across the whole cross-section and were close to the top surface. At greater depths, approximately 4-5.5 μm, evidence for a uniform intergranular oxidation was observed that was adjacent to the inner zone of the cross section shown in Fig. 4-8d,f and Fig.4-9c,e. The intergranular oxidation was again distributed uniformly throughout the whole cross-section. Some small dispersed oxide particles were formed within the grains, surrounded by the intergranular oxidation, as shown in Fig.4-5. In the specimens E1-5 and E1-8, for the outer zone 0-3 μm, globular particles were more dense than the specimens B1 and tended to agglomerated together to form continuous intergranular oxides, as shown in Fig. 4-9d. The thickness of the thin film intergranular oxides in the inner zone was thicker than for the specimen B1, ash shown in Fig. 4-9c,e.

All these observation suggests that oxygen from the atmosphere dissolves at the surface of the specimens and rapidly diffuses into the bulk metal, forming internal oxidation with different morphologies. Therefore, the formation of internal oxides were a continuous development process and varied with different furnace atmosphere conditions, such as oxygen partial pressure and the exposure time in the furnace. Within exposure time of approximately 5.8h, just before start of the boost process, internal oxides were developed to their highest level, by which numerous internal oxides formed at both outer zone and inner zone. A study of the morphology of the internal oxidation zones revealed that internal oxidation developed faster within the base process rather than the boost process. After long cycle carburisation, the internal oxidation region remained generally as two distinct zones with distinct morphology characteristics.

4.1.3 Elemental Distribution

EPMA and EDS was used at different stages to show the internal oxide growth process at different stages. Within the treatment cycle, after short heating time 0.25h, some precipitate phases existed below the interface between the surface oxide layer and the bulk matrix, however, it was quite difficult to identify which elements were rich in the precipitate phase. EPMA line scan, shown in Fig. 4-10, showed that the surface oxide layer was rich Si, Mn and Cr. Close to the surface layer, there was little depletion of the alloying elements Cr and Mn to a depth of 1-3μm. Si content was richer in this region. After heating 0.5h, Cr, Mn was observed in the precipitate phase, whilst below the Cr and Mn rich region, there was a depleted zone of Cr and Mn, as shown in Fig. 4-11. After heating 1h, three alloy elements Cr, Mn and Si were observed to be enriched within the uniform intergranular oxidation phase, as shown in Fig. 4-12. Heating up to long cycle times, an elemental distribution was formed where Cr, Mn and Si were rich in larger oxide precipitates close to the surface in outer zone as complex oxides, whilst the Si was dominant oxide at deeper grain boundaries as intergranular oxides within inner zone, as shown in Fig. 4-13, 4-14. As the Si content in the bulk metal was increased, the incorporation of Si was observed to increase the amount of internal oxidation even after short heating times (0.25h), as shown in Fig 4-15.

X-ray mapping at different depths of the internal oxidation layer also showed that at the outer zone, larger globular particles were rich of Cr Mn and O, Si was also observed in this zone, as shown in Fig.4-16. In the inner zone, the intergranular oxidation was rich Si and O, as shown in Fig. 4-17.

4.2. The Specimens Carburised Following the Boost Process (Carburised Procedure 2)

4.2.1 Introduction

The samples were placed within the furnace and carburised at 930°C in the boost process. Then, the samples were removed at different carburising times in the range of (0.5-16.5)h in order to observe the internal oxides growth process in this carburising condition.

4.2.2 Morphology of Internal Oxidation Zone

The morphology of the internal oxidation zone in this process was quite different than with the first carburising procedure. Fig. 4-18, 4-19 shows the morphologies of the internal oxidation zone for carburising over a time range 0.5-16.5h for the specimens C2, E2. After short heating times 0.5-1.0h, a surface oxide layer was formed to the depth of approximately 1.5μm that appeared as continuous layer. Meanwhile, a very small precipitate phase, formed just below the metal/ scale interface, as shown in Fig. 4-18a, b, 4-19 a, b. The precipitates appeared to be elongated and were orientated approximately normal to the surface. Continuously heating samples for approximately 3.0h, the precipitates were clearly visible as elongated oxides growing along grain boundaries approximately normal to the surface. The thickness of the intergranular oxide films increased with increasing carburising time. Small dispersed oxide particles were observed in the internal oxidation zone after 12.5h heating, as shown in Fig. 4-18e, 4-19f. The internal oxides grew slowly when compared with the specimens in the first carburised procedure, at same exposure time, the internal oxides for these specimens were less numerous, and also the penetration depth of the internal oxides for these specimens was shallower than for the specimens carburising using procedure one.

In the steel with the highest Si content in the bulk metal, the thickness the intergranular oxide films increased compare Fig. 4-18d-f, 4-19d-f. Additional small dispersed oxides were observed around intergranular oxides in the internal oxidation zone. The reaction time for the formation of the internal oxides was shorter for higher Si bulk content.

Typical surface topography of different depths of internal oxidation for specimen C2-7 is shown in Fig.4-20. The intergranular oxidation was observed at different depth layers of 1.58μm and 2.39μm. The thickness of the intergranular oxides in the layer close to the surface (1.58μm) was thicker than at depths closer to the internal oxidation front of 2.39μm, as shown in Fig.4-20b. In this case, it was observed that as soon as the internal oxides nucleated, internal oxides were uniform distributed across layer, as shown in Fig. 4-20a.

4.2.3 Elemental Distribution

X-ray mapping showed that the surface oxidation scale was mainly rich in Fe and O. Cr and Mn content were enriched at the interface between the surface layer and the bulk, as shown in Fig. 4-21. All the specimens studied showed that the internal oxidation zone was mainly rich in Si and O, as shown in Fig. 4-22.

These observations confirmed that for the boost process, only Si oxides formed. Since grain boundary diffusion of oxygen was faster than bulk diffusion, it was expected that a higher oxygen potential would exist at grain boundaries compared with the bulk material. Therefore, grain boundaries became preferential sites to precipitate internal oxides.

4.3 Specimens Carburised at Different Carbon Potential

4.3.1 Introduction

The samples were placed into the commercial gas carburising furnace at 930°C for 6.6h with a different carbon potential in the range (0.4-1.2)%C to observe the influence of the carbon potential on internal oxidation.

4.3.2 Morphology and Elemental Distribution of the Internal Oxidation Zone

The specimens carburised at different carbon potentials showed slightly different morphologies, as shown in Fig. 4-23. For the higher carbon potential with C content in range of 0.72-1.2% C, the internal oxidation zone consisted mainly of intergranular oxidation. The morphology was similar to the specimens in carburisation using procedure two. The uniform continuous oxides, as thin films precipitated along grain boundaries, as shown in Fig 4-23 b-c. There was a surface oxidation layer for all the specimens. However, in the low carbon potential 0.4%C, the morphology of the internal oxidation zone was slightly different and consisted of intergranular oxidation accompanied with small dispersed internal oxide particles, whilst larger oxides were observed close to the surface region, as shown in Fig. 4-23a.

Elemental X-ray mapping of the specimens with higher carbon potentials in range of 0.72-1.2% C showed that the internal oxidation zone was mainly Si and O rich, as shown in Fig. 4-24. In the specimen with low carbon potential of 0.4%C, intergranular oxides were mainly Si oxides, while, the larger oxides close to the surface were rich in Cr and Mn, as shown in Fig. 4-25.

This observation indicated that carbon potential affected the internal oxidation zone not only the morphology but also the transformation kinetics of the internal oxide phase.

4.4 Specimens Carburised at Controlled and Uncontrolled Base Process (Carburised Procedure 4)

4.4.1 Introduction

The samples in this case were placed into the furnace at 800°C for 2.0 h with the carbon potential of 0.3%C, 0.4%C, and 0.6% C and for the uncontrolled carbon potential in range (0.3-0.6) % to observe the influence of the furnace atmosphere on the formation of internal oxidation.

4.4.2 Morphology and Elemental Distribution of the Internal Oxidation Zone

The morphology of the internal oxidation zone for all the treated specimens had similar features, as shown in Fig. 4-26a-d. The internal oxides grew along grain boundaries as a uniform thin film close to the surface. The specimens with uncontrolled atmosphere condition (B4-4) had a denser internal oxidation zone when compared with the controlled specimens, as shown in Fig. 4-26d. A surface oxide layer was formed in the specimen to a depth of approximately 1.5-2.5μm. For the uncontrolled condition, the internal oxides began to grow to a larger size under the controlled conditions. Three specimens had no obvious differences in the morphology of the internal oxidation zone, as shown in Fig. 4-16 a, c, here a very thin surface layer up to 1 μm in thickness.

The results of x-ray mapping on all of the specimens showed that the three alloy elements Cr, Mn and Si were rich in the internal oxide phases along grain boundaries, as shown in Fig. 4-27, b.

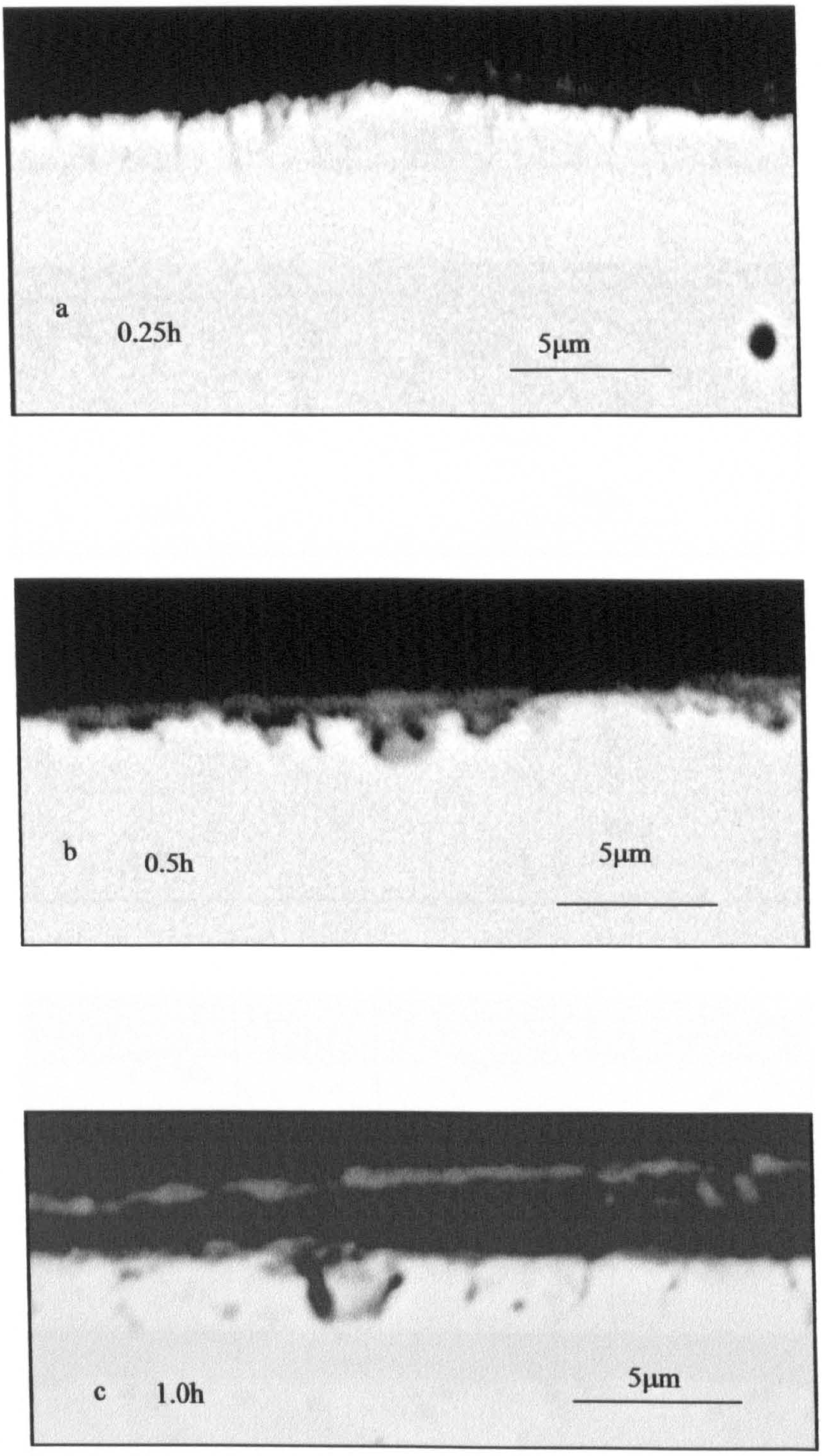

Fig. 4-1 Morphology of the internal oxidation zone in specimens B1 series (0.19%Si), carburised using procedure 1

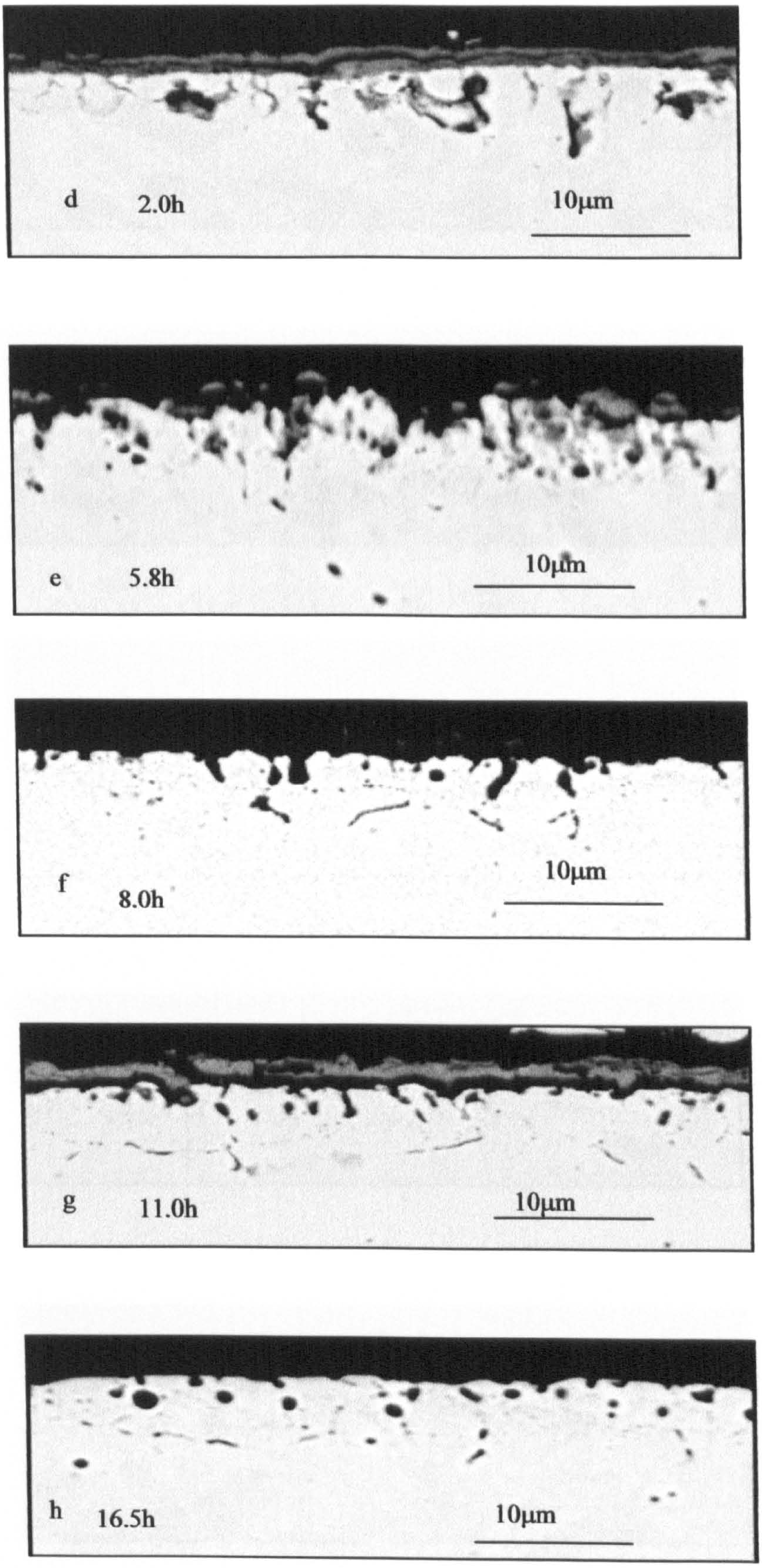

Fig. 4-1 Morphology of the internal oxidation zone in specimens B1 series (0.19%Si), carburised using procedure 1

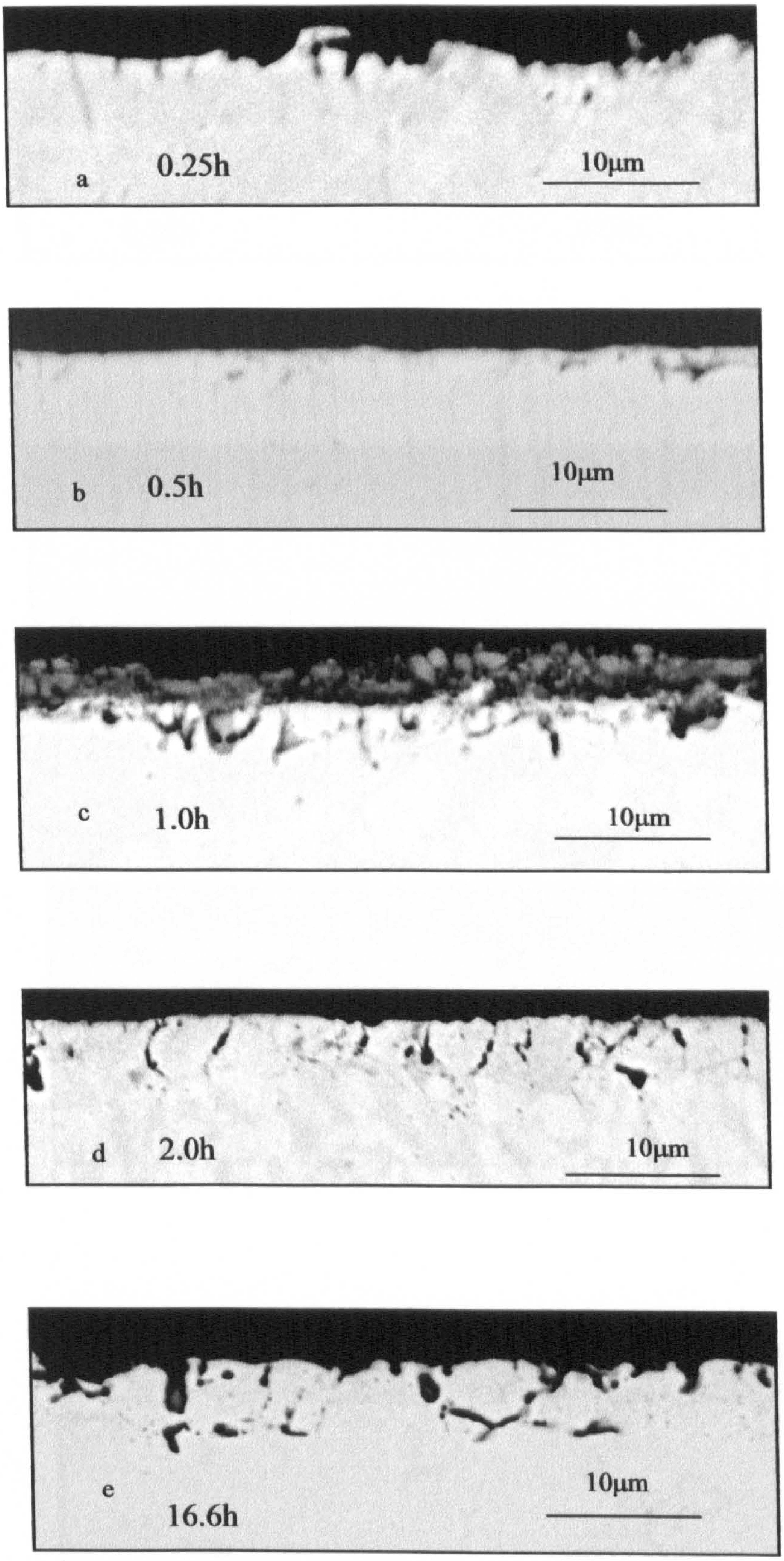

Fig. 4-2 Morphology of the internal oxidation zone for specimens C1series (0.31%Si), carburised using procedure 1

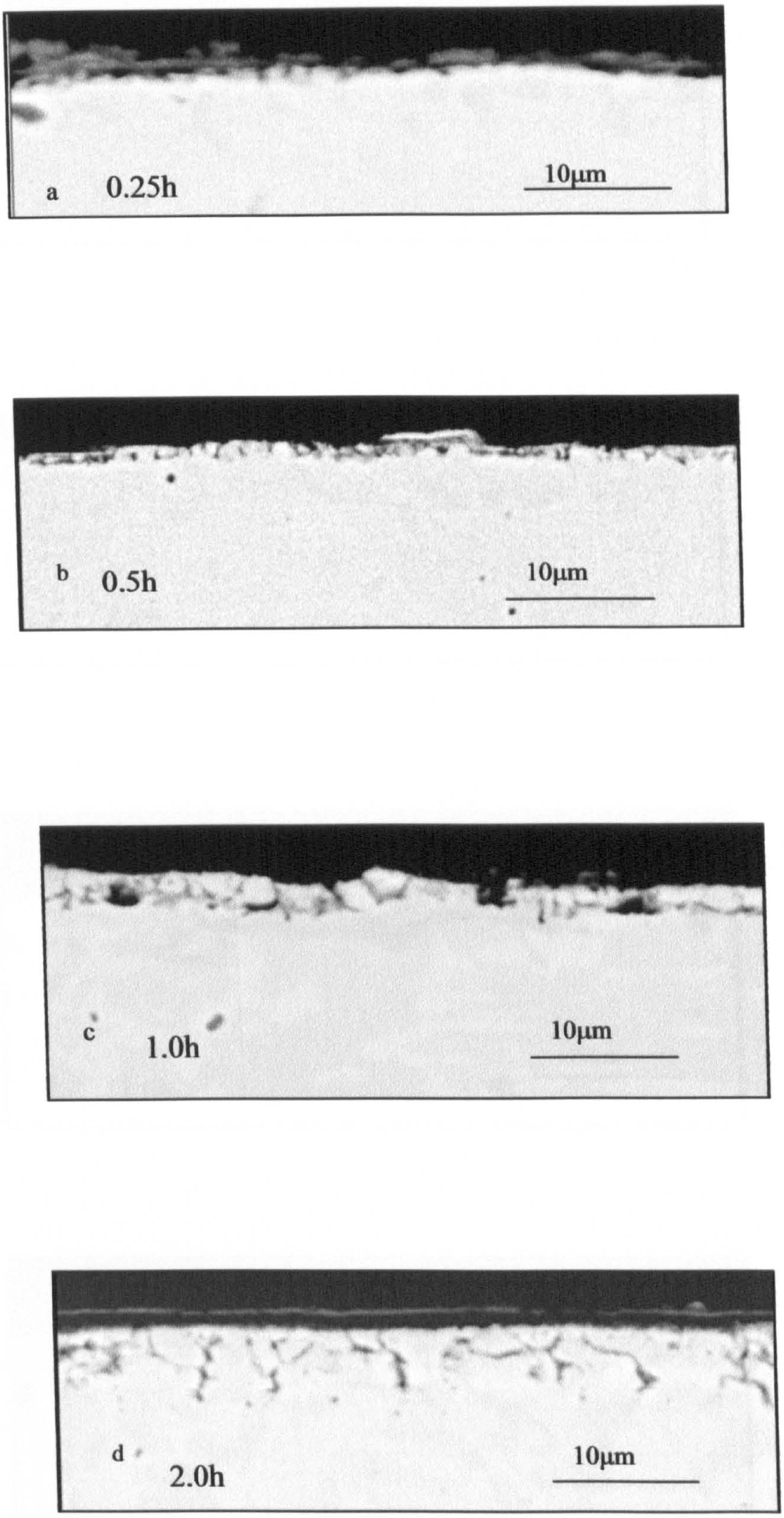

Fig. 4-3 Morphology of the internal oxidation zone in specimens E1 series (0.77%Si) carburised using procedure 1

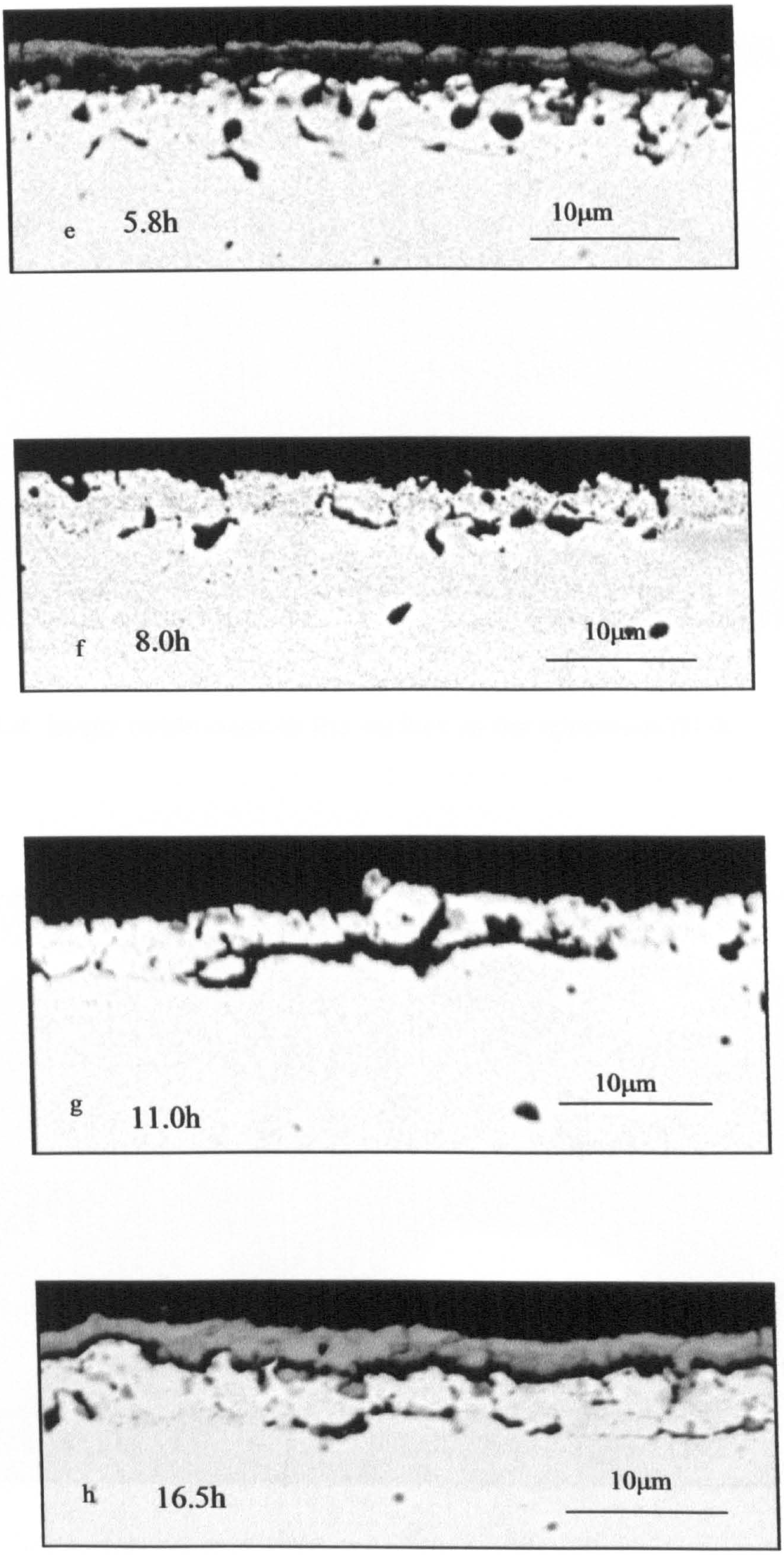

Fig. 4-3 Morphology of the internal oxidation zone in specimens E1 series (0.77%Si), carburised using procedure 1

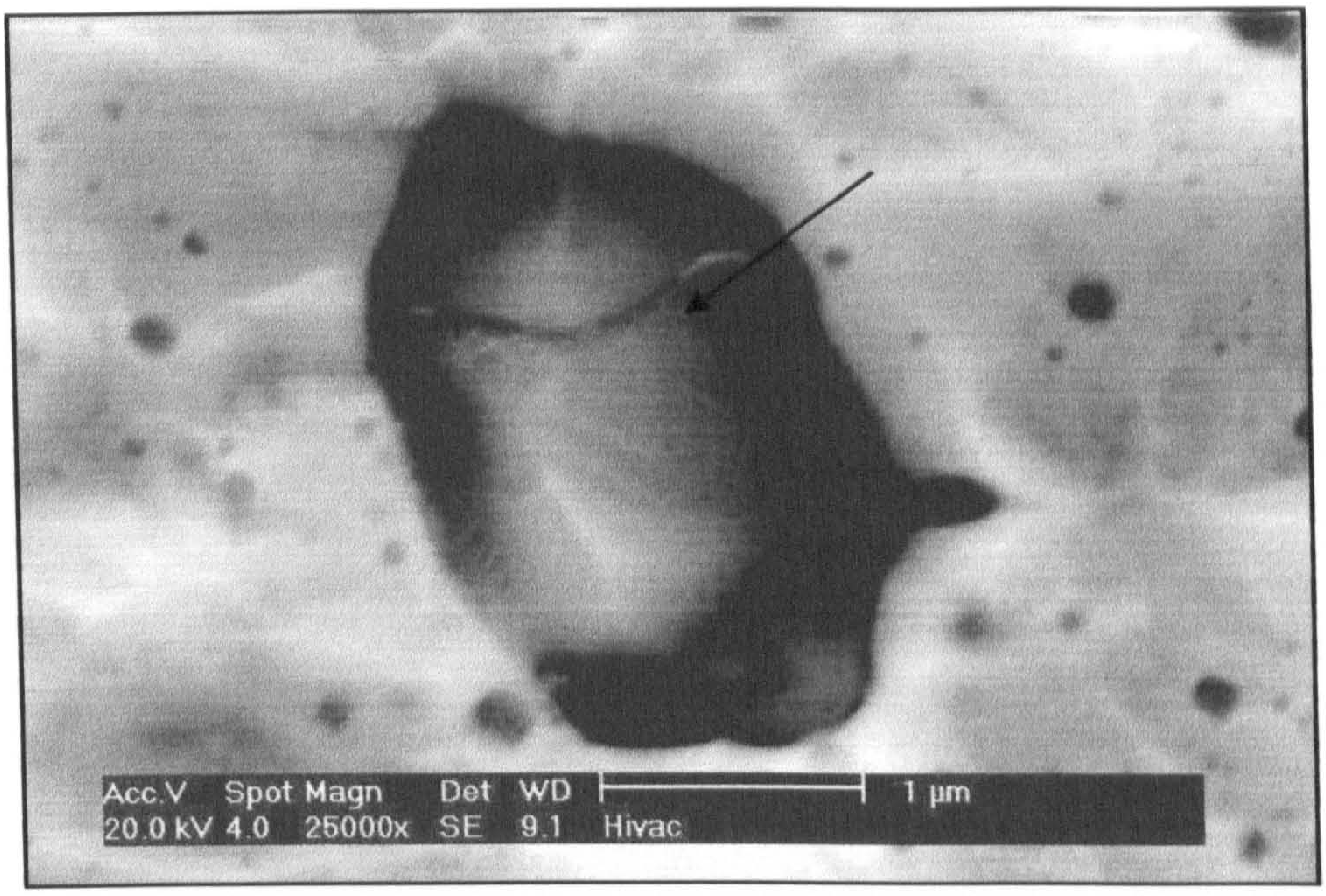

Fig. 4-4 larger oxide close to the surface in the specimen B1-8

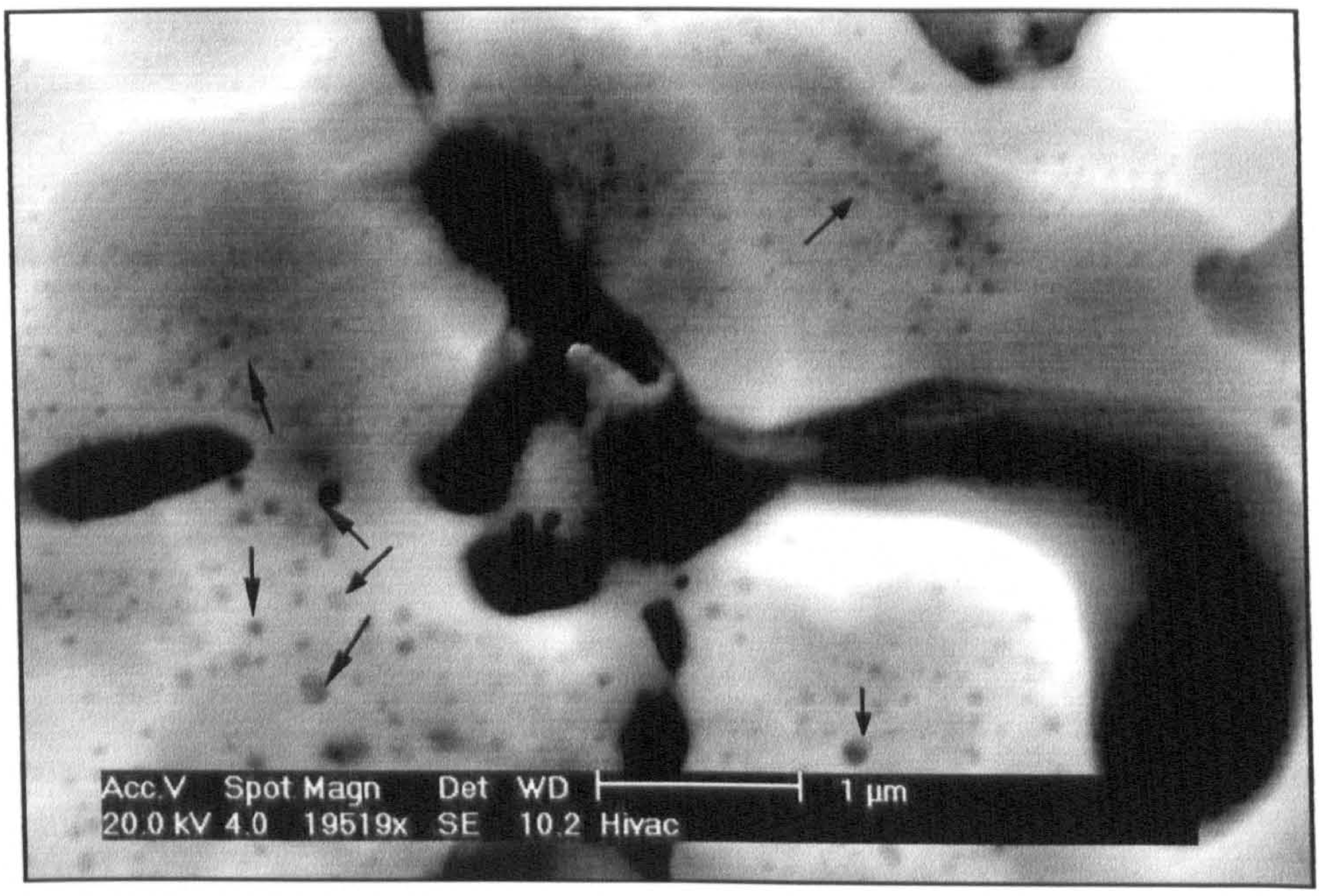

Fig. 4-5 Small dispersed oxide particles precipitated around the intergranular oxides (specimen E1-5)

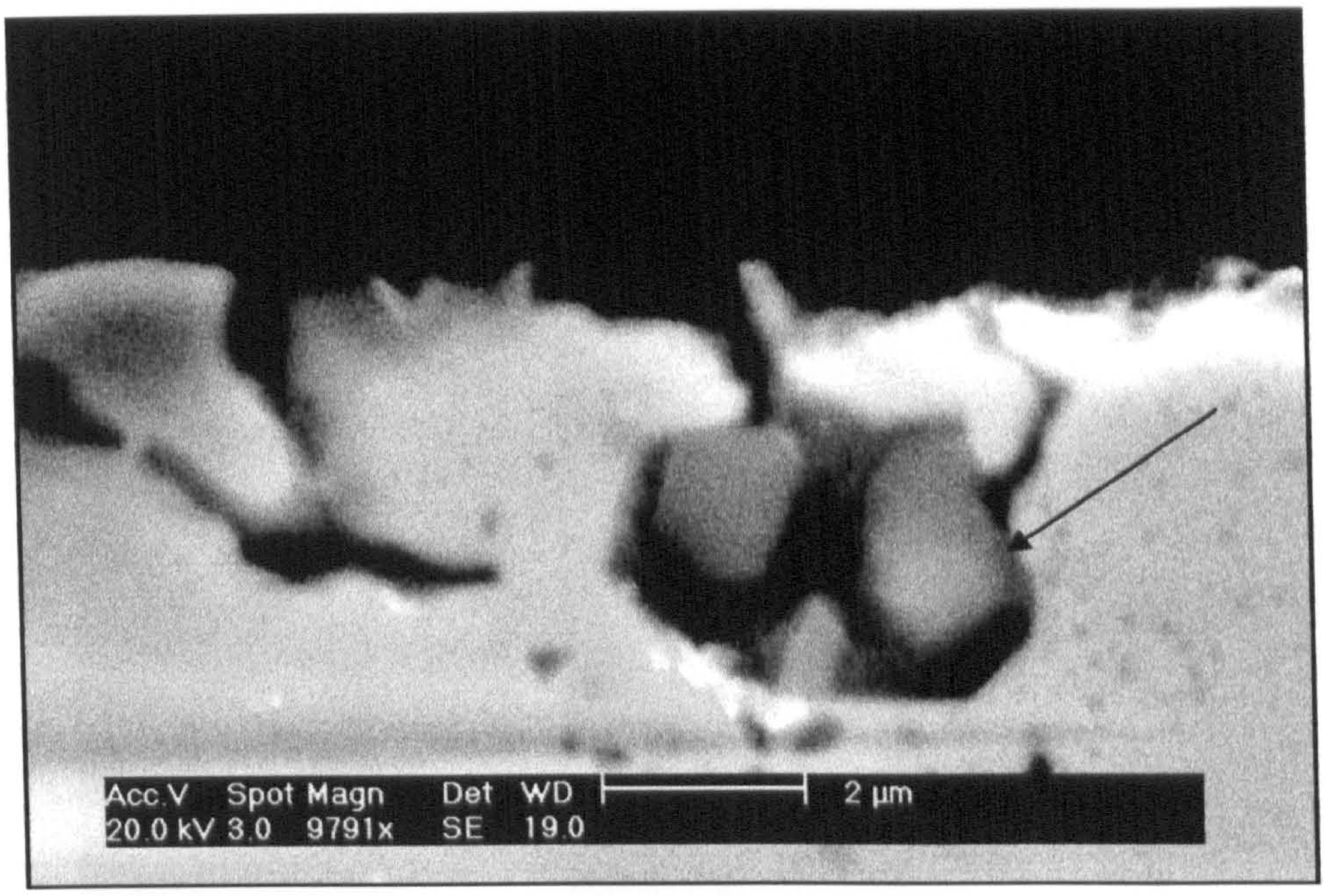

Fig. 4-6 Agglomerated oxides in the internal oxidation zone in the specimen E1-6, carburised using procedure 1.

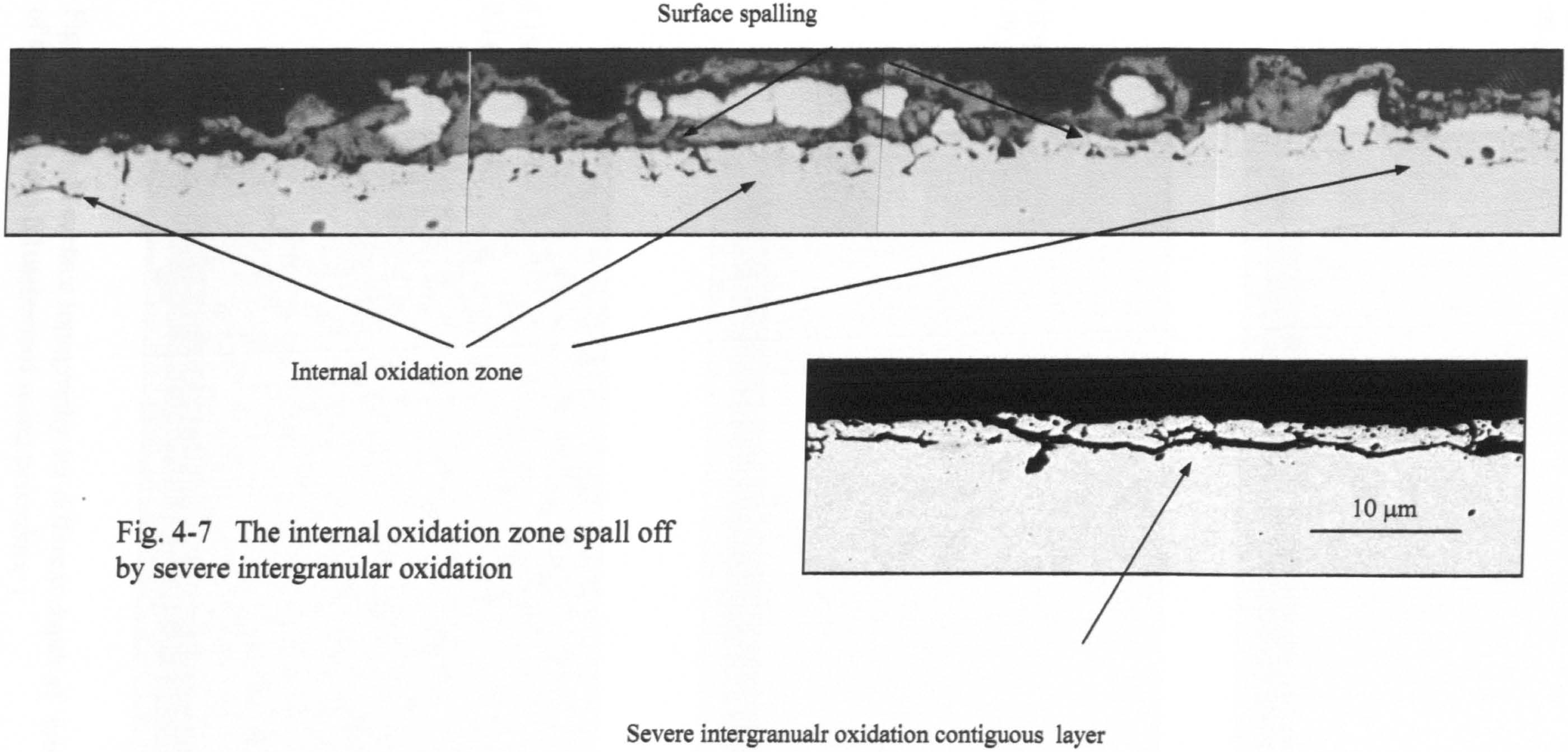

Fig. 4-7 The internal oxidation zone spall off by severe intergranular oxidation

a. B1-4 (2.0h)
depth 1.56 μm

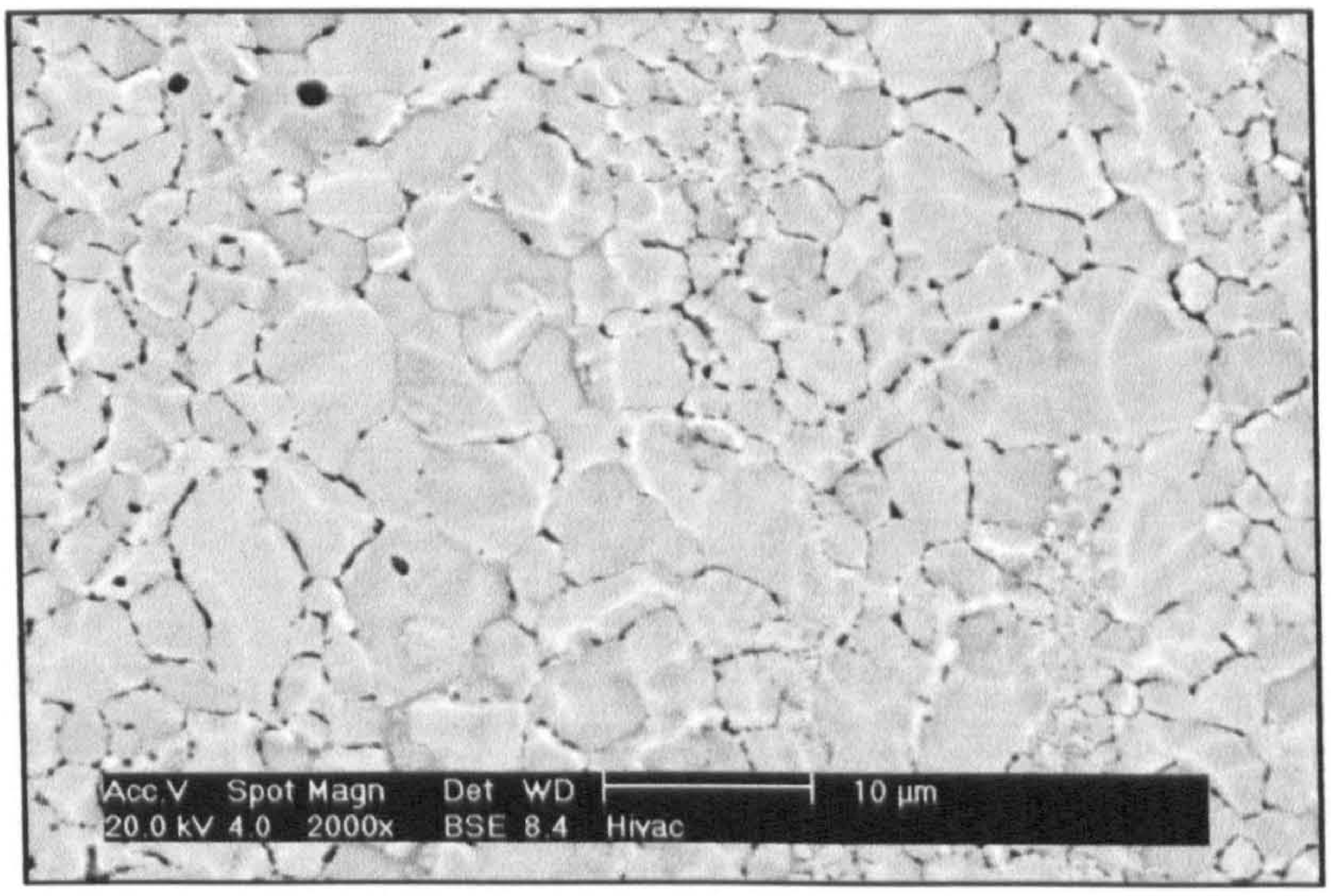

b. B1-4 (2.0h)
depth 3.34 μm

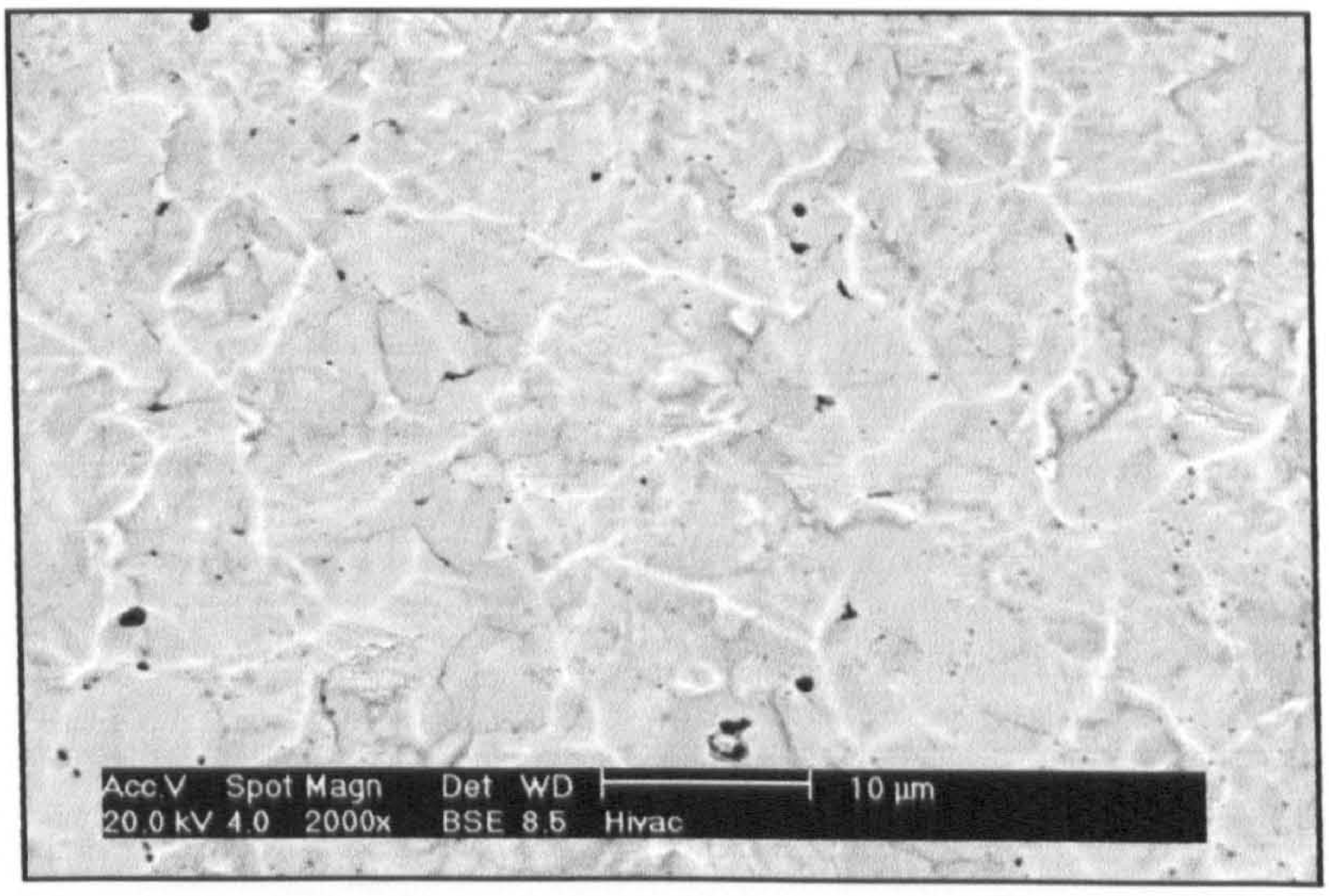

c. B1-5 (5.8 h)
depth 2.14 μm

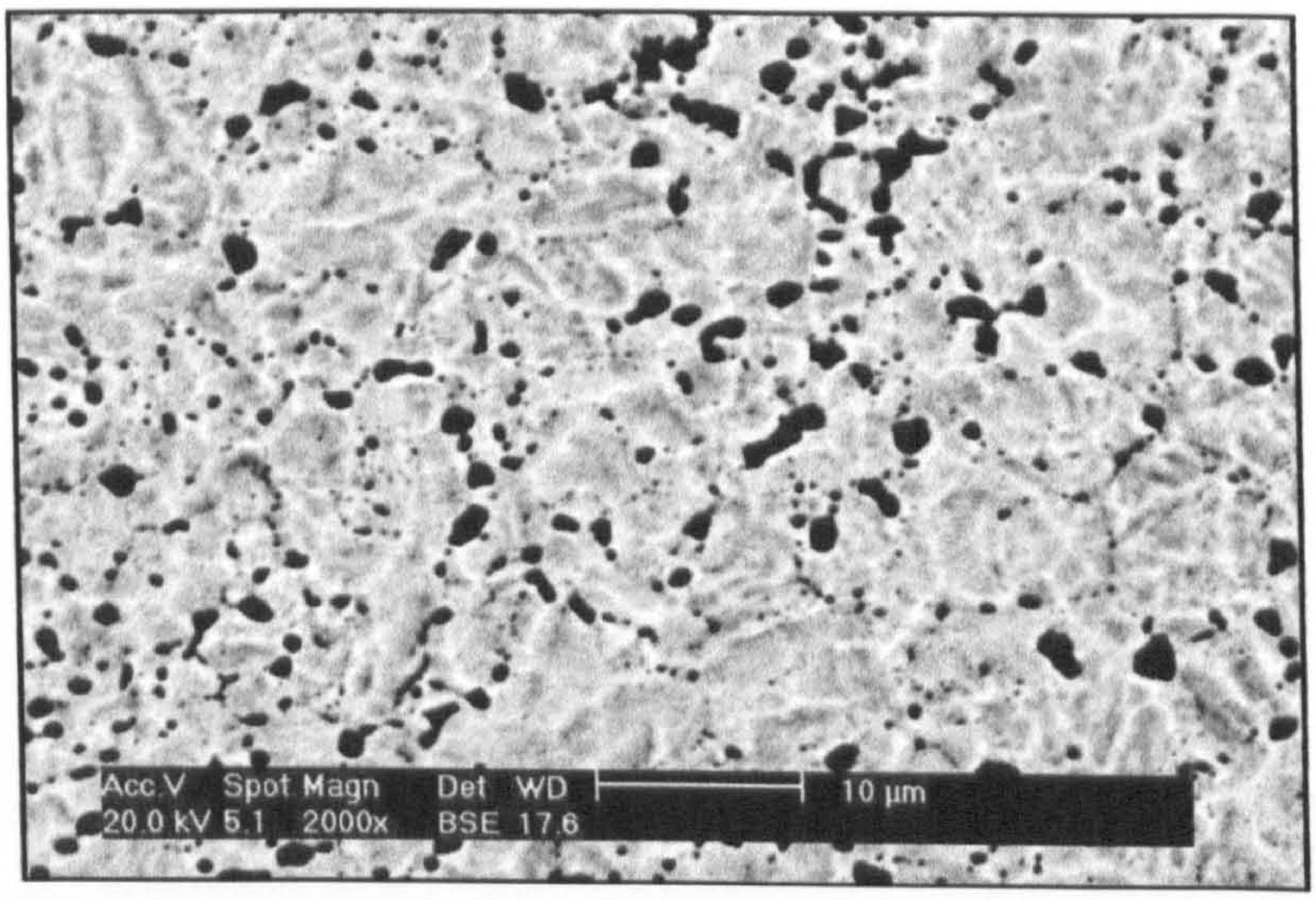

Fig. 4-8 Typical surface topography for different depth of internal oxidation layer of the specimens B1carburised using procedure 1

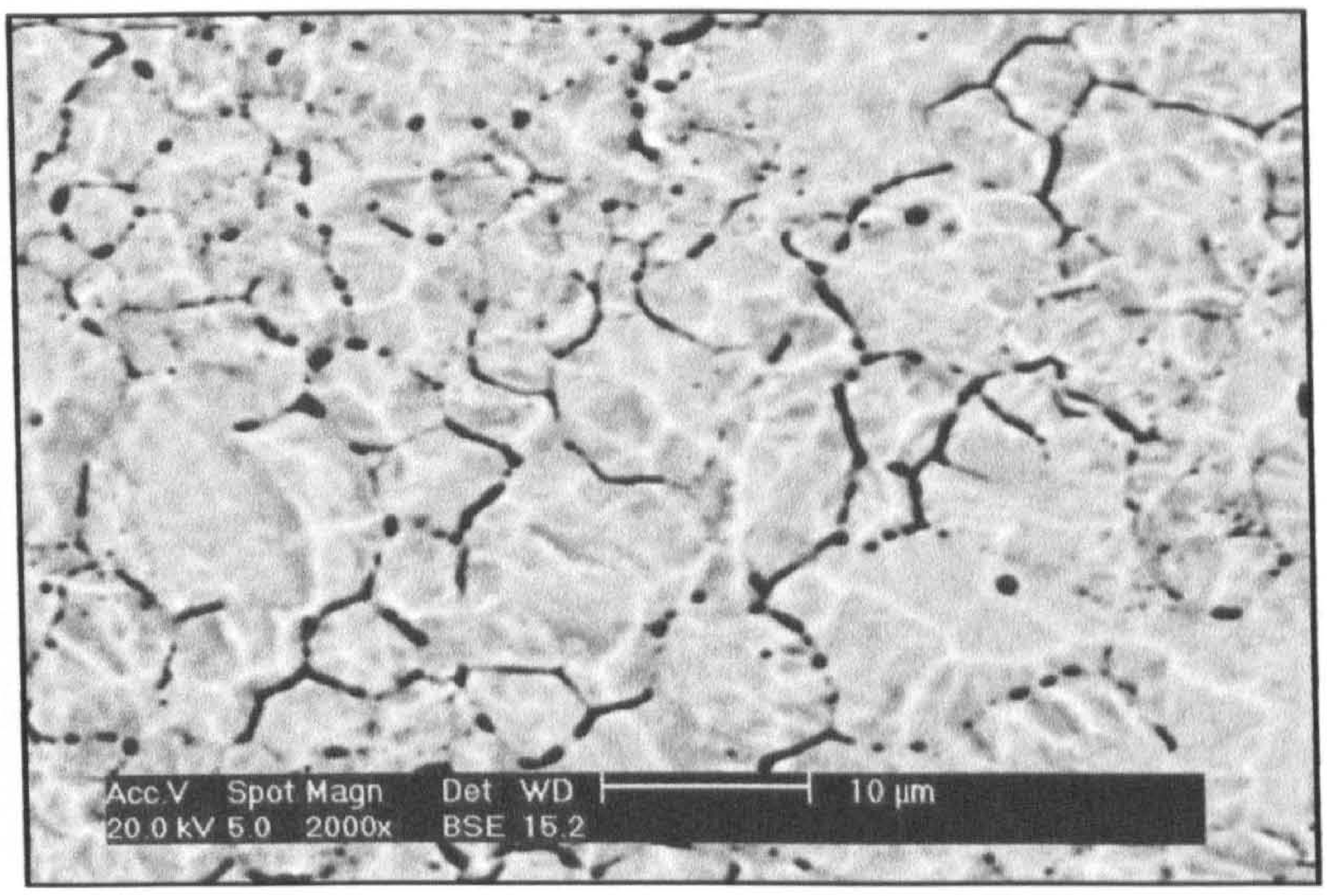

d. B1-5 (5.8h)
depth 4.70 µm

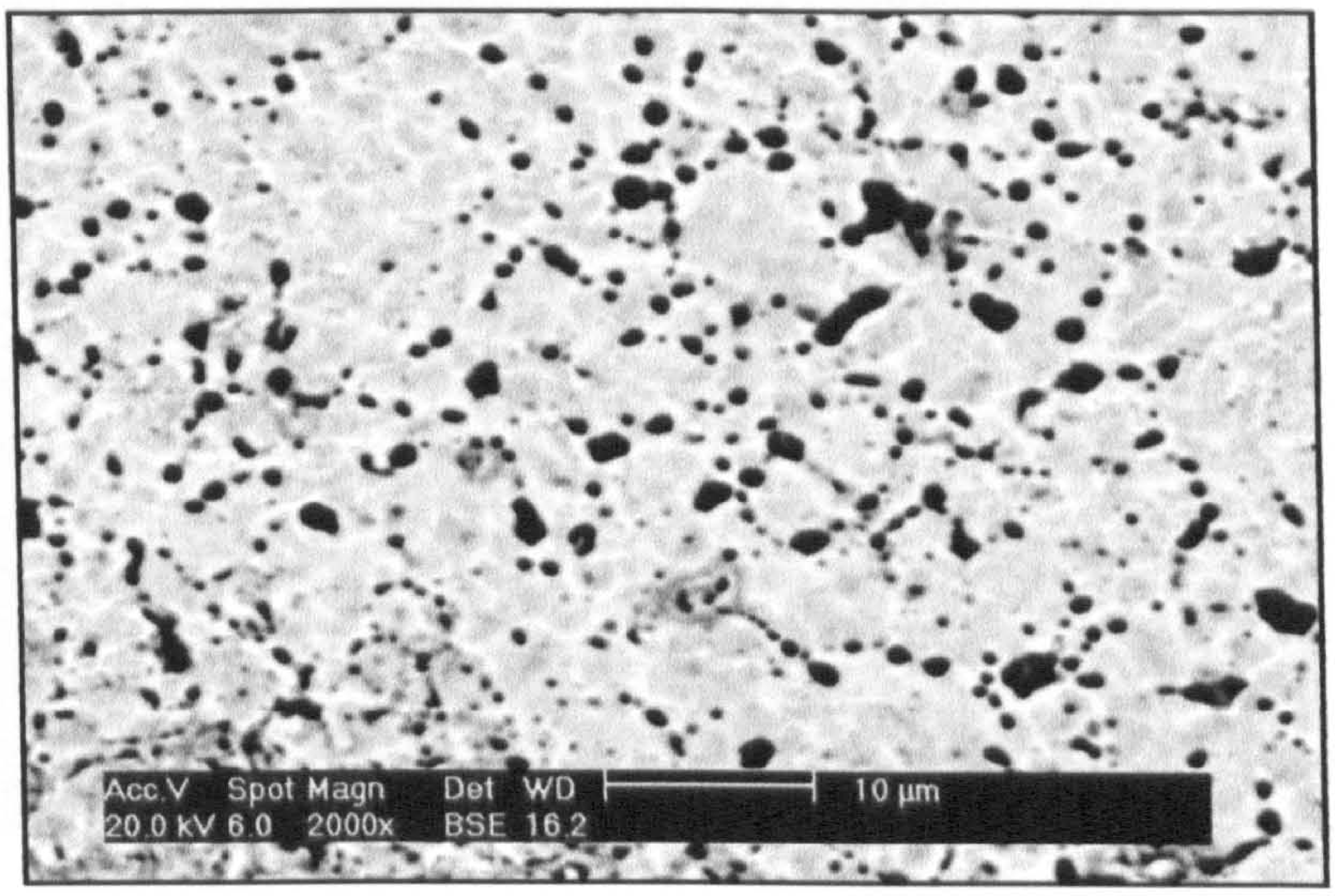

e. B1-8 (16.6h)
depth 1.9µm

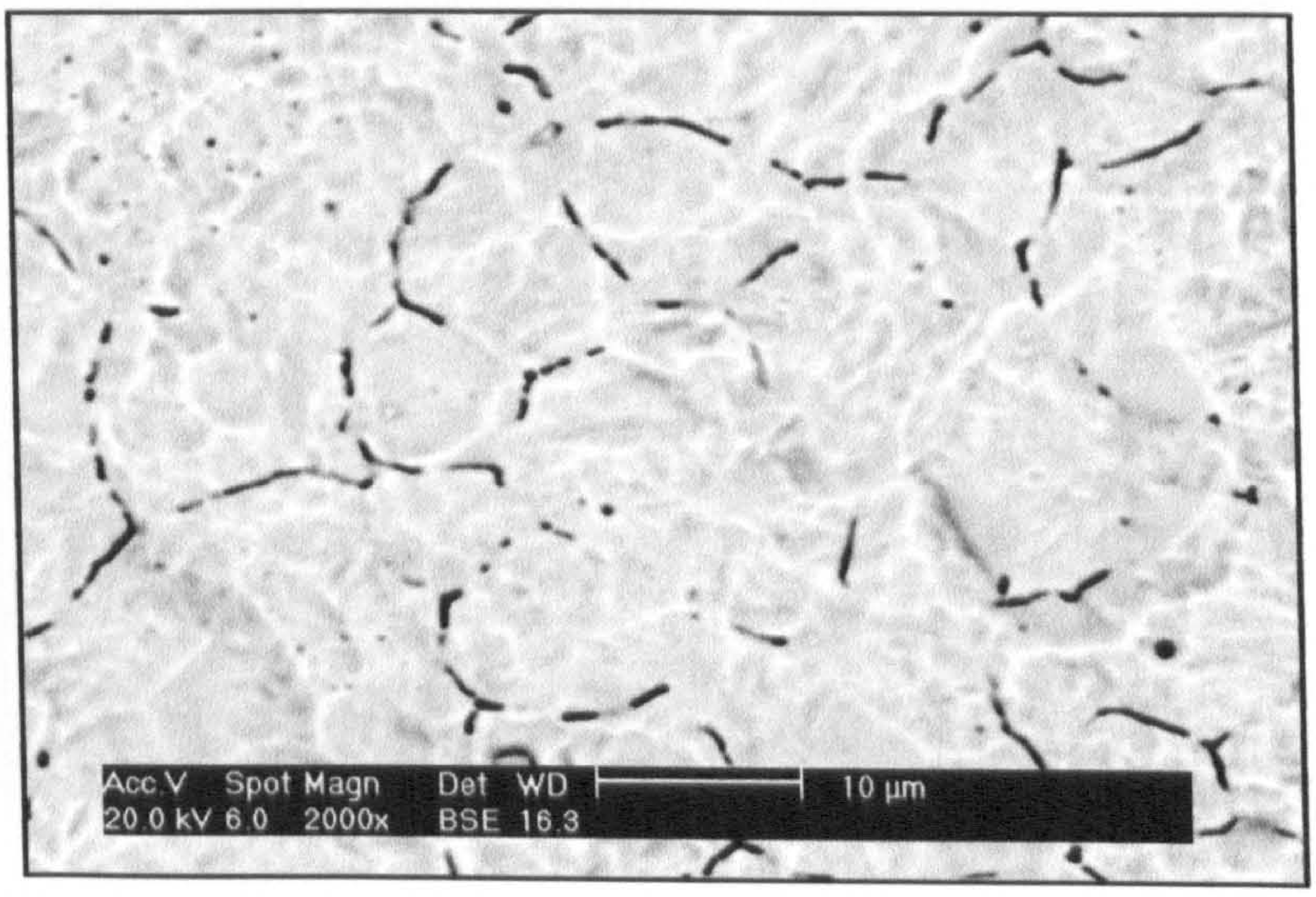

f. B1-8 (16.6h)
depth 2.49 µm

Fig. 4-8 Typical surface topography for different depth of internal oxidation layer of the specimens B1carburised using procedure 1

a. E1-4 (2.0h)
depth 2.20 μm

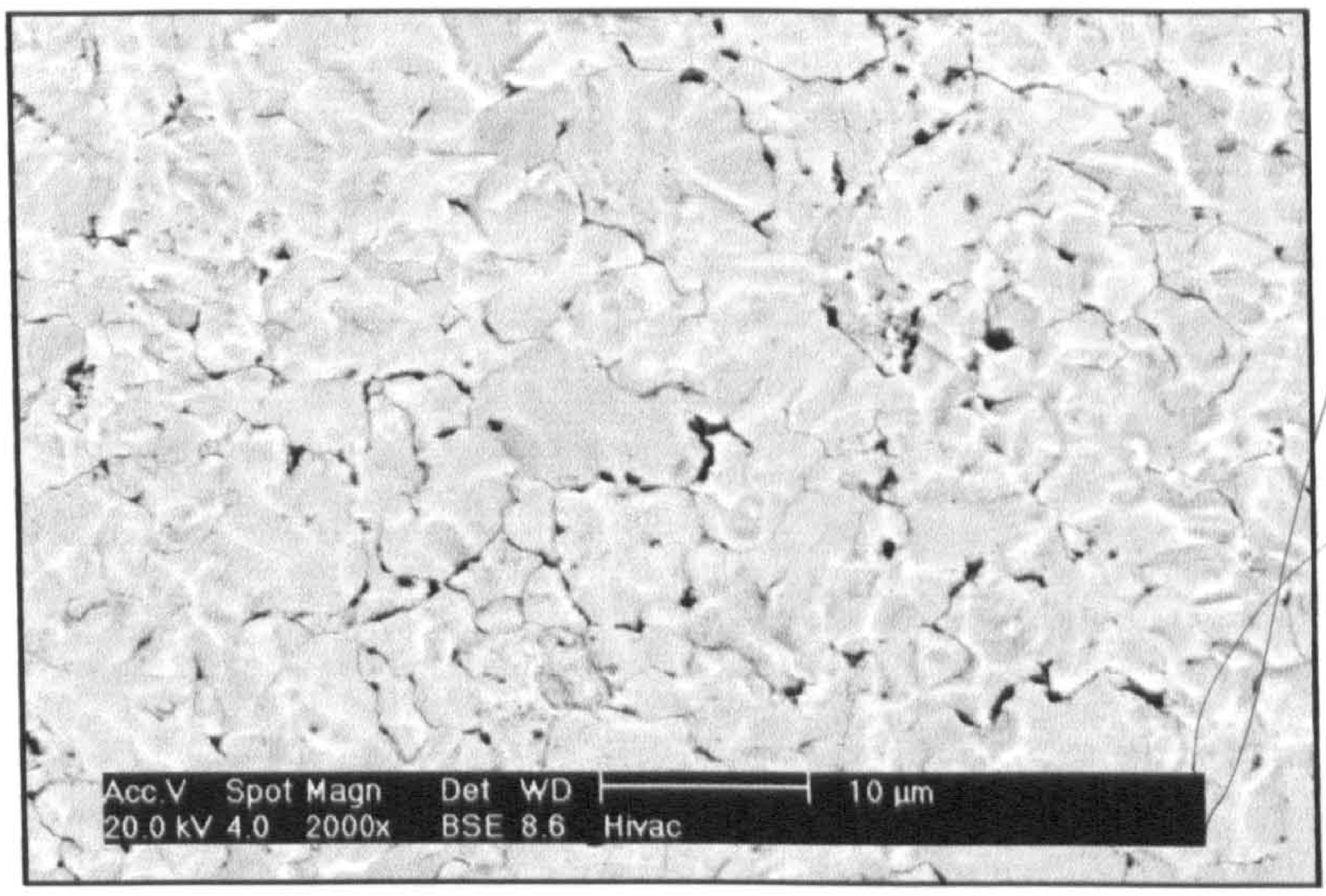

b . E1--5 (5.8 h)
depth 3.14 μm

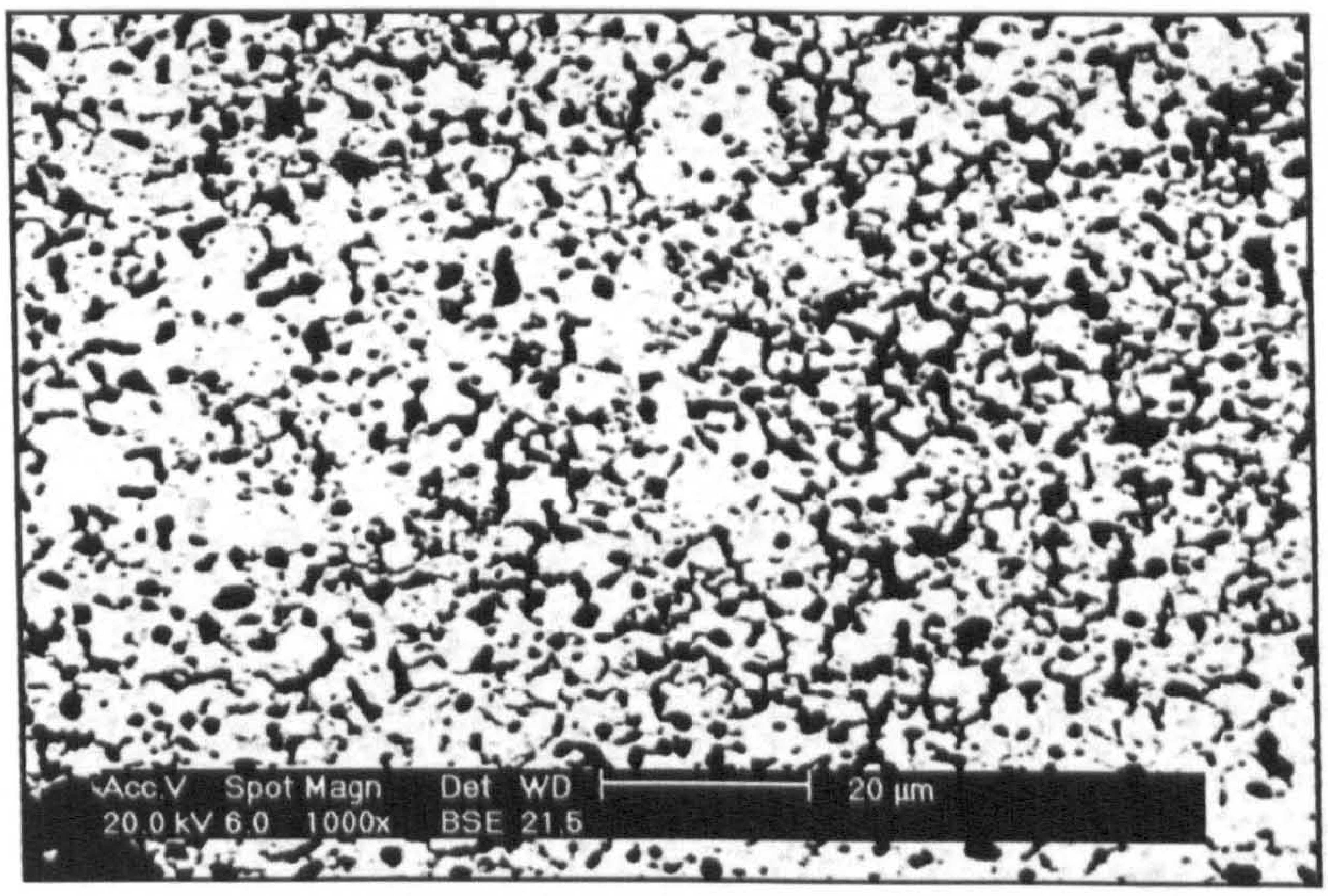

c. E1--5 (5.8 h)
depth 4.30 μm

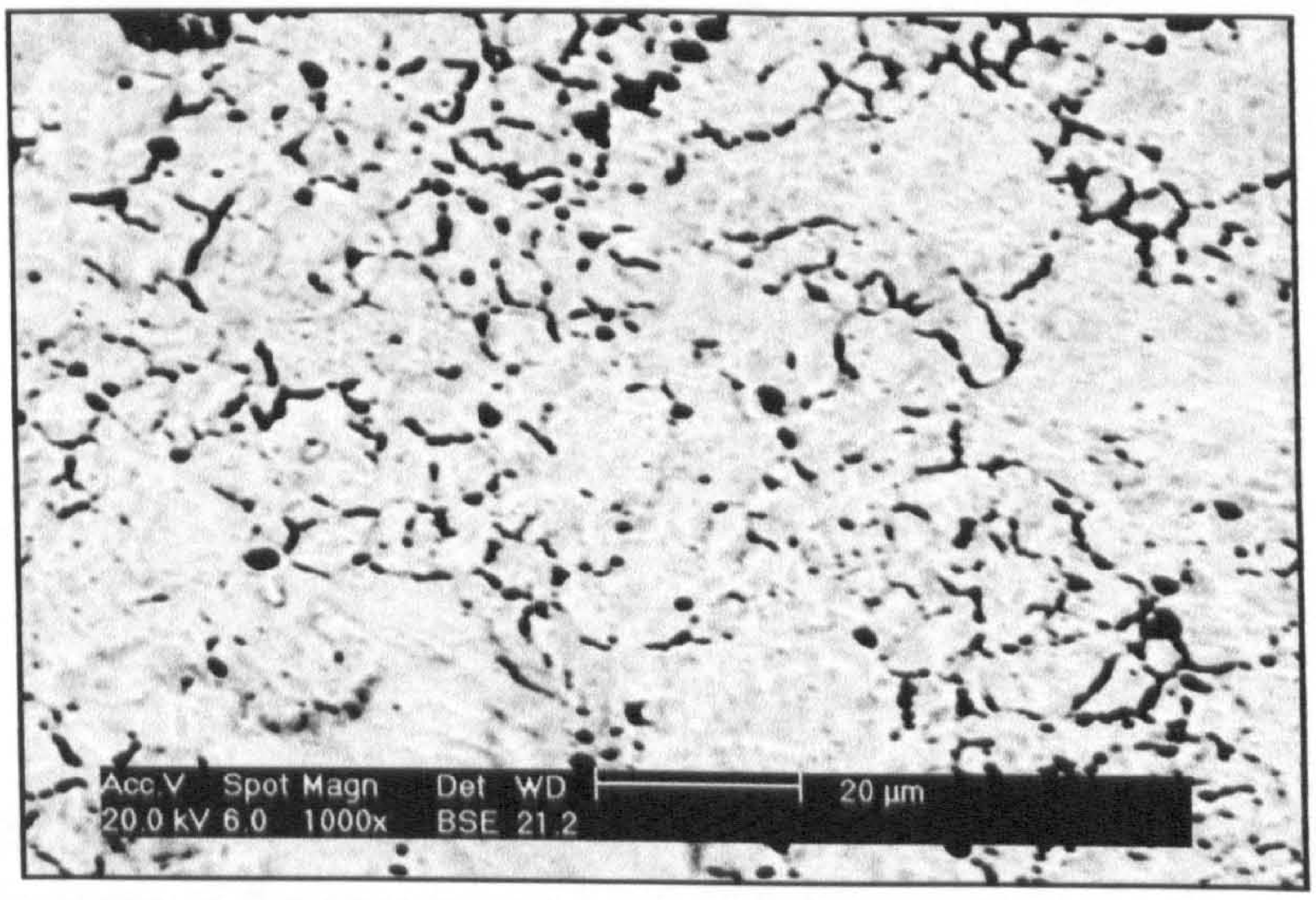

Fig. 4- 9 Typical surface topography for different depth of the internal oxidation layer of the specimens E1(0.77%Si) carburised using procedure 1

d . E1--8 (16.6 h)
depth 1.50 μm

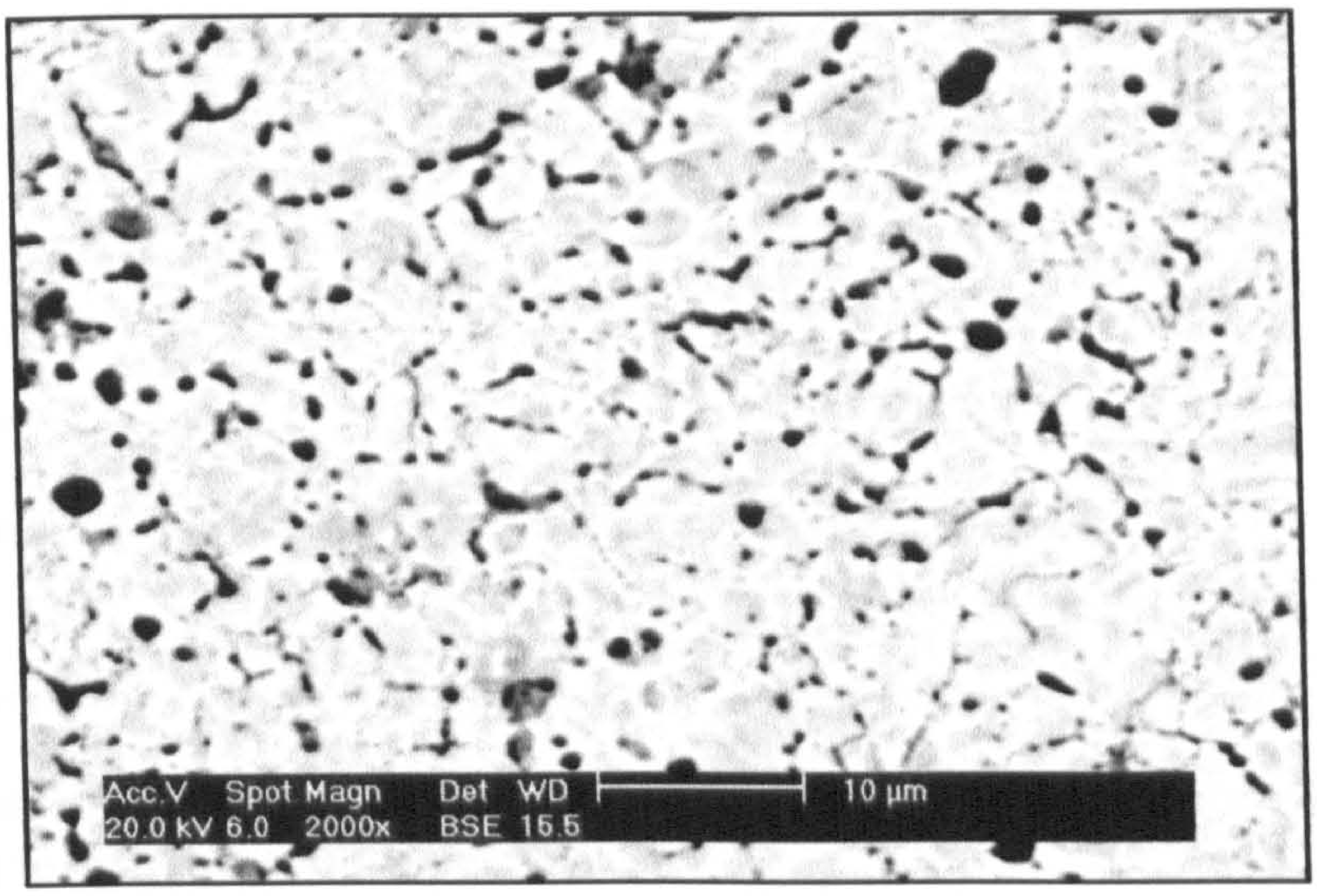

e . E1--8 (16.6 h)
depth 2.9 μm

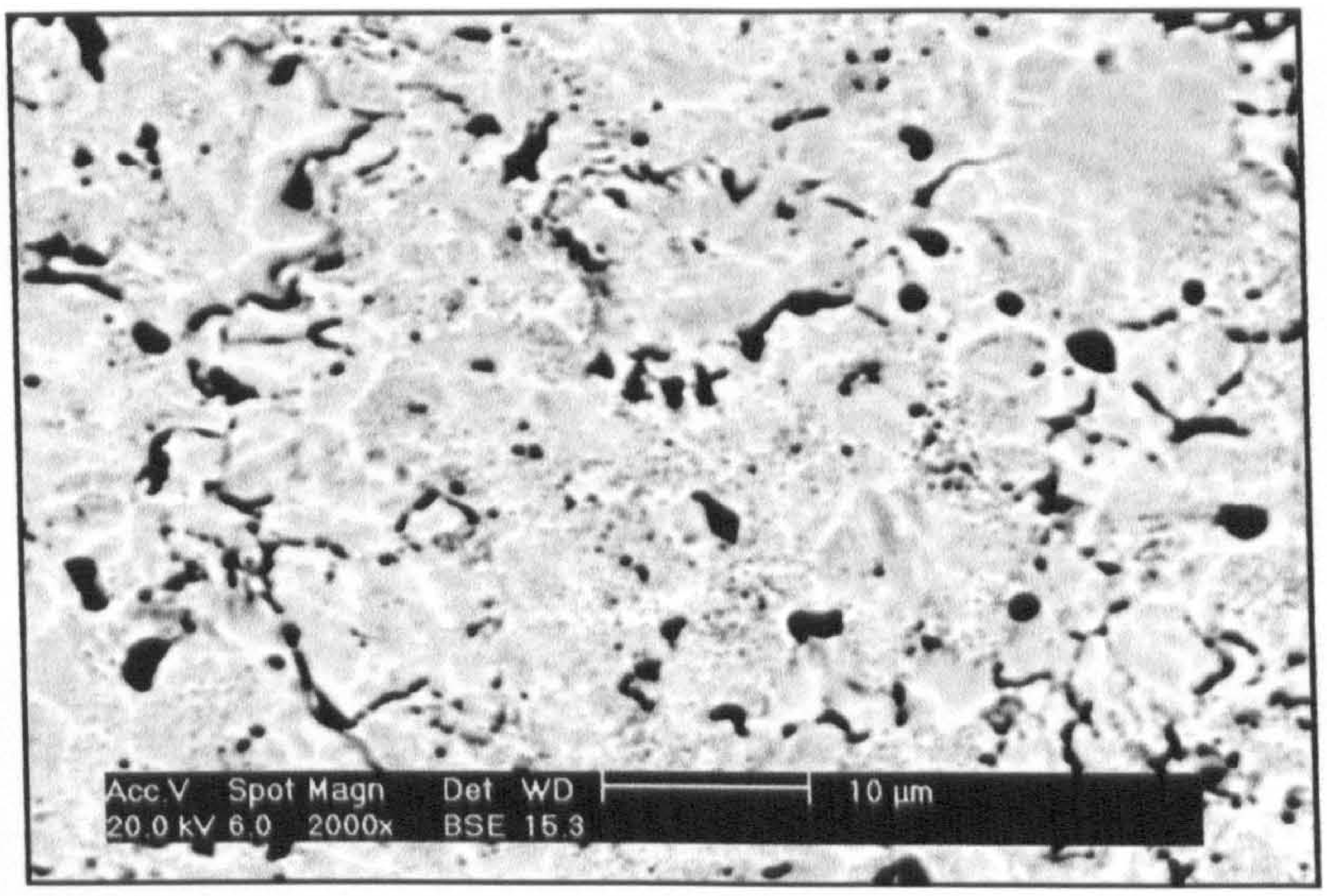

Fig. 4- 9 Typical surface topography for different depth of the internal oxidation layer of the specimens E1(0.77%Si) carburised using procedure 1

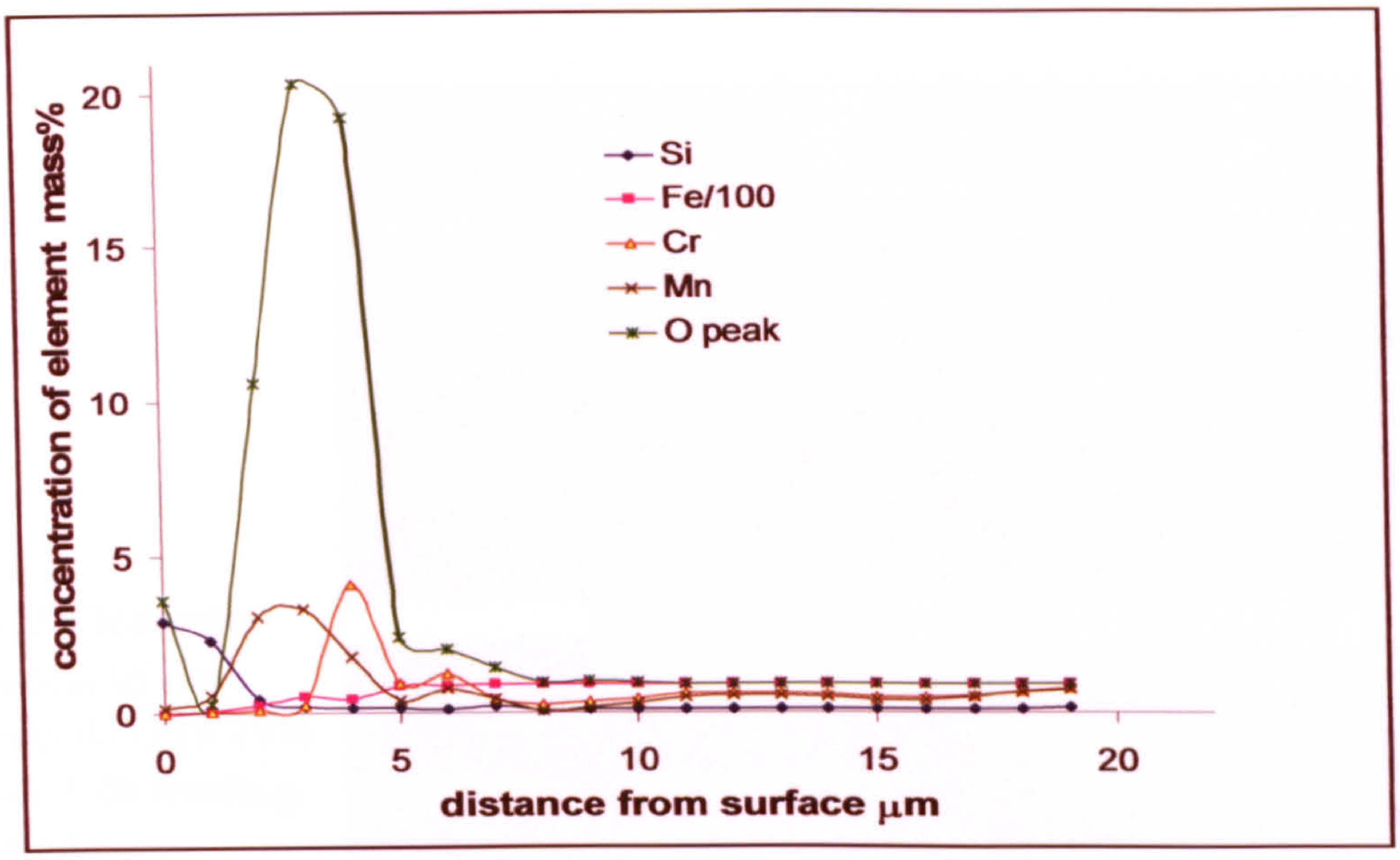

Fig. 4-10 Surface oxide layer was strong rich Si, Mn and Cr after short time heating (0.25h) in specimen B1-1 (EPMA line scan).

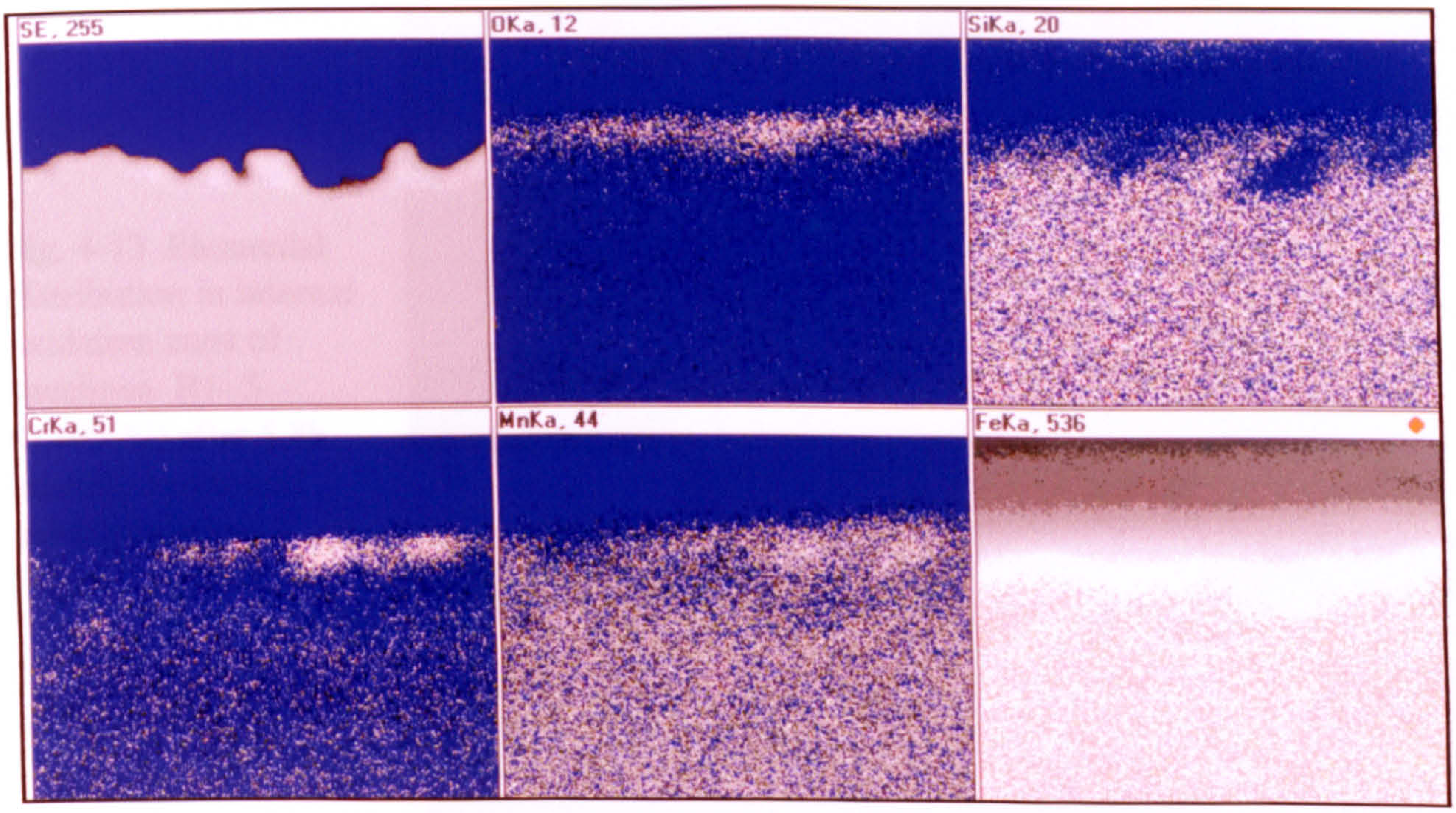

Fig. 4-11 Cr and Mn oxides precipitated at surface region and alloy elements depletion below the oxides in specimen B1-2, heating 0.5h, carburised using procedure 1

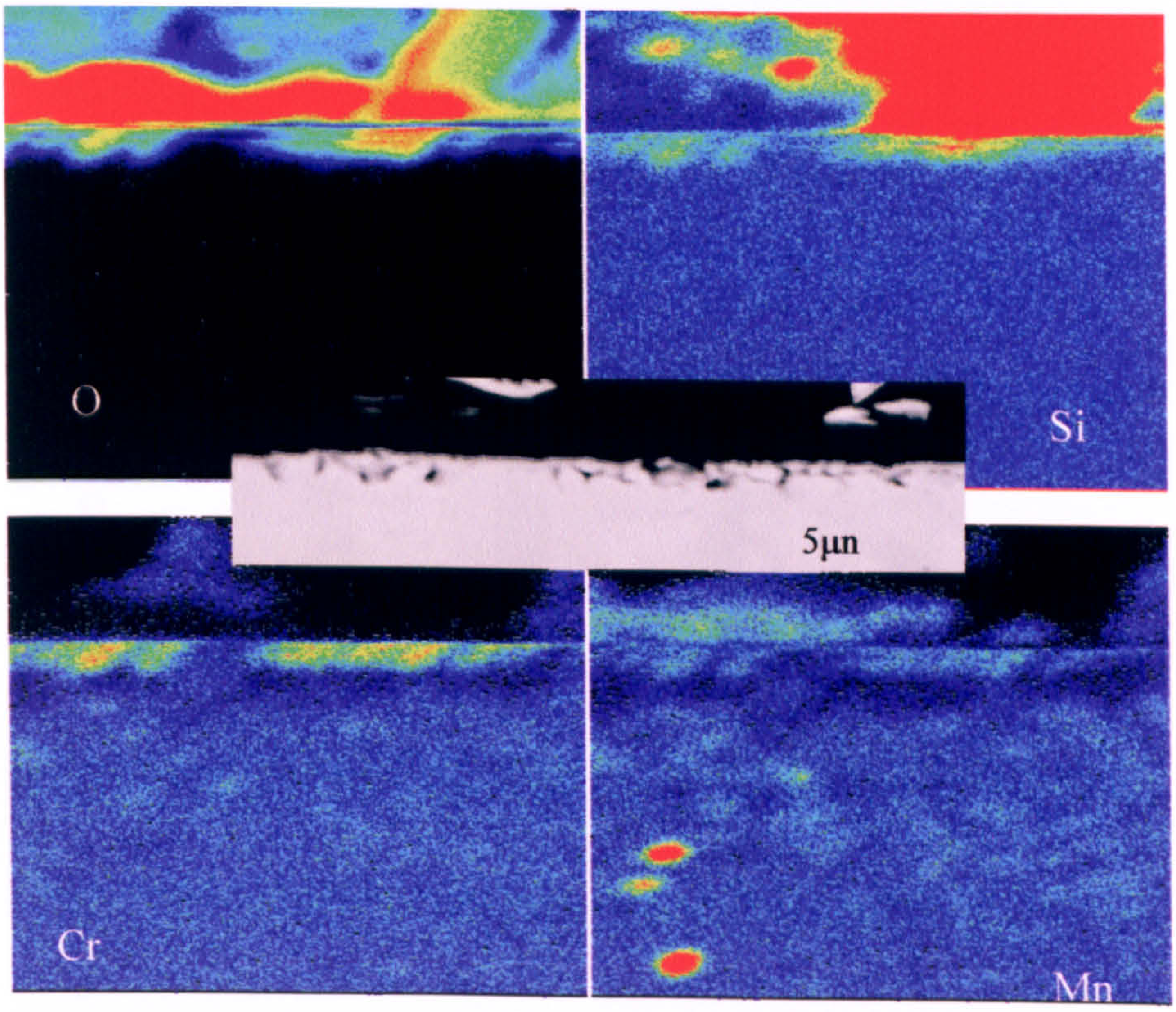

Fig. 4-12 Elemental distribution in the specimen B1-3 (0.19% Si) after 1.0h heating, carburised using procedure 1

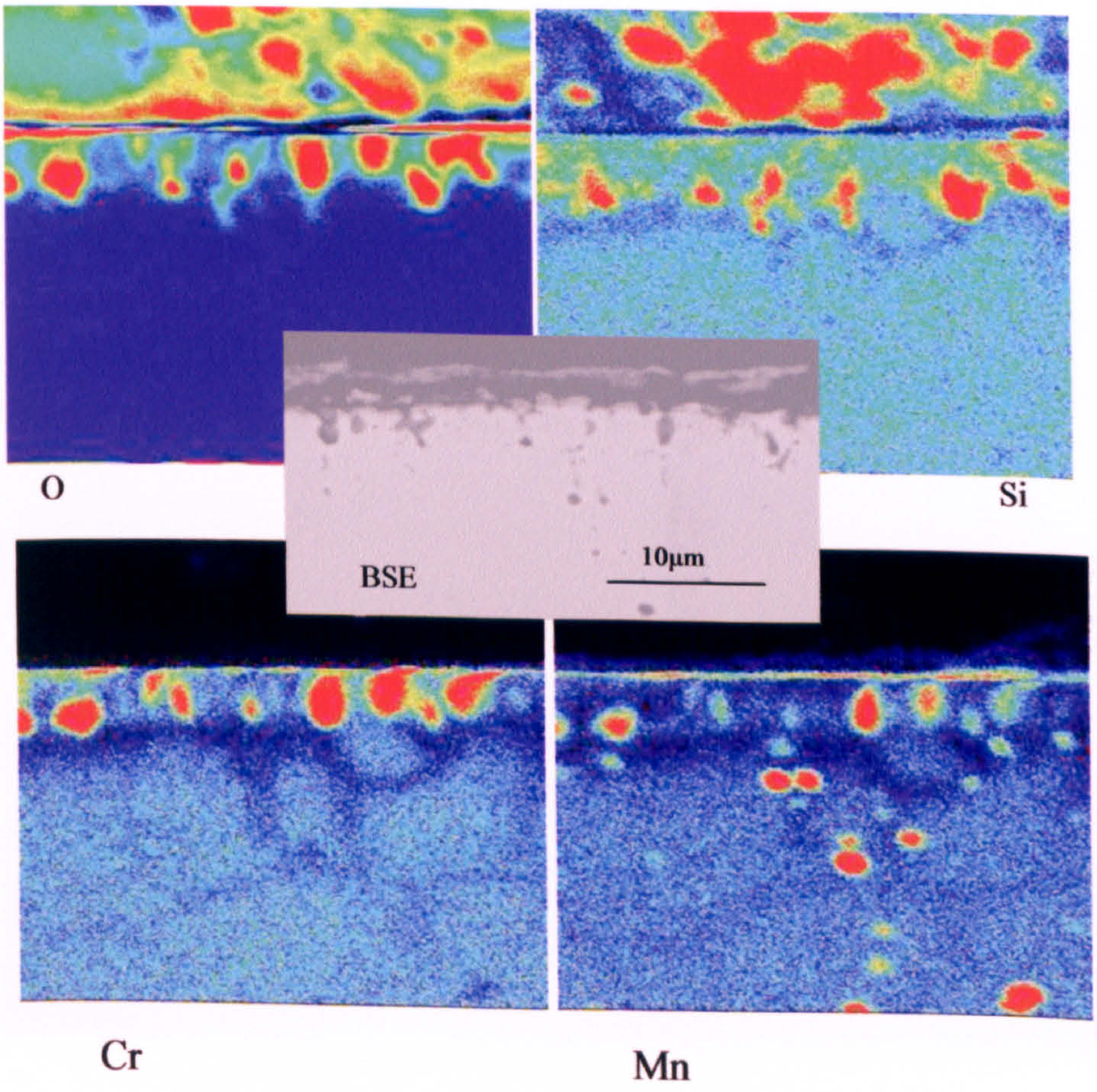

Fig. 4-13 Elemental distribution in internal oxidation zone of specimen B1- 5 (0.19%Si) after 5.8h heating, carburised using procedure 1

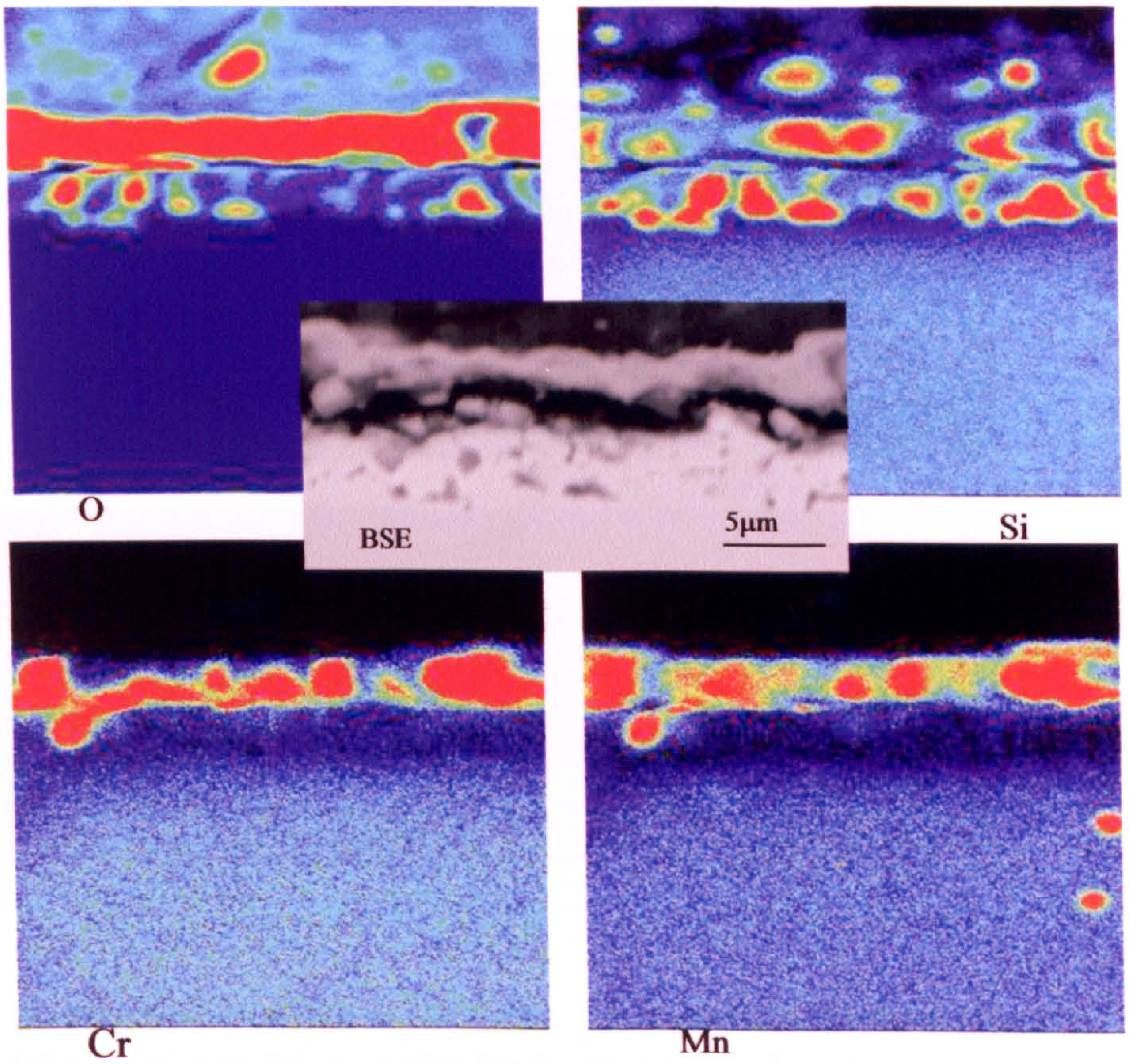

Fig. 4-14 Elemental distribution in the internal oxidation zone of the specimen E1-7 (0.77%Si) after 11.0 h heating, carburised using procedure1

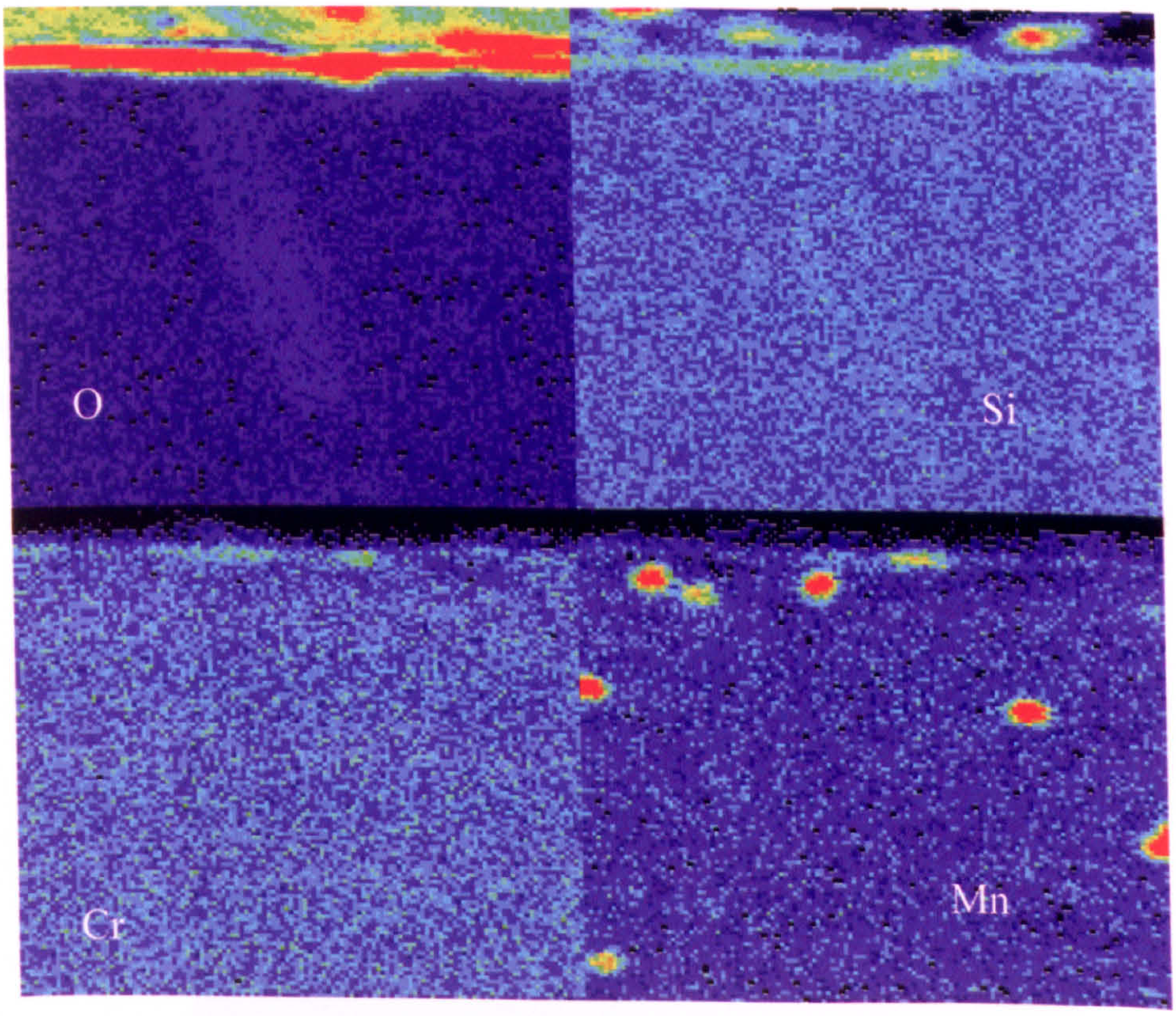

Fig. 4-15 Elemental distribution in the internal oxidation zone of the specimen E1-1 (0.77% Si) after 0.25 h heating, carburised using procedure 1

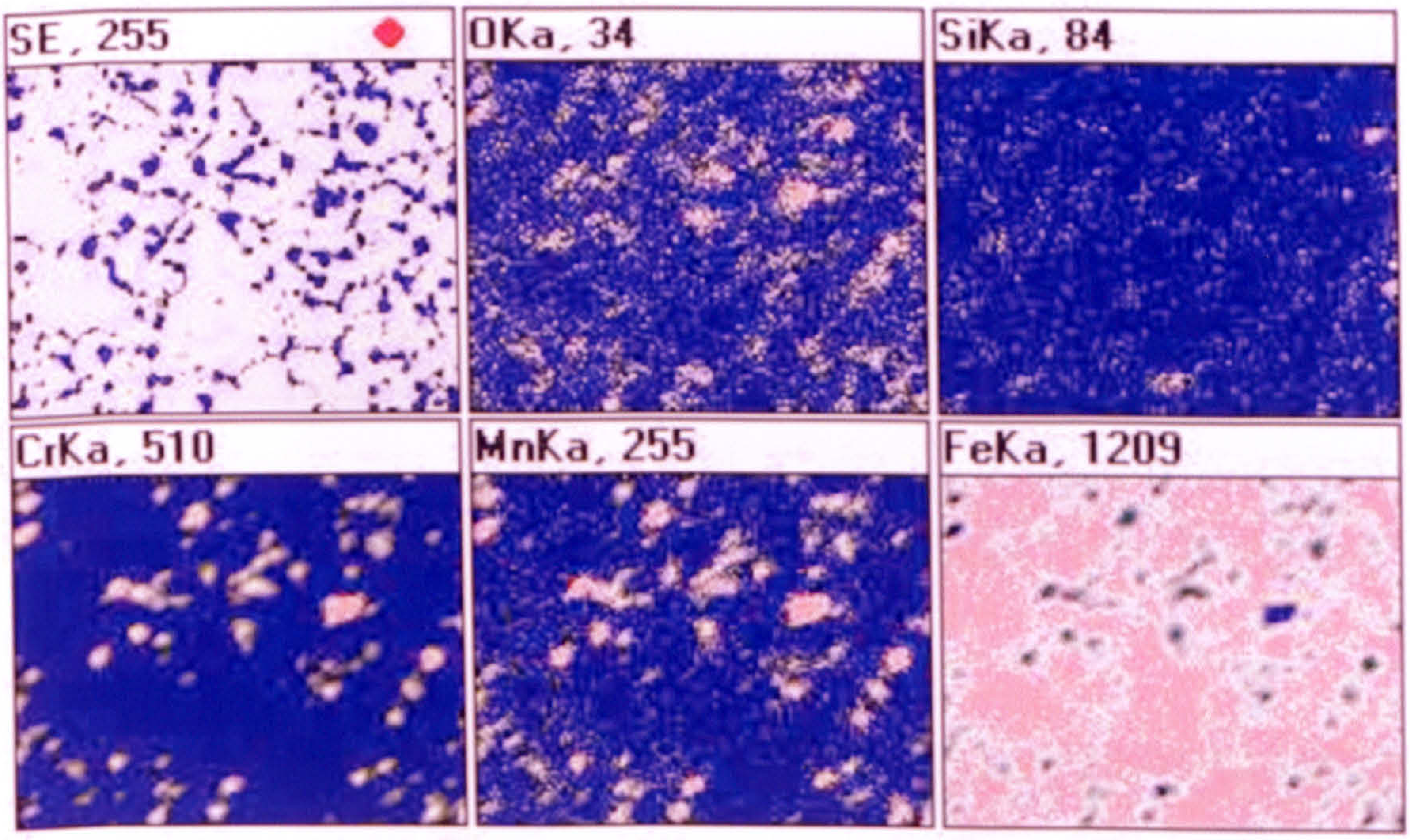

Fig. 4-16 Elemental distribution in depth layer (2.54 µm, related to cross section image outer zone) of the specimen B1-5, carburised using procedure 1

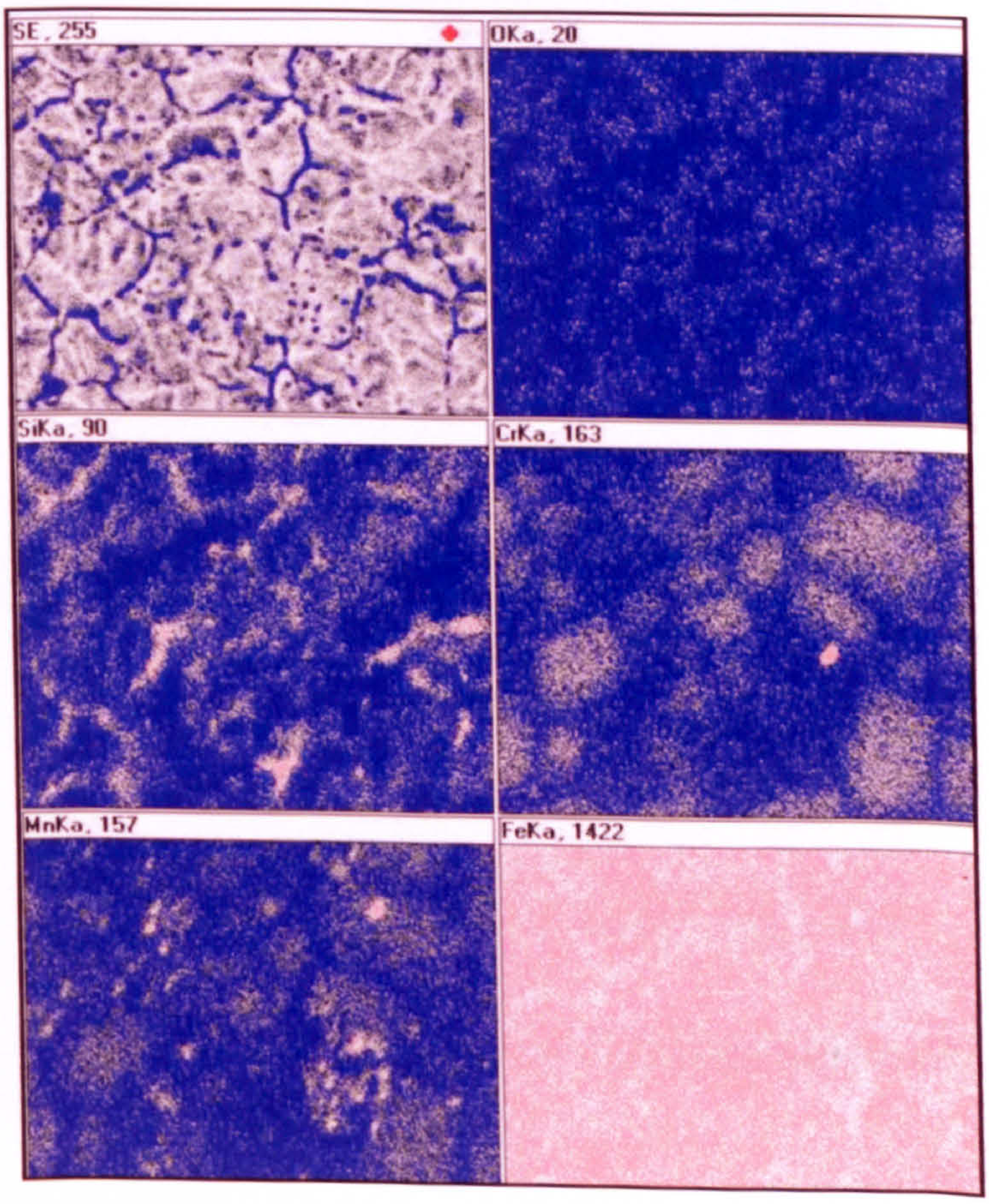

Fig. 4-17 Elemental distribution in depth layer (4.78 µm, related to cross section image inner zone) in the specimen B1-5, carburised using procedure 1

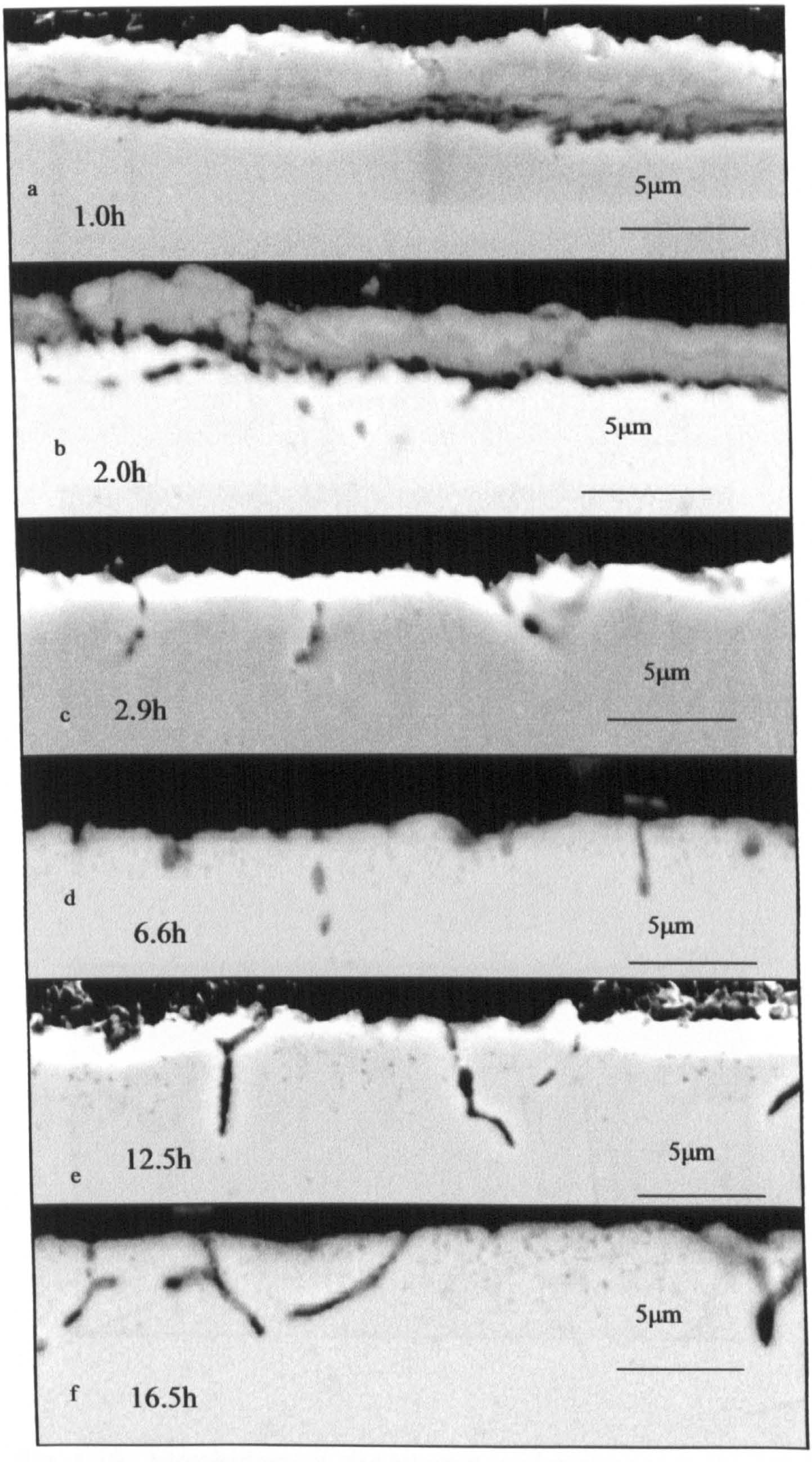

Fig. 4-18 Morphology of the internal oxidation zone in the specimens C2 series (0.31%Si), carburised using procedure 2

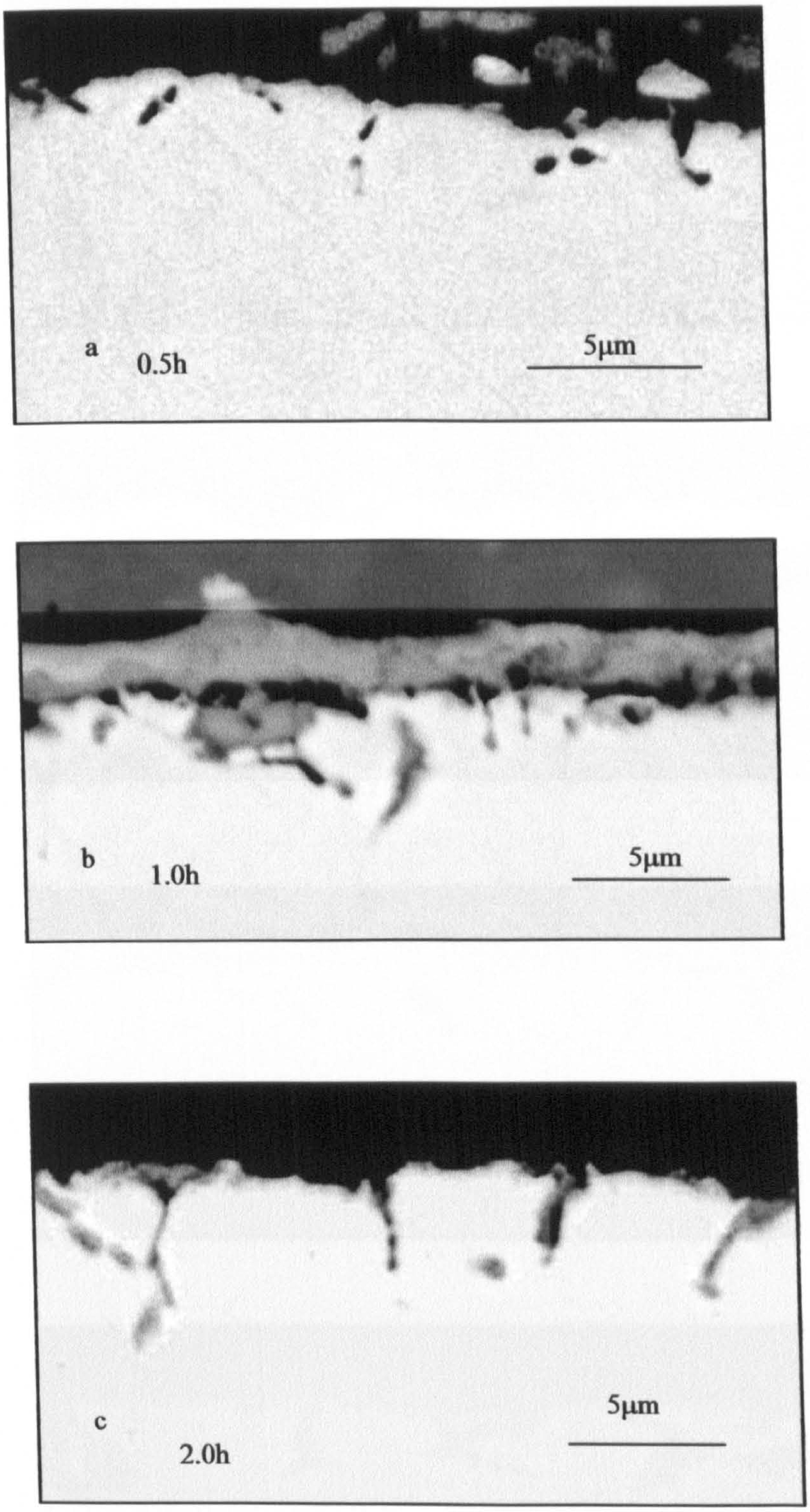

Fig. 4-19 Morphology of the internal oxidation zone in the specimens E2 series (0.77%Si), carburised using procedure 2

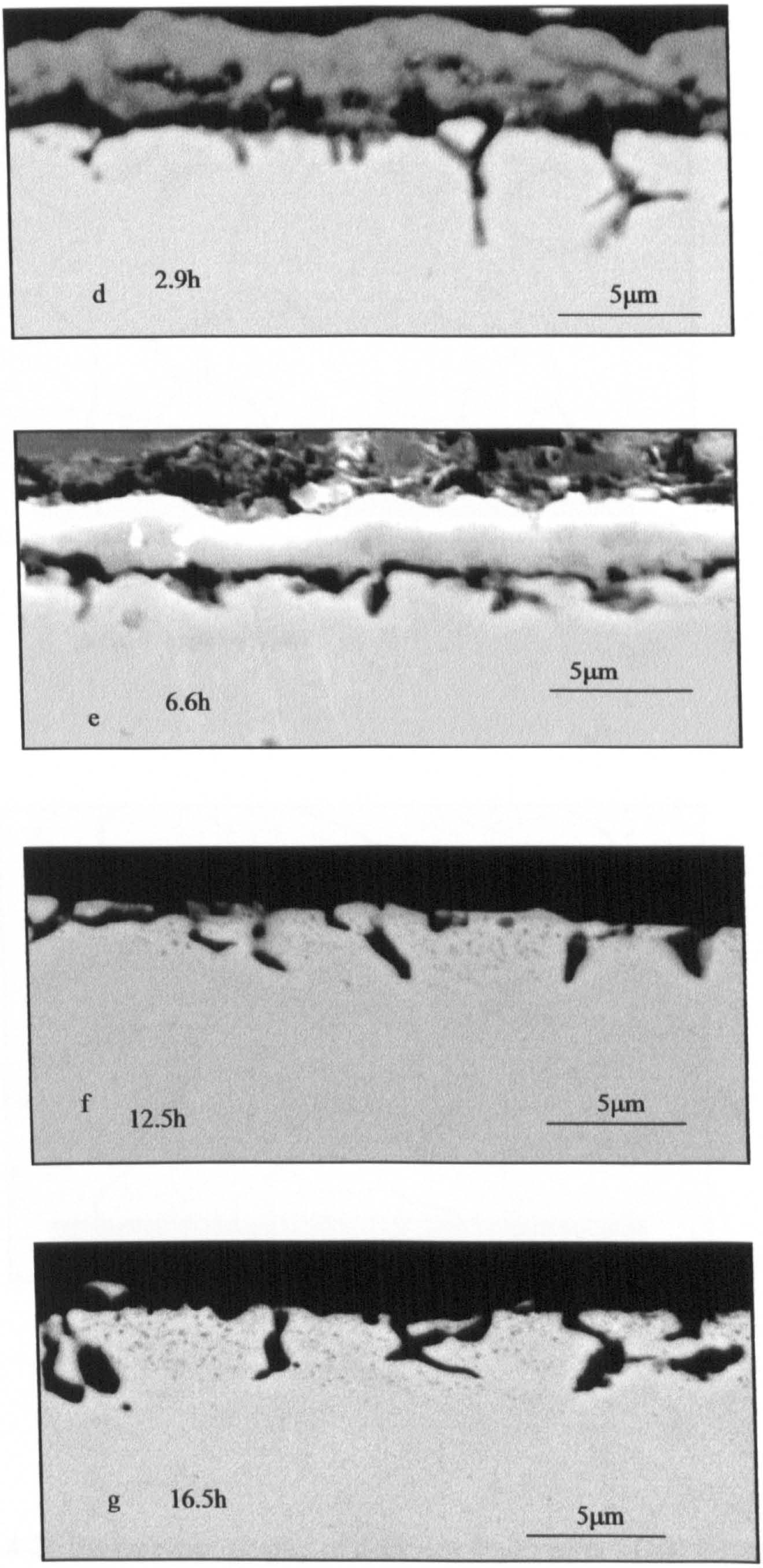

Fig.4-19 Morphology of the internal oxidation zone for specimens E2 series (0.77%Si), carburised using procedure 2.

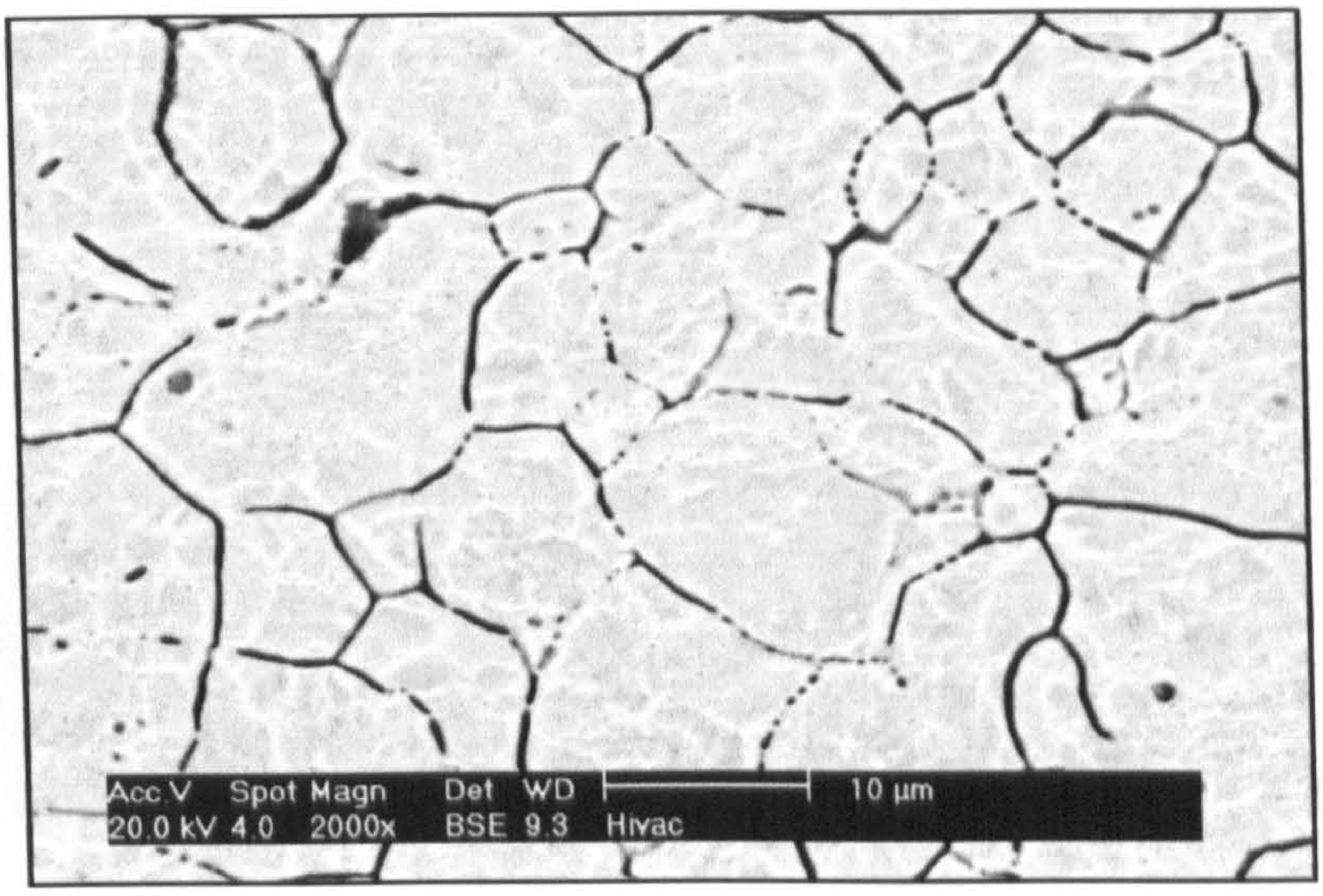

A C2-7 depth 1.58µm

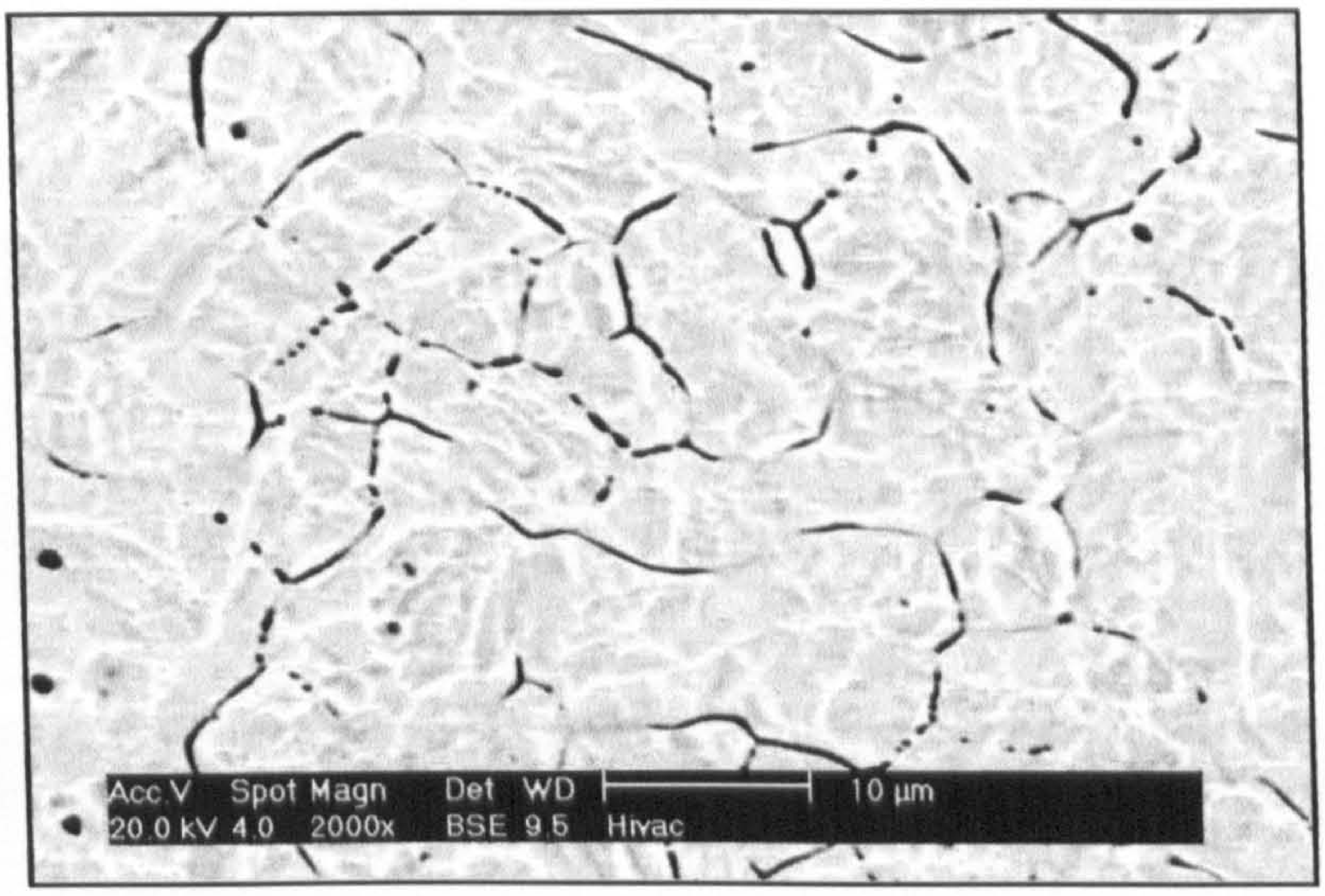

B C2-7 depth 2.59µm

Fig. 4-20 Surface topography of different depth layer of the internal oxidation in specimen C2-7 (16.6h)

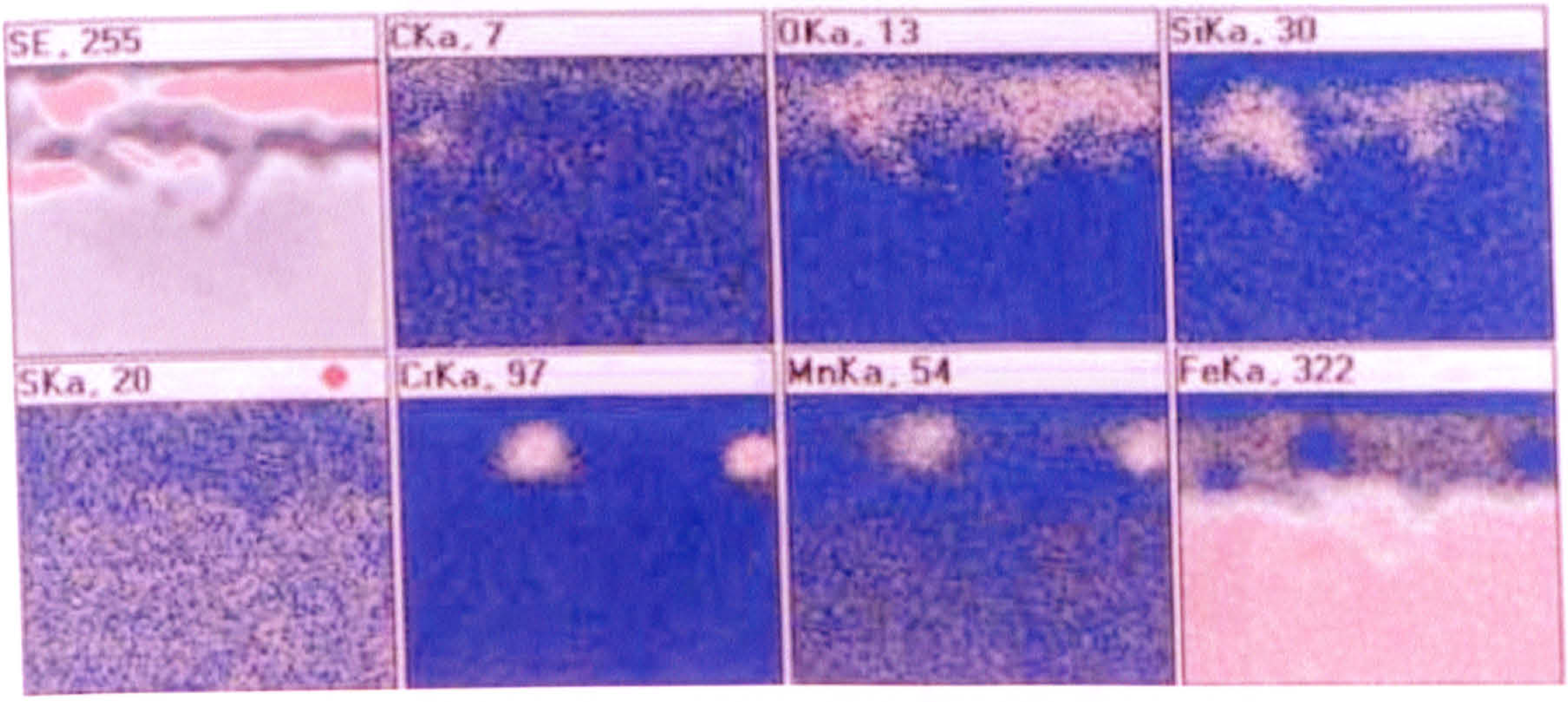

Fig. 4-21 Elemental distribution in the internal oxidation for the specimen E2-2 (0.77%Si), carburised using procedure 2.

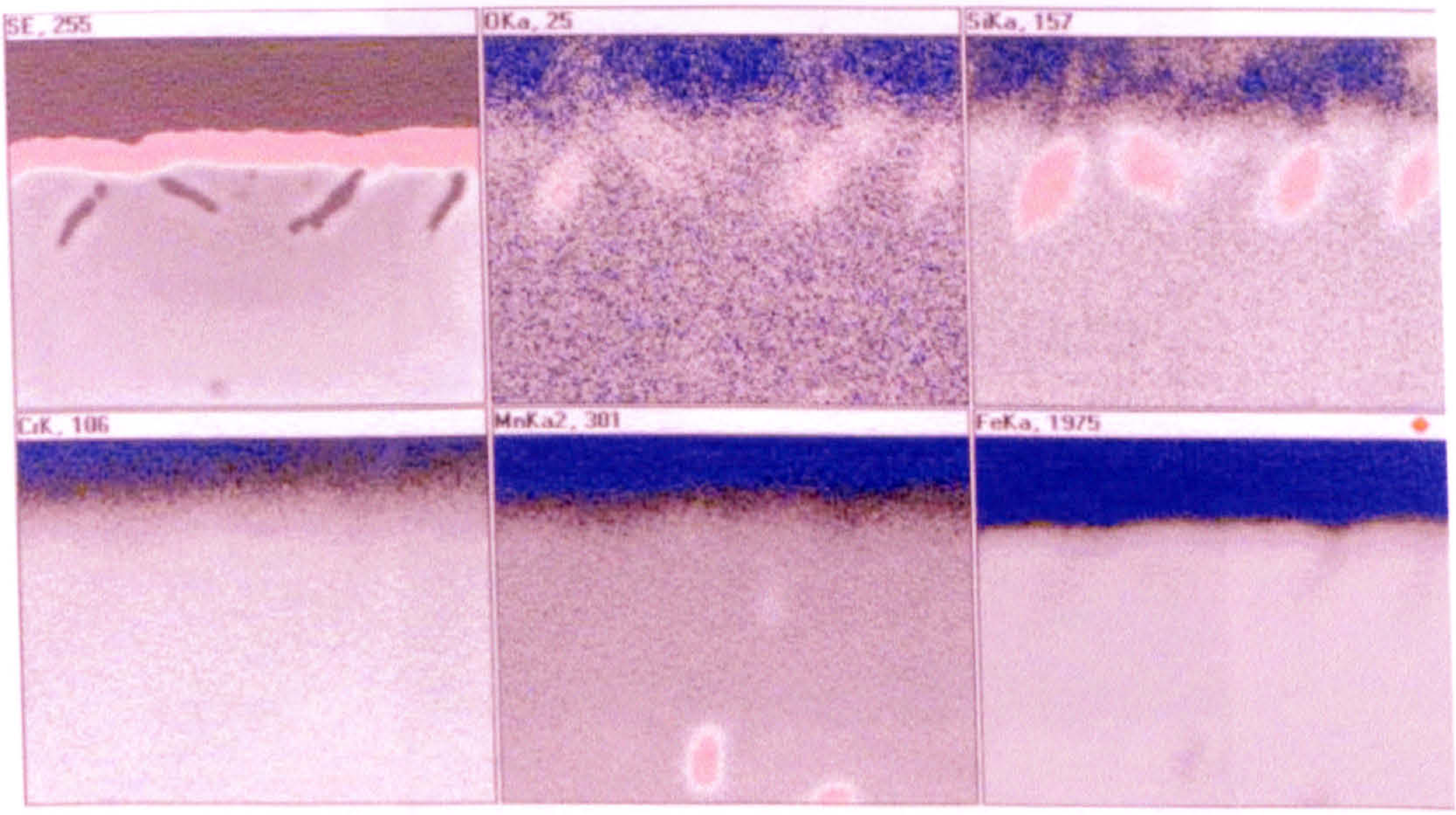

Fig. 4-22 Si rich in the internal oxidation zone for the specimen C2-6 (0.31%Si) carburised using procedure 2

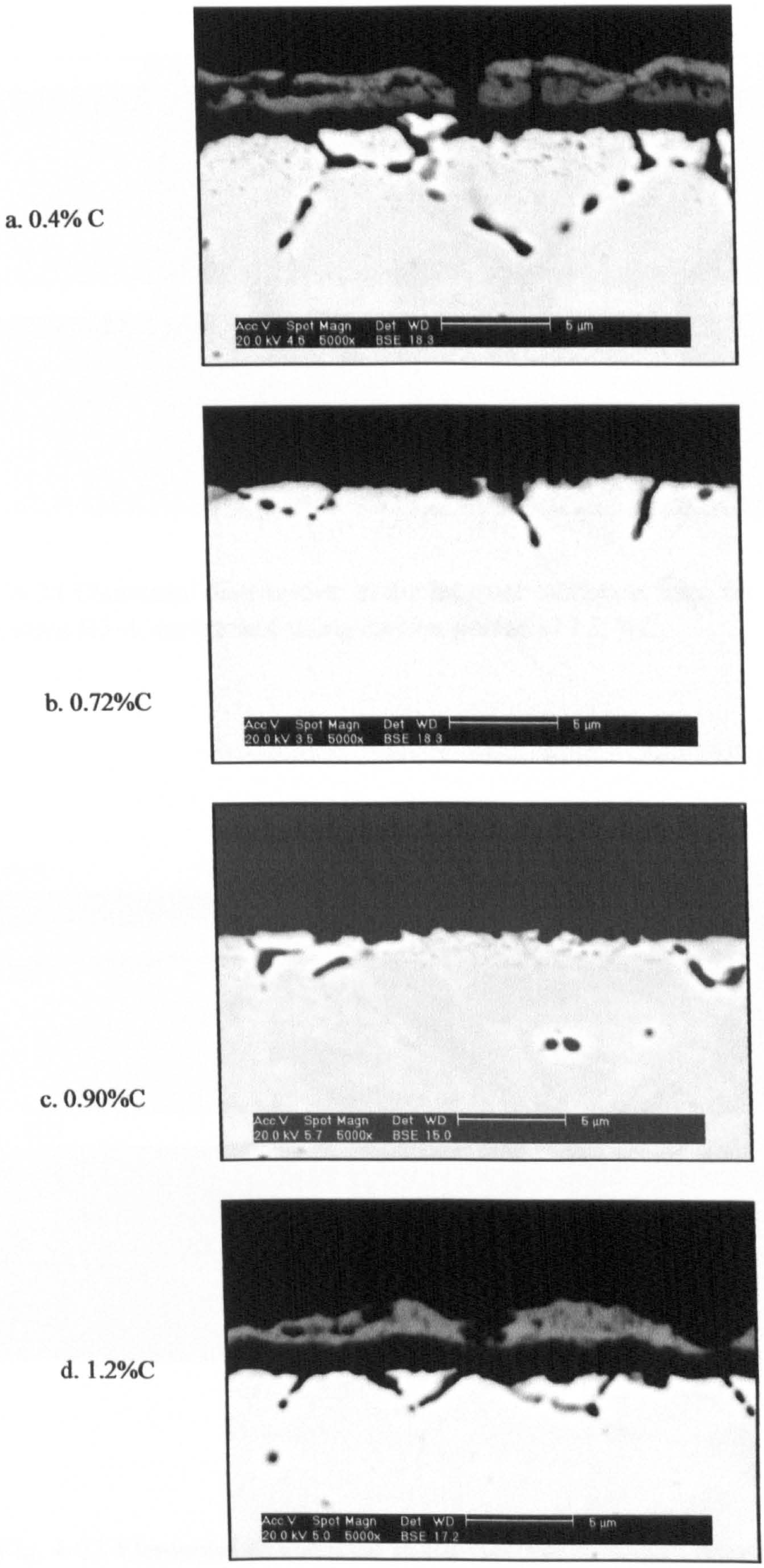

a. 0.4% C

b. 0.72%C

c. 0.90%C

d. 1.2%C

Fig. 4- 23 Morphology of the internal oxidation zone for specimens (B3) with different carbon potential (%C)

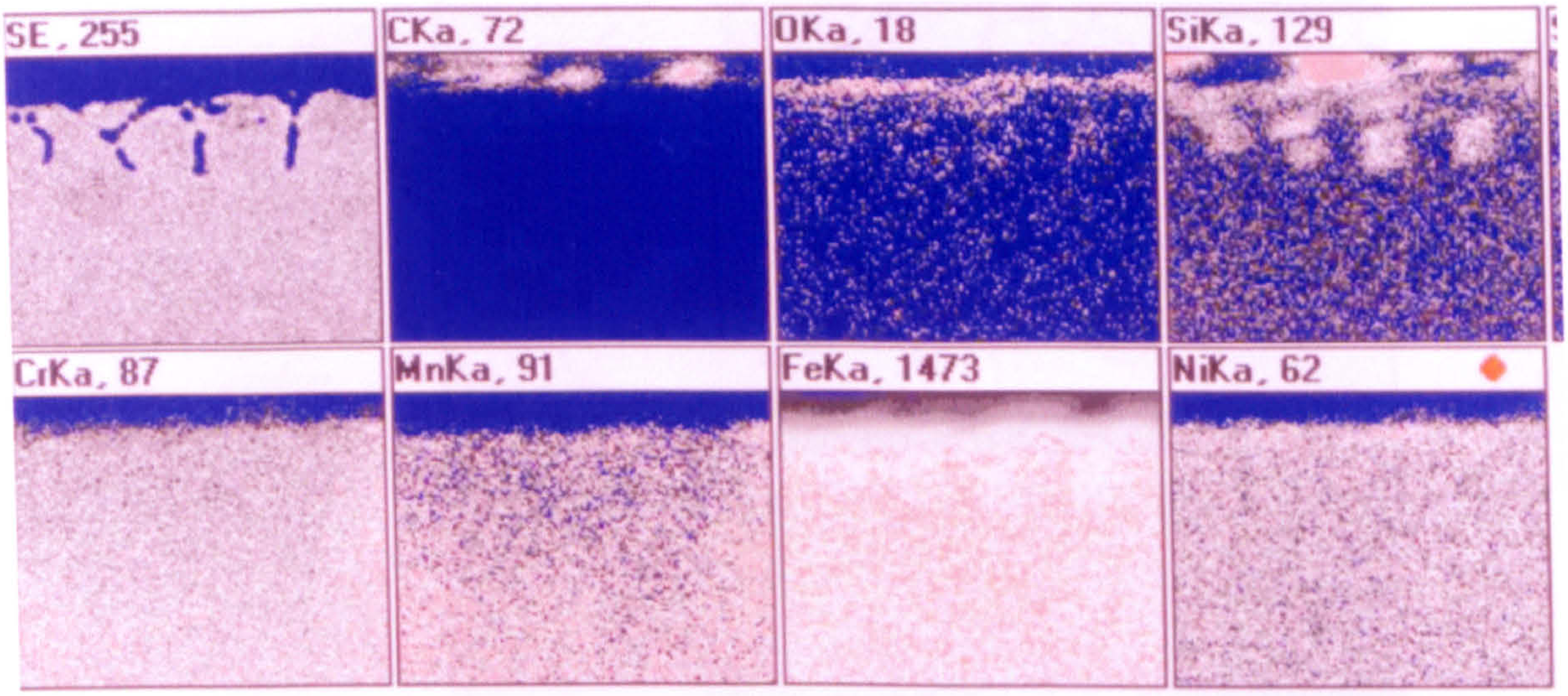

Fig. 4-24 Elemental distribution in the internal oxidation zone for the specimen B3-4, carburised using carbon potential 1.2 %C.

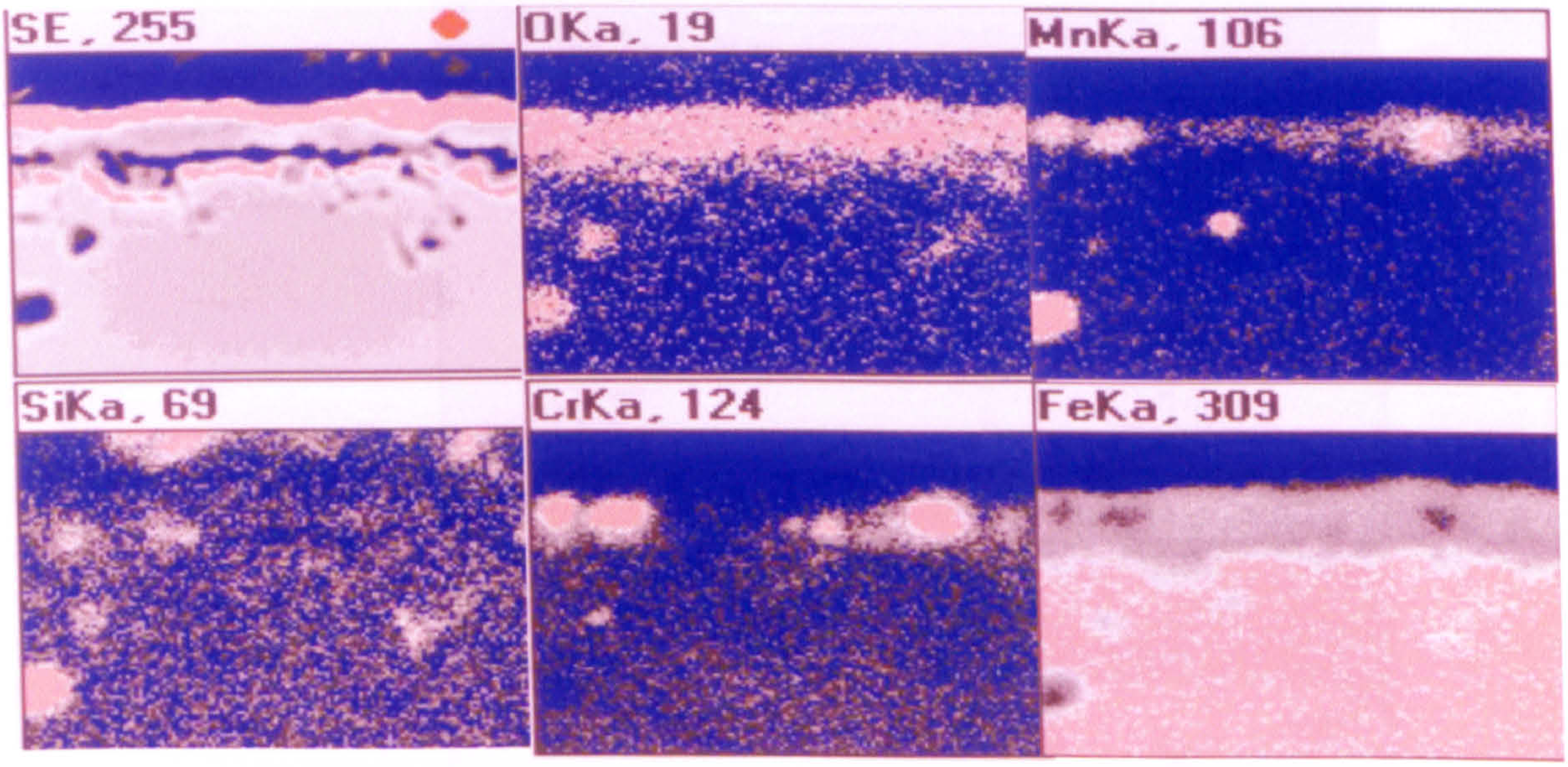

Fig. 4-25 Elemental distribution in the internal oxidation zone for the specimen B3-4, carburised using carbon potential 0.4 %C.

a. 0.3% C

b. 0.4%C

c. 0.6%C

d. 0.3-0.6%C

Fig. 4-26 Morphology of the internal oxidation in different furnace atmosphere condition in the base process for the specimens B4 series

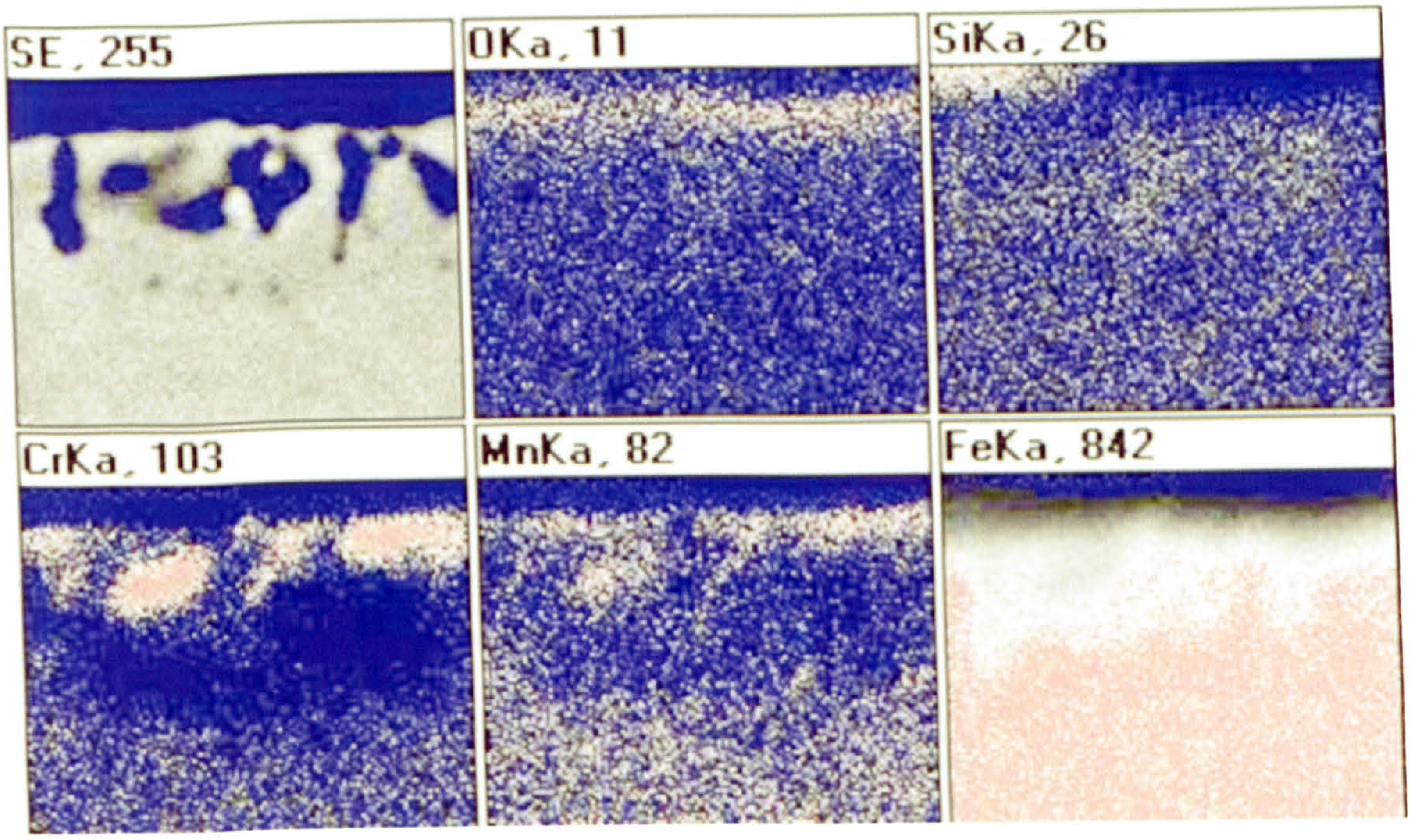

a. specimen B4-3, 0.6%C, control atmosphere

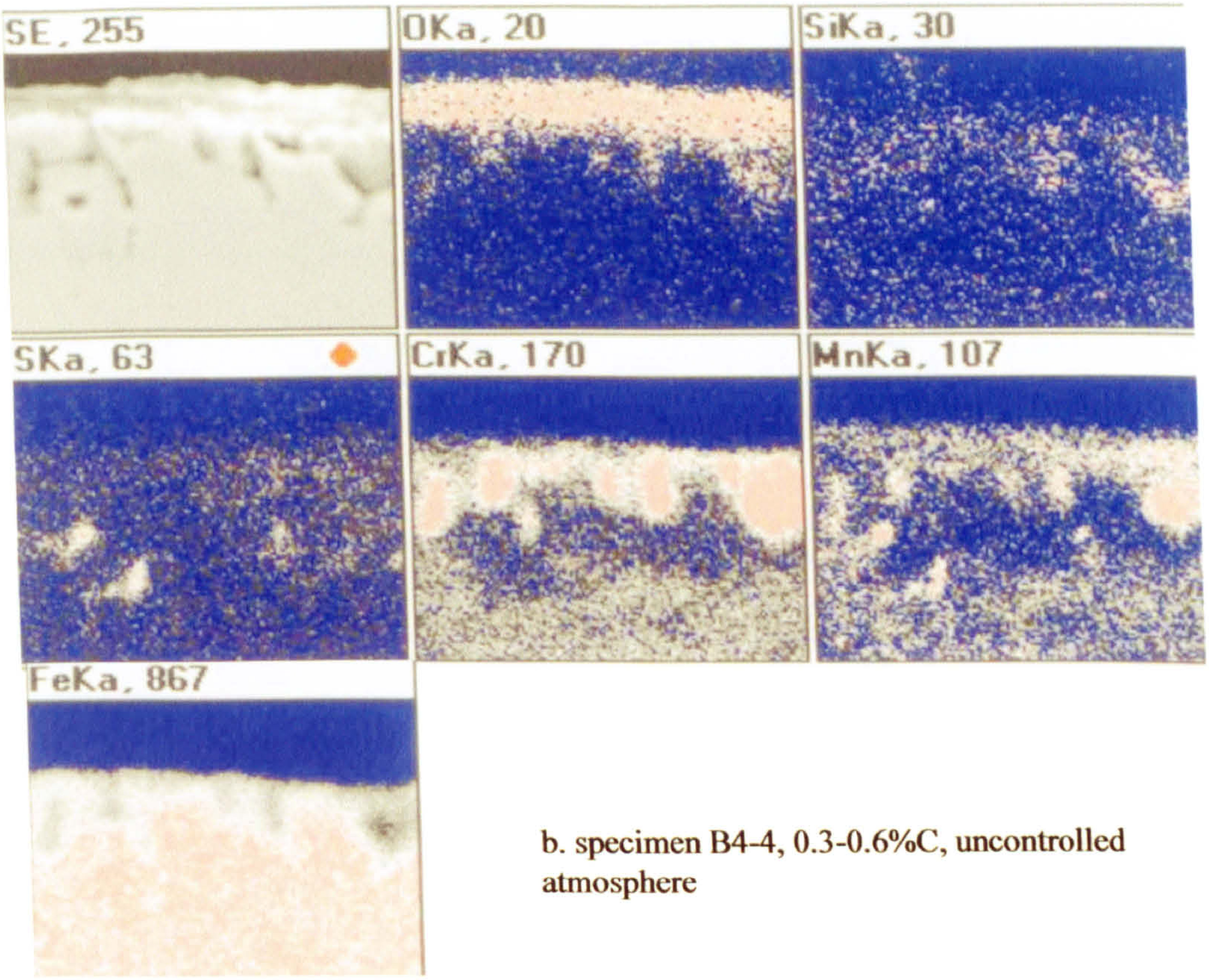

b. specimen B4-4, 0.3-0.6%C, uncontrolled atmosphere

Fig. 4-27 Elemental distribution in the internal oxidation zone for the specimens B4

CHAPTER 5

QUANTITATIVE AND QUALITATIVE EVALUATION OF THE INTERNAL OXIDATION ZONE

5.1 Composition Gradients in the Internal Oxidation Zone

5.1.1 Oxygen Penetration

In the oxidation process, oxygen atoms are adsorbed onto the metallic surface. From there, the oxygen atoms diffuse inwards along grains and subgrain boundaries into the lattice. Once there, they can chemically combine with available substitutional elements that have a high oxidation potential to form oxides with elements, such as in this case, Si, Mn and Cr. Oxygen penetration into the matrix was observed for all the specimens studied. A typical composition gradient for oxygen in the carburised specimens is shown in Fig. 5-1. The penetration depth of the oxygen as a function of exposure time is shown in Fig. 5-2. The results indicate that as soon as the specimens were put into the carburising atmosphere, a high concentration of oxygen gathered around the specimens and a greater oxygen concentration gradient is built up between the surface and matrix of the specimens. It can be observed that the oxygen penetrated faster in the base process (heating time < 5.0hrs) than the boost process. The penetration depth of oxygen remained approximately 15-20 μm in the specimens B1 and C1 series. In the specimens E1 series, the oxygen penetrated to the depth of approximately 7-8 μm. The depth of oxygen penetration was greater than the depth to which the internal oxides formed.

5.1.2 Alloy Elements

During the carburising process, oxygen diffused inwards from the surface, while the alloying elements in the steel diffused outwards to the surface, reacting with oxygen at the internal oxidation front. The typical composition gradient of alloy elements was examined using EPMA line scanning for the cross section specimens, as shown in Fig. 5-3. The results indicate that the alloy element concentration varied with depth to a greater extent than the oxygen. However, the alloy distribution correlated with the variation in oxygen content. It was observed that the alloy elements were particularly rich at the oxidation interface close to the surface and adjacent to the internal oxides. For example, the Si content in the specimen B1-7 reached 0.86% in the vicinity of Si oxides, which was much higher than its bulk content, which was 0.19%Si. Cr and Mn behaved in a similar manner. Fig. 5.4-5.5 give GDOES results showing the typical concentration profiles of Cr, Mn and Si in the internal oxidation region as a function of depth below the carburised surface up to a total depth of 10μm. The first peak was always a strong signal of O and Si at the surface of the specimens. A Mn peak signal then appeared in a depth range of approximately 0.3-1.6 μm, followed by a Cr at approximately 0.5-2.0 μm. Interesting, second Si peak signal was observed following Mn and Cr peak signal or sometimes accompanied the first Cr peak signal. During initial exposure of 2h, Si, Cr and Mn were all concentrated within the first 500nm of the surface. Interestingly, both Cr and Mn also peaked ~2μm below the surface, although the intensity of the peak was substantially less than the one close to the surface. The principal change after 5.8h exposure was a significant reduction in the intensity of the first Si peak, but an increase in the intensity and width of the second Si peak. Fig. 5.4 to 5.5 results also show that in the internal oxidation zone, the concentration of alloying elements was much higher than the average bulk content. For example, in the internal oxidation zone of the specimen B1-6, the concentration of Cr was approximately four times that of the bulk content (1.06%Cr), Mn was approximately three times that of the bulk content (0.90%Mn), Si was approximately three times its bulk content (0.19%Si).

5.2 Penetration Depth of Internal Oxides

5.2.1 Penetration Depth and Exposure Time

The depth of the uniform internal oxidation front from the interface between surface oxide scale and external surface of the bulk metal were measured. Usually, the internal oxidation front was very flat and it was possible to obtain reasonably accurate measurements. The measured depth is plotted in Fig. 5-6, 5-7. All the specimens carburised using procedure 1 and 2 (see Chapter 3, Table 3-3) showed that the penetration depth of internal oxides increased with increasing exposure time.

In the carburising procedure 1, for time in range 0.25-2.0 h, the penetration depth of the internal oxides increased sharply with increasing exposure time. All the specimens revealed similar penetration rates in this heating time range to a depth of approximately 4.0-5.0 μm. The penetration depth of the internal oxides increased rapidly up to 5.8h to a depth of approximately 6.5 μm for specimen B1-5 and 4.50 μm for specimen E1-5. It then increased slowly as exposure time, as shown in Fig. 5-6. The penetration depth reached approximately 7.30 μm for specimen B1-8 and 5.30 μm for specimen E1-8.

The penetration depth of the internal oxides for specimens that were carburised using procedure 2 increased continuously with increasing carburising time, as shown in Fig. 5-7. After the long cycle carburisation, it either slowly increased or even slightly decreased, approximately constant. The reason for this is not well understood, a possible reason may be that during the carburising process, the internal oxidation zone of the surface spalled off by a breakdown of the severe intergranular oxide film.

The oxidation rate for the B1 series of specimens was faster than for the E1series using the same carburising procedure. For the same exposure time, the penetration depth of the internal oxides in the B1 series of specimens was deeper than the E1 series. Comparing the different carburising procedures, the oxidation constant and the penetration depth of the internal oxides in the specimens that were carburised using procedure 1 was larger than in the specimens that were carburised using procedure 2.

5.2.2 Penetration Depth and Carbon Potential

The penetration depth of the internal oxides in the specimens with different carbon potential is shown in Fig. 5-8, for specimens carburised at 930°C for 6.6h (carburising procedure 3). The penetration depth of the internal oxides decreased with increased carbon potential. At a carbon potential in the range of 0.71- 1.2%, the penetration depth of the internal oxides was slightly different to the depth in range of 3.48-2.52μm. However, there were no obvious difference between carbon potential of 0.9 % and 1.2%. In the specimen (B3-1) with low carbon potential (0.4%C), the penetration depth of the internal oxides was obviously deeper than the other specimens to the depth 5.2μm. It was twice tmes the depth the specimen B3-4.

In order to the study influence of controlled and uncontrolled atmospheres in the base process on the internal oxidation, the specimens were carburised at 800°C for 2.0h at different controlled carbon potential conditions and uncontrolled conditions (carbon potential varied in the range of (0.3-0.6) %). In this case, the penetration depth of the internal oxides was also increased with decreasing carbon potential, as shown in Fig. 5-9. The deepest penetration depth was observed in the specimen (B4-4) with uncontrolled carbon potential to a depth of approximately 4.55μm, followed by specimen B4-1 with 0.3%C to a depth of approximately 3.80 μm. The penetration depth of the internal oxides in the specimen B4-3 with 0.6%C was approximately 2.50μm.

The quantitative evaluation of the specimens indicated that as the carbon potential increased in the furnace, the penetration depth of the internal oxides was decreased. This agreed with previous research by Chatterjee-Fischer (1978).

5.3 Area Fraction of Internal Oxides in Internal Oxidation Zone

5.3.1 Area Fraction of the Internal Oxides and Exposure Time

The area fraction of the internal oxides in the internal oxidation zone (A) determined the density level of the internal oxidation zone. It was measured on a SEM image of the internal oxidation zone in the cross section specimens using an image analysis system. It gave an information about the development of the internal oxidation in the carburising process, as shown in Fig.5-10. For the specimens carburised using the carburising procedure 1, the area fraction of the internal oxides in the internal oxidation zone increased sharply with increased exposure time up to a peak value of 5.8h. In this case, the area fraction of the internal oxides in the internal oxidation zone was 0.275 for specimen B1-5 and 0.39 for specimen E1-5. Then, it dropped sharply up to 8.0h. The two specimens series (B1, E1) with different Si content had the same trend. The low peak value at 8.0 h and16.6h may be caused by the spallation phenomena of the internal oxidation zone. For the specimens carburised at the boost process (carburising procedure 2), the area fraction of the internal oxides in the internal oxidation zone was increased sharply at the early carburising stage with increasing carburising time. After long cycle heating, it remained at constant level, as shown in Fig. 5-11. At the early carburising stage, increase rate of the area fraction of internal oxides for the C2 series of specimens was slightly larger than that in the E2 series. after 6.6h, the approximate area fraction value was 0.10 for the specimen C2-5 and 0.11for the specimen E2-5. After this period, the area fraction of the internal oxides for the E2 series of specimens was approximately twice as larger as that of the area fraction in the C2 series. It confirmed that the internal oxides nucleated very quickly in the E2 specimens due to the high Si content of the bulk metal.

5.3.2 Area Fraction of the Internal Oxides and Carbon Potential

As the carbon potential in the furnace was increased, the area fraction of the internal oxides in the region internal oxidation decreased continuously and almost linearly as shown in Fig. 5-12. The area fraction of the internal oxides in the specimen C3-1 (0.4%C) was 0.21 and was approximately twice as larger as the specimen C3-4 (1.2%C), in which the area fraction of the internal oxides was approximately 0.11. Comparing with the four specimens using different controlled carbon potential conditions and uncontrolled conditions, in which carbon potential varied in range of 0.3-0.6%, as shown in Fig. 5-9, the area fraction of internal oxides in the specimens B4-4 (uncontrolled carbon potential) and B4-1 (control carbon potential at 0.3%) was approximately 0.14 and was higher than the other two specimens B4-2 and B4-3. The specimen B4-3 (0.6%C) had the lowest area fraction of approximately 0.08 among the four specimens. The results indicted that the lower carbon potential in the furnace, the higher area fraction of internal oxides in the specimen. Thus, it has been shown that internal oxidation in carburised steel could be controlled by the carbon potential.

5.4 Depletion of Alloy Elements in Surface Region

The EPMA line scans were carried out for specimens that were carburised using procedure 1, the mass percent of the alloying element in the matrix was obtained. After carburising, the depletion of the alloying element in the matrix was observed for all the specimens examined close to the surface region, as shown in Fig. 5-13. The information from the line scans are summarised in Table 5-1 and 5-2 in term of:

- The minimum elemental composition of the matrix which occurs at or near the surface.
- The mean depletion value of alloying elements in the internal oxidation zone.
- Bulk content analysis determined just beyond the depleted zone.
- Maximum depth of alloy element (Si, Cr and Mn) depletion.

As exposure time increased, the depletion depth of alloying element increased, as shown in Fig.5-14. As the penetration depth of internal oxides developed quickly in the base process, the depletion depth of the alloying element also developed quickly in the base process. The minimum alloying element content in depletion zone with exposure time is shown in Fig. 5-15. It indicated that as soon as specimens were heated, the internal oxides were formed and it caused immediately depletion of alloy elements in the surface region of matrix. After long cycle carburising, the alloy elements were severely depleted and were much lower than the bulk concentration. For example, the mean depletion value for the alloy elements in the depleted zone of specimen C1-8 was up to 57%, for the depletion of was approximately Cr 41%, Mn 57% and Si 38.7%. The minimum alloy element content in the depletion zone was 0.21%Cr, 0.06%Mn and 0.11% Si, compared with the bulk content of 0.96% Cr, 1.00% Mn and 0.31% Si. The depth of the depletion zone was approximately 30 μm. It was much deeper than the depth of the internal oxidation zone measured by the SEM image, implying that alloying elements diffused from the subsurface towards the areas of oxide formation.

The relationship between depletion of alloy elements and Si bulk content is shown in Fig. 5-16. As Si bulk content increased, depletion of Cr and Mn in the surface region increased as well. However, comparing sample with 0.31%Si bulk content with sample with 0.77%Si bulk content, the depletion of Cr and Mn retained a similar level. This is consistent with morphology observations that as Si increased in bulk matrix, more Si oxides were formed instead of Cr and Mn complex oxides. Therefore, the degree of depletion of Cr and Mn did not increase significantly as Si content further increased

(The raw analytical data relevant this section can be found in Appendix 1 at the end of the thesis)

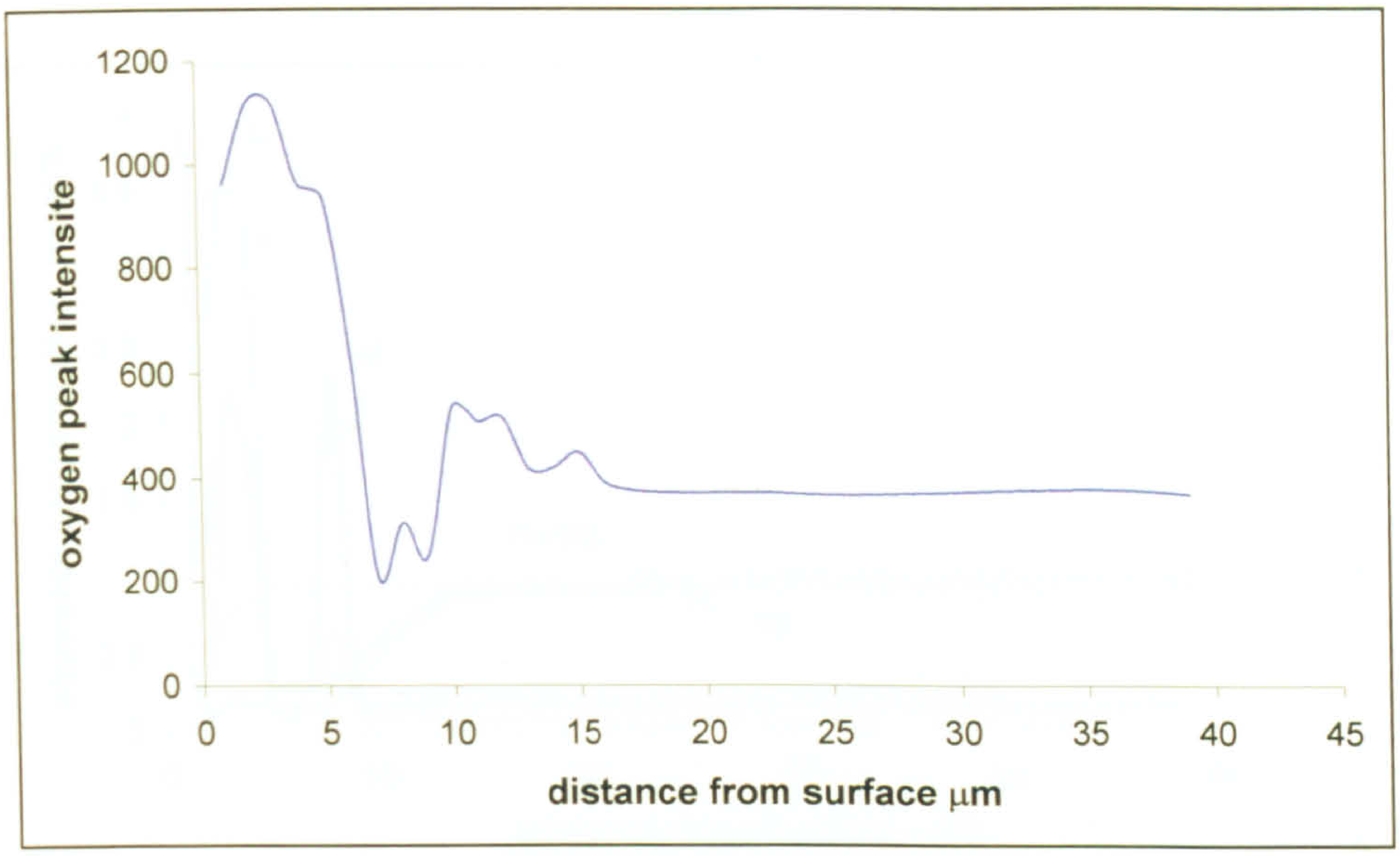

Fig. 5-1 Oxygen penetration in the specimens C1-8 carburised at the procedure 1 for 16.6h by EPMA line scan

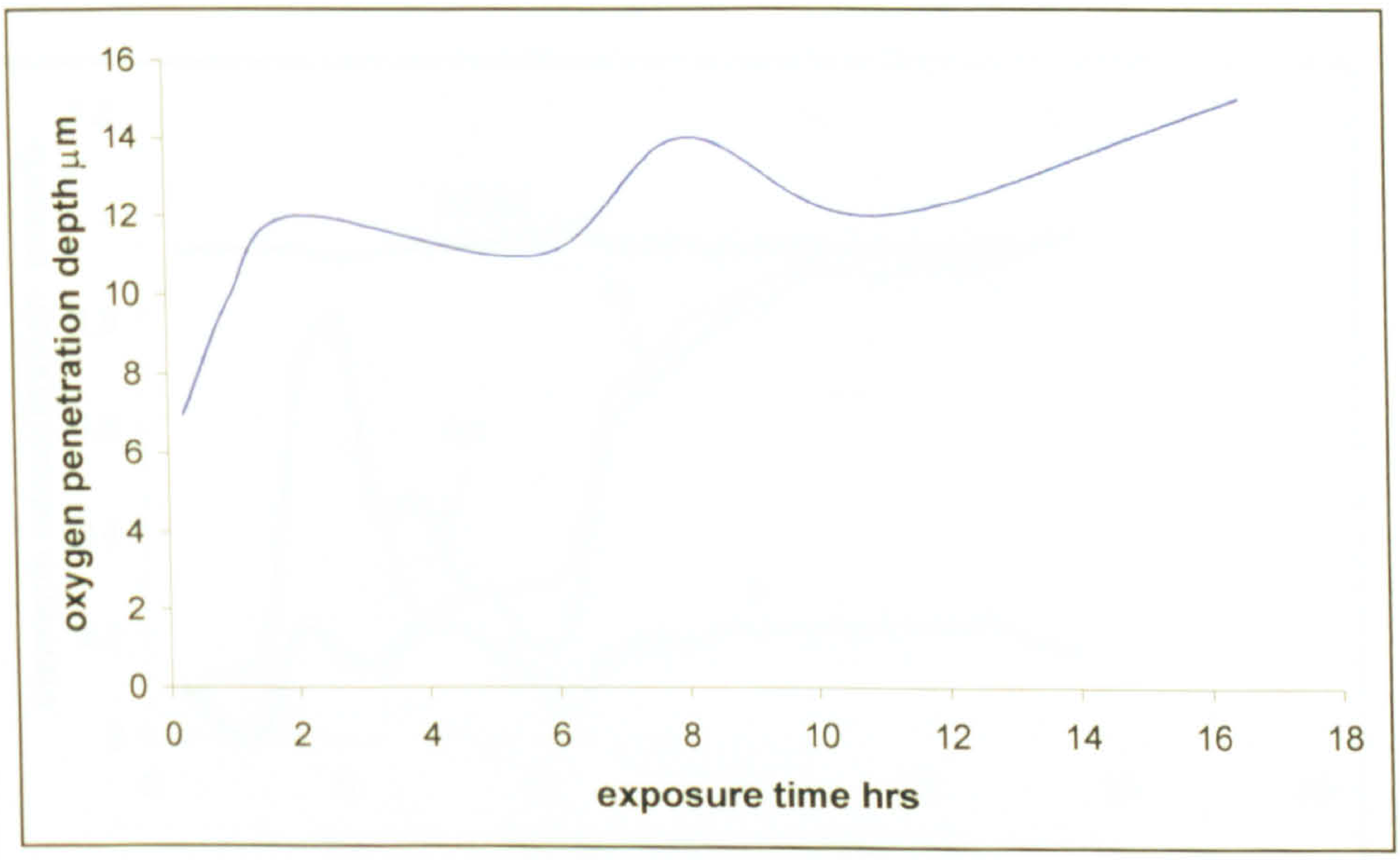

Fig. 5-2 Depth of oxygen penetration at different heating time for the specimens B1 carburised using the procedure 1

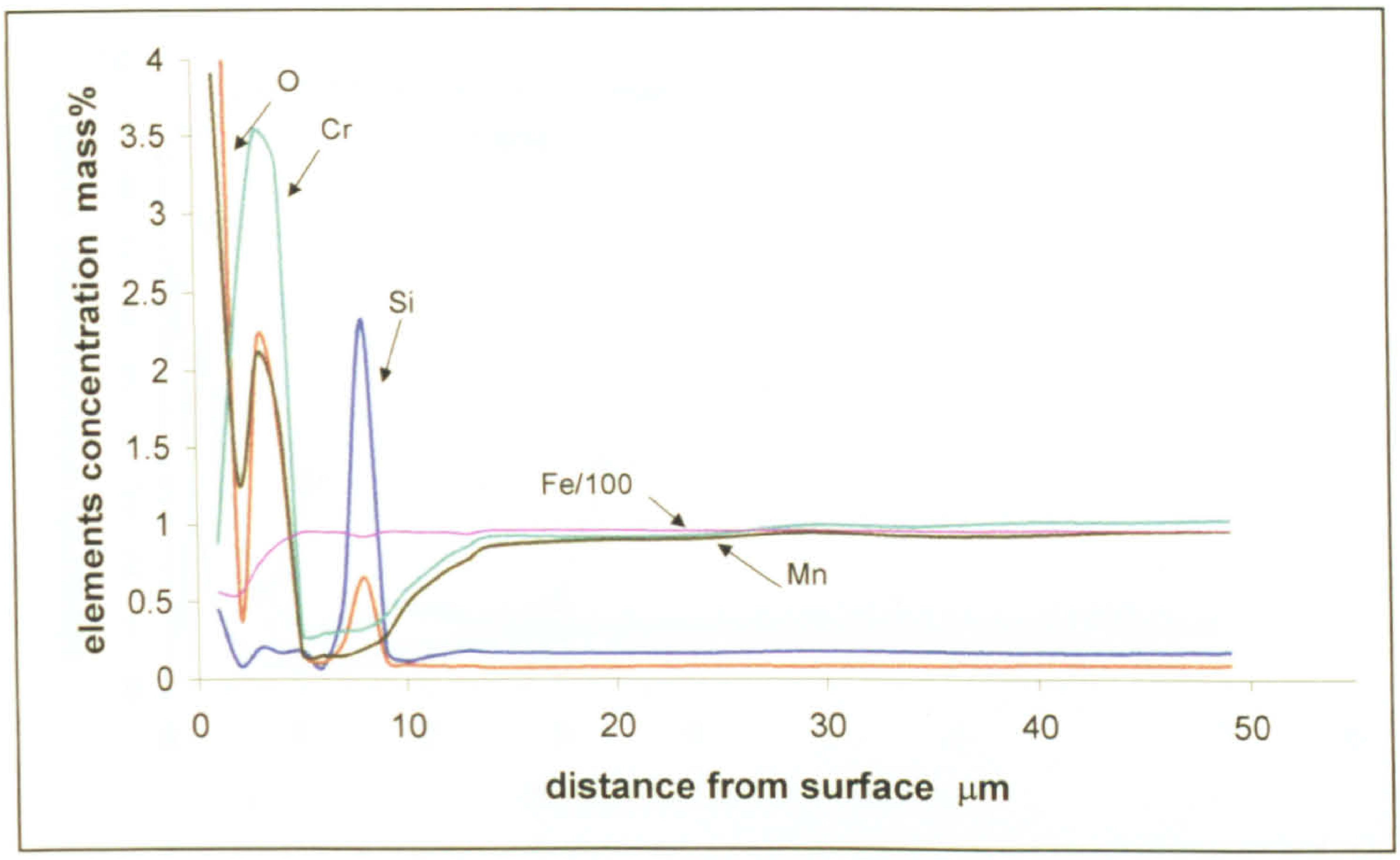

Fig.5-3 Elements distribution in specimens B1-6 carburised at the procedure 1 for 8.0h by EPMA line scan

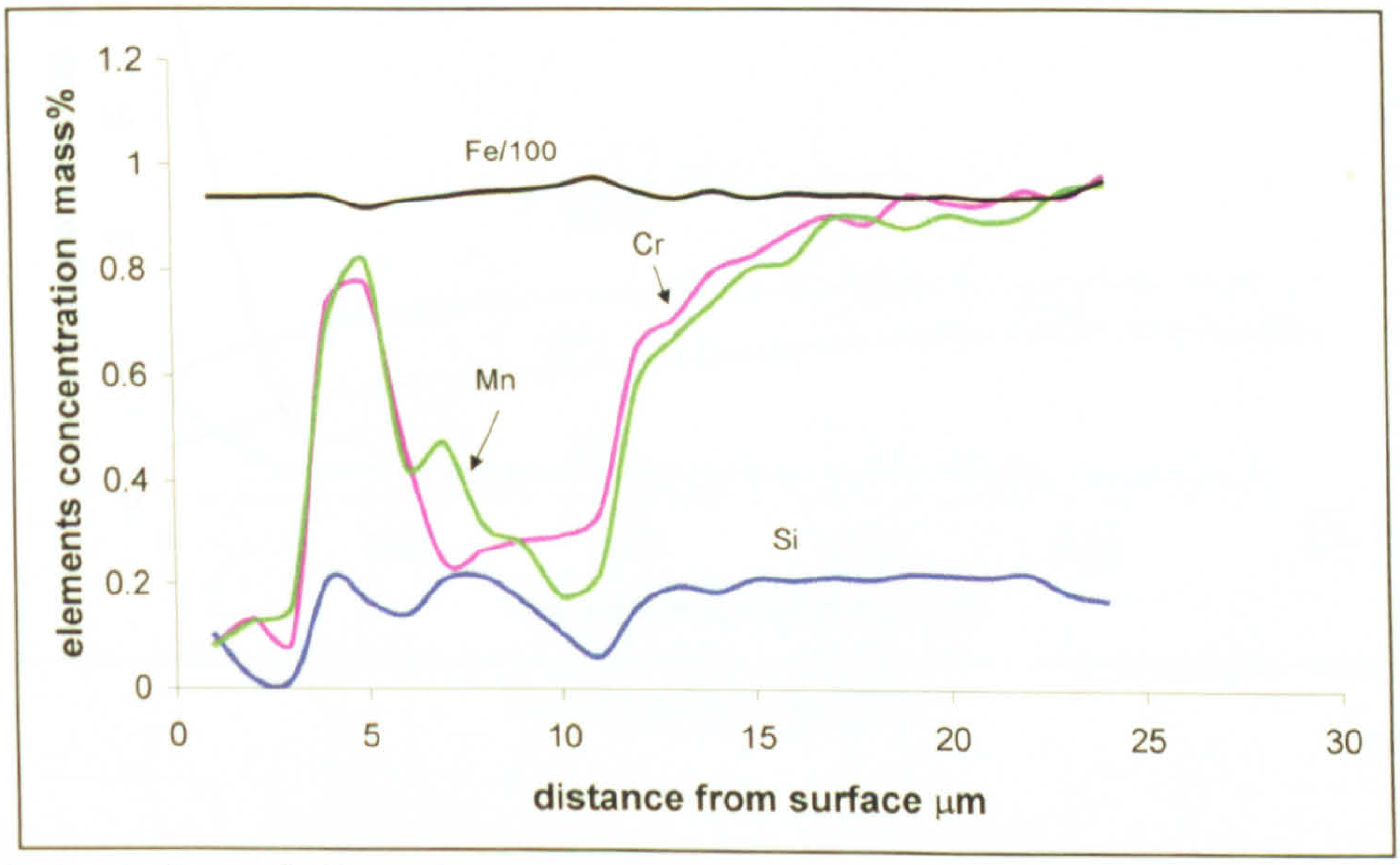

Fig. 5-13 Depletion of alloy element in the matrix of the sepcimen B1-8 carburised at the procedure 1 for 16.6h

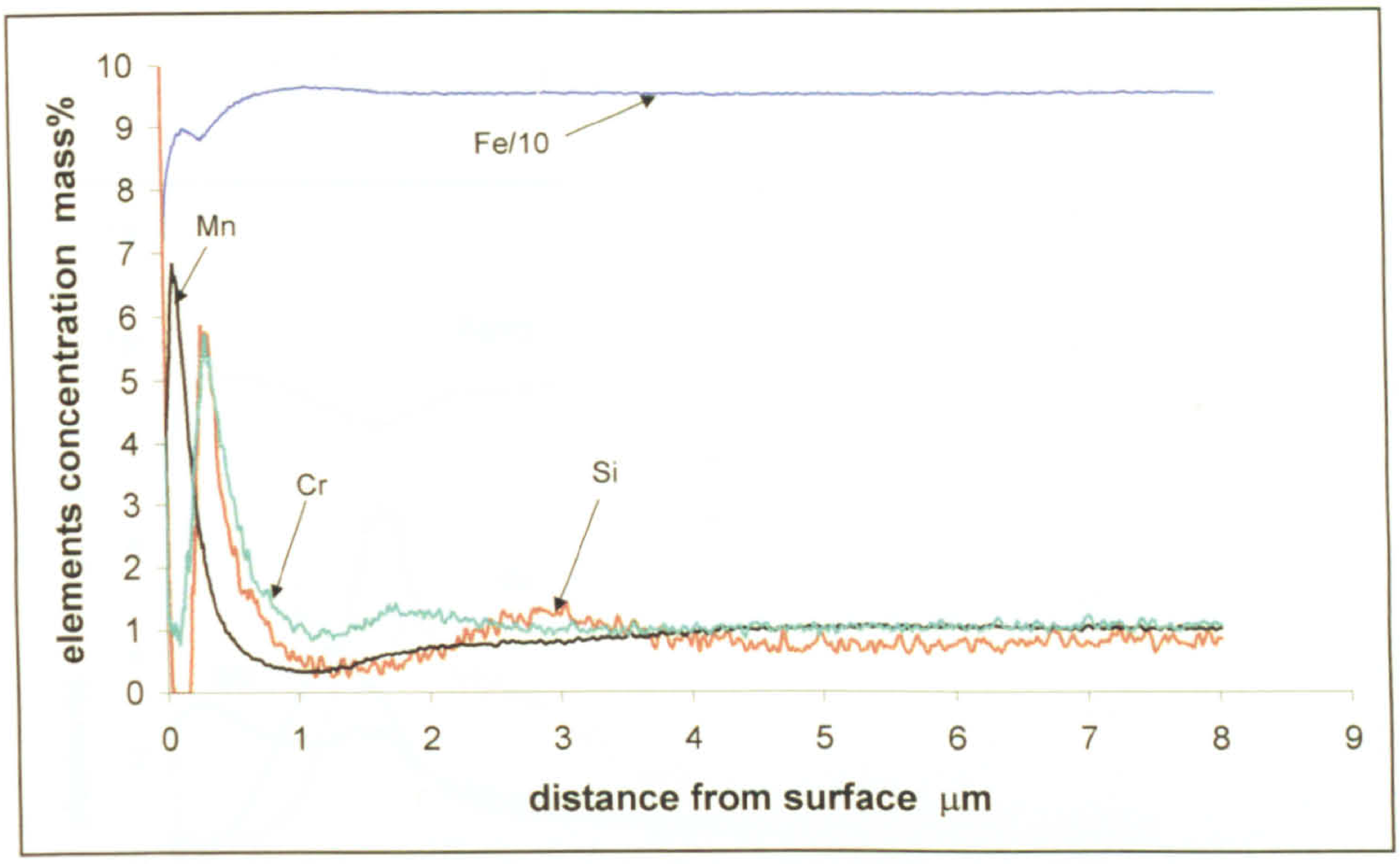

a. internal oxidation region

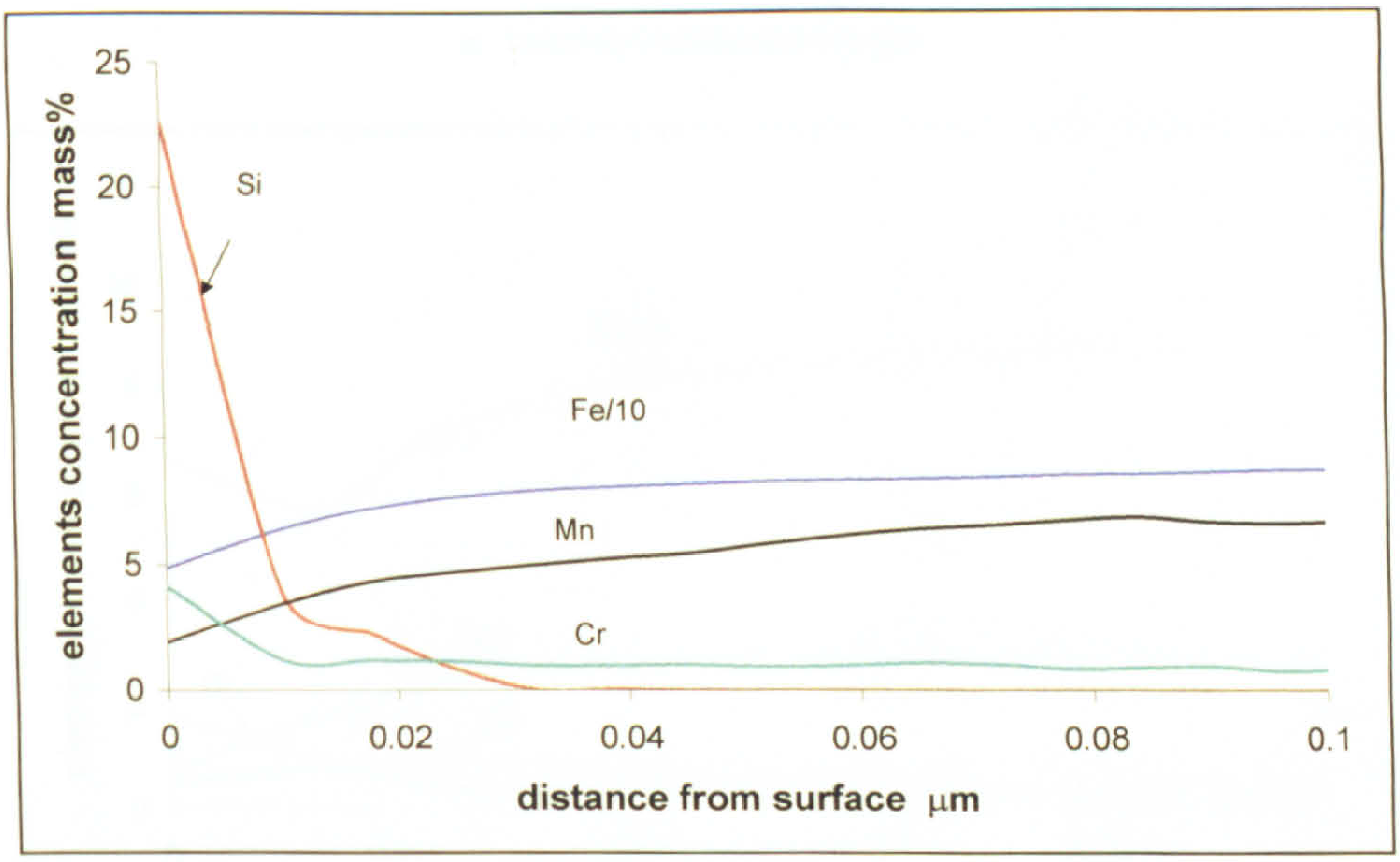

b. top surface region

Fig. 5-4 Elements depth profile in specimen B1-4 carburised using the procedure 1 for 2.0h by GDOES.a. internal oxidation region ; b. top surface region

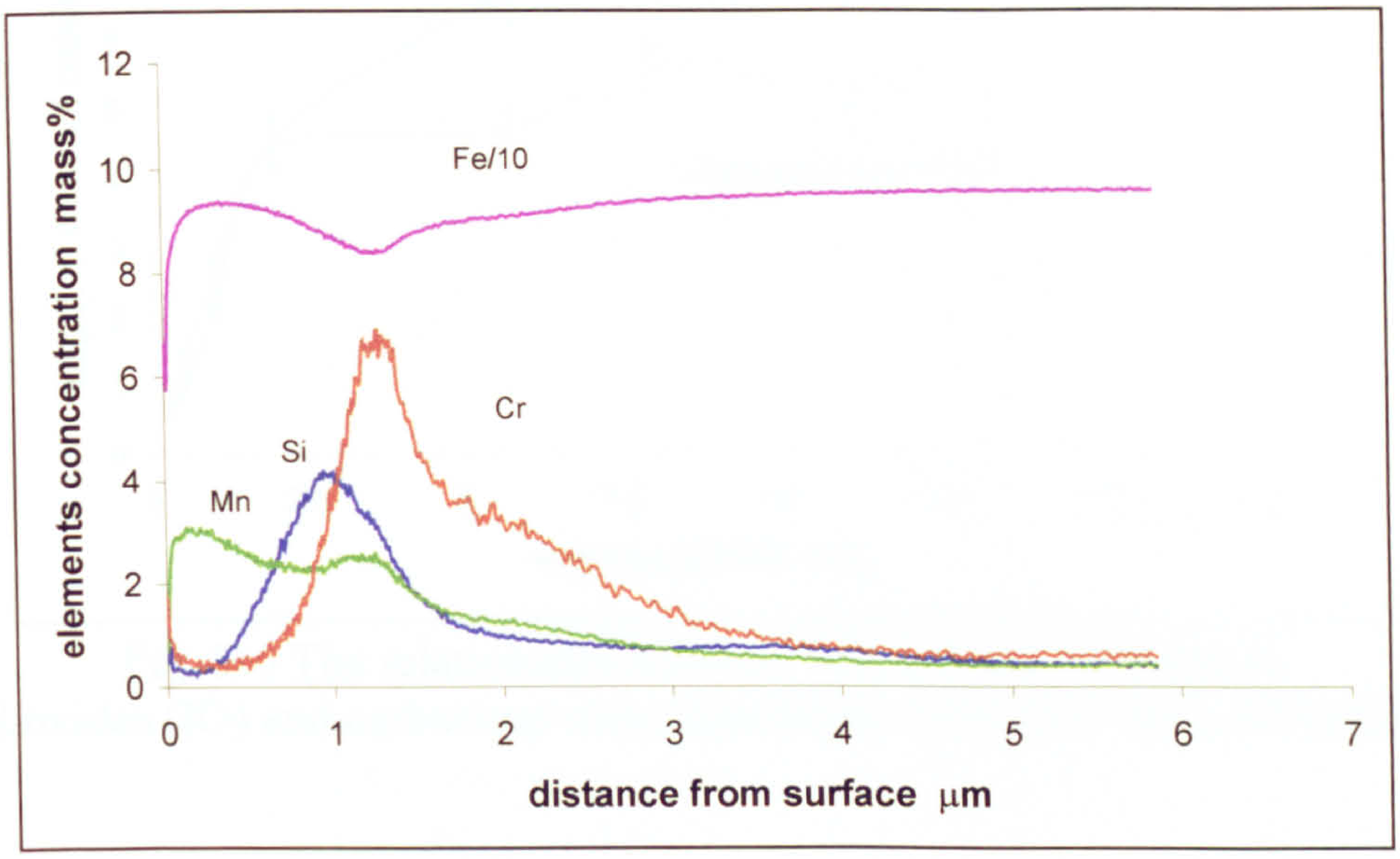

a. internal oxidation zone

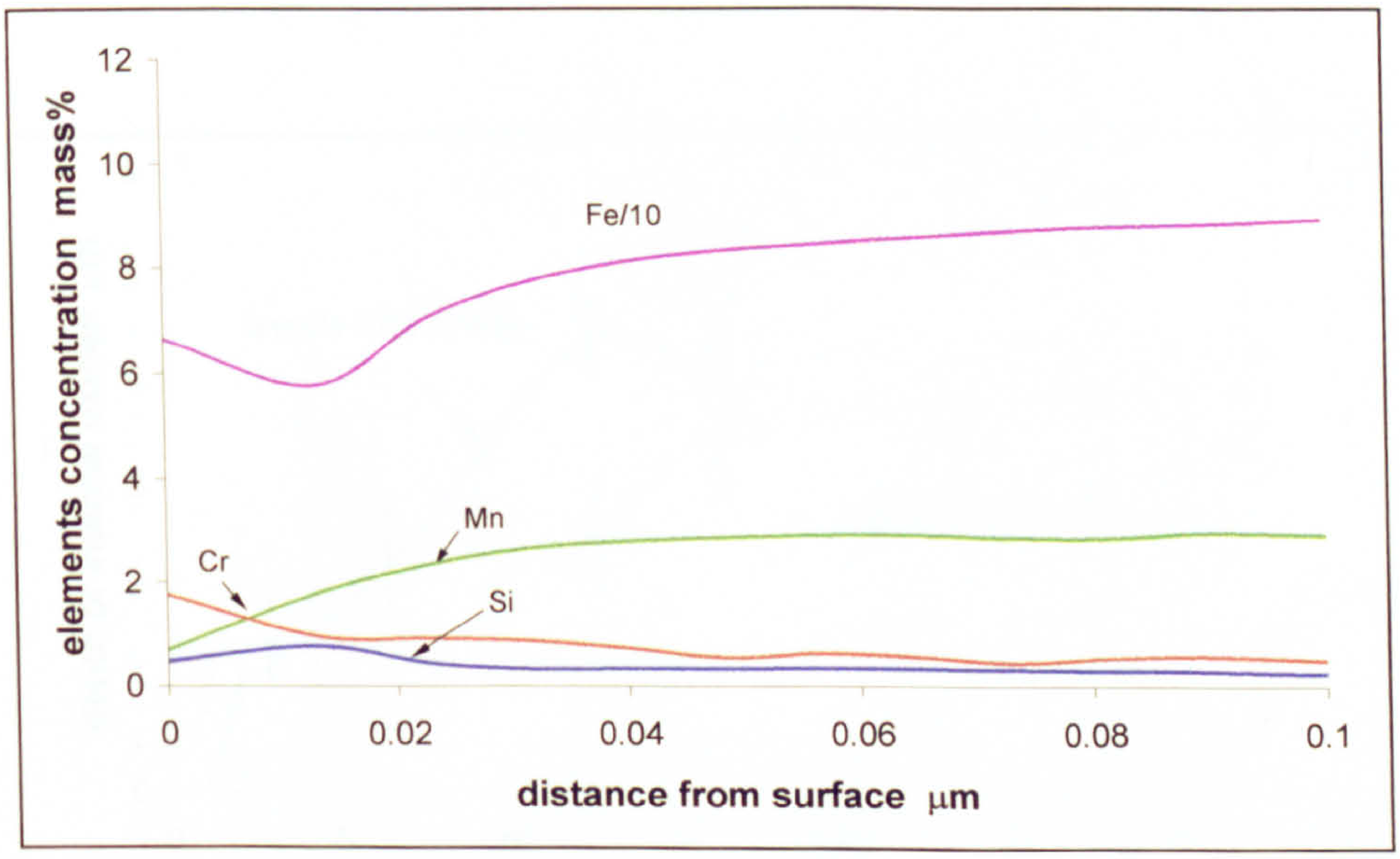

b. top surface region

Fig. 5-5 Elements depth profile in the specimen E1-6 (0.77% Si) carburised at the procedure 1 for 8.0h by GDOES. a. internal oxidation region; b. top surface region

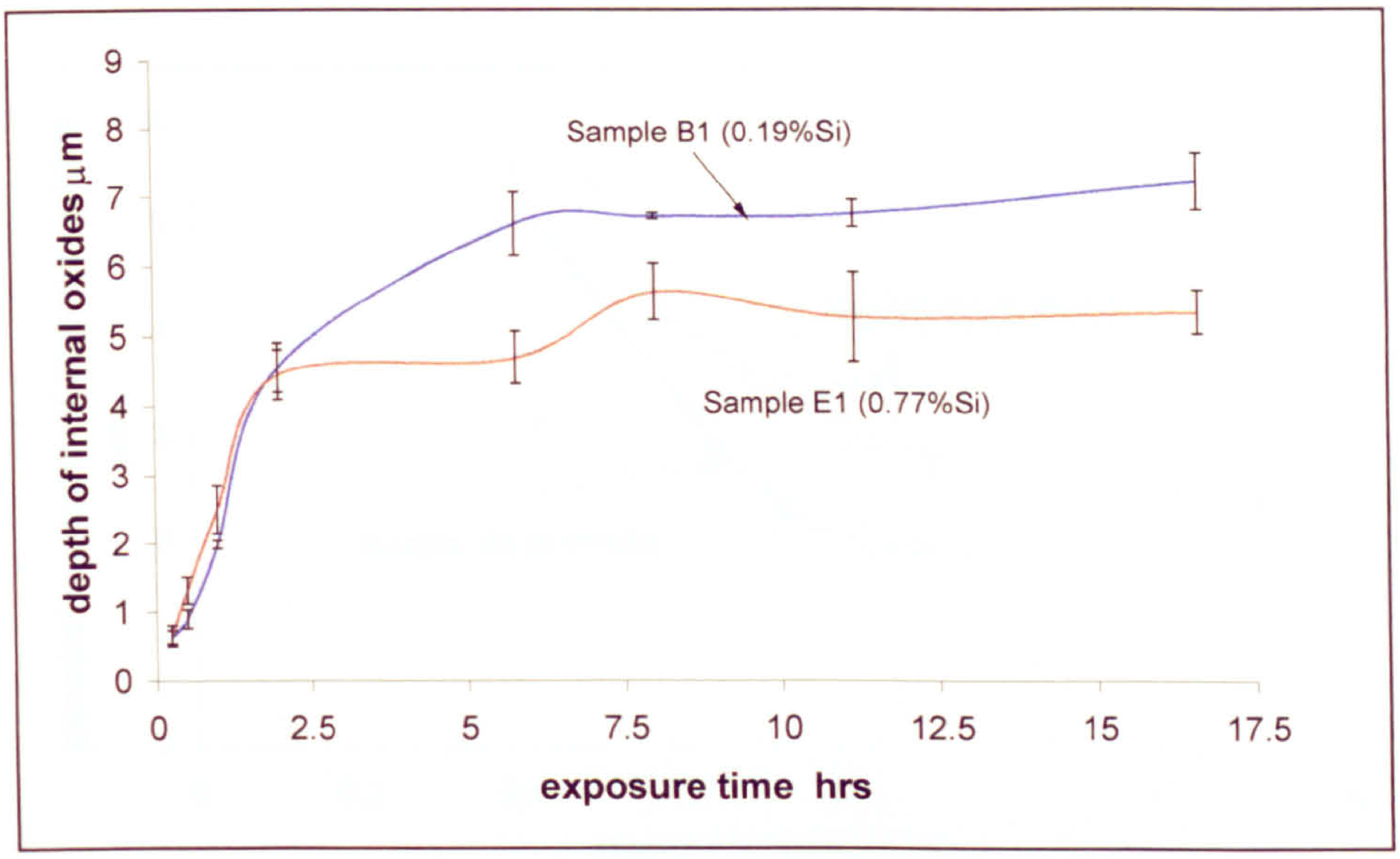

Fig. 5-6 The relationship between the penetration depth of Internal oxides (IO) and carburised time, specimens carburised using the procedure 1

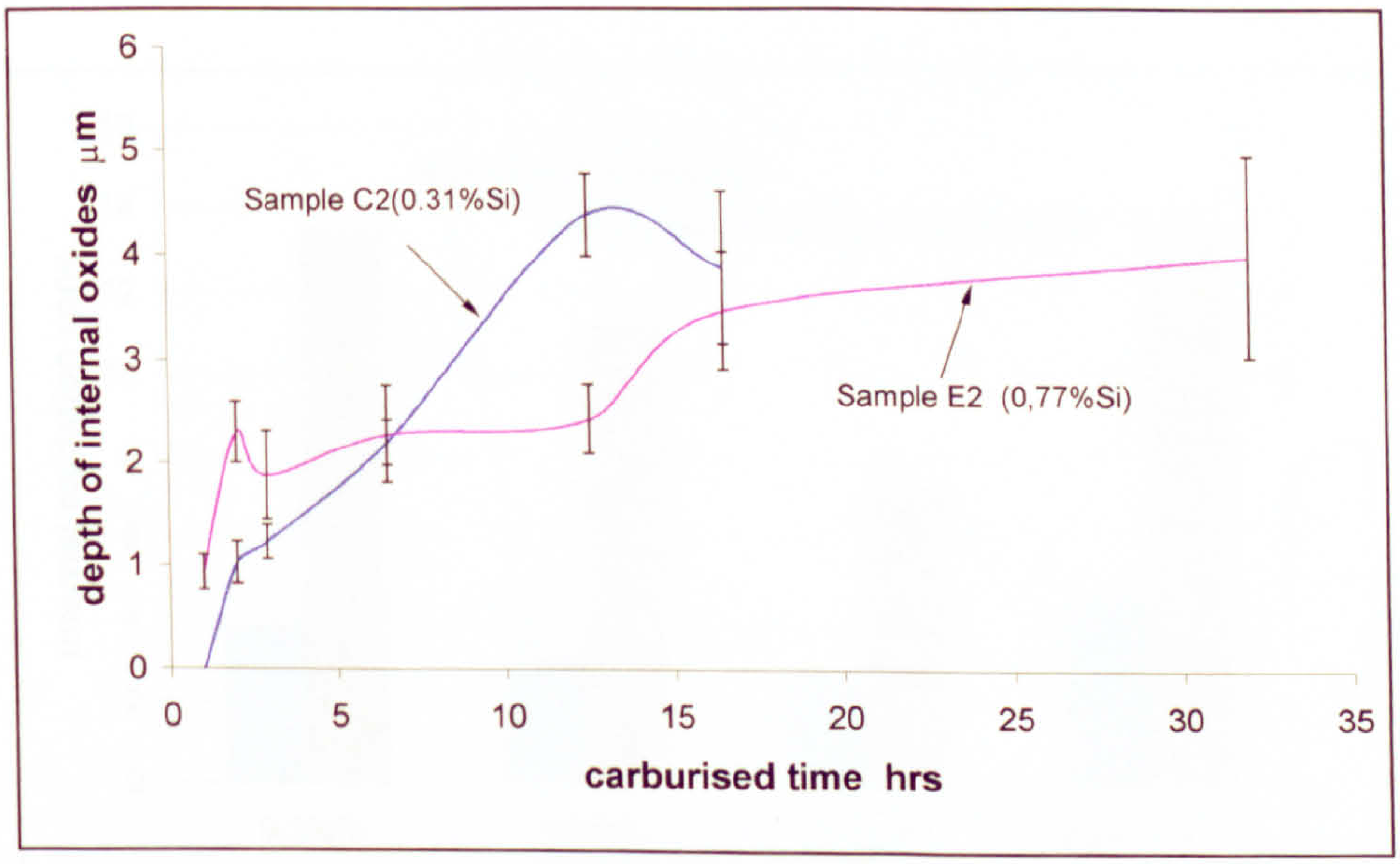

Fig. 5-7 The relationship between the penetration depth of the internal oxides and carburised time, sepcimens carburised using the procedure 2

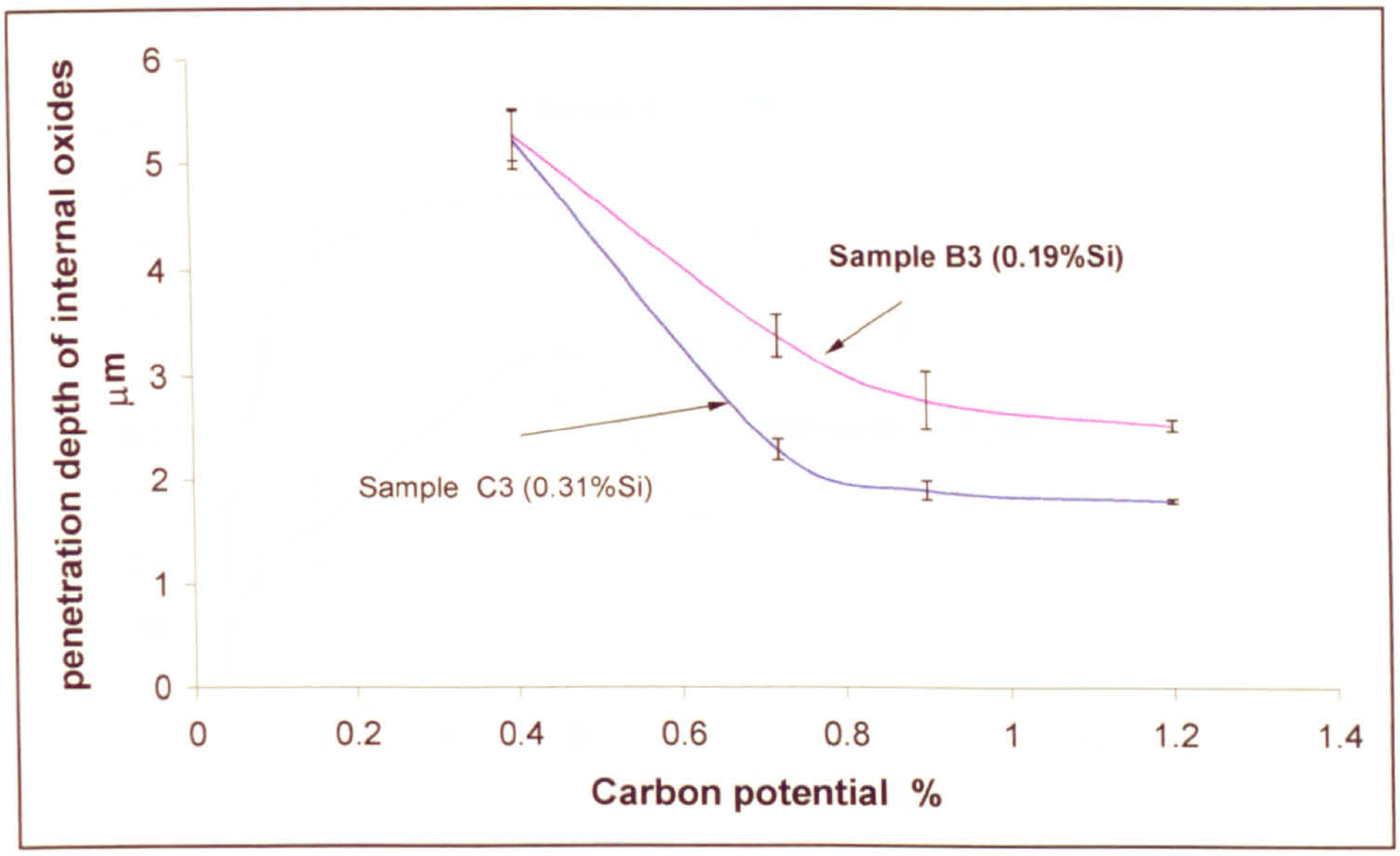

Fig. 5-8 The relationship between penetration depth of internal oxides (IO) and carbon potential, specimens carburised using the procedure 3 (930°C, 6.6h)

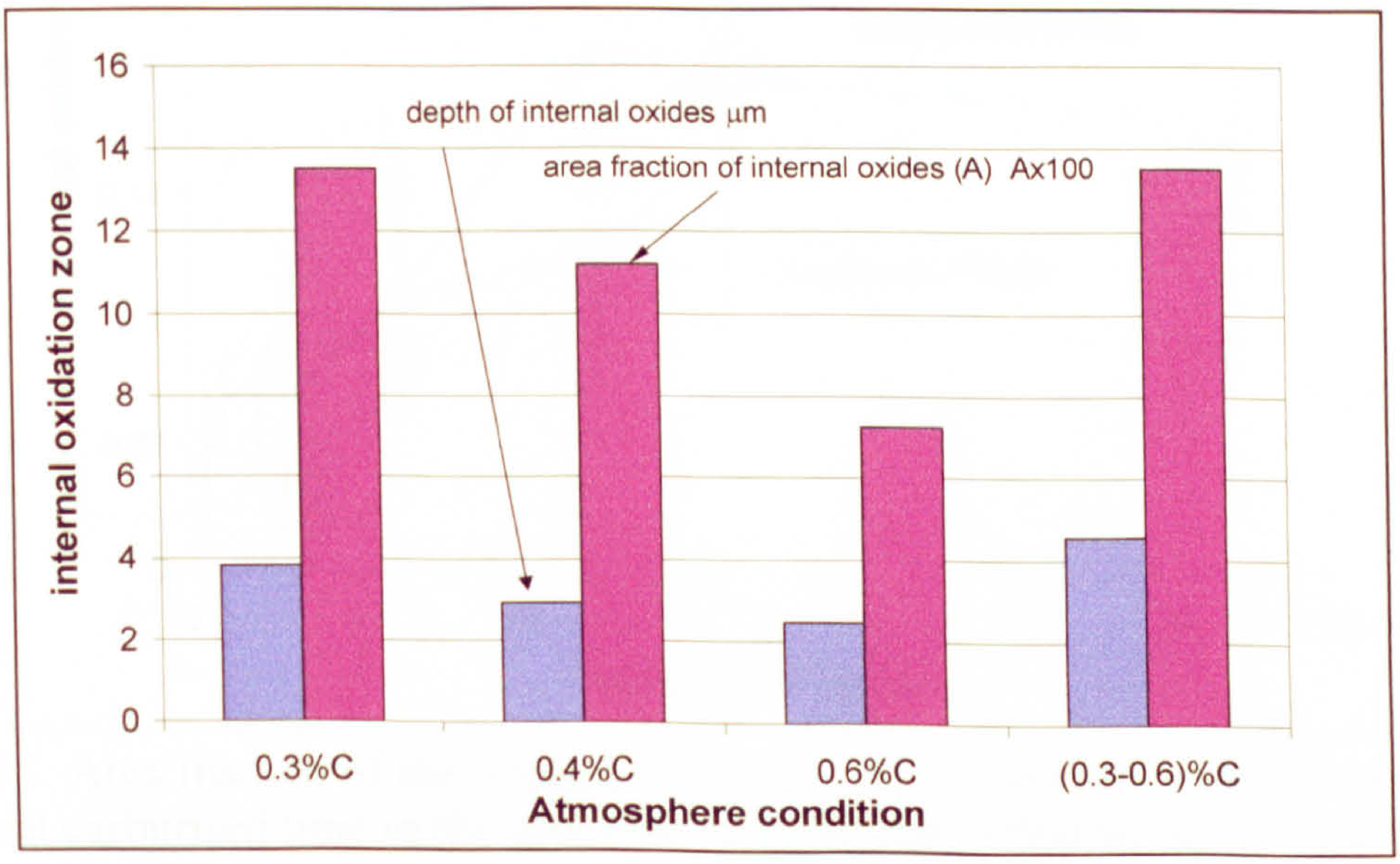

Fig.5-9 Comparing with internal oxidation zone at different atmosphere condition in base process, speciemens carburised using the procedure 4

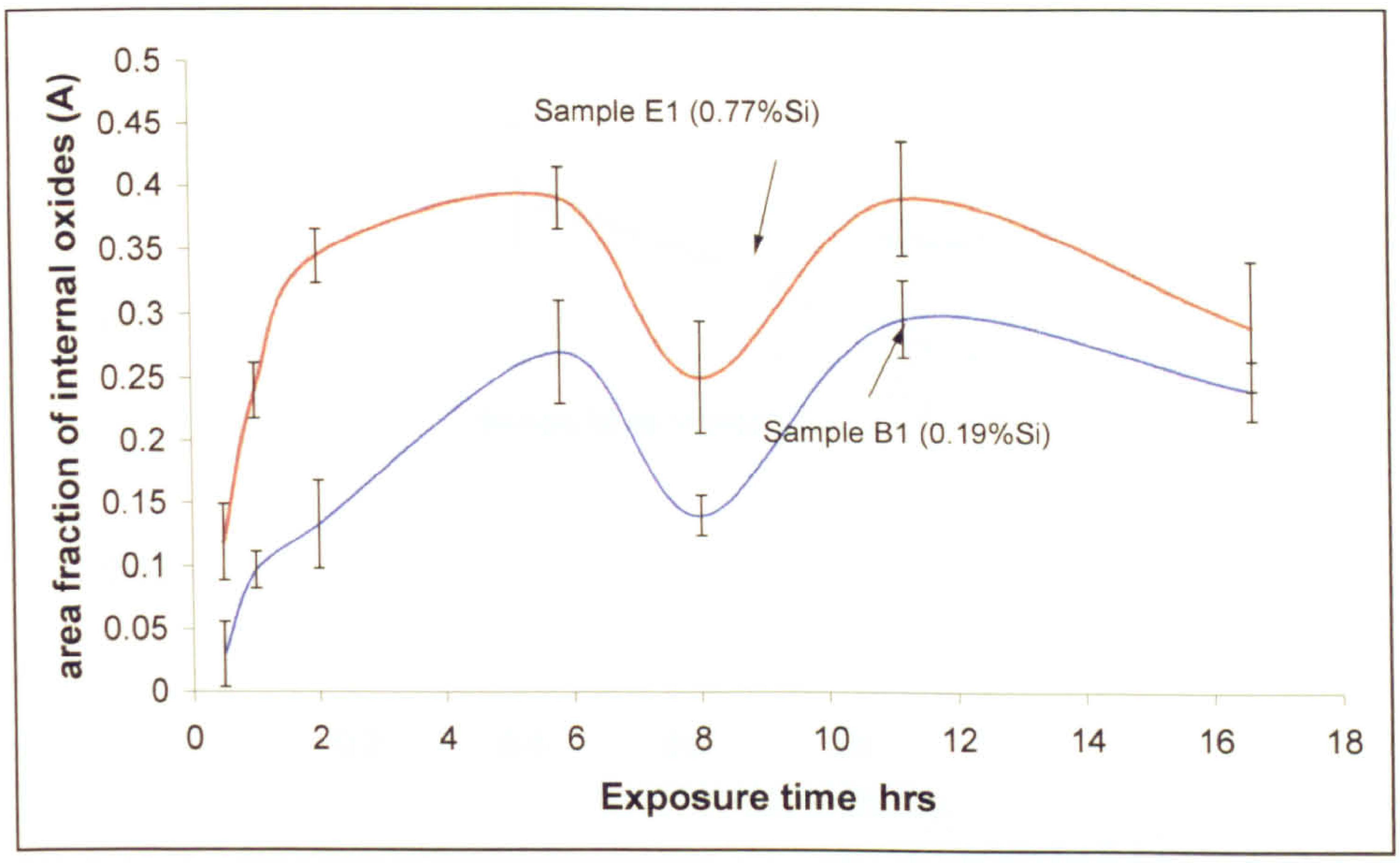

Fig. 5-10 Area fraction of the internal oxides (A) in the internal oxidation with different exposure time in specimens B1 and E1carburised using the procedure1

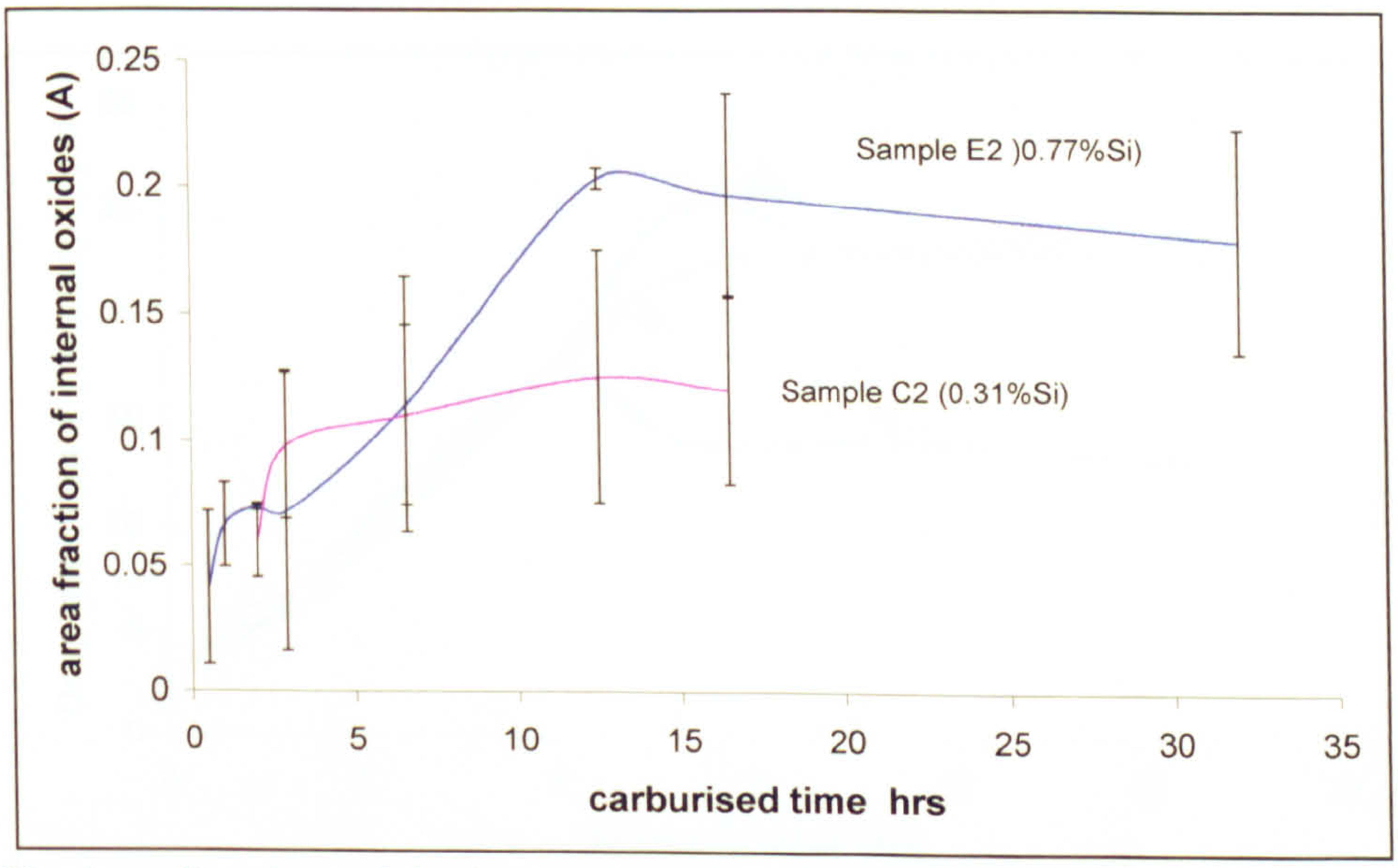

Fig. 5-11 Area fraction of the internal oxides (A) in the internal oxidation zone with different carburised time in the specimens C2, E2 carburised using the procedure 2

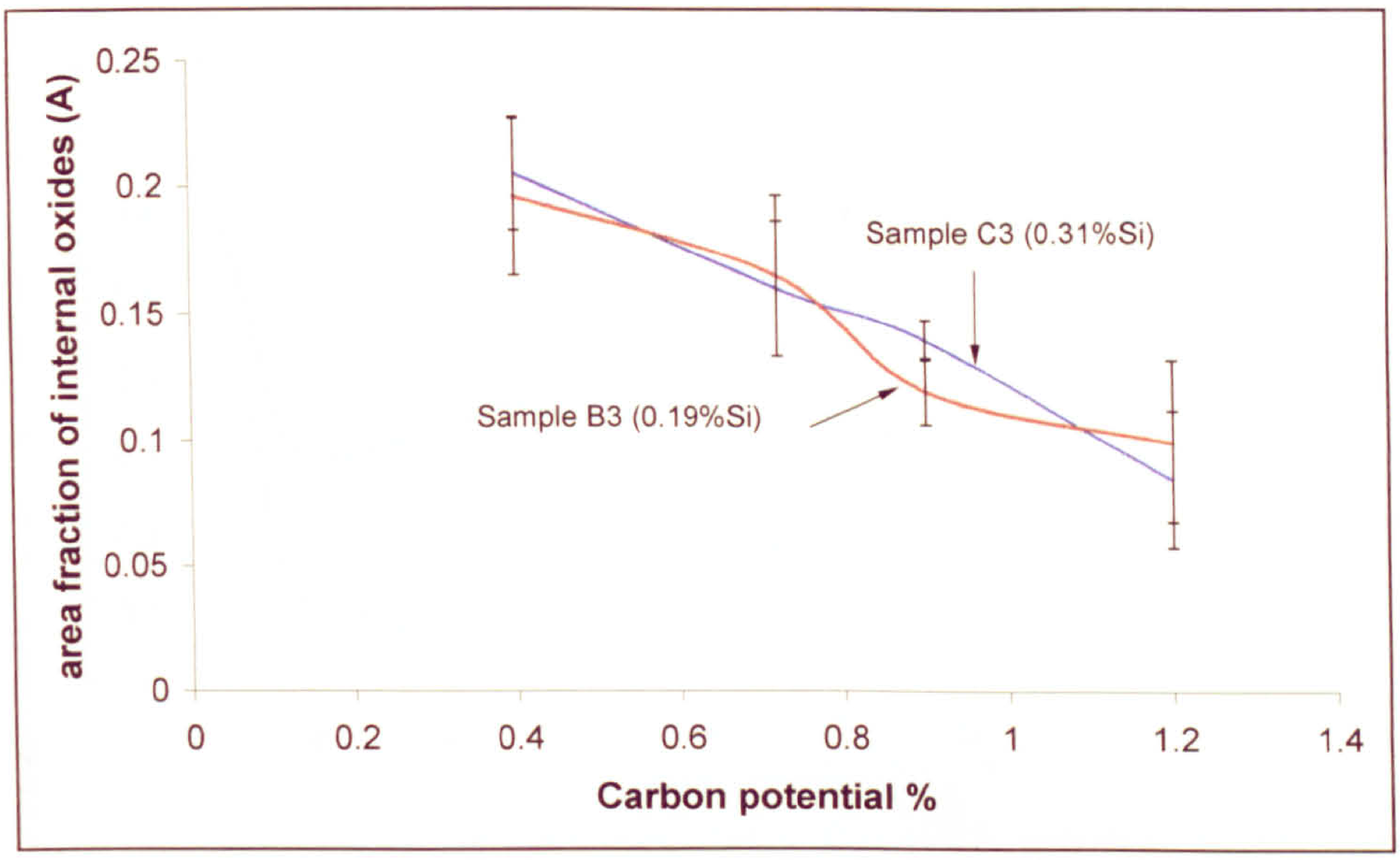

Fig. 5-12 The relationship between area fraction of the internal oxides and carbon potential, specimens C3 and B3 carburised using the procedure 3

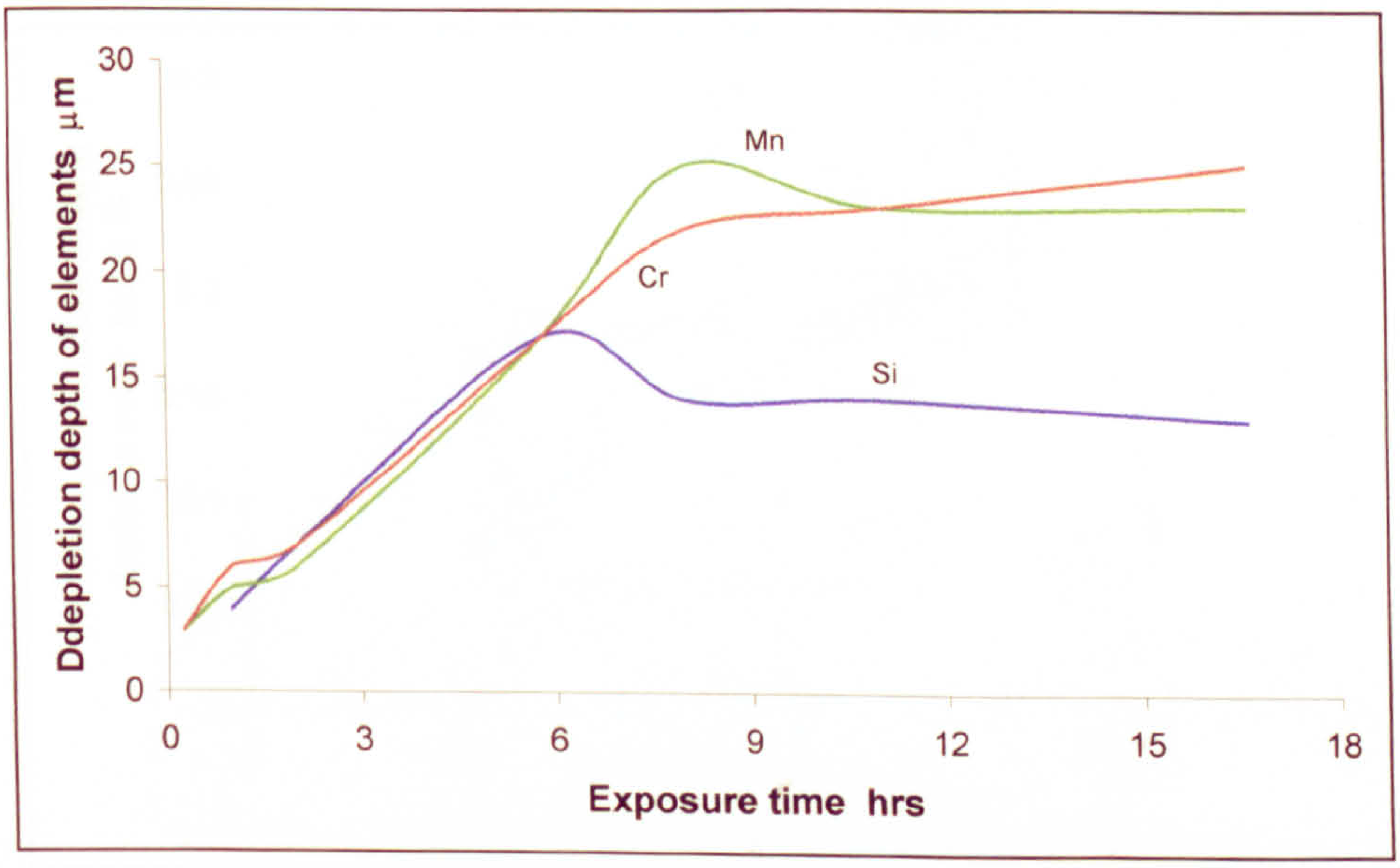

Fig. 5-14 The depletion of the alloying elements with the carburised time in the specimens B1 carburised using the procedure1

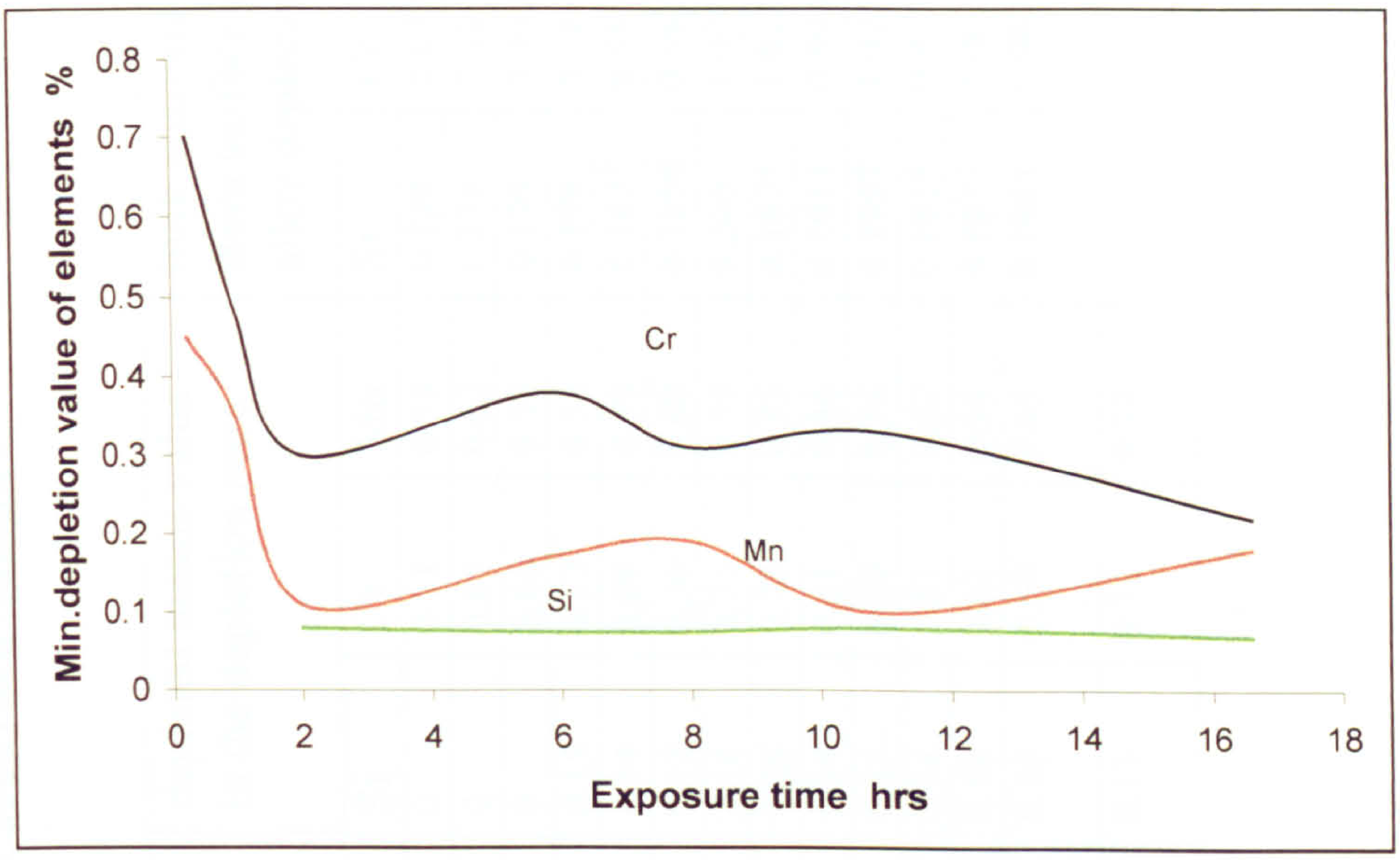

Fig. 5-15 Minium element content in depletion zone asfunction of carburised time for specimens B1carburised using the procedure 1

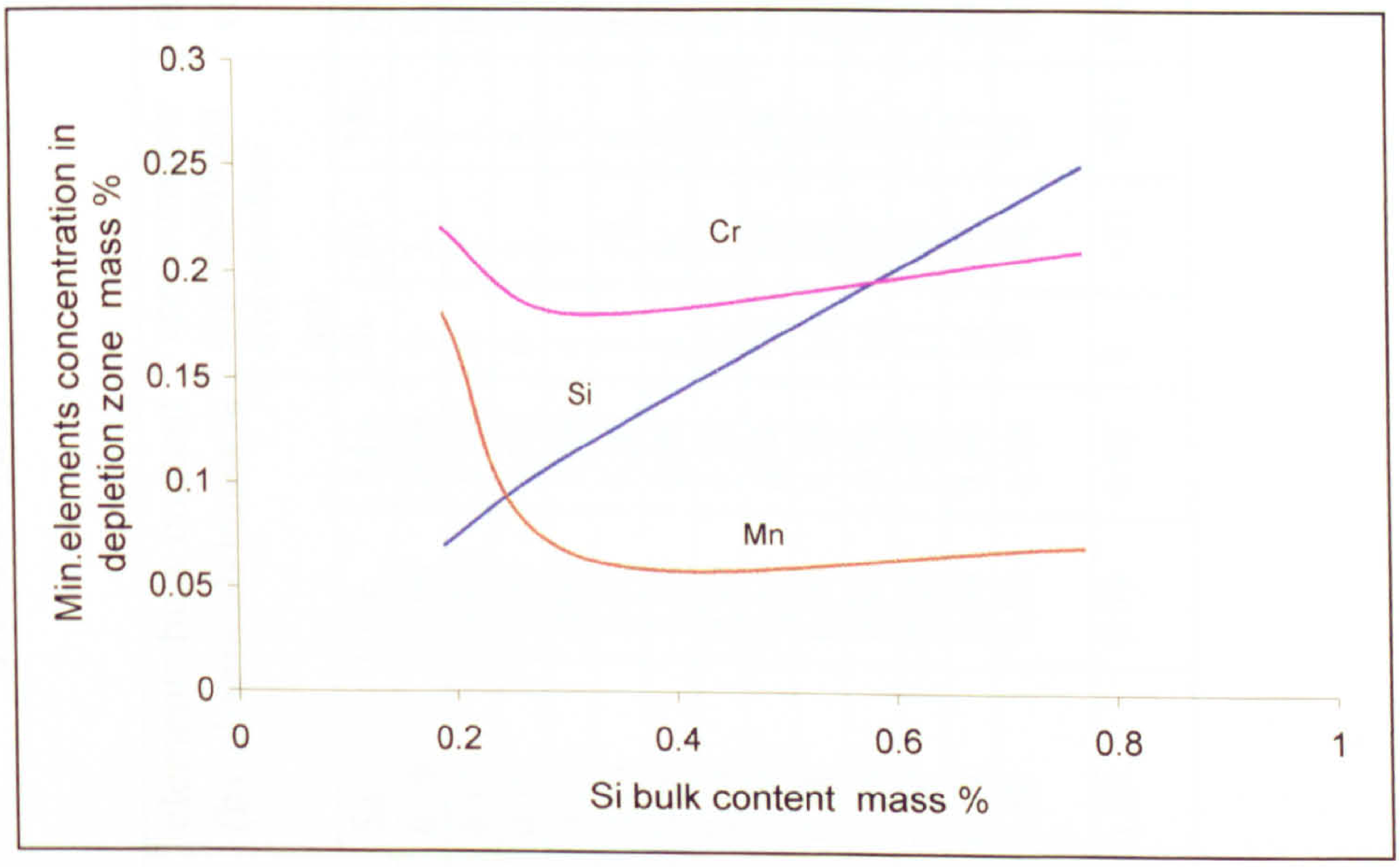

Fig. 5-16 Minium element content in depletion zone as function of Si bluk content for specimens carburised using the procedure 1 for 16.6h

Table 5-1 EPMA Study of Alloy Depletion Near the Surface of Carburised Samples

ple ID	Heating Time hrs	elements bulk content (by chemicals)mass%			approximately depleted depth from surface µm			depleted (increase +) value min(max)			depleted means value in the depletion zone			bulk analysis (at distance from surface just beyond alloy depletion) mass%		
		Si	Cr	Mn	Si	Cr	Mn	Si	Cr	Mn	Si	Cr	Mn	Si	Cr	Mn
B1-1	0.25	0.19	0.99	0.98	0	3	3	0.24+	0.68	0.44	0	0.71	0.58	0.220	1.073	0.950
	0.25	0.19	0.99	0.98	0	3	3	0.21+	0.71	0.49	0	0.81	0.62	0.210	1.11	1.040
B1-3	1.0	0.19	0.99	0.98	0	5	4	1.68+	0.45	0.27	0	0.66	0.52	0.199	0.999	0.918
	1.0	0.19	0.99	0.98	4	7	7	0.14	0.52	0.34	0.15	0.57	0.53	0.198	0.98	0.842
B1-4	2.0	0.19	0.99	0.98	8	10	8	0.11	0.36	0.13	0.14	0.69	0.39	0.1925	0.985	1.590
	2.0	0.19	0.99	0.98	6	4	5	0.05	0.23	0.09	0.12	0.36	0.60	0.1858	0.987	1.368
B1-5	5.8	0.19	0.99	0.98	17	17	17	0.10	0.43	0.24	0.14	0.75	0.55	0.206	1.037	1.098
	5.8	0.19	0.99	0.98	18	18	18	0.08	0.33	0.22	0.18	0.77	0.55	0.1875	1.021	0.975
B1-6	8.0	0.19	0.99	0.98	10	22	22	0.08	0.29	0.15	0.14	0.61	0.46	0.1911	0.9984	0.948
	8.0	0.19	0.99	0.98	14	24	29	0.07	0.34	0.16	0.13	0.59	0.54	0.1957	1.0234	0.994
B1-7	11.0	0.19	0.99	0.98	11	29	28	0.1	0.39	0.11	0.14	0.81	0.67	0.1835	0.997	2.555
	11.0	0.19	0.99	0.98	14	17	17	0.09	0.28	0.08	0.14	0.62	0.54	0.1877	1.002	0.9692
B1-8	16.6	0.19	0.99	0.98	13	19	23	0.08	0.20	0.18	0.15	0.60	0.65	0.1841	0.9823	0.9393
	16.6	0.19	0.99	0.98	9	>21	>21	0.06	0.24	0.18	0.13	0.72	0.71			

Table 5-2 EPMA Study of Alloy Depletion Near the Surface of Carburised Samples

Sample ID	Heating Time hrs	elements bulk content (by chemical)			approximately depleted depth from surface μm			depleted (increase +) value min(max)			depleted means value in the depletion zone			bulk analysis (at distance from surface just beyond depletion zone (Wt %)		
		Si	Cr	Mn	Si	Cr	Mn	Si	Cr	Mn	Si	Cr	Mn	Si	Cr	Mn
B1-8	16.6	0.19	0.99	0.98	13	19	23	0.084	0.197	0.185	0.154 /19%	0.601 /40%	0.649 /31.7%	0.1841	0.9823	0.9393
	16.6	0.19	0.99	0.98	9	>21	>21	0.064	0.24	0.177	0.128 /32.5%	0.722 /27.8%	0.707 /25.8%			
C1-8	16.6	0.31	0.96	1.00	50	43	43	0.12	0.15	0.07	0.25 /	0.62 /	0.62 /	0.3078	0.9394	0.9063
	16.6	0.31	0.96	1.00	23	38	30	0.11	0.21	0.06	0.19 /	0.57 /	0.43 /	0.3007	0.9357	0.9600
E1-8	16.6	0.77	1.03	0.81	9	10	30	0.186	0.23	0.054	0.587 /23.8%	0.551 /46.5%	0.43 /46.3%	0.7863	0.9922	0.7642
	16.6	0.77	1.03	0.81	16	23	26	0.327	0.179	0.084	0.579 /24.8%	0.662 /35.7%	0.58 /26.4%	0.7989	0.9991	0.7264

CHAPTER 6

THE MORPHOLOGY AND COMPOSITION OF INTERNAL OXIDES

6.1 Introduction

This chapter is concerned with a cross- sectional Transmission Electron Microscopy study of the oxide phases present in the internal oxidation zone.

The specimens used in this current research are shown in Table 6-1. The specimens were carburised at different process conditions, as shown in Table 3-2. The specimen 16MnCr5 was carburised using a commercial vacuum carburising process. Four types of internal oxide phases were observed in this current research: complex oxide; intergranular oxide; agglomerated oxide and small dispersed oxide particles.

Table 6-1 Specimens Use in TEM Study

Specimen ID	Carburised condition
B1-5	Procedure 1
C1-4	procedure 1
C1-8	procedure 1
E1-5	procedure 1
E1-8	procedure 1
C2-6	procedure 2
C5	procedure 5
D5	procedure 5
16MnCr5	vacuum carburisation

6.2 Complex Internal Oxides

A low magnification cross-sectional overview of the internal oxidation zone in the specimen C5 is shown in Fig. 6-1. It revealed details of the internal oxidation zone: the outer zone consisted in globular oxides close to surface and the inner zone intergranular oxides remote form surface. Higher magnification TEM bright field imaging revealed the larger phases to be complex oxides that had a different shape and structure in different specimens, but could be classified as three kinds of morphology: cubic, ellipsoid and spherical. The cubic oxide, as shown in Fig. 6-2, was usually a Cr and Mn complex oxide with dimensions approximately 1.0-2.0μm that had clearly delineated boundaries with the matrix. Ellipsoid complex oxides also observed in this study that were rich in Cr and Mn, as shown in Fig. 6-3. The combined analysis using SAD electron diffraction pattern and EDS elemental spot analysis identified that some of the Cr and Mn complex internal oxides were $Cr_{1.5}Mn_{1.5}O_4$, having a cubic structure (a=0.8455nm), spinel type (Fig. 6-2); Mn_2CrO_4, having cubic structure (a=0.8413nm) (Fig 6-3a); $CrMnO_4$ orthorhombic structure (a=0.4399nm, b=0.4441nm, c=0.288nm), distorted rutile type (Fig.6-12). The roughly spherical precipitates were mainly Mn and Si complex oxides, as shown in Fig. 6-4. Some of them had a clearly boundary with the matrix but others did not. The combined analysis using SAD electron diffraction pattern and EDS elemental spot analysis identified that some of them were Mn_2SiO_4, as spherical shapes having a orthorhombic structure, a=0.62583nm, b=1.06039nm, c=0.49030nm (Fig. 6-4b); $MnSiO_3$ of approximately 2.5μm with a monoclinic structure, a=0.9864nm, b=0.9179nm, c=0.5298nm (Fig. 6-4a) and $MnSiO_3$ as spherical shape of triclinic structure, a=0.7699nm, b=1.222m, c=0.6702nm (Fig. 6-4c). The detailed analytical data for the phases identify is shown in Table 6-2 and 6-3. Some spherical internal oxides were observed in the specimen carburised using the boost process (procedure 2) and identified by EDS as Si oxides, as shown in Fig. 6-5. The larger internal oxides were crystalline. A few of the complex oxides contained Al. The Al in the steel also reacted with the oxygen and combined with Si, Mn and Cr to form complex oxides, as shown in Fig. 6-6. A different contrast feature was observed using bright field imaging of the internal oxide precipitates. Small second phase precipitates were observed, associated with the cubic internal oxides (Fig. 6-2). It was observed that a higher stressed region existed around the larger complex oxides.

Semi-quantitative X-ray spot analysis was performed using the TEM. The cubic oxide phases showed the Cr/Mn ratio to be closer to 1/1-2/1. The roughly spherical Mn and Si oxide phases showed a Mn/Si ratio to be closer to 1/1, 2/1 and 3/1. The data agrees with the results from the SAD electron diffraction patterns.

Table 6-3 Structure Parameter of Internal Oxides

Sample	**oxide**	**figure No.**	**Card No**	**type**	**system**	**Parameter (nm)**		
						a	**b**	**c**
C_5	$Mn_{1.5}Cr_{1.5}O_4$	6-2a	33-892	spinel type	cubic	0.8455		
C1-8	Mn_2CrO_4	6- 12	36-546	spinel	cubic	0.8413		
E1-5	MnCrO4	6- 13	33-893	distorted rutile	orthorhombic	0.4399	0.4441	0.2888
C1-8	$MnSi\ O_3$	6-4 c	13-138	pyroxenoid	triclinic	0.7699	1.222	0.6702
C5	$MnSi\ O_3$	6-4a	26-1249		monoclinic	0.9864	0.9179	0.5298
16MnCr5	Mn_2SiO_4	6-4b	35-0748	olivine group	orthorhombic	0.6258	1.0604	0.4903
C5	SiO_2	6- 10a	11-252		hexagonal	0.5002		

These determinations indicated that the internal oxides were formed with different shapes and compounds in the different carburising process. The furnace atmosphere dictated which oxides were formed. In other words, the oxygen partial pressure in the atmosphere affects on the formation of the internal oxides.

TEM also revealed that the microstructure around the internal oxide precipitates was different from the bulk matrix, which was tempered martensitic. A pearlitic microstructure is observed around the complex oxides close to the surface, as shown in Fig. 6-7.

6.3. Intergranular Oxides

The prior austenite grain boundaries in all the specimens exhibited intergranular oxidation. At the early carburizsing stage (2.0h heating), the uniform primary intergranular oxides formed, as shown in Fig. 6-8. This intergranular oxidation precipitated along the grain boundaries close to the surface oxide continuous layer. EDS spot analysis identified that the intergranular oxides were formed from three alloy elements, Cr, Mn and Si. The surface oxide continuous layer was mainly rich in O, Fe, with some Si and Mn observed in the surface scale. Si is rich in the surface /surface oxide layer interface, Mn is strong rich within the surface continuous layer. Cr appeared later close to the surface oxide layer /matrix interface region. Semi quantitative depth profile analysis of the surface oxide continuous layer and the primary intergranular oxides is shown in Fig. 6-18. The TEM bright field image revealed that the surface continuous oxide layer was polycrstalline, as shown in Fig. 6-9. After long cycle carburising, the intergranular oxides precipitated along grain boundaries deeper into the specimen (Fig. 6-1). Higher magnification TEM bright field images showed that the intergranular oxides were formed as a uniform thin film of thickness ranging from 50 to 400 nm precipitated along the grain boundaries, as shown in Fig. 6-10. Most of the intergranular oxides were identified as Si-oxides using a combination of EDS and SAD, e.g. SiO_2 in hexagonal structure, a=0.5002nm, c=0.5454nm (Fig. 6-10a). As the Si content increased in the bulk material, the thickness of the film of the intergranular oxides increased. SAD pattern showed the Si-oxides were mostly crystalline, however, some Si-oxides were amorphous (Fig. 6-5a), especial for the intergranular oxides close to the surface. It was observed that Some of Si intergranular oxides appeared as part crystalline, part as amorphous, as shown in Fig. 6-11a.

6.4 Agglomerated Oxide Phases

Some larger oxides that were observed for different specimens close to the surface consisted of more than one complex oxide. They were agglomerated oxide phases which consisted of Cr-Mn complex oxide precipitates (such as $CrMnO_4$) and Mn-Si or Si-oxides, as shown in Fig. 6-12, 6-13. The distribution and concentration of elements in the agglomerated oxide phases (Fig. 6-12, 6-13) are shown in Table 6-4 and 6-5. The X-ray mapping on an agglomerated oxide phase (Fig. 4-6) is shown in Fig. 6-14. The results indicated that cubic shaped Cr-Mn complex oxides, such as $CrMnO_4$ in Fig. 6-13, formed first in the inner of the agglomerated oxide phases, then, Mn-Si or Si oxides formed around the agglomerated oxide phase.

Table 6-4 EDS Semi-quantitative analysis on the agglomerated oxide phase (Fig. 6-12)

intensity %

Analysed point	O	Si	Cr	Mn	Fe
1	14.95		49.94	24.51	10.60
2	13.81		50,06	25.56	10.50
3	14.03		49.98	28.05	10.94
4	13.93		49.46	27.93	8.88
5	17.59.19		27.94	19.80	43.67
6	16.71	4.18	26.94	18.87	33.05
7	18.19	10.60	1.16	8.37	60.80
8	14.01	1.62	44.19	23.29	16.46
9	16.39	9.82	9.07	12.5	51.92

6.5 Small Dispersed Oxide Particles

Small dispersed precipitate particles were always observed in the specimens studied around the grain boundaries and the complex oxides in the internal oxidation zone with dimensions approximately 50nm, especial for specimens with higher Si content. Typical small dispersed oxide particles are shown in Fig. 6-11, 6-15 and 6-16. Some small dispersed oxide particles precipitated by combining together with other phase

Table 6-5 EDX Semi-quantitative analysis on the agglomerated oxide phase (Fig. 6-13)

Intensity %

Analysed point	O	Si	Cr	Mn	Fe
1	15.11	4.04	27.52	13.59	35.46
2	14.68	0.29	45.00	21.08	17.15
3	11.86	2.09	41.06	23.52	21.84
4	18.85	12.07	9.80	3.70	53.52
5	11.72	11.60		1.44	73.32
6	19.21		44.30	17.04	19.54
7	13.82		54.40	9.93	22.63
8	17.07		45.49	21.37	19.18
9	15.07	1.28	43.40	20.63	19.27
10	17.32	11.1	0.85	1.17	67.58

this may be carbides, as shown in Fig. 6-17. The small dispersed oxide particles exhibited rectangular, cubic and spherical morphologies shape. The small dispersed internal oxide precipitate particles had a clear boundary with the matrix.

EDS spot analysis was carried out on the small dispersed oxide particles using TEM. Some of these were identified as rich in O, Cr and Mn in the specimen with median Si bulk content (Fig. 6-15 b). Most of the small dispersed particles were identified as Si - oxides, especially in the specimens with higher Si bulk content (Fig. 6-15 a, c).

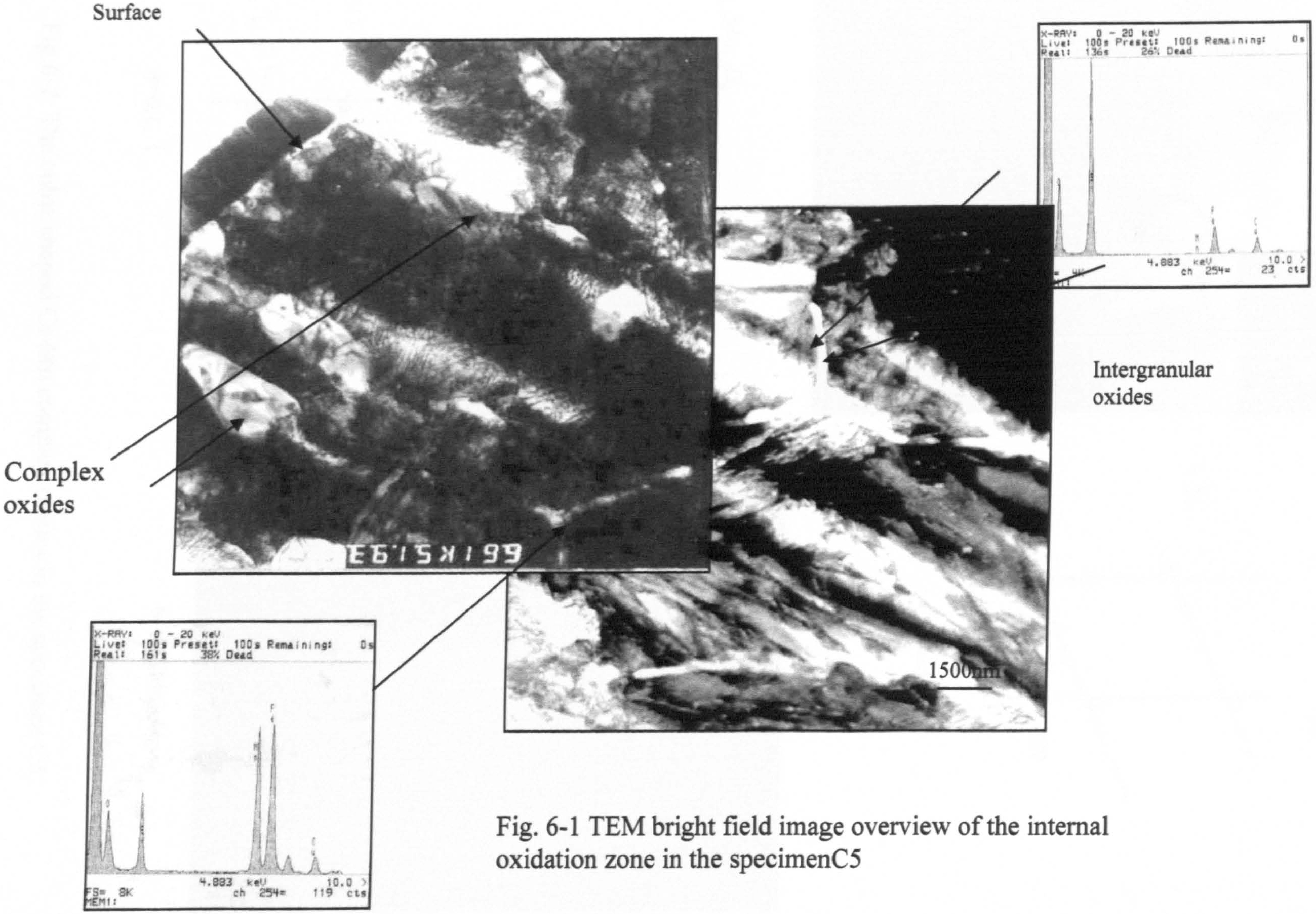

Fig. 6-1 TEM bright field image overview of the internal oxidation zone in the specimenC5

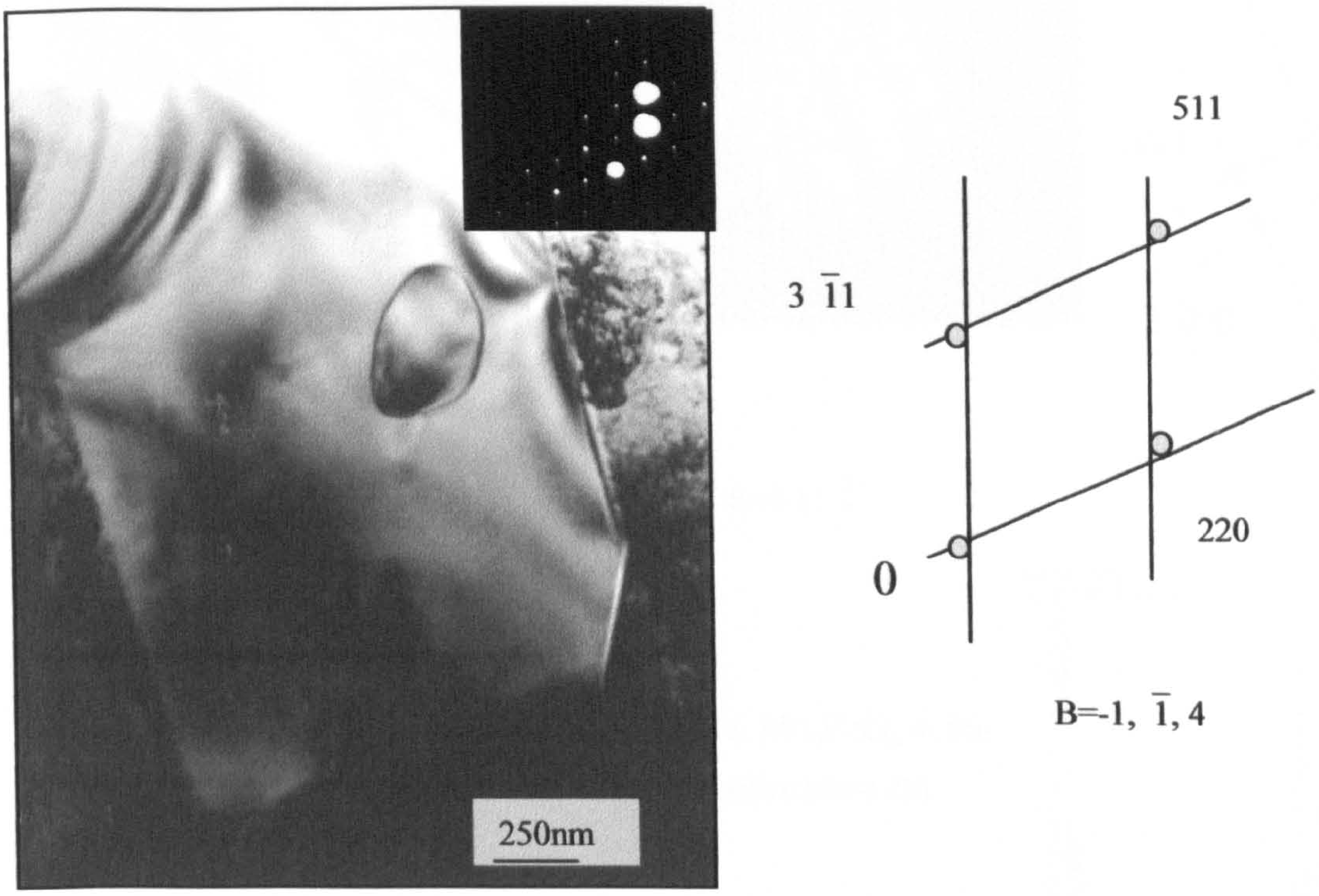

a. $Cr_{1.5}Mn_{1.5}O_4$

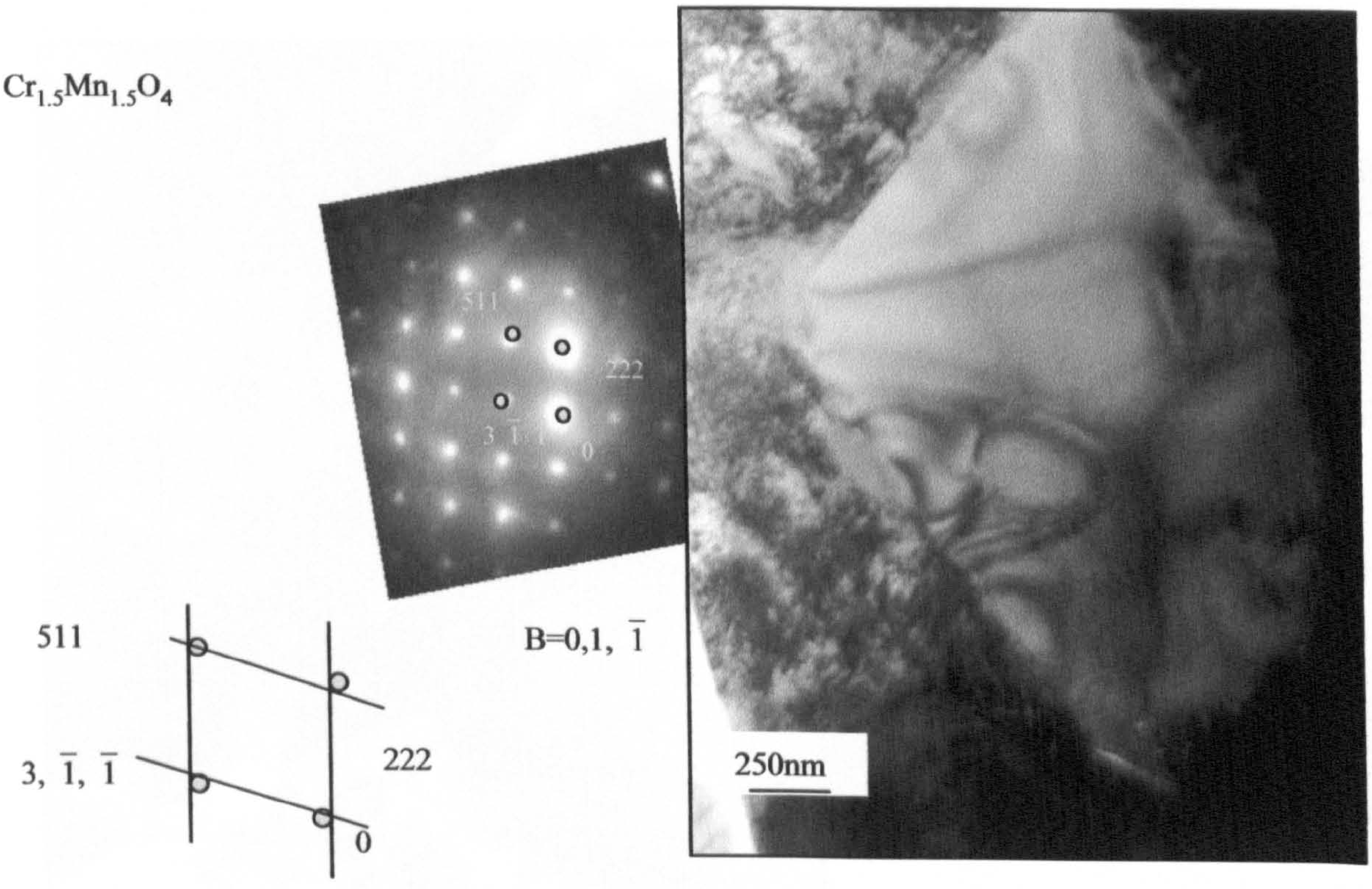

b. $Cr_{1.5}Mn_{1.5}O_4$

Fig.6-2 The cubic shaped Cr-Mn complex oxides in the specimen C5.

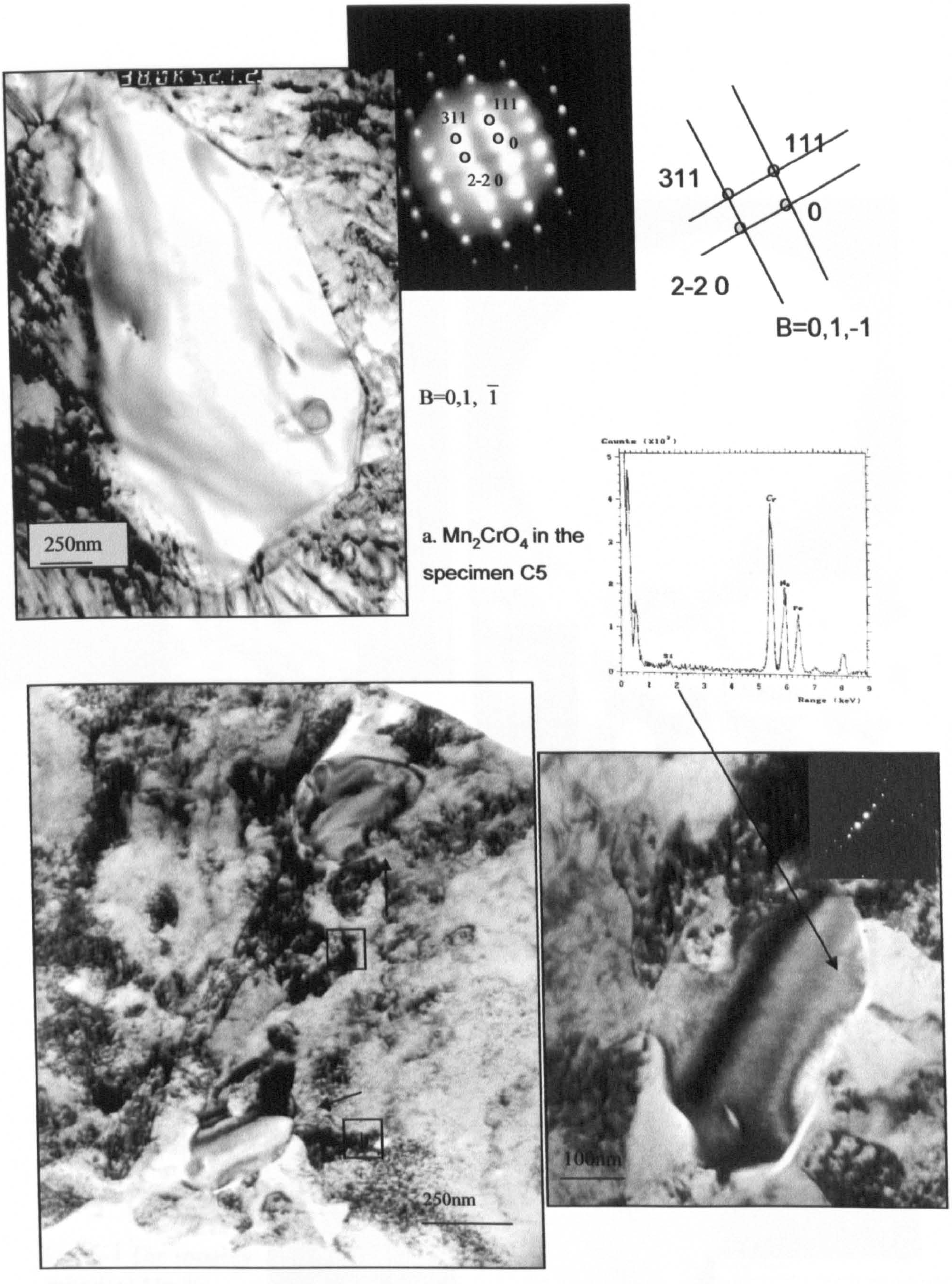

a. Mn_2CrO_4 in the specimen C5

c. Cr and Mn complex oxides in the specimen B1-5, left image oxide particle b

b, internal oxides in the specimen B1-5

Fig. 6-3 The ellipsoid shaped Cr-Mn complex oxide precipitated in the specimens

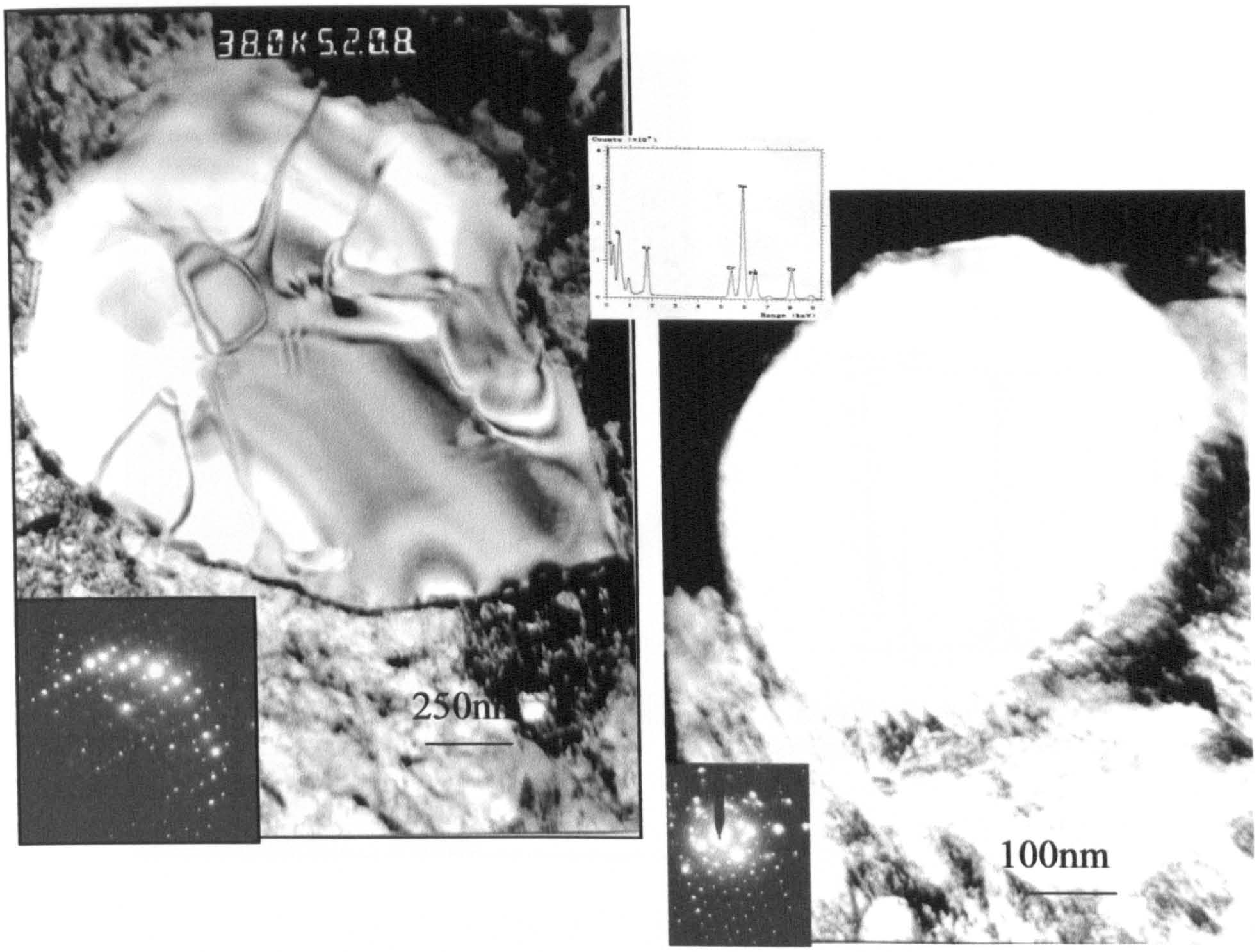

a. $MnSiO_3$ in the specimen C5

16MnCr5

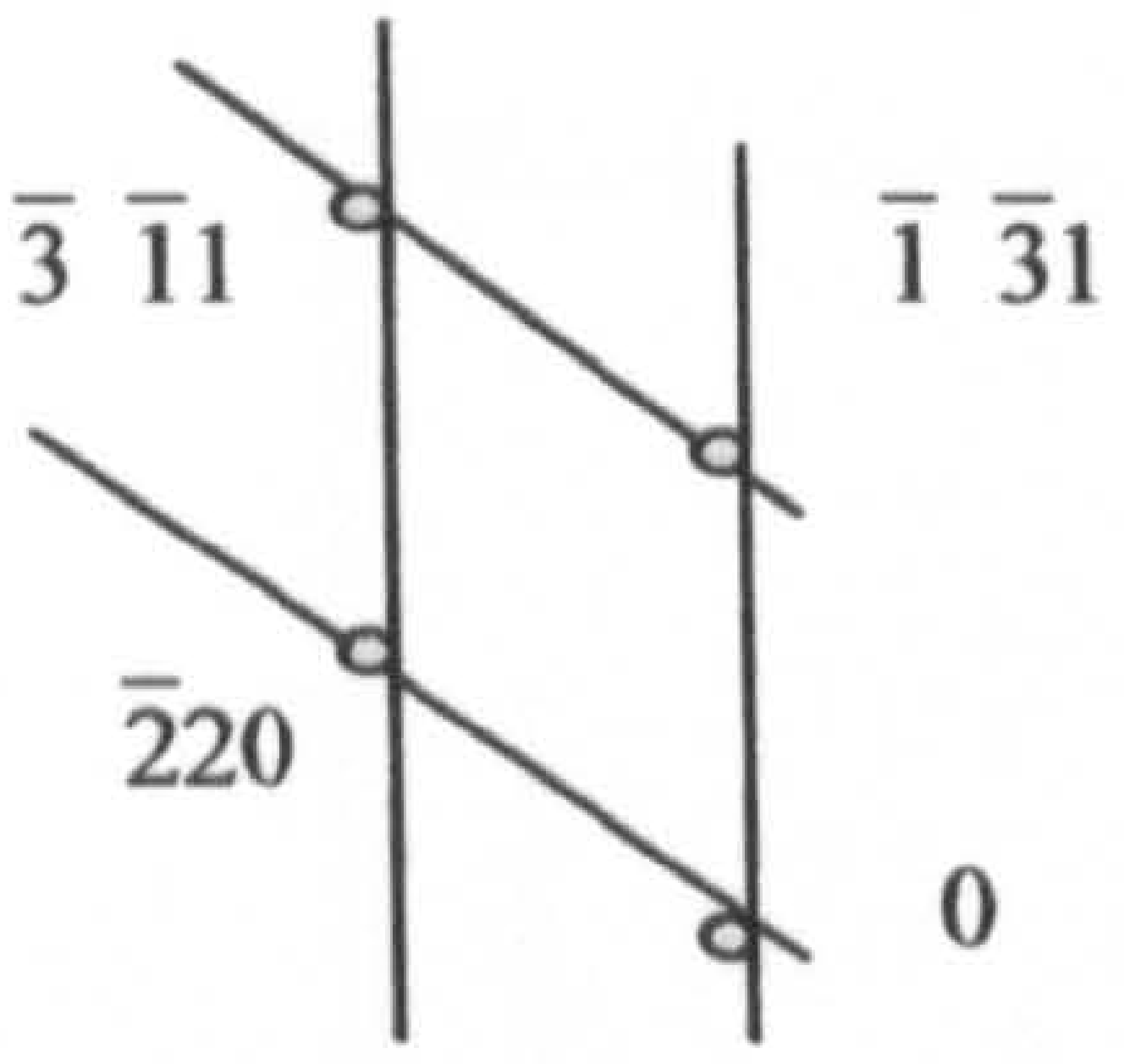

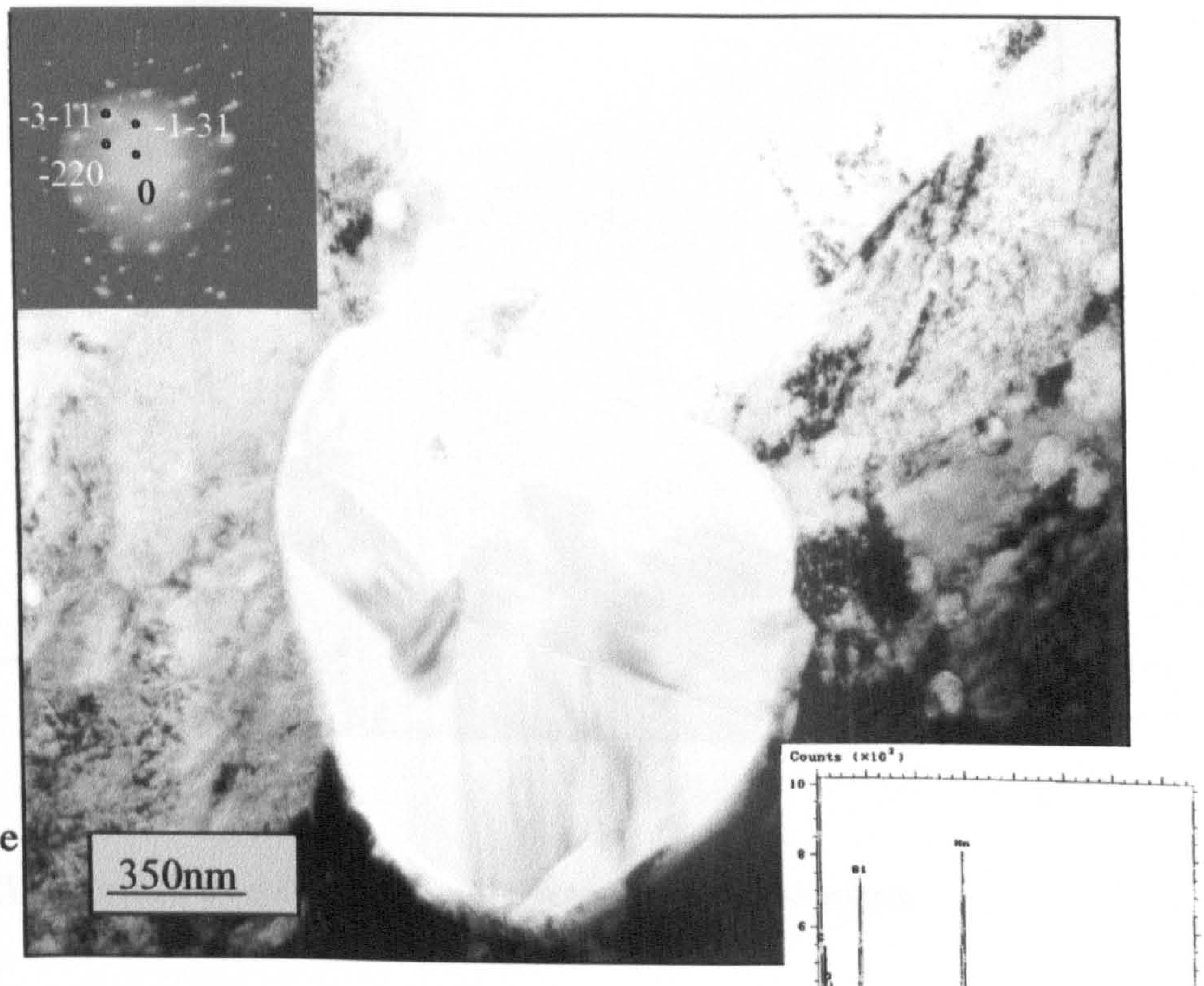

Fig. 6-4 The roughly spherical Mn-Si complex oxides in the specimens

c, $MnSiO_3$ in the specimen C1-8.

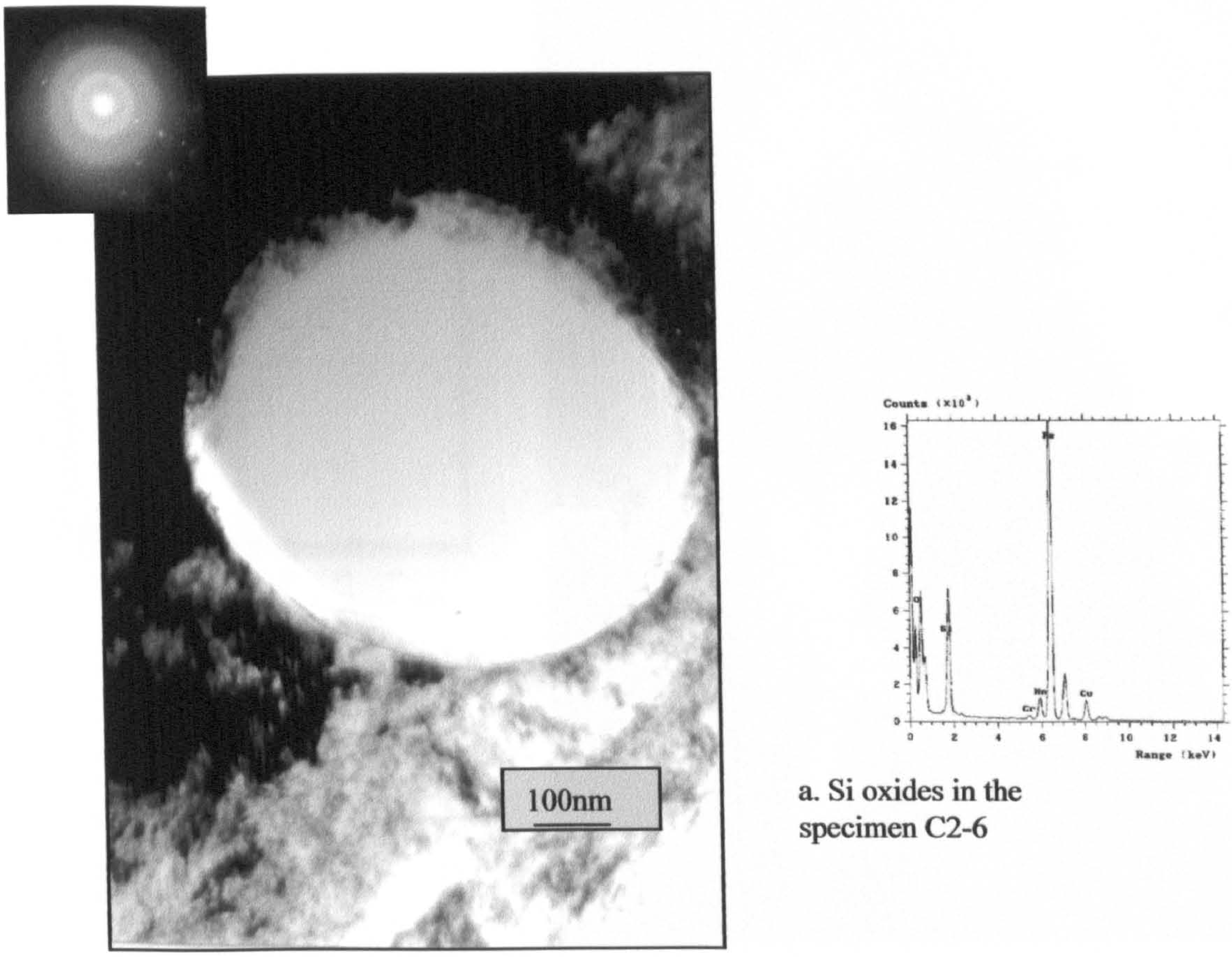

a. Si oxides in the specimen C2-6

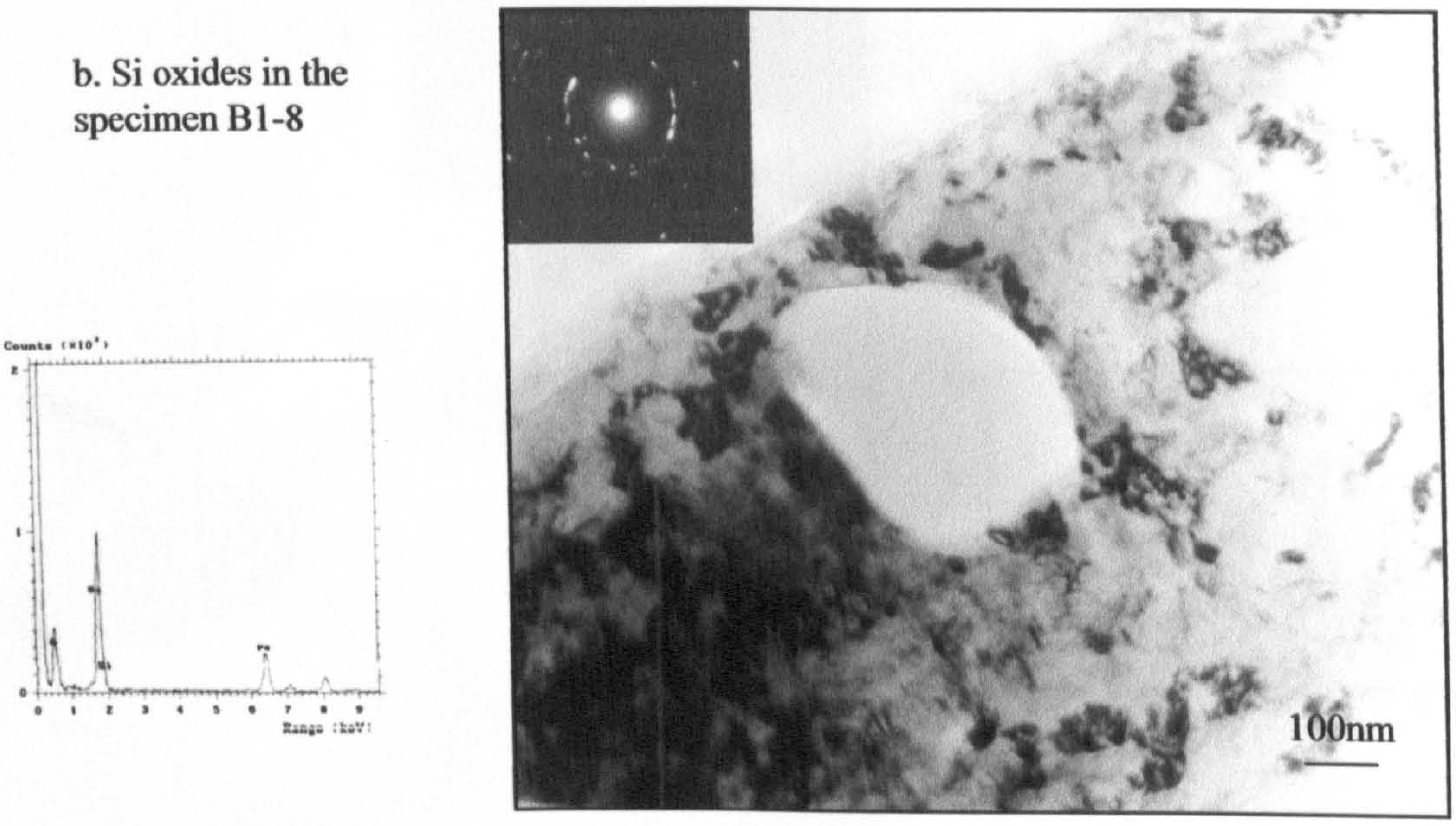

b. Si oxides in the specimen B1-8

Fig. 6-5 Small Si oxides as spherical precipitates in the specimens

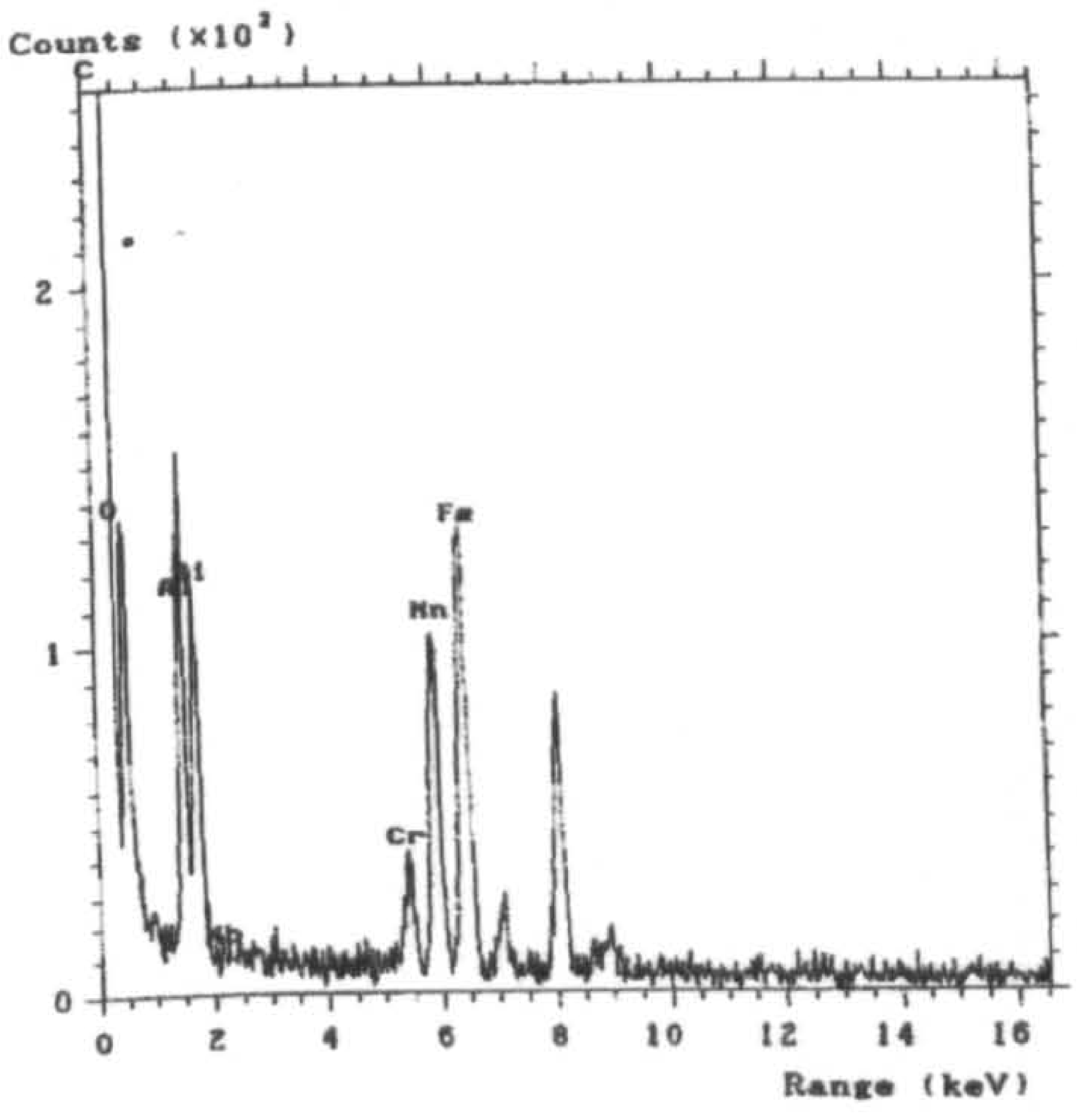

a. Al, Si, Mn and Cr complex oxide in the specimen C5

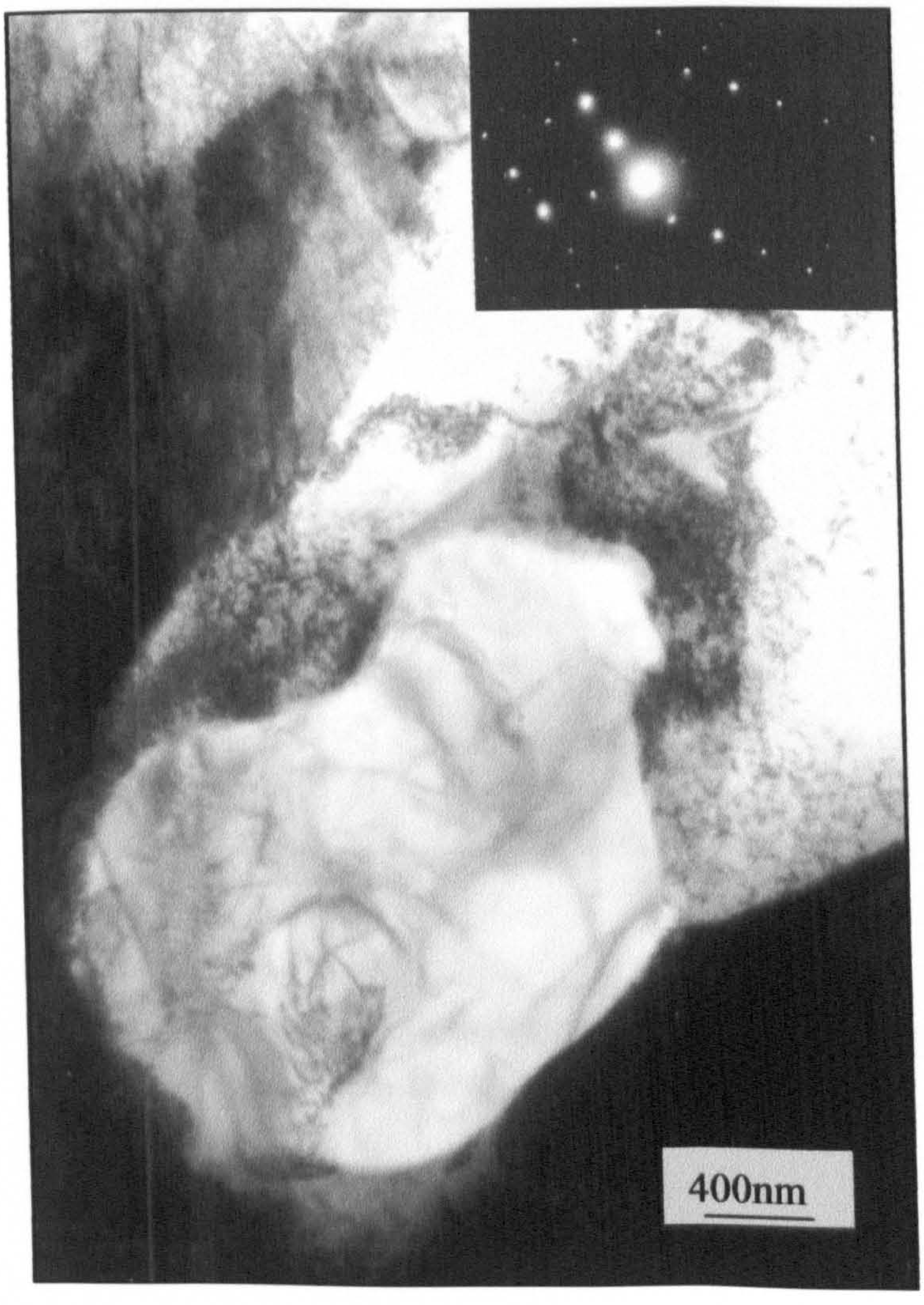

b. Al-oxide in the specimen D5

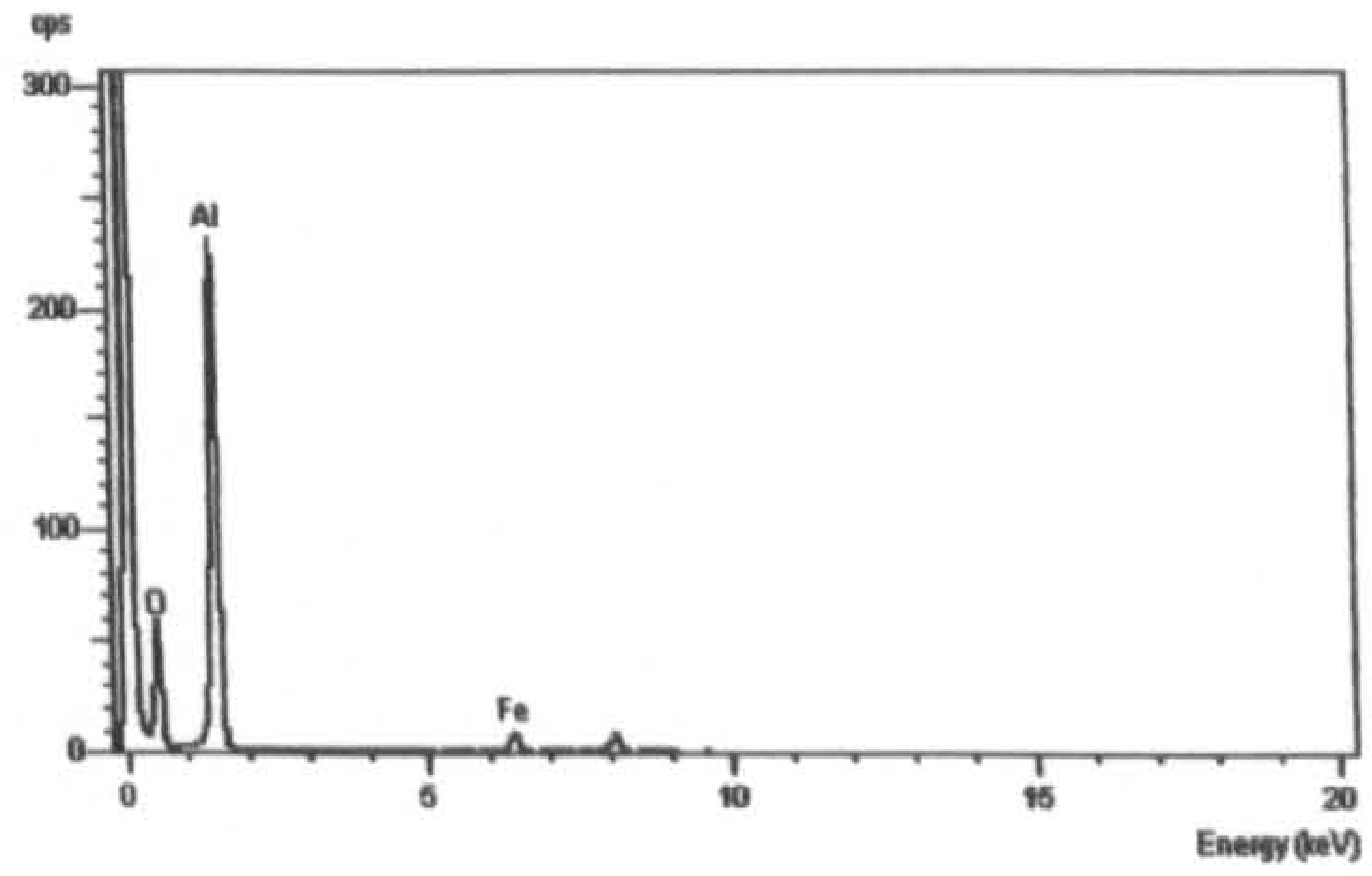

Fig. 6-6 Complex oxides in the specimens

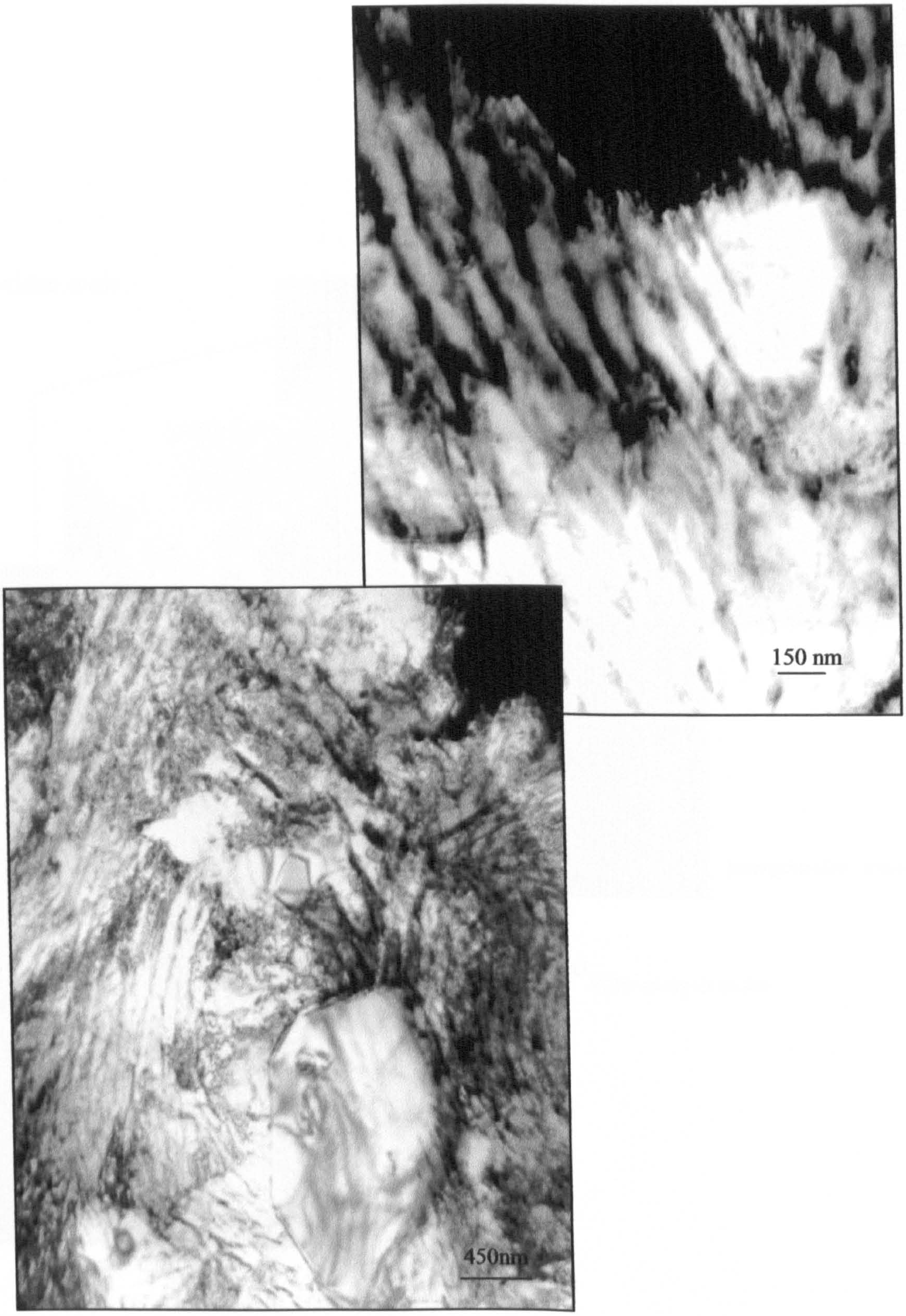

Fig. 6-7 Pearlite microstructure around internal oxide particle in the specimen C5

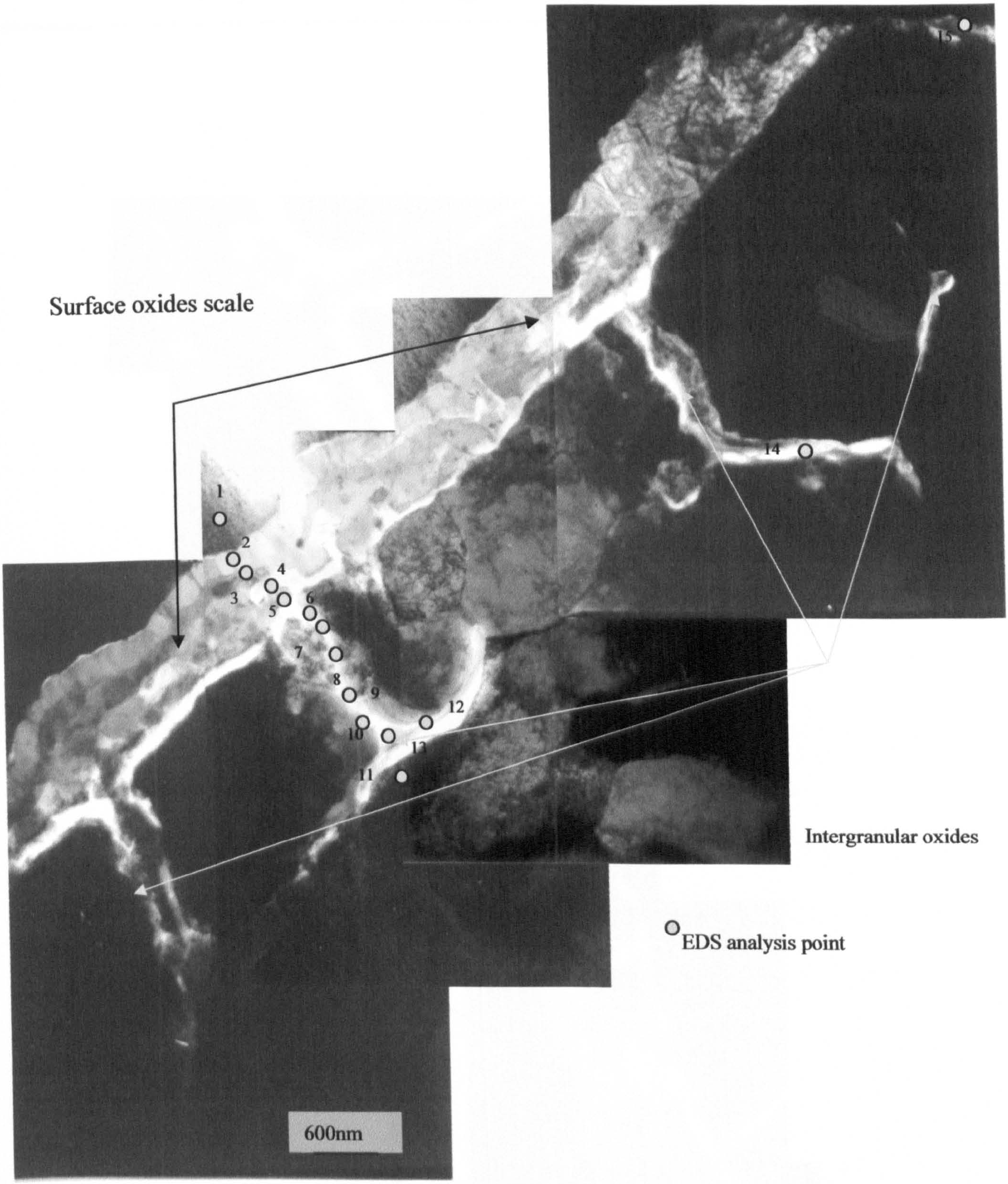

Fig. 6- 8 Intergranular oxides in the specimen C1-4. The Cr, Mn and Si rich in the interngranular oxides

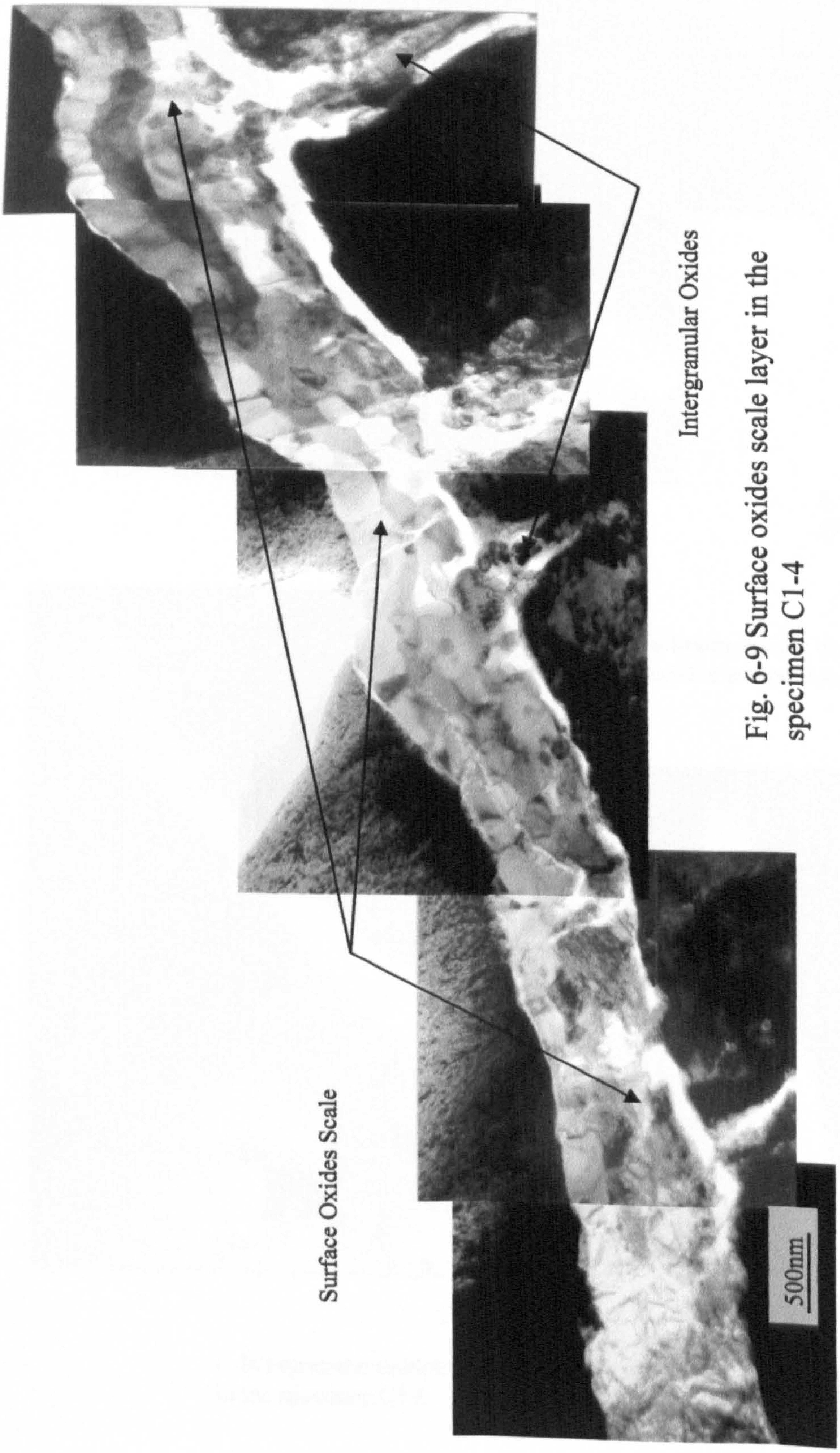

Fig. 6-9 Surface oxides scale layer in the specimen C1-4

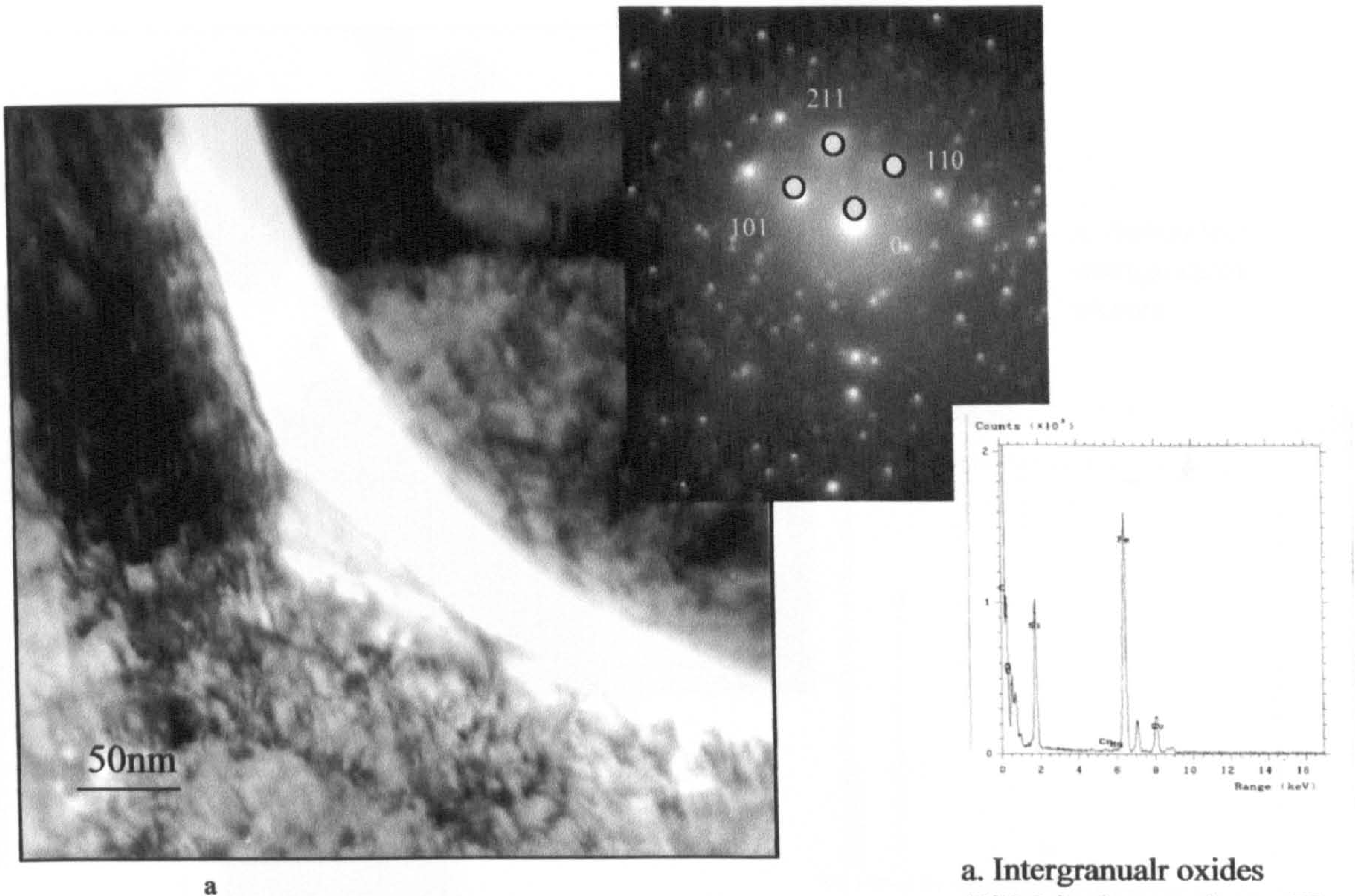

a. Intergranualr oxides (SiO_2) in the specimen C5

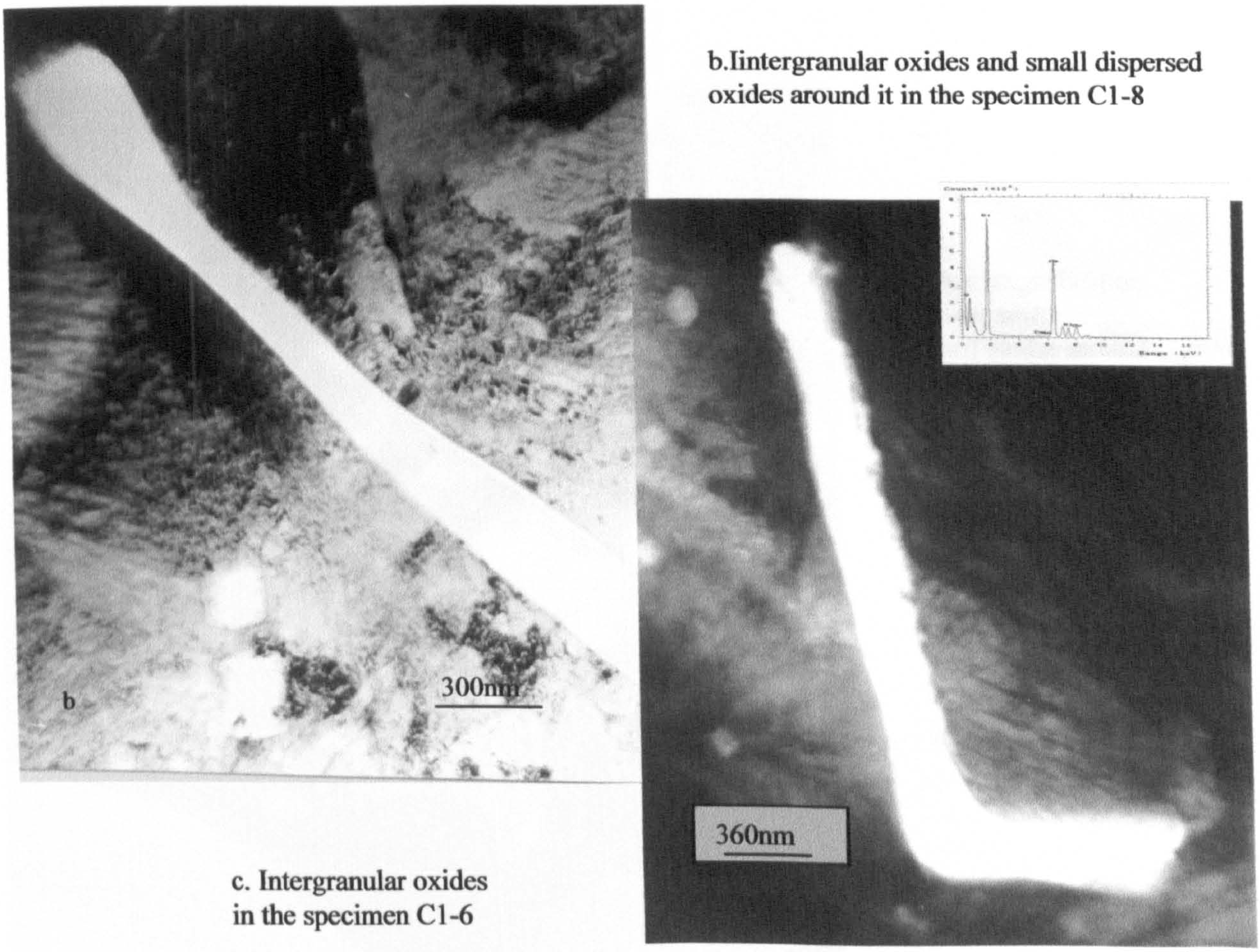

b.Iintergranular oxides and small dispersed oxides around it in the specimen C1-8

c. Intergranular oxides in the specimen C1-6

Fig. 6-10 Intergranular oxides (Si oxides) in the specimens

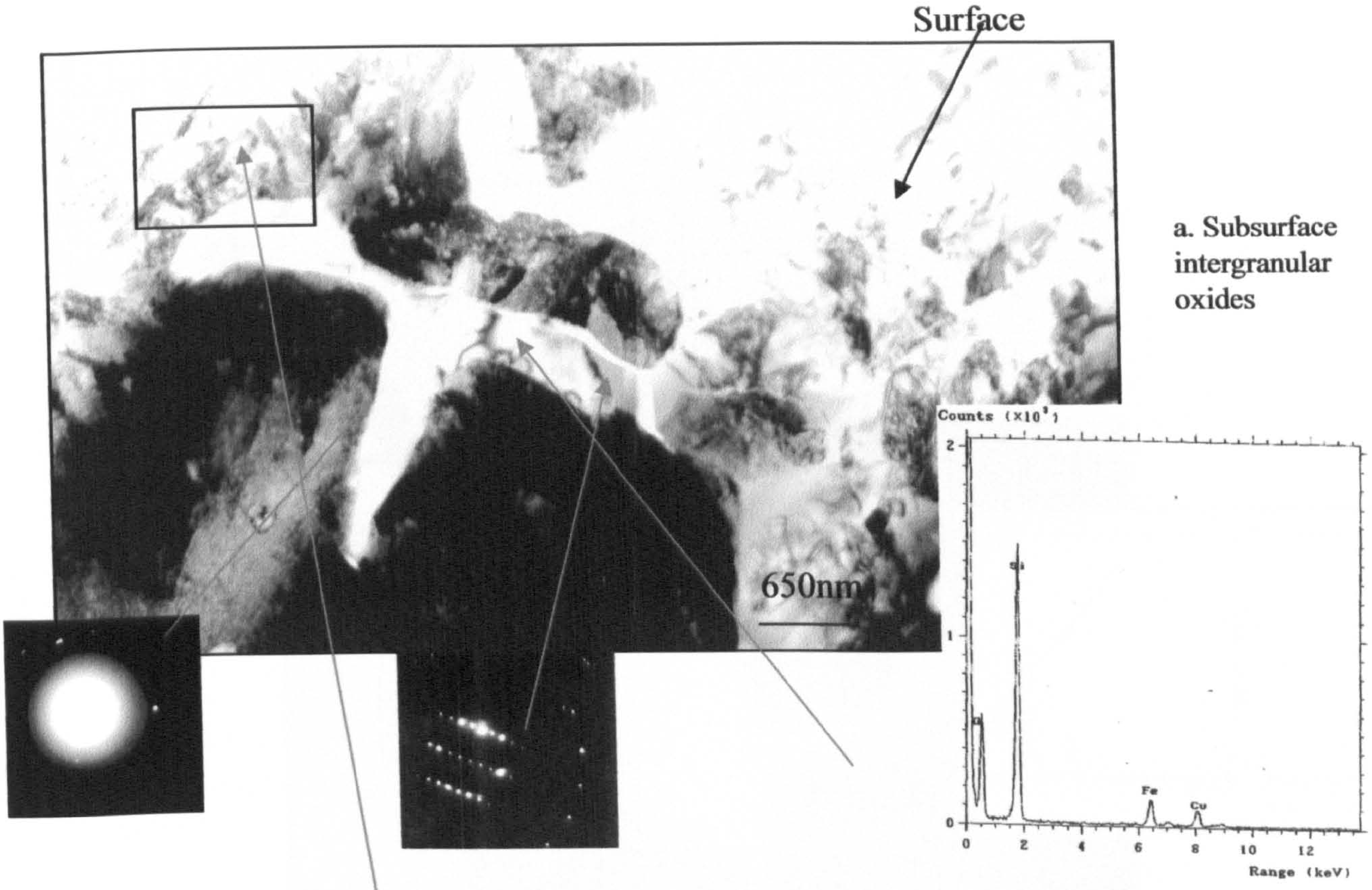

a. Subsurface intergranular oxides

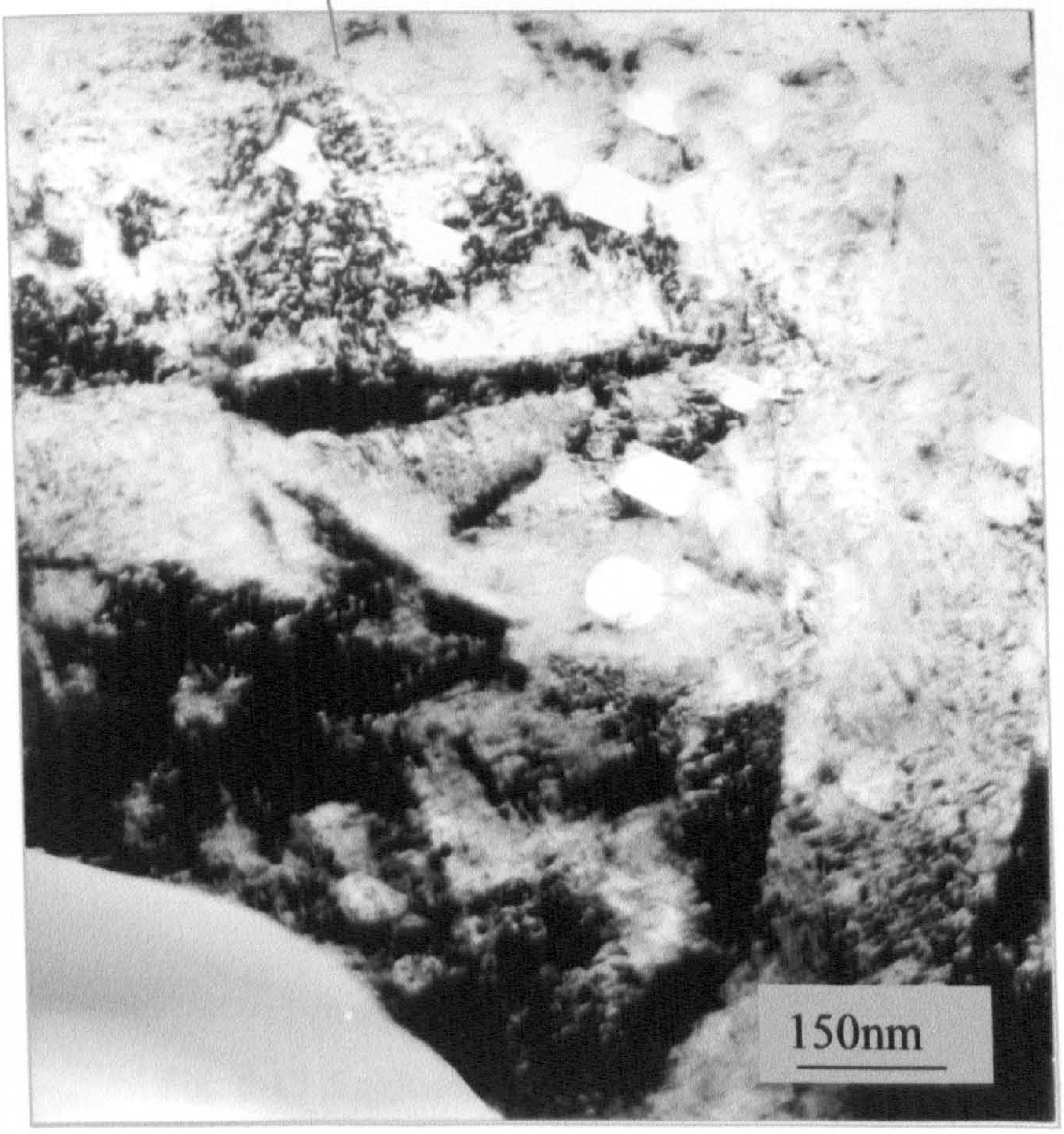

b. Higher magnification in A zone, small dispersed oxides around the intergranular oxide

Fig. 6-11 Intergranular oxides in the specimen E1-5

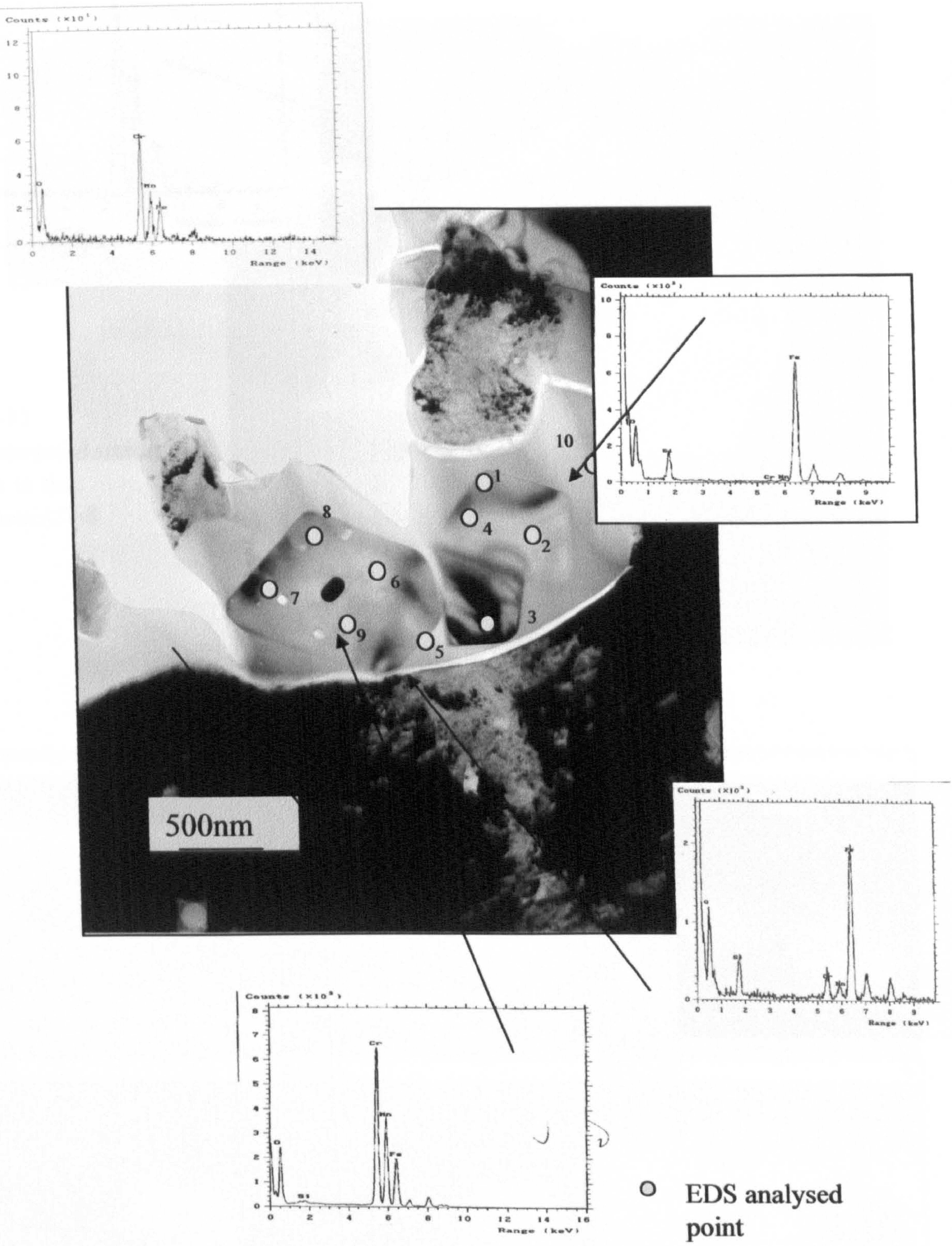

Fig. 6-13 Agglomerated oxide phases in the specimen E1-5

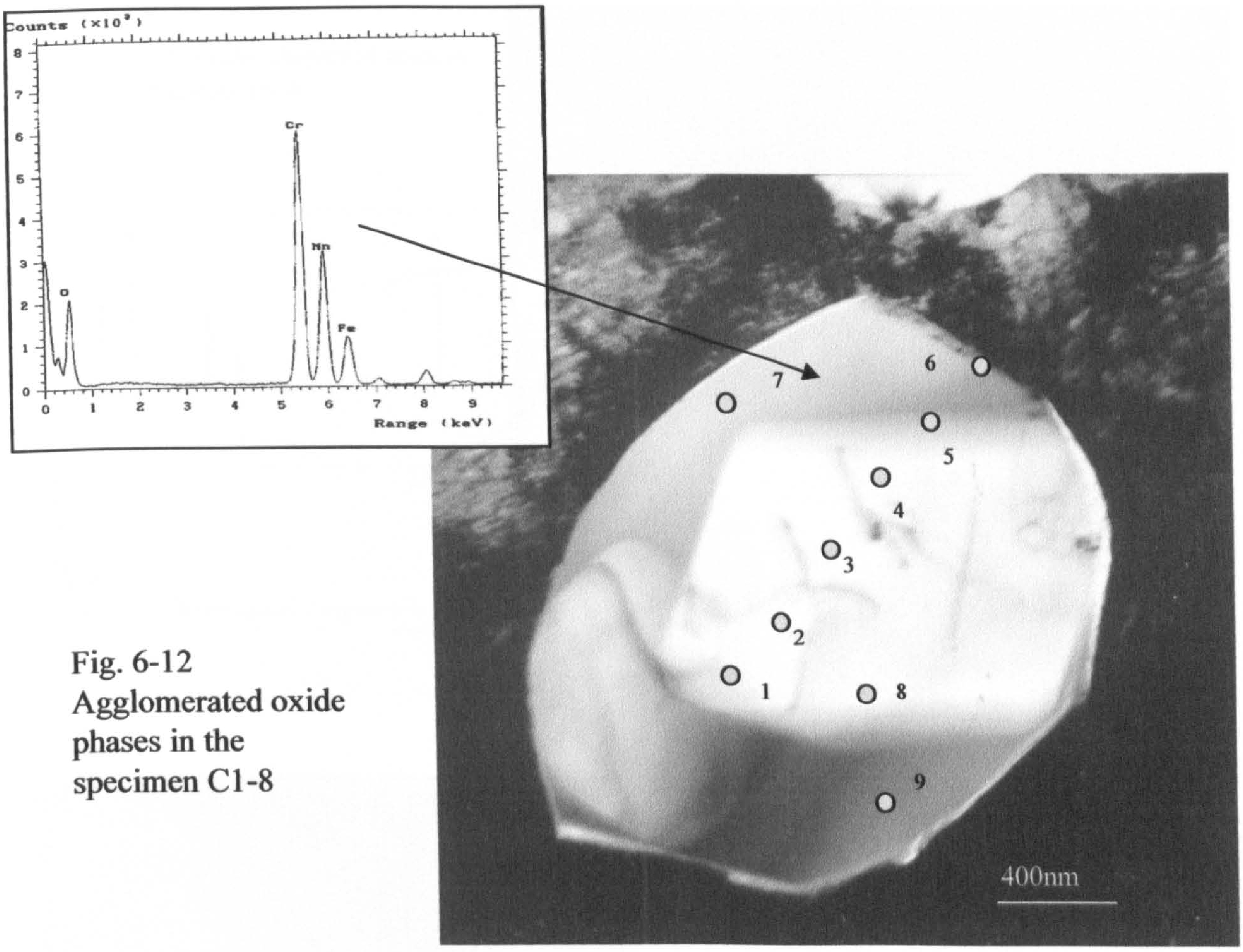

Fig. 6-12
Agglomerated oxide
phases in the
specimen C1-8

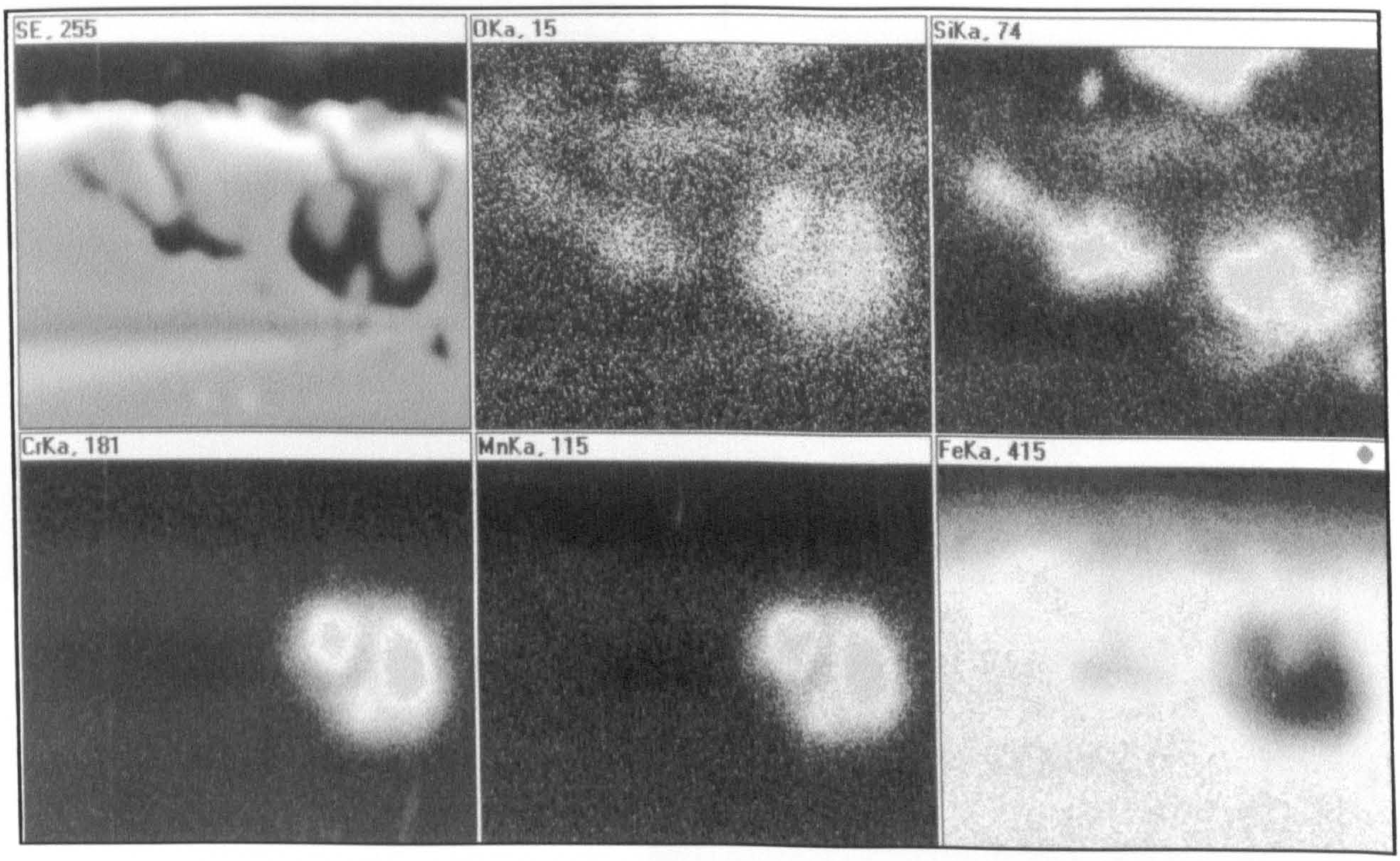

Fig.6-14 X-Ray mapping on an agglomerated oxides in the specimen E1-8

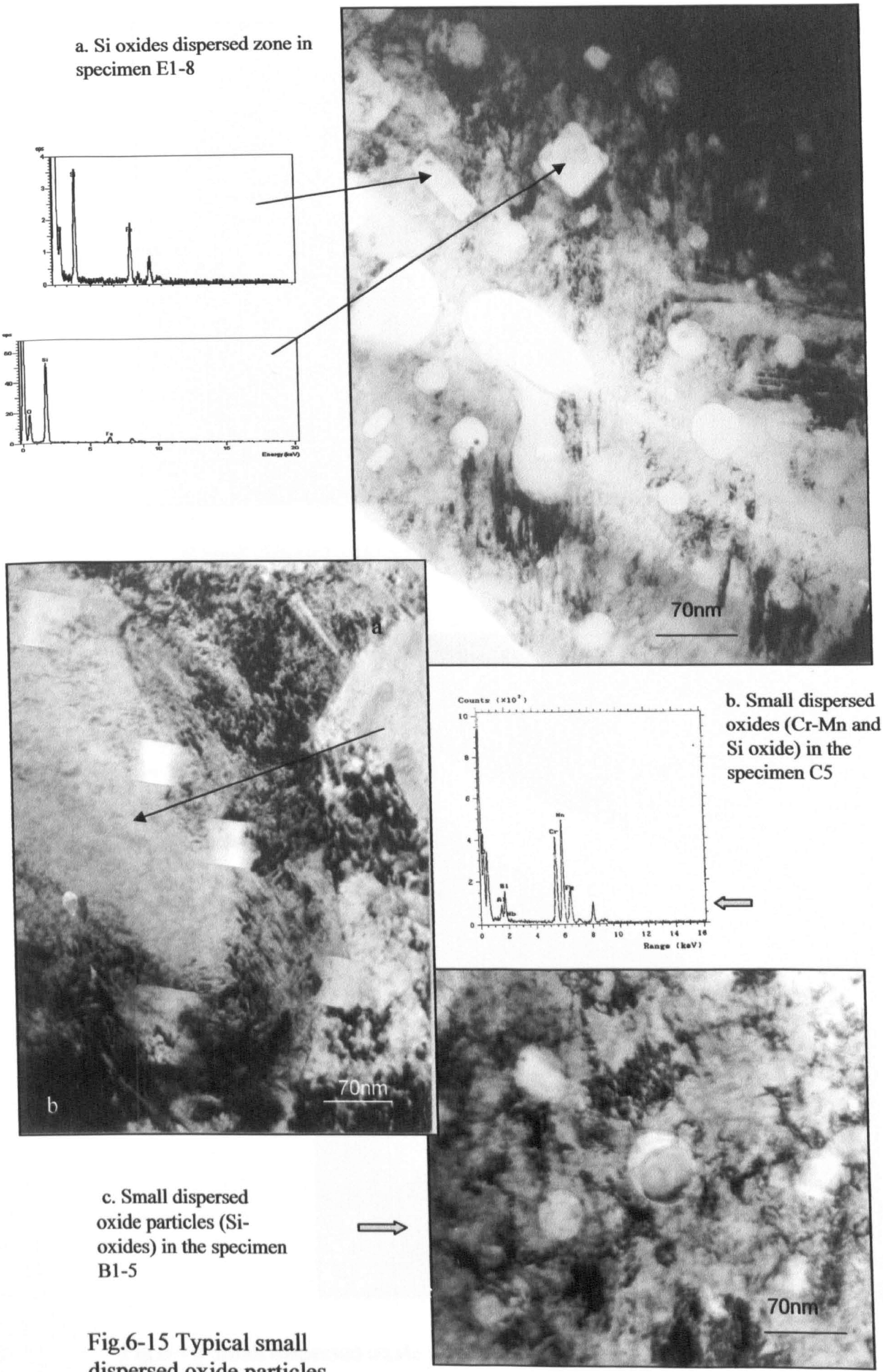

a. Si oxides dispersed zone in specimen E1-8

b. Small dispersed oxides (Cr-Mn and Si oxide) in the specimen C5

c. Small dispersed oxide particles (Si-oxides) in the specimen B1-5

Fig.6-15 Typical small dispersed oxide particles

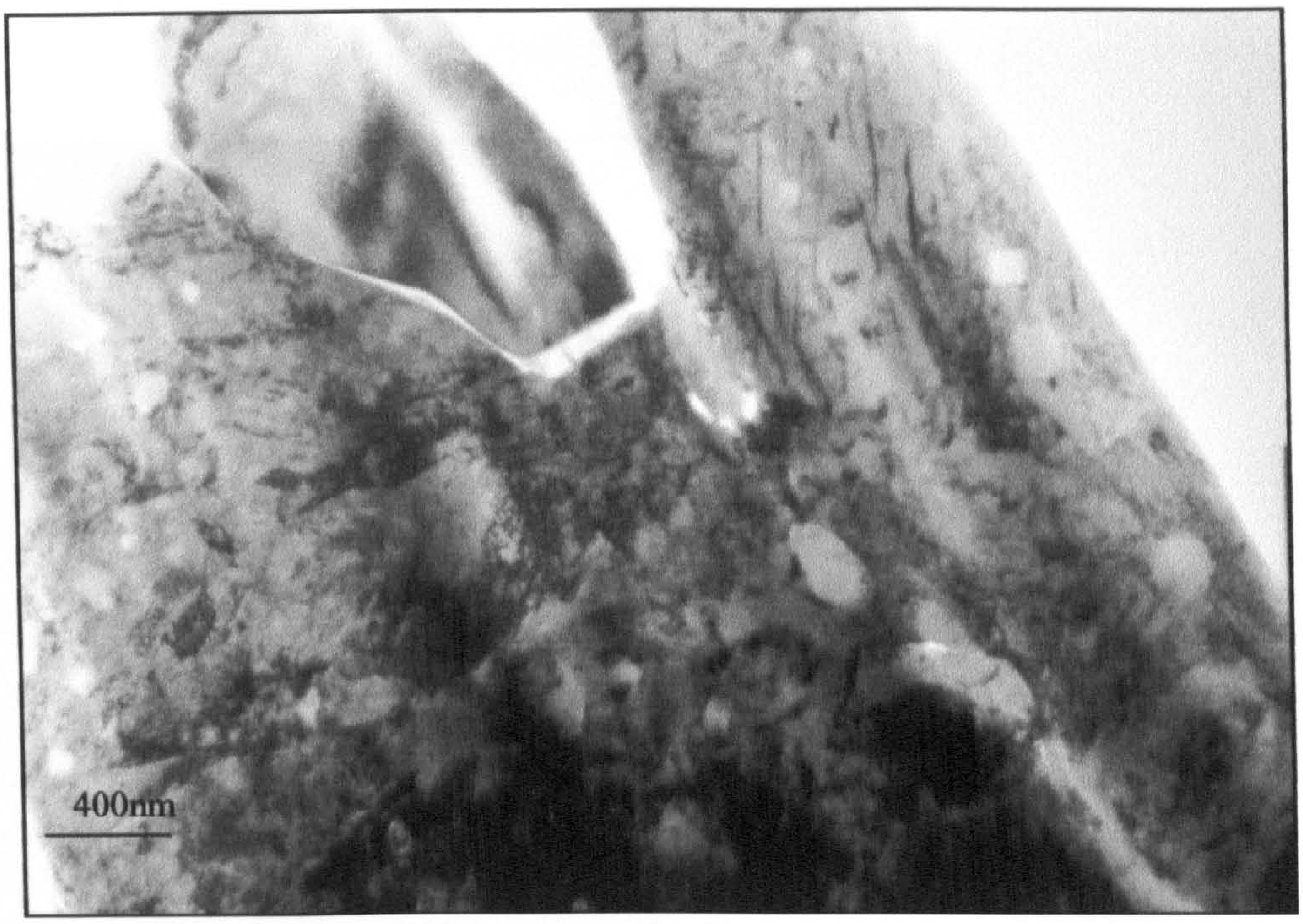

a) Small dispersed oxide particles around larger oxides in the specimen D5

b). Small dispersed oxide particles around intergranular oxides

Fig.6-16 Small dispersed oxide particles around larger oxide and intergranular oxide

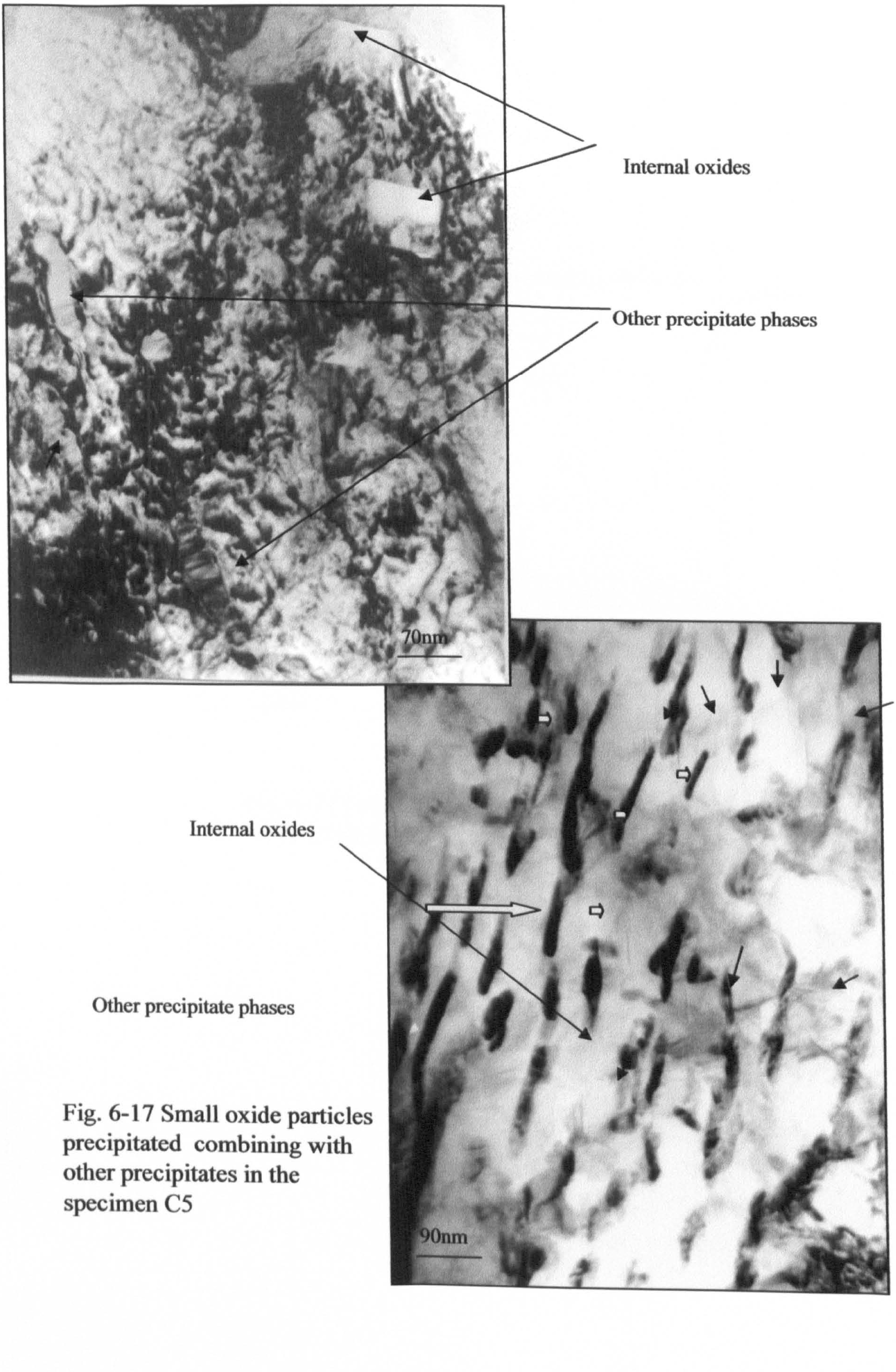

Fig. 6-17 Small oxide particles precipitated combining with other precipitates in the specimen C5

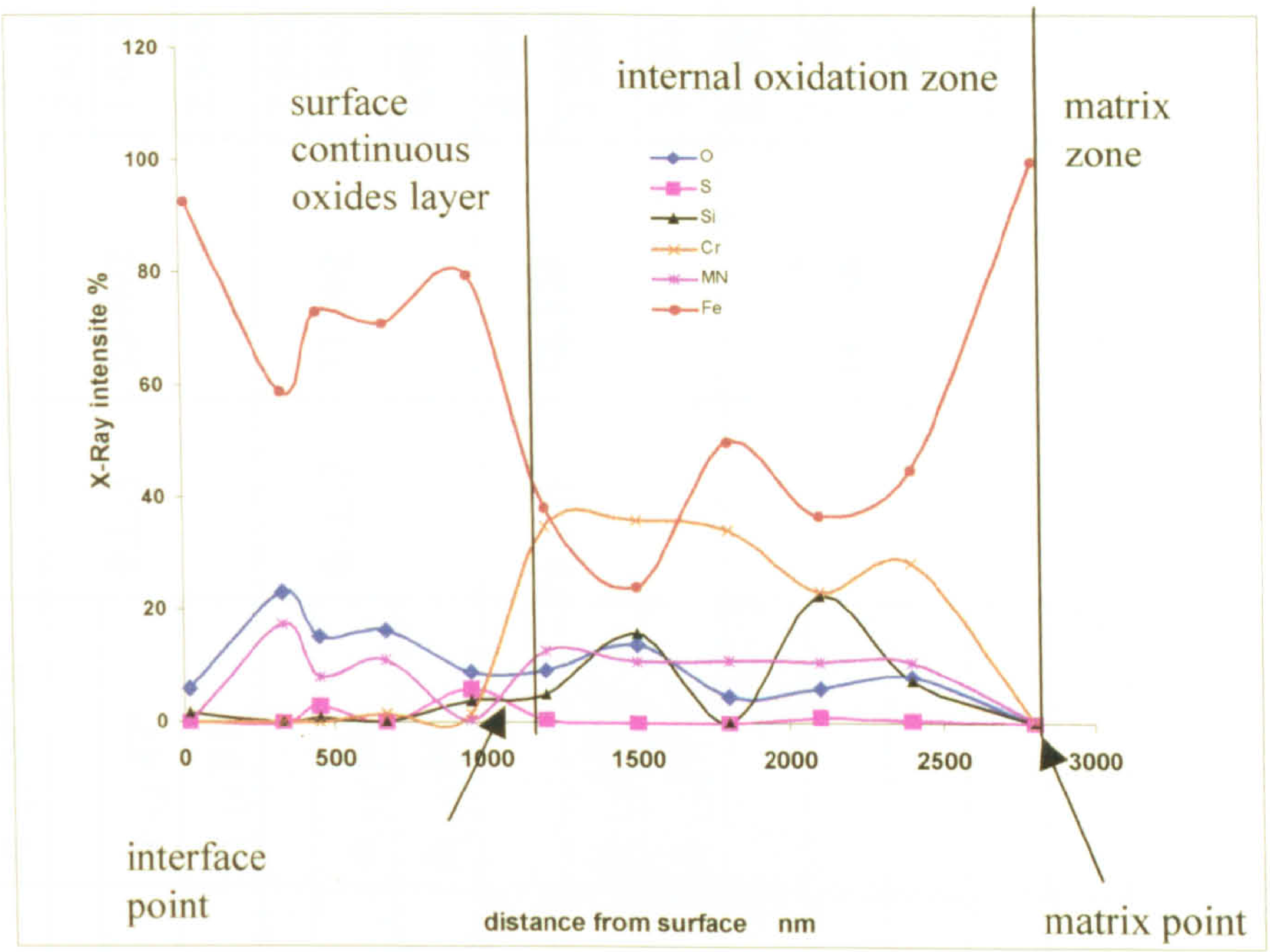

Fig. 6-18 Elements concentration distribution in the surface region in the specimen B1-4

Table 6-2 Electron Diffraction Pattern Data

Sample	Figure No	point	R mm	d Å	measured α°	calculated α°	B	card date			
								Card No	d Å	I/I_1	phase
C5	6-2a	1	9.25	2.549			-1,-1,4	33-892	2.545	311	$Mn_{1.5}Cr_{1.5}O_4$
		2	14.5	1.626	$\alpha_{1,2}$ 29°$_1$	$\alpha_{1,2}$29°50'$_1$			1.625	511	
		3	7.5	3.144	$\alpha_{2,3}$ 63°	$\alpha_{2,3}$ 64°26'			2.985	220	
C5	6-2b	1	7.0	2.482			0,1,-1	33-892	2.438	222	$Mn_{1.5}Cr_{1.5}O_4$
		2	9.9	1.679	$\alpha_{1,2}$ 45°	$\alpha_{1,2}$ 47°			1.625	511	
		3	6.6	2.519	$\alpha_{1,3}$ 80°	$\alpha_{1,3}$ 81°			2.545	311	
B1-5	6-3b	1	5.7	2.844			0,-1,-2	33-892	2.985	220	$Mn_{1.5}Cr_{1.5}O_4$
		2	6.55	2.4755	$\alpha_{1,2}$ 31°	$\alpha_{1,2}$ 30°			2.545	311	
		3	3.4	4.769	$\alpha_{1,3}$ 91°	$\alpha_{1,3}$ 90°			4.88	111	
C1-8	6- 12	1	3.2	5.067			0,1,-1	36-546	4.929	111	Mn_2CrO_4
		2	6.6	2.5205	$\alpha_{1,2}$ 60°	$\alpha_{1,2}$58°52'			2.522	311	
		3	5.6	2.8955	$\alpha_{2,3}$31°50'	$\alpha_{1,2}$31°48'			2.981	220	
C1-8	6- 4c	1	7.0	2.3758				13-138	2.382	311	$MnSiO_3$
		2	5.0	3.326					3.320	131	
		3	4.5	3.696					3.700	220	
		4	3.0	5.543					5.540	120	
		5	2.5	6.652					6.670	020	

Table 6-2 Electron Diffraction Pattern Data

Sample	Figure No	point	R mm	d Å	measured α °	Calculated α°	B	Card date			
								Card No	d Å	I/I$_1$	phase
C5	6-4 a	1	4.50	3.6958				26-1249	3.63	111	$MnSiO_3$
		2	6.60	2.5198					2.516	002?	
		3	2.60	6.397					6.560	110	
C5	6-10a	1	6.65	2.5008			-1,11	11-252	2.50	110	SiO_2
		2	10.5	1.584	$\alpha_{1,2}$ 19°	$\alpha_{1,2}$ 19°54'			1.566	211	
		3	5.0	3.326	$\alpha_{1,3}$ 47°	$\alpha_{1,3}$ 47°13'			3.40	101	
E1-8	6-13	1	5.05	3.2108			0,0,-1	33-893	3.130	110	$MnCrO_4$
		2	7.4	2.191	$\alpha_{1,2}$ 45°	$\alpha_{1,2}$ 45°			2.212	200	
		3	5.15	3.1485	$\alpha_{2,3}$ 45°	$\alpha_{2,3}$ 45°			3.130	110	
16CrMn5	6-4 b	1	3.50	4.750				35-0748	5.305	311	Mn_2SiO_4
		2	3.75	4.4348					4.450	131	
		3	4.50	3.698					3.627	220	
		4	6.50	2.585					2.559	120	
		5	7.50	2.217					2.231	020	
		6	8.0	2.0788					2.096	010	
		7	10.5	1.584					1.572		

CHAPTER 7

INFLUENCE OF SILICON ON THE INTERNAL OXIDATION OF CARBURISED STEEL

7.1 Introduction

The carburised steel with different Si content in the range (0.11-0.77) %, are shown in Table 3-1, specimens A- E, and were selected in order to study the influence of silicon content on the internal oxidation phenomenon. The steels were carburised following two types of commercial gas carburising procedure. One group of specimens was carburised following procedure 1 for exposure times 2.0h and 16.6h, as shown in Table 3-3 specimens A1-4,B1-4, C1-4, D1-4, E1-4 and specimens A1-8, B1-8, C1-8, D1-8, E1-8; A second group of specimens was carburised following procedure 5, as shown in Table 3-3, specimens A5, B5, C5, D5, E5. After carburising, the internal oxidation zone of the specimens was examined using SEM, EDS, GDOES, quantitative image analysis and micro-hardness.

7.2 Morphology and Elemental Distribution in the Internal Oxidation Zone

All the specimens carburised at the lower temperature base process (2.0 h, 800°C) were observed to have very similar morphology of internal oxidation zone. Typical cross-section images of the specimens are shown in Fig 7-1a-e. A continuous surface oxide layer was observed for all the specimens studied. The internal oxides appeared as thin films precipitated along grain boundaries close to the surface and were visible around the full periphery of the examined specimen. A plan view image of the specimens confirmed that these primary intergranular oxides were uniformly distributed throughout whole oxidation layer, as shown in Fig. 4-8a and 4-9a. However, the intergranular oxides in the specimens with low Si content (A1-4, B1-4) were thin and relatively more perpendicular to the surface (Fig. 7-1a, b). Thicker intergranular oxides were observed in the specimens with higher Si contents (C1-4, D1-4, and E1-4) (Fig. 7-1 c, d, e). Typical X-Ray mapping is shown in Fig. 7-2 and Fig. 4-27a which indicated that in the low temperature base process, three alloy elements Cr, Mn and Si reacted with the oxygen to form internal oxides and was rich within the internal oxidation zone. After long cycle carburising (16.6h), the morphology of the internal oxidation zone in the specimens with different Si content was quite different, as shown in Fig 7-3 a-e. Similar morphologies were observed in the group of specimens A5- E5 where a network of intergranualr oxidation was observed and more prevalent in the specimens A5-E5 series, as shown in Fig. 7-4 a-e. All the specimens displayed an outer layer of larger oxides close to the surface and an inner layer zone with intergranular oxides remote from the surface close to the internal oxidation front. Small dispersed oxide particles were always observed in the internal oxidation zone of the specimens studied. Typical surface topography of the internal oxides in different depth layers are shown in Fig. 7-5 and Fig. 7-6. Fig.7-5 related to the outer layer zone of the cross section image, in which the larger oxides distribute uniformly within the grains and on the grain boundaries. Fig. 7-6 relates the inner layer zone of the cross section image, in which the intergranular oxides distributed along the grain boundaries.

The internal oxides in the specimens with low Si content were observed mainly as larger oxides and relatively thin intergranular oxides. As the Si content increased in the bulk metal, thicker, more continuous intergranular oxides were observed instead of the larger oxides. The proportion of the larger oxides decreased and became more confined towards the surface, whilst the proportion of the intergranular oxidation and small dispersed oxide particles increased. The continuous internal oxides layer that was generally parallel to the surface was observed in the cross section of the specimens with high bulk Si content, as shown in Fig. 7-7, 7-8. This morphology was associated with the supply of Si and oxygen at the reaction front and caused the severe intergranular oxidation. Therefore, once a continuous internal layer developed, it spalled off leaving an internal oxidation zone at the surface region, as shown in Fig. 4-7. X-ray mapping of the specimen showed that larger oxides were rich in Cr, Mn and some Si. The intergranular oxidation and small dispersed oxide particles was rich in Si. Typical elements distributions are shown in Fig. 7-9, 7-10. Mn oxides were also observed accompanying the Si oxides in the intergranular oxides (Fig. 7-9).

The morphologies that observed in the specimens studied can be classified into three types, as shown in Fig. 7-11.

Type 1: Larger oxide particles were observed at the near surface, usually elongated and normal to the surface and followed by partial intergranular oxidation on grain boundaries and some small dispersed oxide particles around it. This type was observed for the specimens with low Si content, Si content< 0.31% (Fig. 7-3 and 7-4 a, b), as shown in Fig. 7-11a.

Type 2: Larger oxide particles were observed at the near surface, usually elongated and normal to the surface followed by uniform, continuous intergranular oxidation on grain boundaries, with small dispersed oxide particles around it them. The intergranular oxides grew to be become a network. This type was observed for the specimens with medium Si content 0.31% (Fig. 7-3c and 7-4 c), as shown in Fig. 7-11b.

Type 3 The larger oxide particles decreased in number relative to type 1 & 2 confined to the surface. It were evident in the internal oxidation zone that the thicker, uniform, continuous intergranular oxidation formed along grain boundaries with small dispersed oxide particles around them. The continuous oxides layer was observed and parallel to the surface, especial in the group of specimens A1- E1. This morphology was observed for specimens with high bulk Si content, Si > 0.31% (Fig. 7- 3, 7-4 d, e), as shown in Fig. 7-11c.

7. 3 Penetration Depth of the Internal Oxide

The penetration depth of the internal oxides from the interface between external oxide scale/external surface of matrix was measured on cross section image of the specimens with different Si content. Mean measured depth was plotted in Fig. 7-12 and Fig. 7-13. At the early carburising stage (the low temperature base process), the penetration depth of the internal oxides was slightly different for the different specimens, as shown in Fig. 7-12. The penetration depth of the internal oxides varied with different Si content for the range of 3.7-4.5 μm. However, after long cycle carburising, the penetration depth of the internal oxides for different specimens was quite different. The penetration depth of the internal oxides varied strongly with different Si content. It increased first with increasing Si content and then, reached a limiting point at which the penetration depth of the internal oxides reached a maximum value. The penetration depth of the internal oxides decreased with further increases in Si bulk content. In this work, the limiting point for silicon content was in the range of 0.19-0.31 %.

7.4 Area Fraction of the Internal Oxides

The area fraction of the internal oxides was calculated using cross sectional SEM images, the mean value is potted in Fig. 7-14. This clearly shows that the area fraction of the internal oxides in the internal oxidation zone increased as Si increased. The area fraction of the internal oxides increased sharply in the range 0.11-0.31% Si, and then, increased relatively slowly, associated with the spallation of the internal oxidation zone near the surface region. This is agreement with the morphology observation.

The area fraction of the internal oxides in the different oxidation depth layers is shown in Table 7-1. It clearly shows that in the outer layer near surface, the area fraction was approximately 0.35-0.40 in the specimens with low bulk Si content and was higher than the specimens with higher bulk Si. However, in the inner layer (intergranular oxidation zone), the area fraction of the internal oxides was increased with increasing Si content.

Table 7-1 Area fraction of the internal oxides in the specimens at different depths layer

specimens ID	Si mass%	outer zone		inner zone	
		area fraction (mean)	Distance from surface μm	area fraction (mean)	Distance from surface μm
A1-8	0.11	0.39	2.83	0.102	4.0
C1-8	0.31	0.417		0.128	
D1-8	0.56	0.265	2.18	0.227	3.71
E1-8	0.77	0.176	1.78	0.23	3.10

The results indicate that the effect of silicon on internal oxidation was small in the early carburising stage of the base process. However, after long cycle carbursing process, as the Si content increased, more intergranular oxidation occurred, whilst the penetration depth of the internal oxides decreased. Therefore, it was concluded that the influence of silicon on the internal oxidation was not only on the penetration depth and population density but also on the morphology of the internal oxidation zone.

7.5 Microhardness

The microhardness through the case into the core was measured for all the specimens carburised in procedure 1, as shown in Fig. 7-15. All the specimens showed that microhardness was low in the surface region exhibiting the internal oxidation. The microhardness of the surface region relative to the internal oxidation zone was also measured for those specimens, as shown in Fig.7-16. The microhardness of three specimens with Si content of 0.11%, 0.31%, 0.77% were compared in Fig. 7-17 and Fig. 7-18. There was a tendency for the higher bulk Si specimens to have a higher hardness and the lower bulk Si content specimens to have a lower hardness in the case layer, up to 0.5mm below the surface. However, at a depth of over 0.5mm, these were a tendency for the lowest silicon specimen to show the highest hardness and high silicon specimen the lowest hardness. The microhardness in surface region of the internal oxidation zone, high silicon specimen show low hardness. Comparing the case depth to 550 HK_{100} for all the specimens, as shown in Fig. 7-19, the results show a decrease with increasing of silicon, with the depth approximately 2.0mm for the specimen with 0.11% Si, decreasing to 1.5mm for the specimen with 0.77%Si.

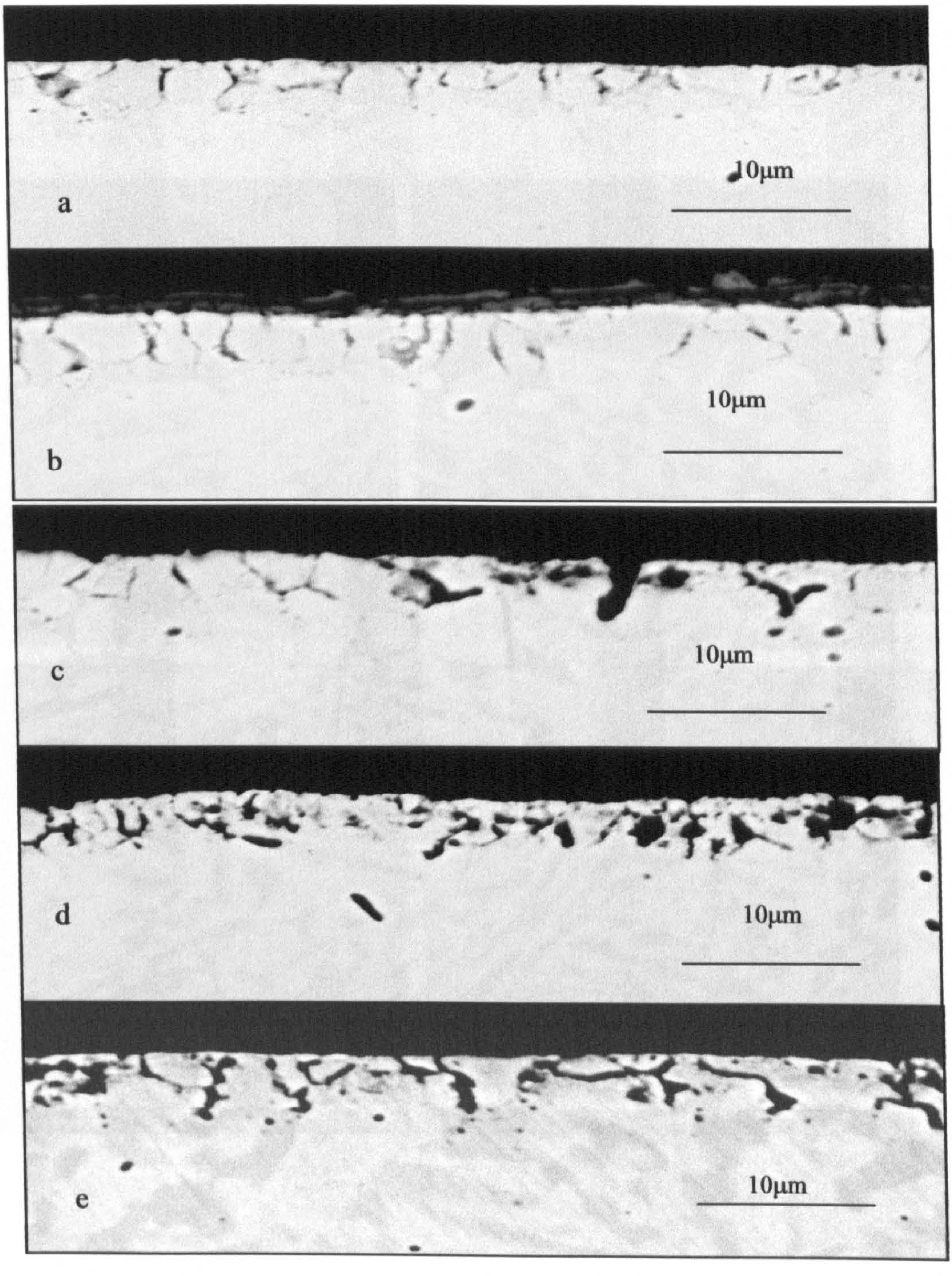

Fig. 7-1 Morphology of the internal oxidation zone in the specimens with different Si content, carburised at procedure 1. 2.0h a) 0.11%Si,b) 0.19%Si, c) 0.31%Si, d)0.56%Si, e) 0.77% Si.

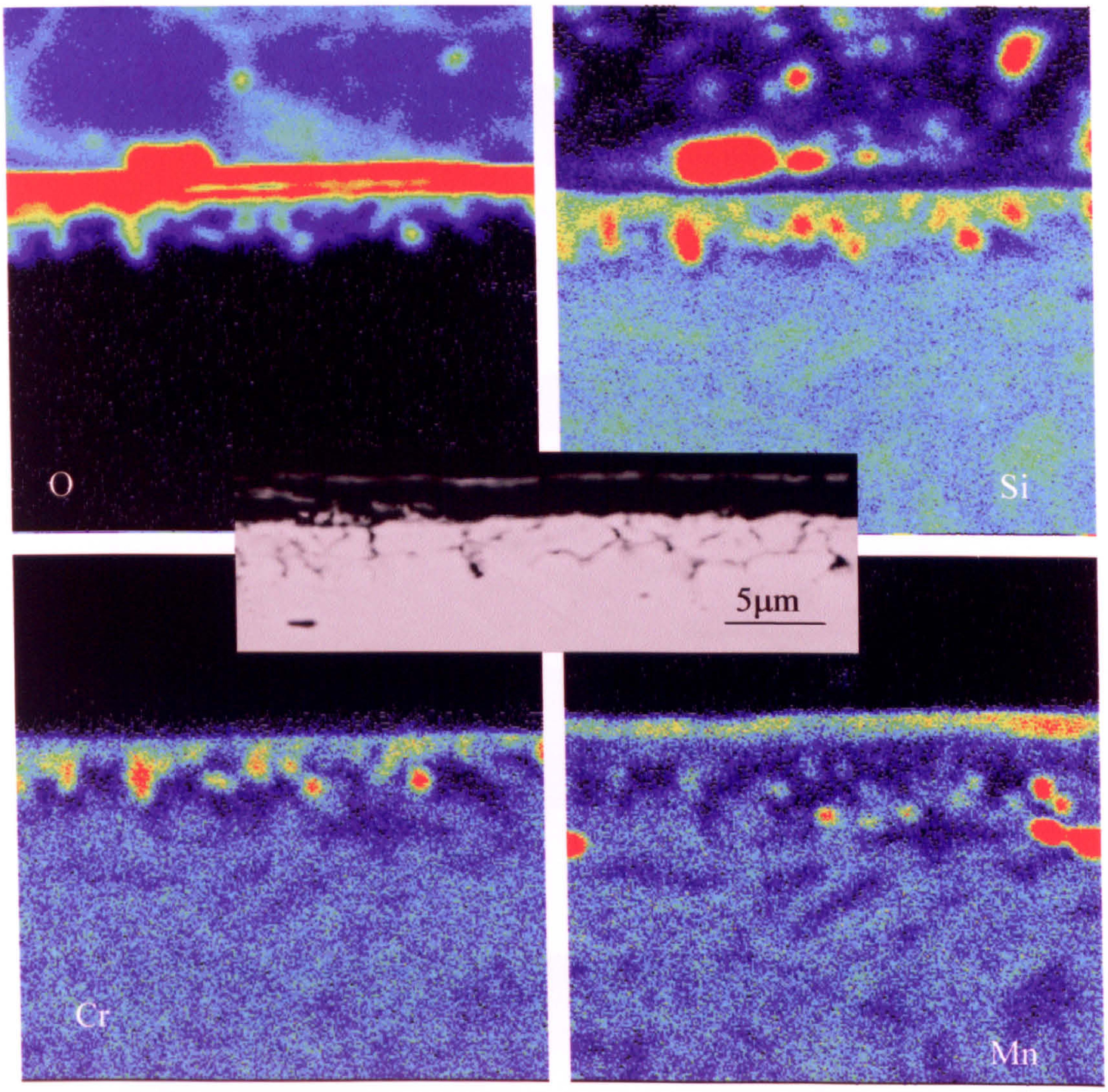

Fig. 7-2 Cr, Mn and Si were rich in the internal oxidation after 2h heating in the specimen D1-4 carburised at procedure 1

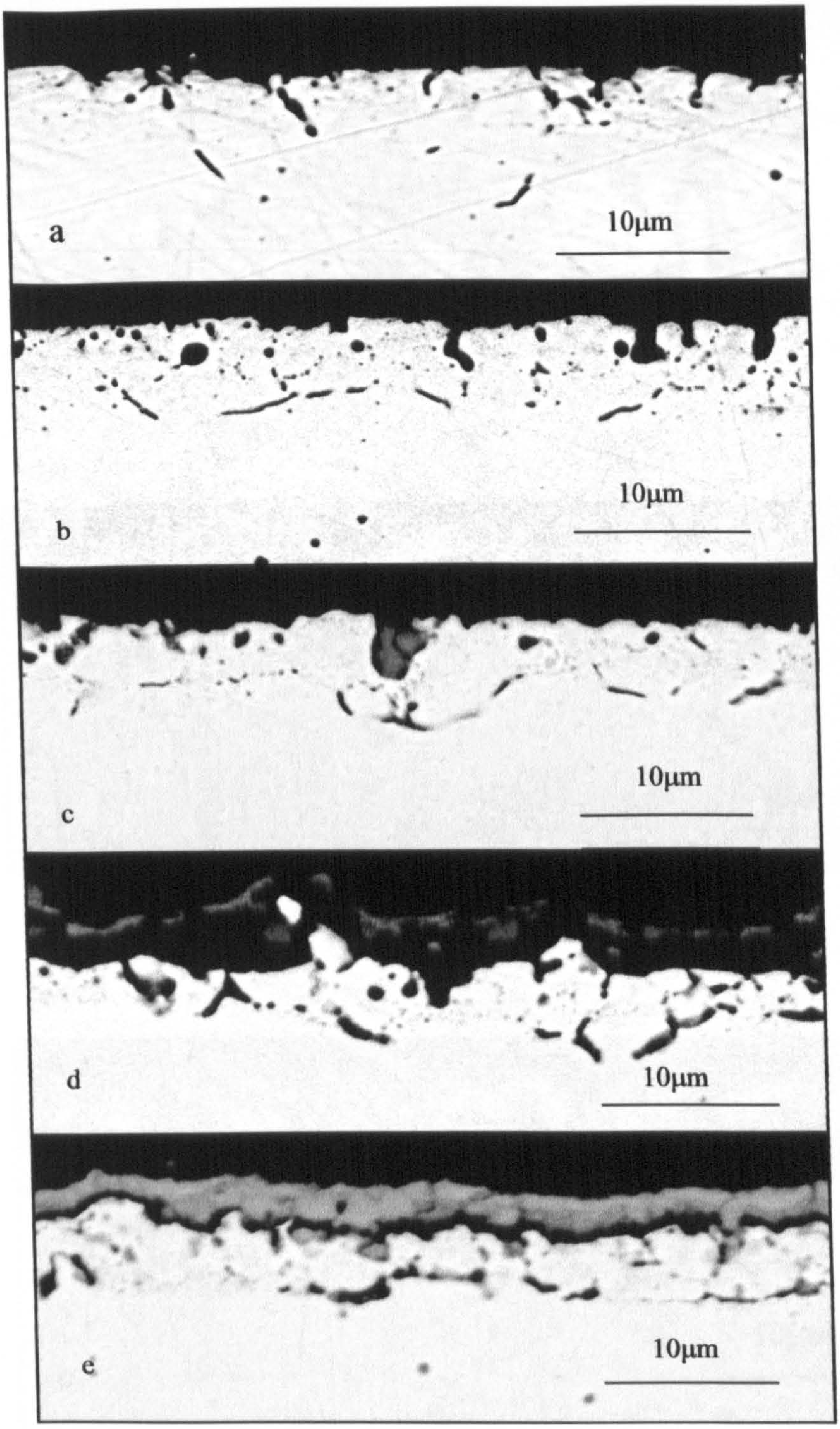

Fig. 7-3 Morphology of the internal oxidation zone in specimens with different Si content, carburised at procedure 1. 16.6h. a) 0.11%Si, b) 0.19%Si, c) 0.31%Si, d)0.56%Si, e) 0.77% Si.

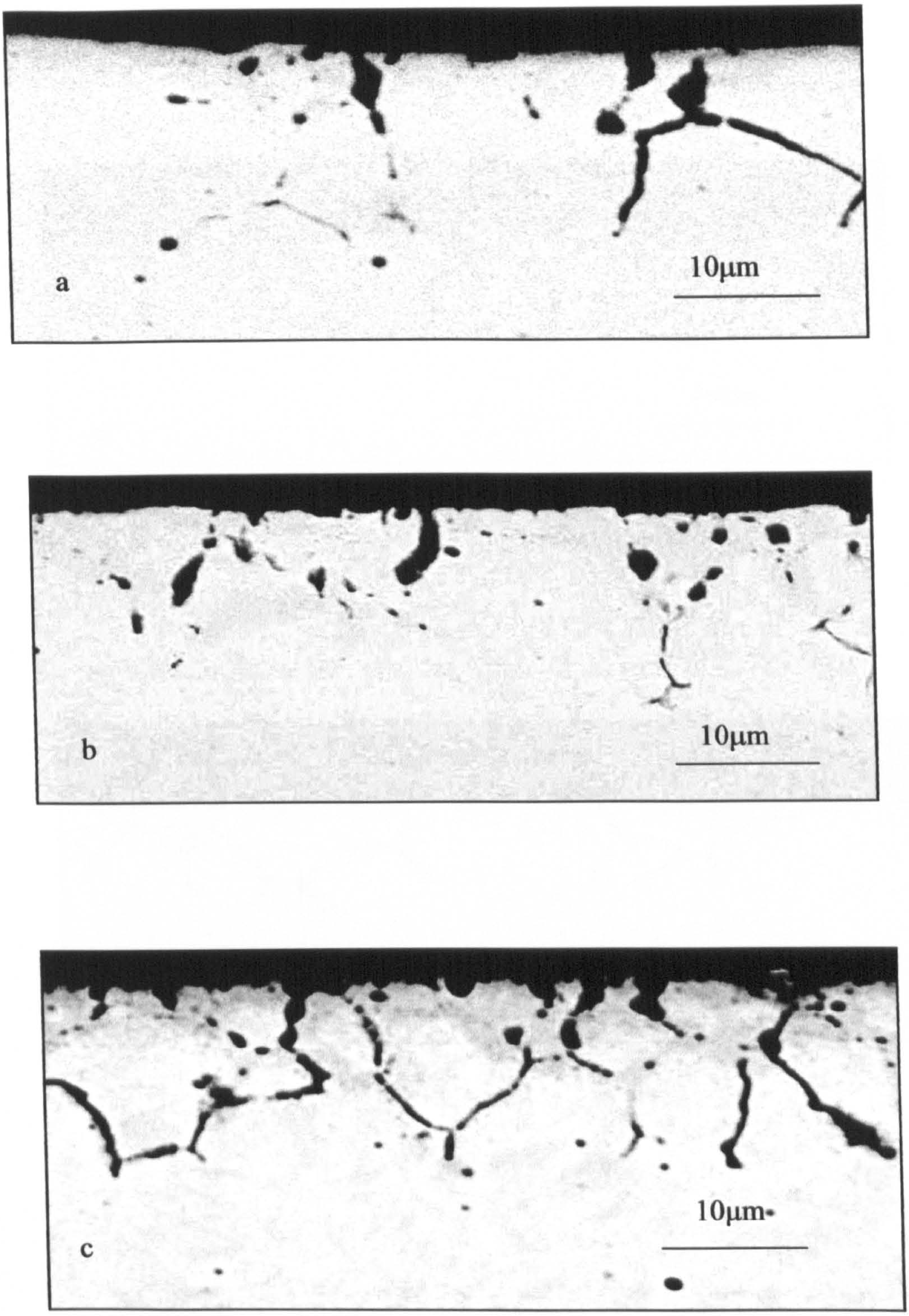

Fig. 7-4 Morphology of the internal oxidation zone in specimens with different Si content, carburised using procedure 5 (Volve), a) 0.11%Si, b) 0.19 %Si, c) 0.31%Si, d) 0.56%Si, e) 0.77% Si.

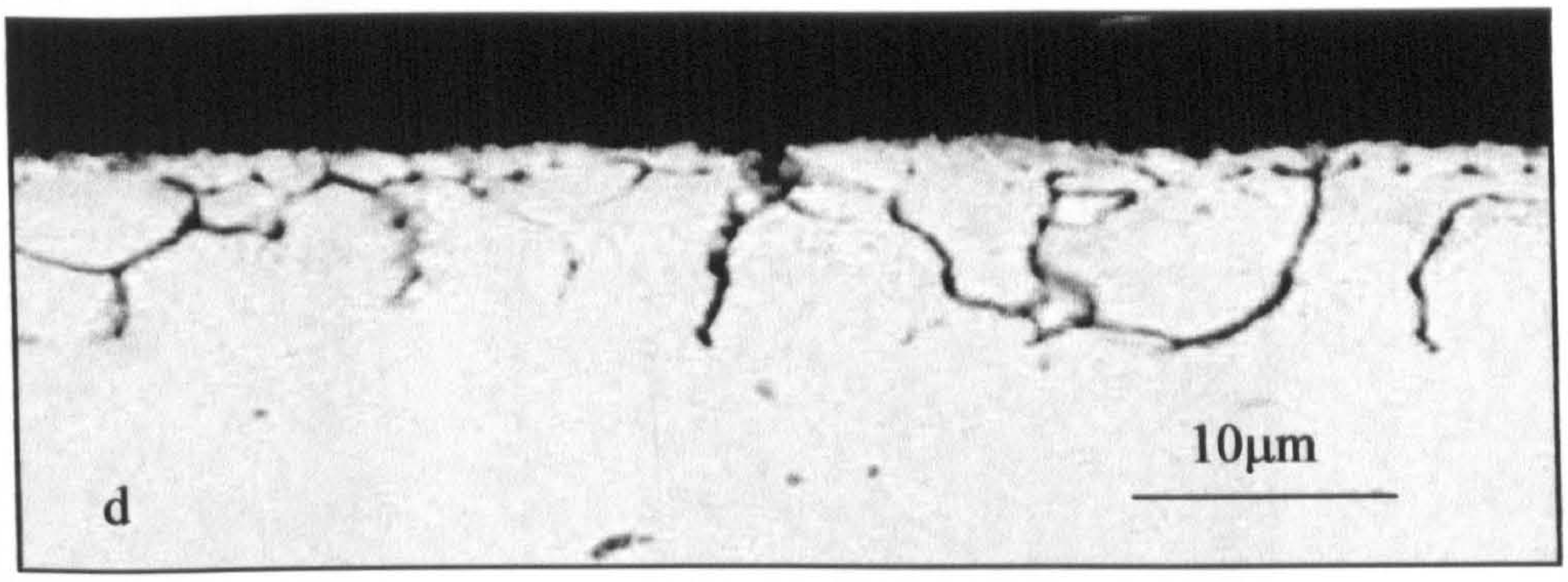

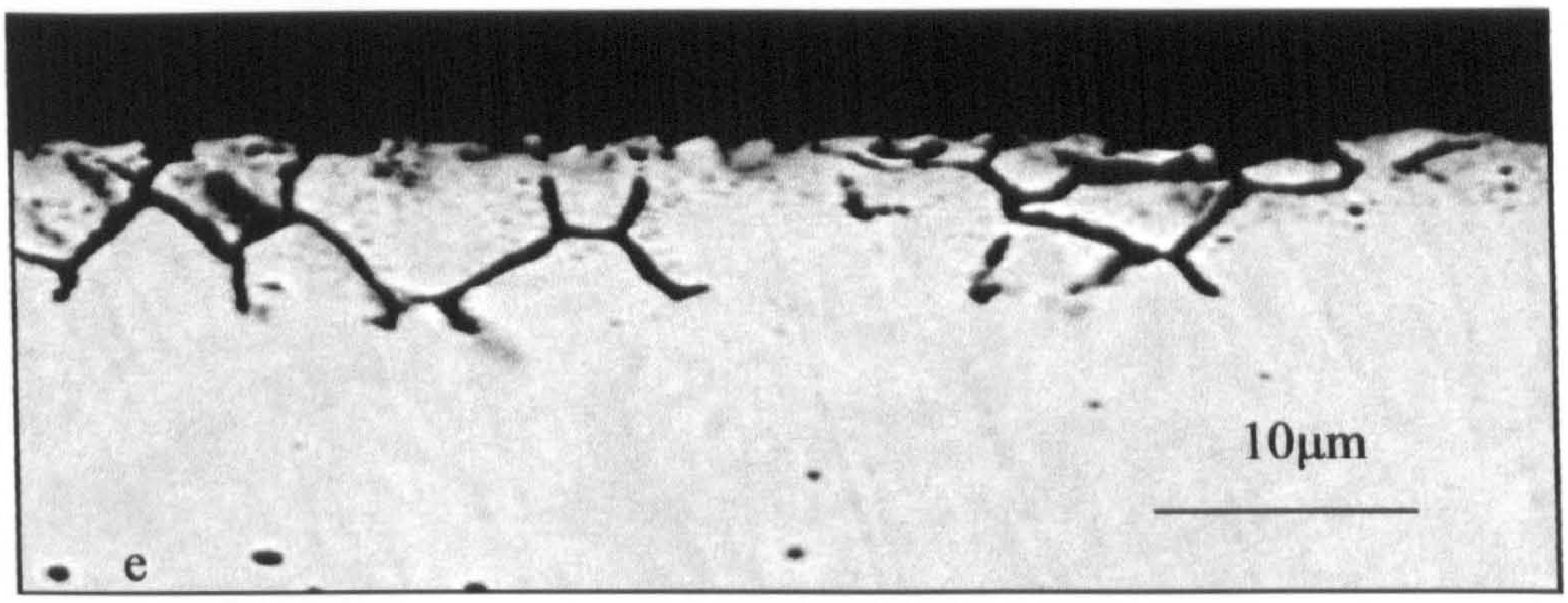

Fig.7-4 Morphology of the internal oxidation zone in specimens with different Si content, carburised using procedure 5 (Volve) a. 0.11%Si, b. 0.19 %Si, c. 0.31%Si, d.0.56%Si, e. 0.77% Si.

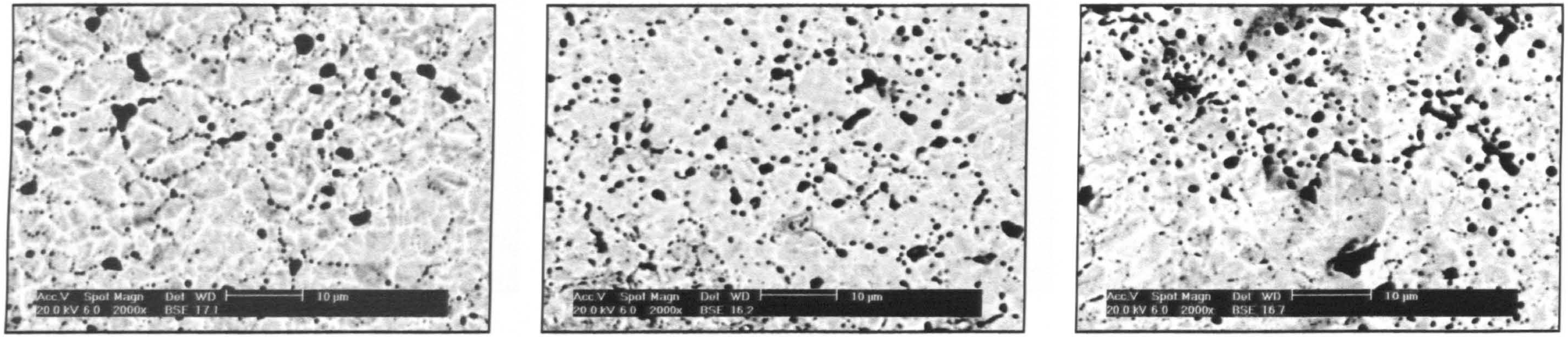

a. A1-8 depth 2.63µm

b. B1-8 depth 1.90µm

c. C1-8 depth 2.10µm

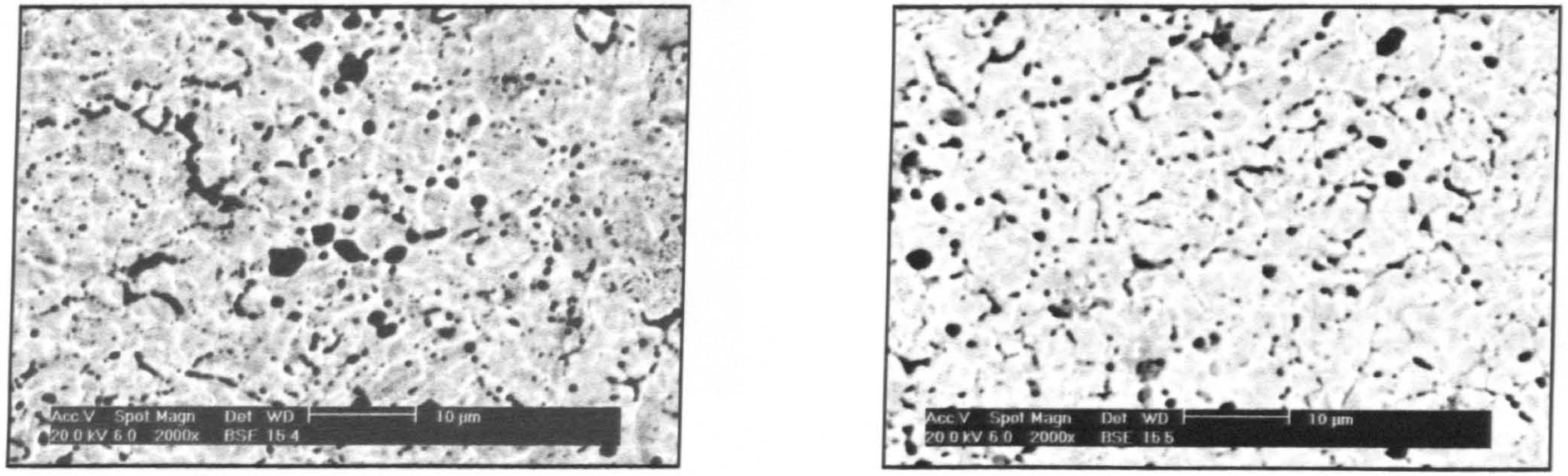

d. D1-8 depth 2.63µm

e . E1-8 depth 1.5µm

Fig. 7-5 Surface topography of the internal oxidation in depth layer related with outer layer zone in the specimens with different Si bulk content

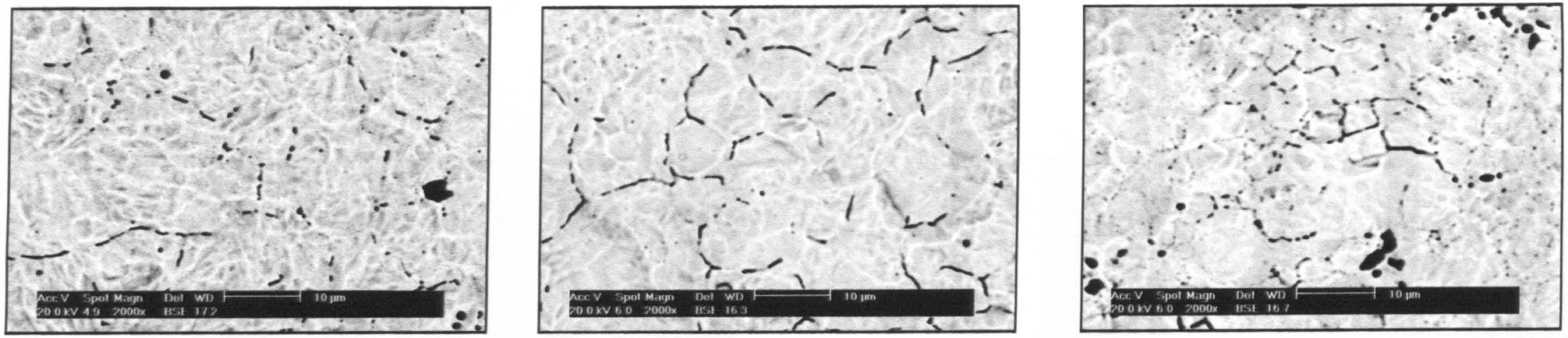

a A1-8 depth 5.9 µm

b B1-8 depth 5.3µm

c C1-8 depth 3.32µm

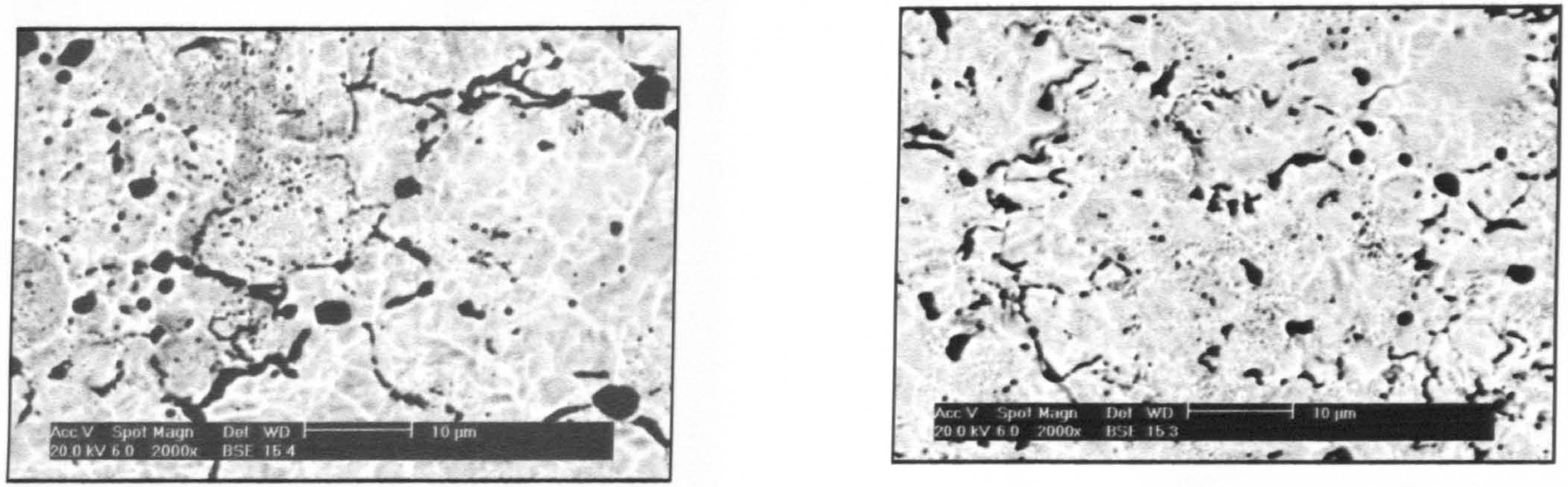

d D1-8 depth 3.8µm

e E1-8 depth 2.9µm

Fig. 7-6 Surface topography of the internal oxidation in depth related with inner layer zone in the specimens with different Si bulk content

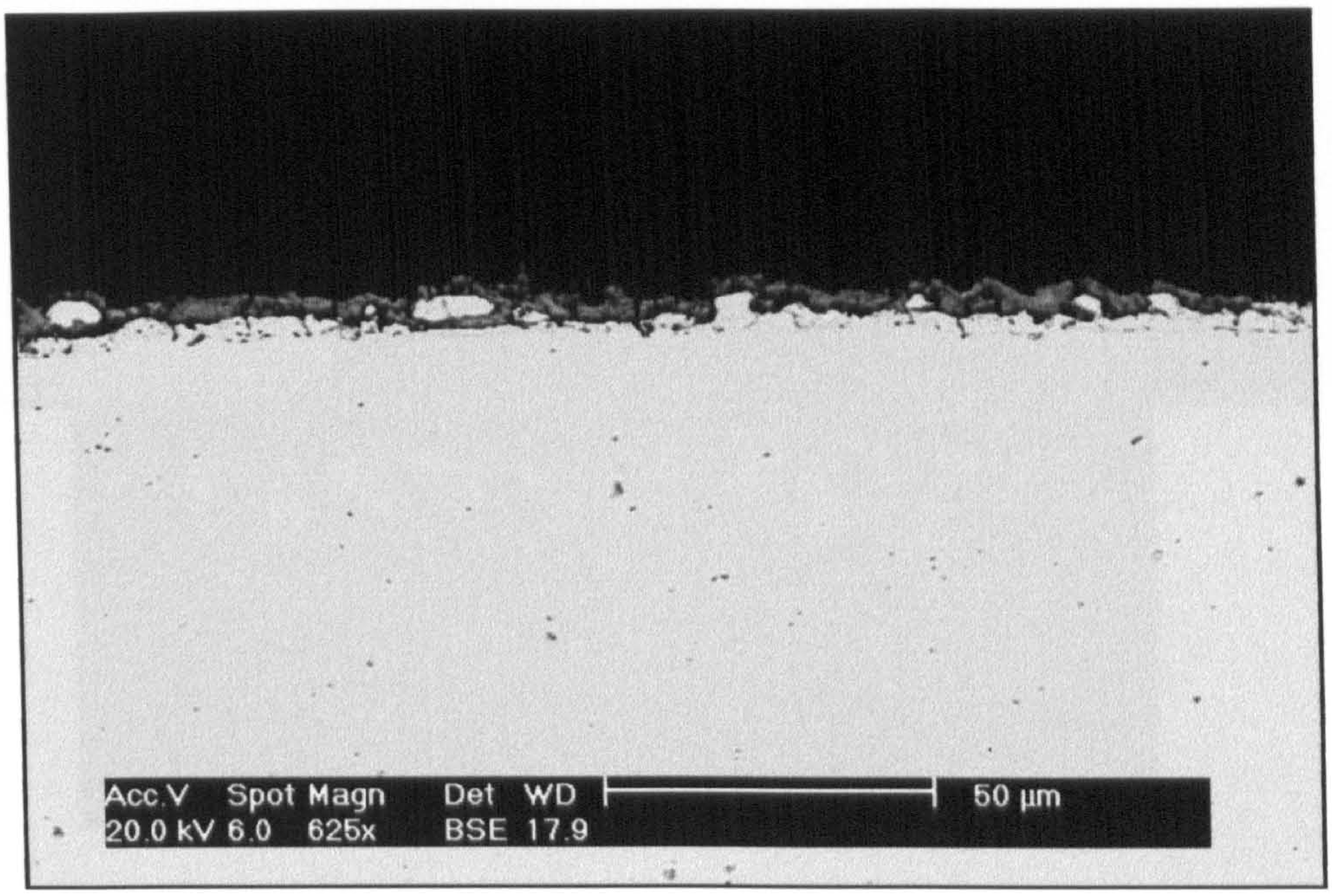

Fig. 7-7 The dented layer in the specimen with high Si content (E1-8,0.77%Si).

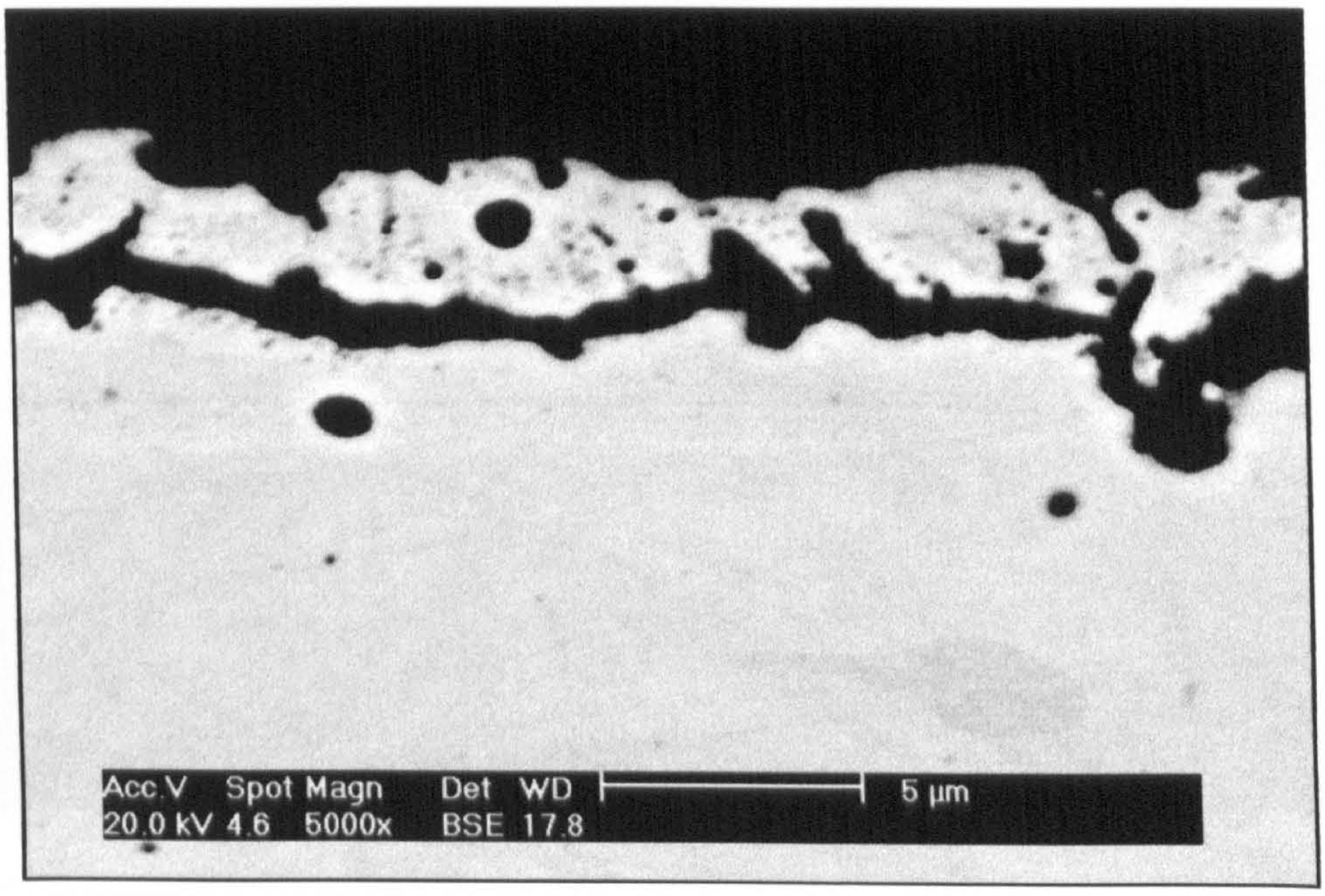

Fig. 7-8 A contiguous layer in the specimen with high Si content (E1-7, 0.77%Si).

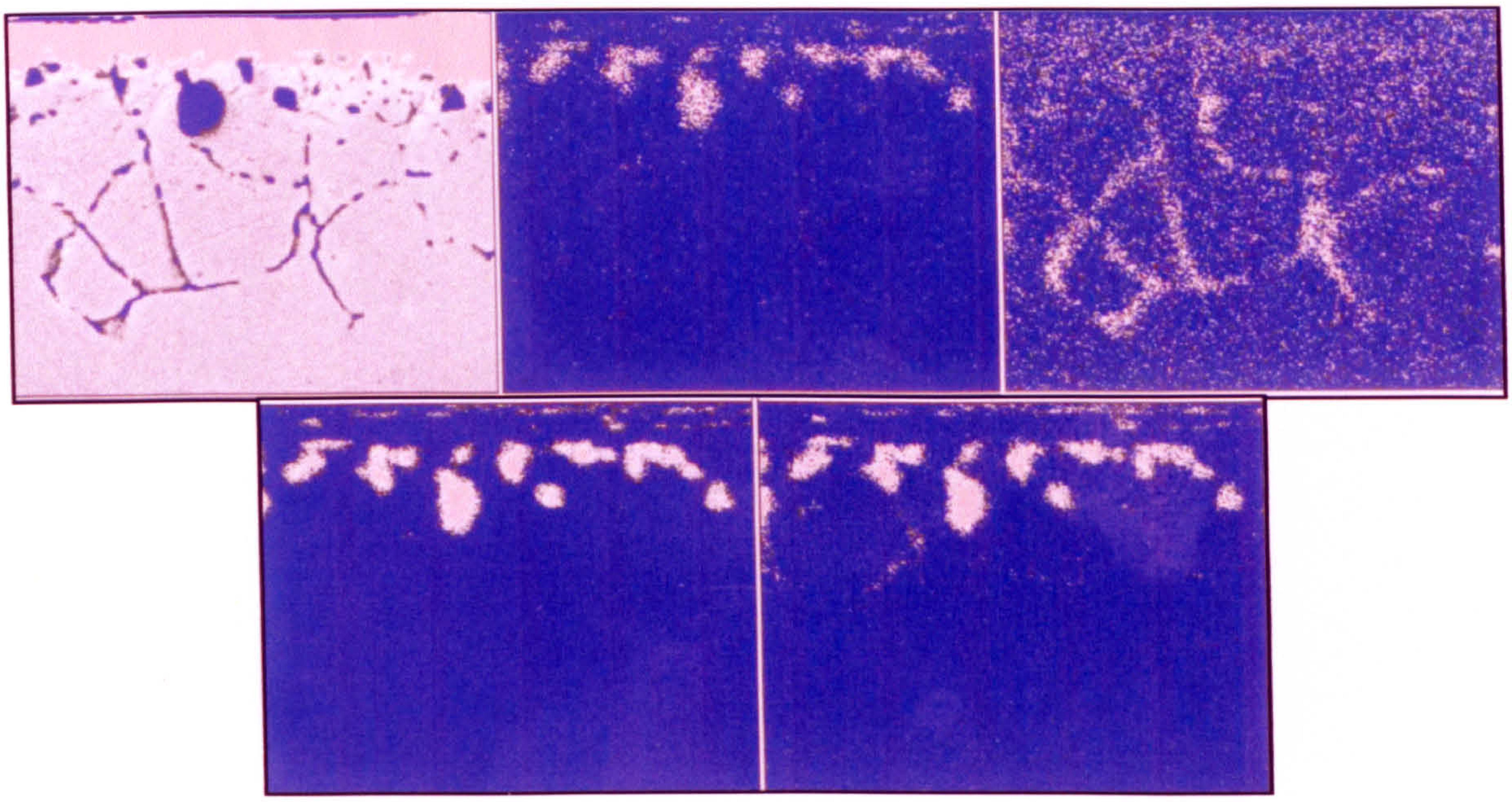

Fig. 7-9 Elemental distribution in the internal oxidation zone of the specimen C5 (0.31%Si) carburised at the procedure 5

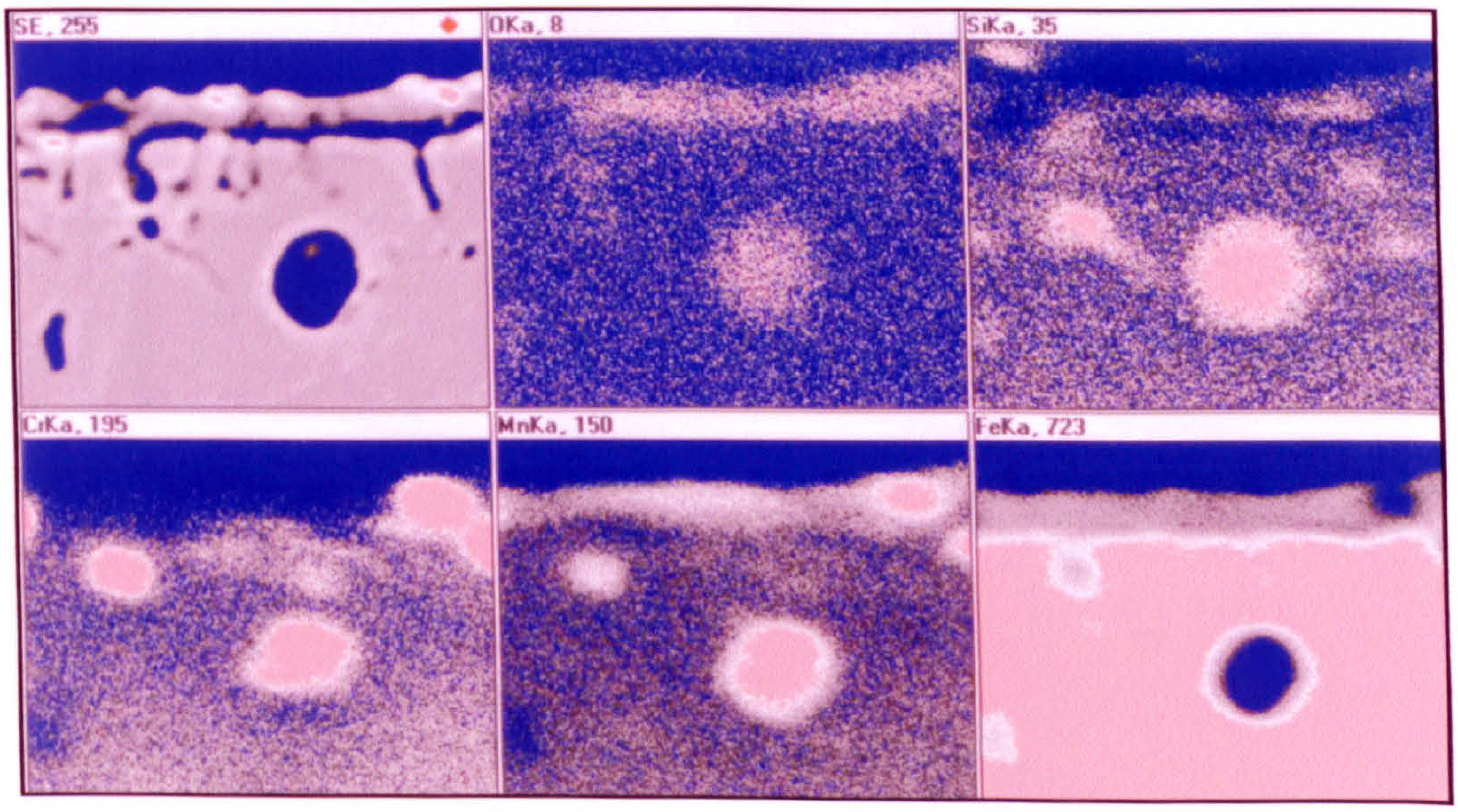

Fig. 7-10 Elemental distribution in the internal oxidation zone of the specimen E1-8 (0.77%Si) carburised at the procedure 1 for 16.6 h.

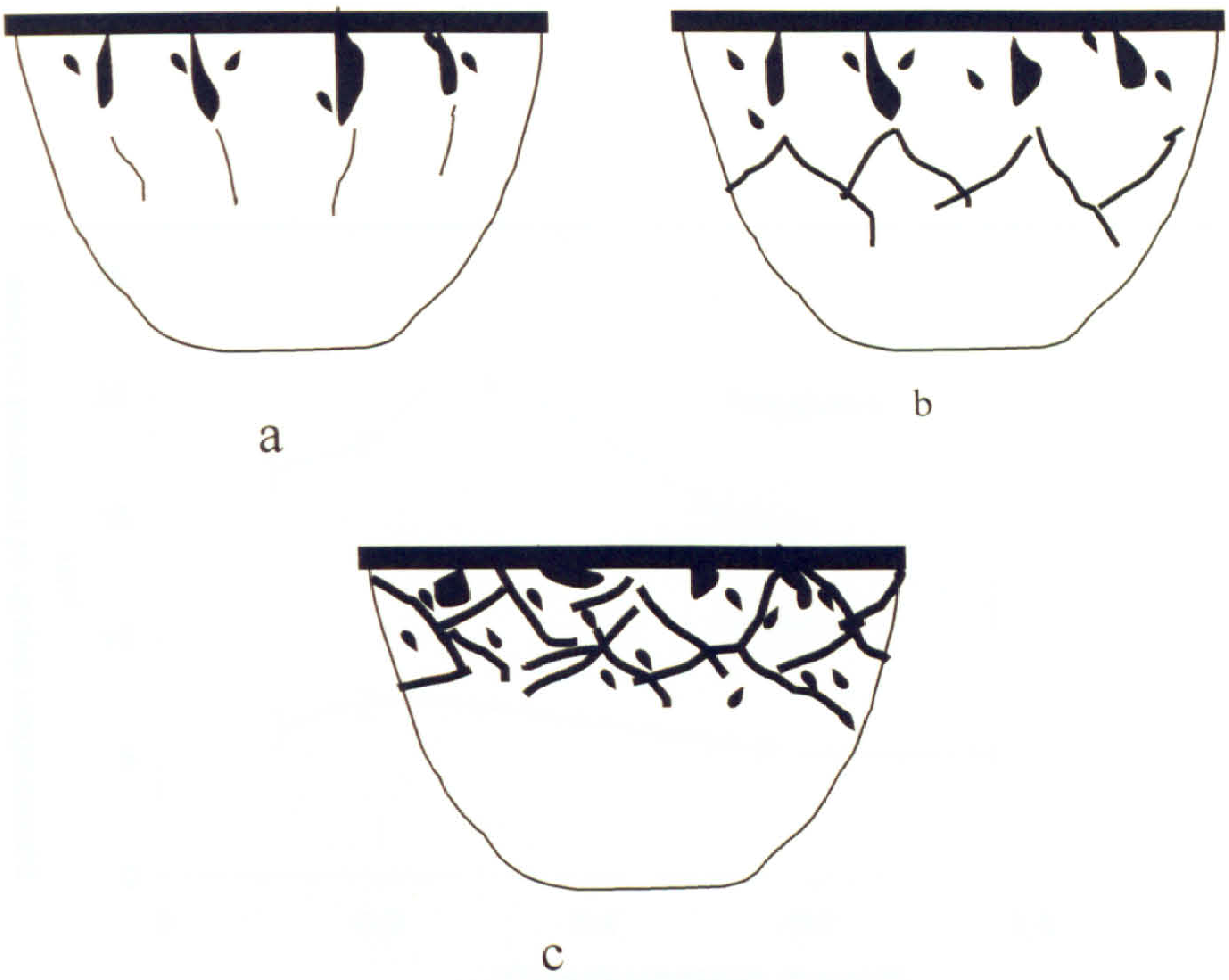

Fig. 7-11 Three type of morphology of the internal oxidation zone

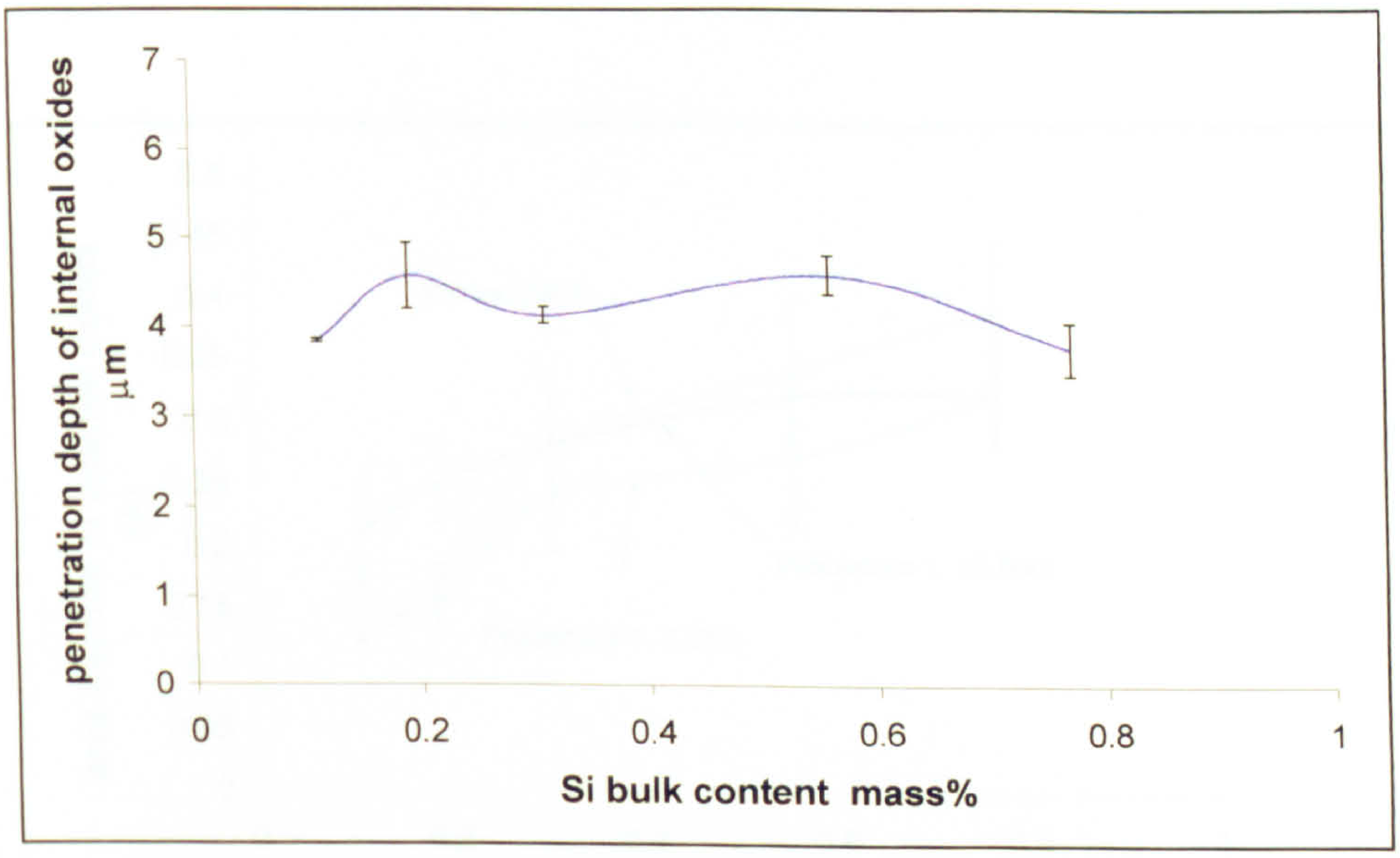

Fig. 7-12 Effect of Si on the penetration depth of internal oxide (IO) in the early stage of the carburising process

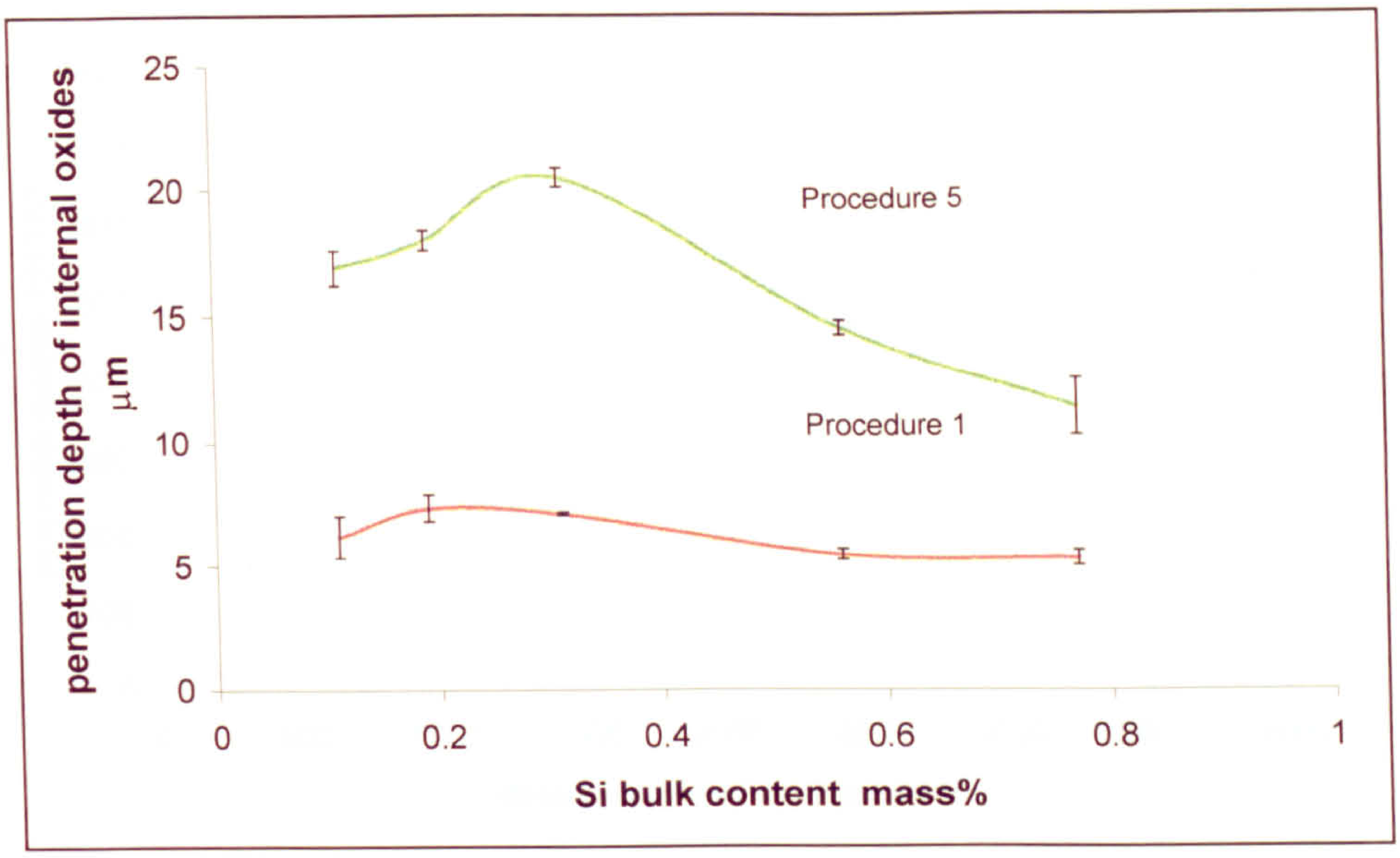

Fig .7-13 Penetration depth of the internal oxides and Si content

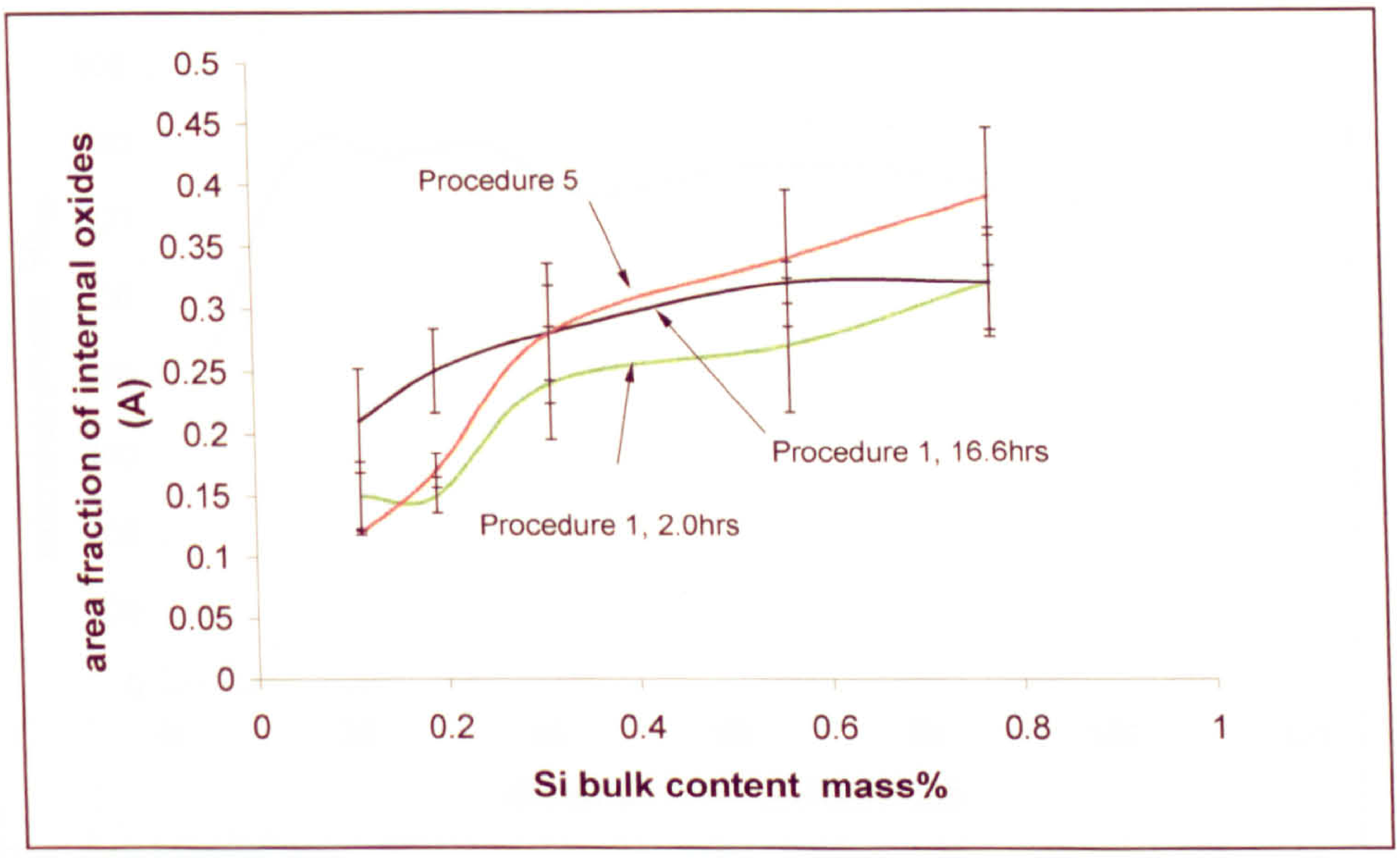

Fig .7-14 Effect of Si content on the area fraction of the internal oxides (I O) in the internal oxidation zone (IOZ)

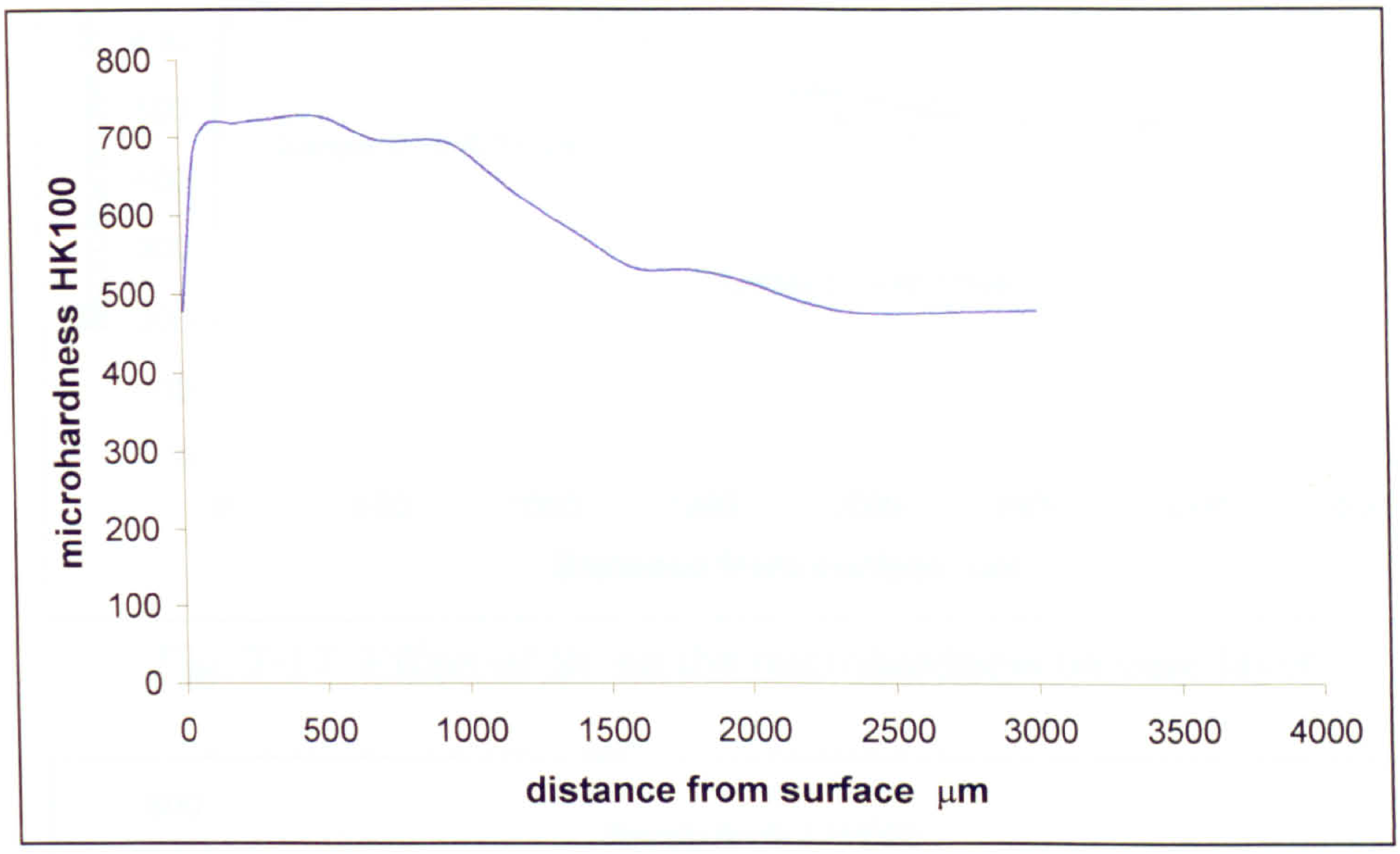

Fig. 7-15 The microharness in case layer of the specimens B1-8 carburised using the procedure 1

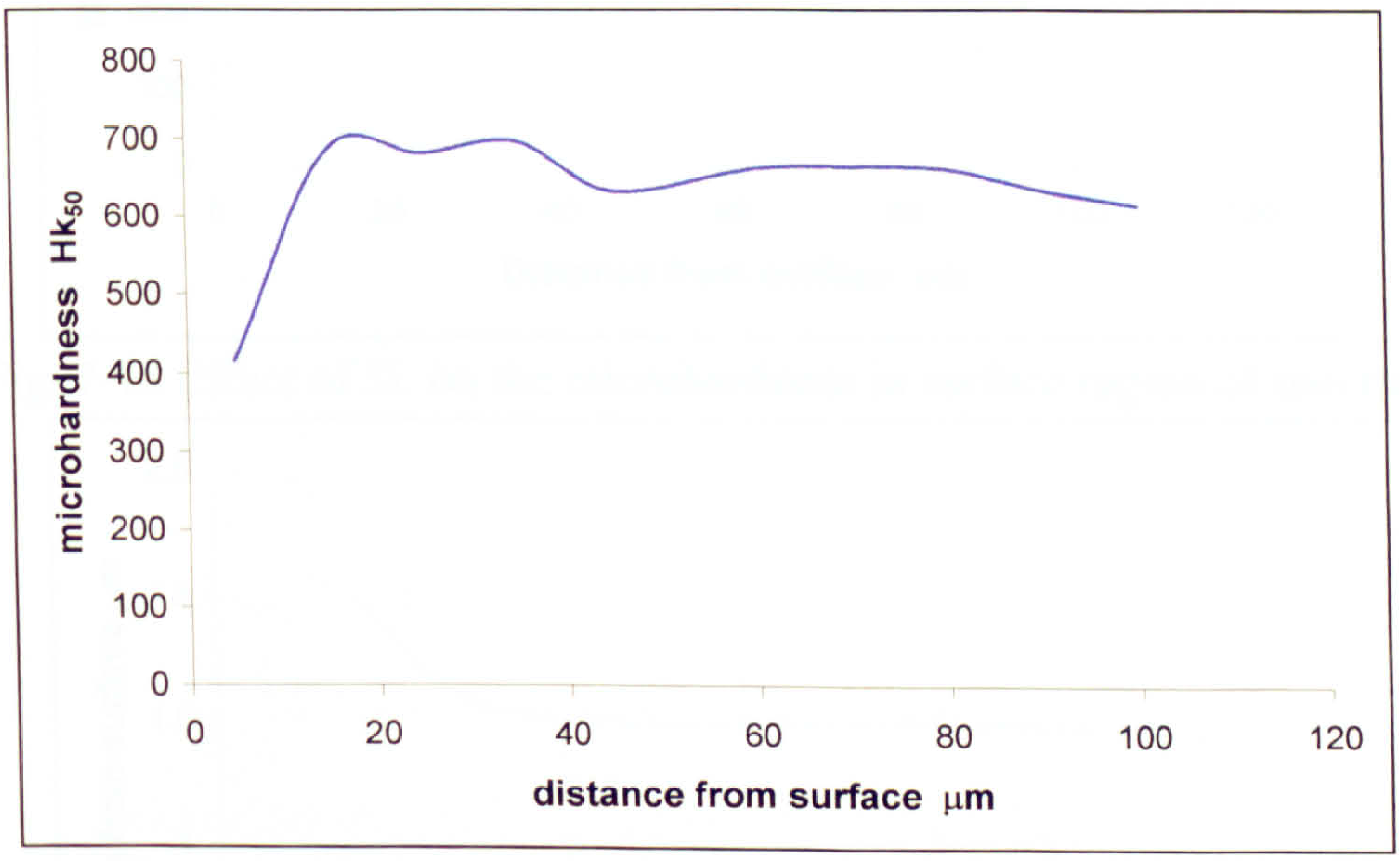

Fig. 7-16 Microharness in surface region of the internal oxidation zone in the specimens B1-8 carburised using the procedure 1

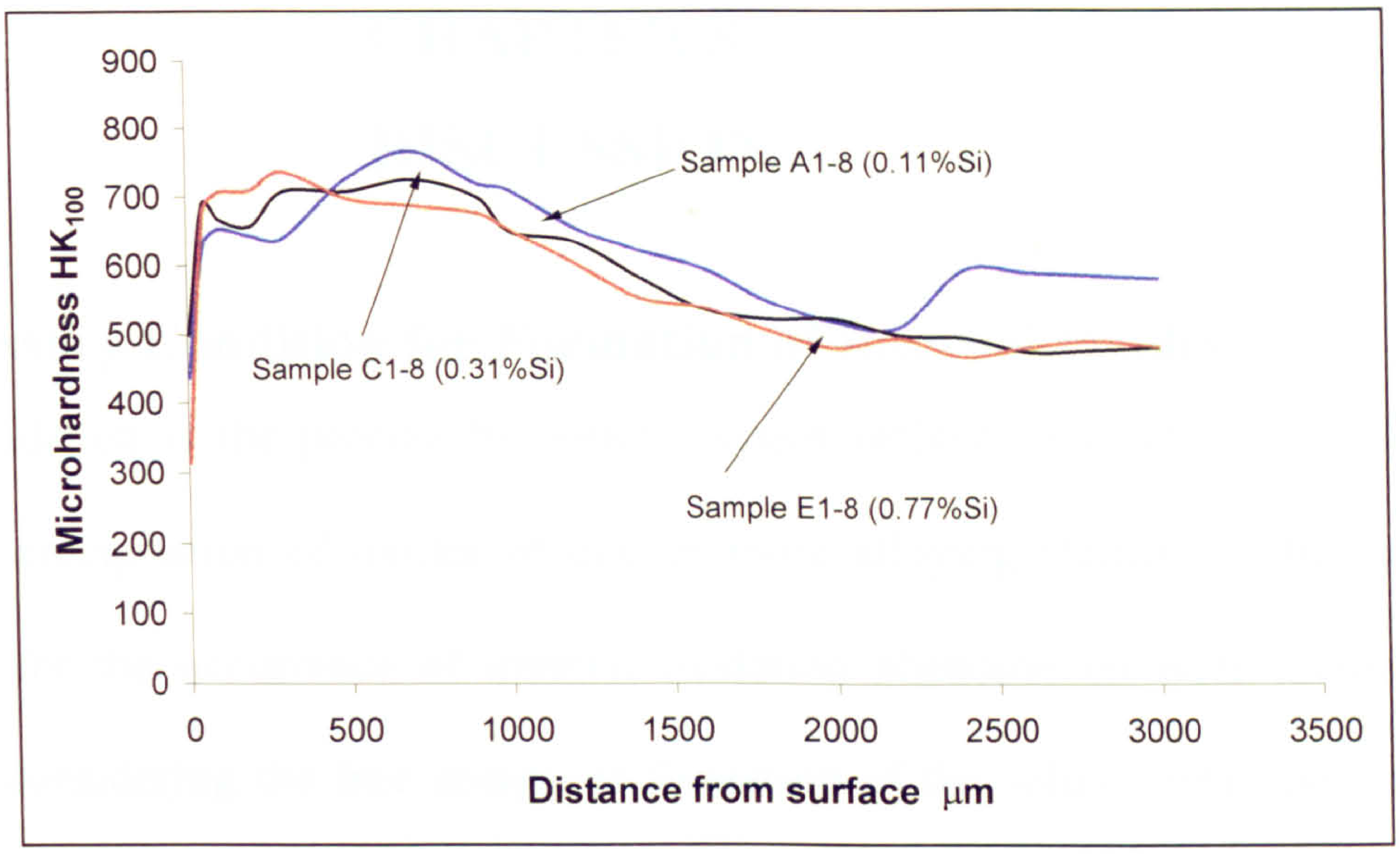

Fig. 7-17 Effect of Si on the microhardness on case layer

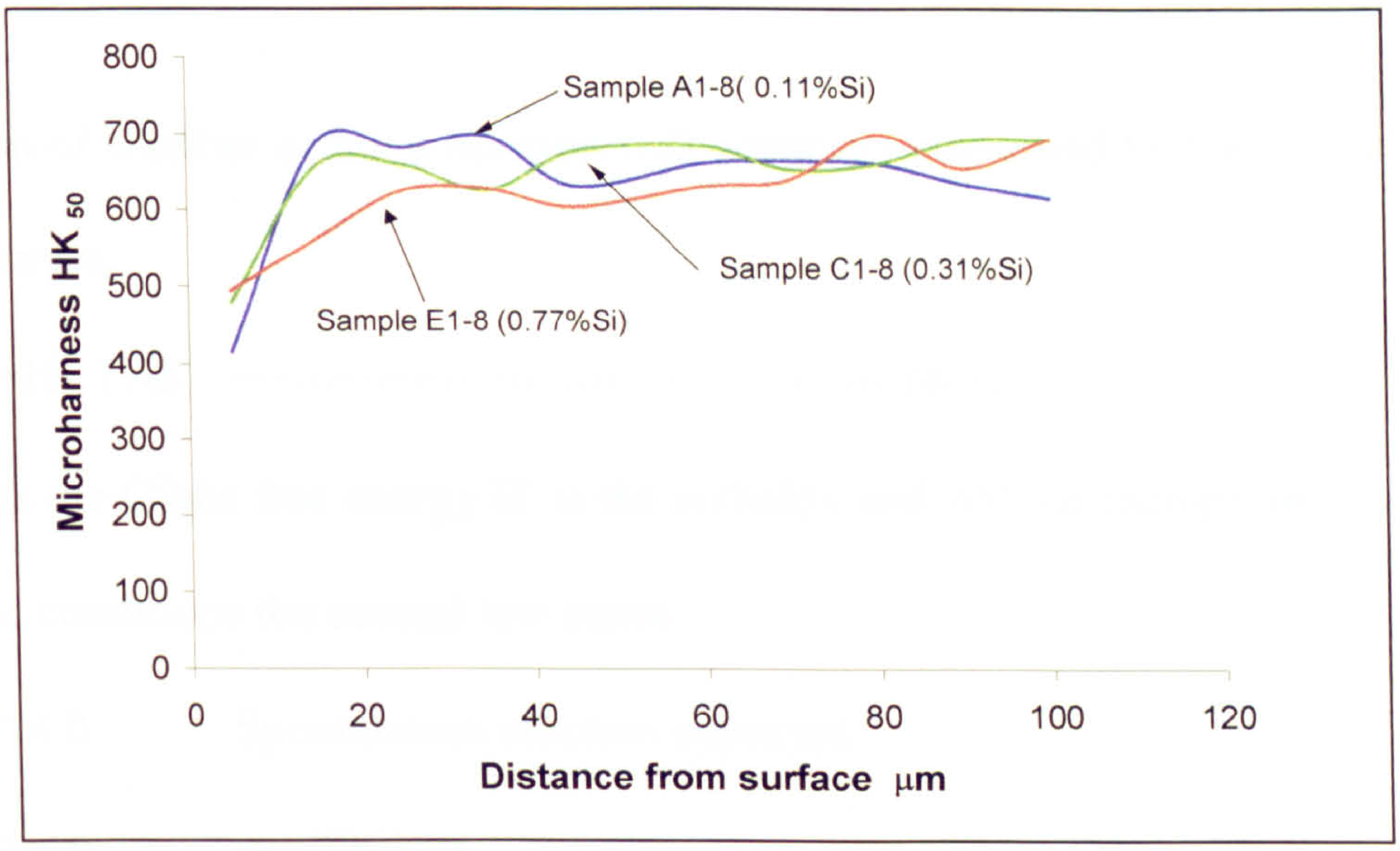

Fig. 7-18 Effect of Si on the microhardness in surface region of specimens

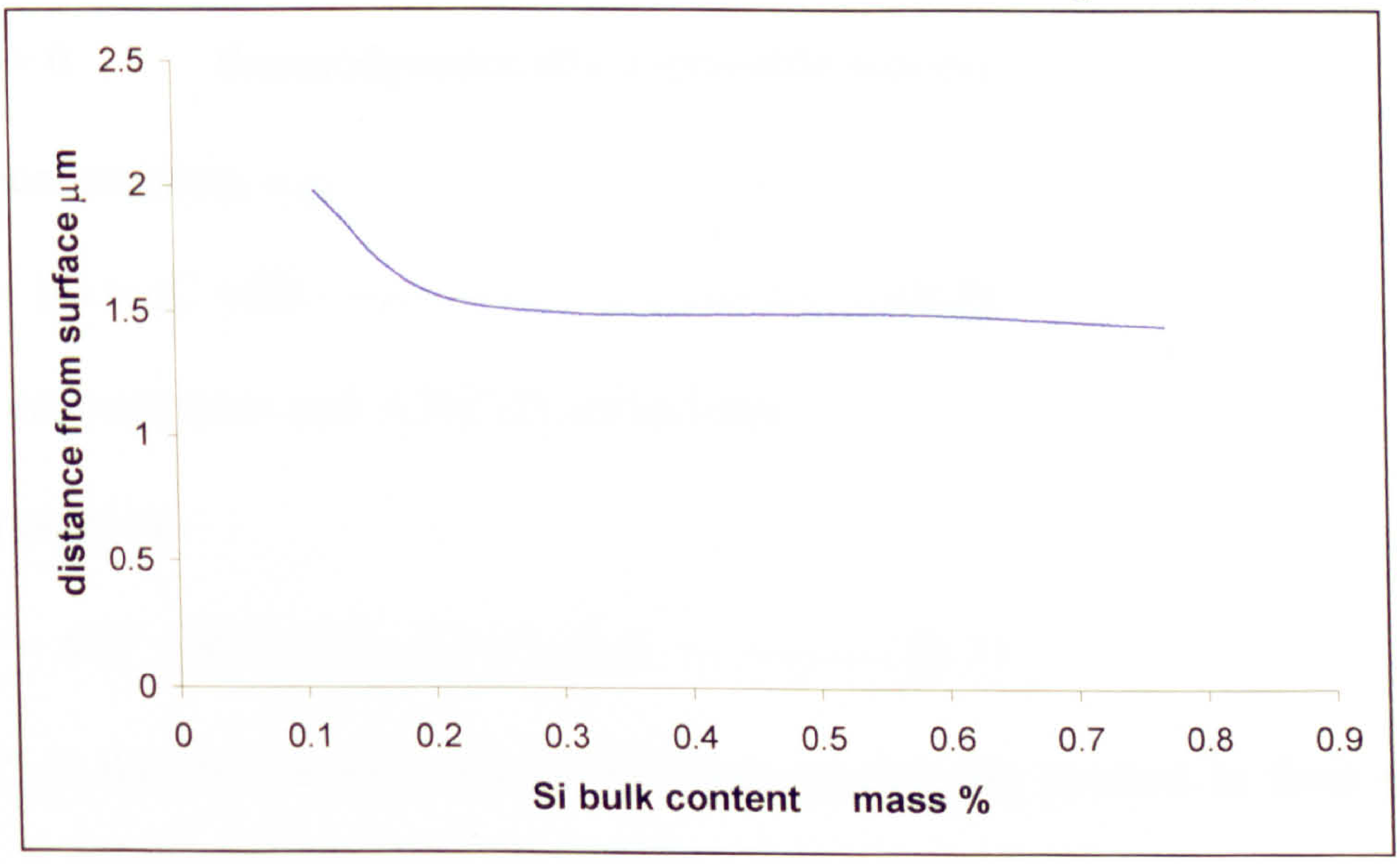

Fig. 7-19 Distance from surface at Microhardness 550HK$_{100}$

CHAPTER 8

DISCUSSION

8.1 Necessary Condition for Formation of Internal Oxides

Internal oxidation is the process by which oxygen diffuses into an alloy and causes subsurface precipitation of oxides of one or more alloying elements. The necessary conditions for the occurrence of internal oxidation phenomenon were mentioned in Chapter 2 considering the free energy of formation of the solute metal oxides, solute concentration and diffusion rate.

The question of whether or not a reaction will occur is determined by the second law of thermodynamics.

$$G' = H' - T\Delta S' \text{ ------------------------------------(8-1)}$$

Where, G' is the Gibbs free energy H' is the enthalpy and ΔS' the entropy of the system. Under these conditions the second law states:

$\Delta G' < 0$ Spontaneous reaction expected

$\Delta G' = 0$ equilibrium

$\Delta G' > 0$ thermodynamically impossible process

For a chemical reaction, e.g.

$$aA + bB = cC + dD \text{ ---------------------------------(8-2)}$$

a, b,c,d are concentration and A,B,C,D are species

ΔG' is expressed as

$$\Delta G' = \Delta G^{\circ} + RT \ln (a^c_C\, a^d_D / a^a_A\, a^b_B) \text{ ------------ (8-3)}$$

Where ΔG° is the free energy change when all species are present in their standard states and a^x_y is the thermodynamic activity which describes the deviation from the standard state for a given species.

For the special case of equilibrium (ΔG' = 0), equation 8-3 reduces to

$$\Delta G^{\circ} = -RT\ln (a^{c}_{C}\, a^{d}_{D} / a^{a}_{A}\, a^{b}_{B})_{eq} \text{ ----------------- } (8\text{-}4)$$

The equilibrium state of a system at constant temperature and pressure is characterised by a minimum in the Gibbs free energy of the system. For complex gas – solid reactions, standard free energies of formation of the various compounds are normally used to estimate the relationship between the composition of the atmosphere and the stability of condensed phases. The Ellingham diagram is usually used to compare the relative stability of each compound in certain temperature and atmospheric conditions, as shown in Fig. 8-1. In these diagrams, the free energy (ΔG) is expressed as kilojoules per mole O_2 so the stability of various oxides may be compared directly. Therefore, knowing the Gibbs standard free energy of oxide formation at a given temperature, we can readily calculate the oxygen partial pressure required for oxidation to occur and allow the oxygen pressure for oxide formation at any required temperature to be determined directly. The lower the position of the line on the diagram, the more stable is the oxide. The more negative ΔG, the more easier it is to form oxides. According to the thermodynamic date, the free energy for the solute elements oxides, such as Cr, Mn, Si have more negatives free energies than the base metal oxide, such as iron oxide. Therefore, the alloy elements in the steel have a higher affinity for oxygen than iron and the base metal iron has a solubility and diffusivity for oxygen which is sufficient to establish the required activity of dissolved oxygen at the reaction front.

Gas carburising is normally carried out at in the temperature range of 900-950°C, using an endothermic carrier gas generated by the controlled combustion of another gas (such as natural gas) with air in the presence of a catalyst at a high temperature. The endothermic atmosphere has a typical composition of 40% H, 20% CO, 0.46% CH_4,

Fig. 8-1 The Ellingham diagram for metallurgical important oxides (ref. Davaid R Gaskell 1973)

0.27% CO_2 and 0.77% H_2O with a balance of nitrogen. The balance of the component gases ensured that the atmosphere was endothermic for the steel for carburising state. However, for those alloying elements in solid solution in the steel that have a greater affinity for oxygen than Fe does, such as Si, Mn Cr and Al, the atmosphere is potentially oxidising. The free energies of formation for these alloy elements oxides were much more negative than the free energy for formation of iron oxide. The alloying element content of the steel was lower than that required for the transition from internal oxidation to external oxidation. Therefore, internal oxidation in steel has occurred during the gas carburising process, even for very short heating times when the atmosphere condition is satisfactory. This was confirmed in the specimen heating 0.25h, as shown in Fig. 4-1a.

8.2 Internal Oxidation Process during the Gas Carburising Process

8.2.1 Oxygen Partial Pressure and Oxidised Alloy Elements

Oxygen partial pressure determines the extent to which the metal and oxide coexist and will determine the equilibrium between metal and metal oxide.

$$M + O_2 \rightarrow MO_2 \text{ ---------------------------------- } (8\text{-}5)$$

If the activities of M and MO_2 are taken as unity. Unitary then equation 8.4 may be used to express the oxygen partial pressure at which the metal and oxide coexist .i.e.

$$P_{O_2}^{M/MO_2} = \exp\frac{\Delta G^\circ}{RT} \text{ ---------------------------- } (8\text{-}6)$$

Where, M is solute metal or alloy element; MO_2 is oxide,

$P_{O_2}^{M/MO_2}$ is oxygen partial pressure in case of form MO_2 oxide.

ΔG^o: The free energy change when all species are present in their standard state.

T: Absolute temperature

R: Gas constant

a: Thermodynamic activity which describes the deviation from the standard state for a given species,

In considering alloy oxidation, the activity of the metal and oxide must also be taken into account, i.e.

$$p_{O_2}^{eq} = \frac{a_{MO_2}}{a_m} \exp\frac{\Delta G^\circ}{RT} = \frac{a_{MO_2}}{a_M} p_{O_2}^{M/MO_2} \text{ ------------ } (8\text{-}7)$$

The values of $p_{O_2}^{M/MO_2}$ may be obtained directly from the oxygen nomograph on the Ellingham diagram. During the commercial carburising process, it was calculated using the equation (Stickels 1991):

$E = KT \log (P_{O2} / 0.209)$ ---------------------------- (8-8)

where, K is the constant, 0.000049593; P_{O2} is oxygen partial pressure; E is measured value of the oxygen probe in system, emf, as voltage output.

Table 3-2 gives the oxygen partial pressure in the different heating stages present in the carbursing process. It shows that the highest oxygen partial pressure in the atmosphere during the gas carburising process was 2×10^{-19} atm at 930°C in the high temperature base process. In the boost process, it was 2×10^{-20} atm, however, the lowest oxygen partial pressure was recorded at 800°C which was the low temperature base process, where the oxygen partial pressure was 2×10^{-21} atm.

Kozlovskii et al (1967) analysed internal oxidation of different elements during carburising in an endothermic atmosphere occurring for the following reactions:

$M + H_2O \leftrightarrow MO + H_2$ ------------------- (8-9)

$M + CO_2 \leftrightarrow MO + CO$ ------------------- (8-10)

The equilibrium constants of these reactions were determined by the ratio of partial pressure of the constitute gases:

$P_1 = P_{H2}/P_{H2O}$ ------------------------------ (8-11)

$P_2 = P_{CO}/P_{CO2}$ ------------------------------ (8-12)

According to the Kozlovskii et al's calculation, the values of the thermodynamic potential for oxidation reaction (8-9) and (8-10) during the heating of iron and various elements to the carburisaion temperature of 930°C were given in Fig. 2-3. This diagram shows that for the elements studied, Ti, Si, Mn and Cr are likely to be oxidised, whereas Fe W, Ni, Mo and Cu will be not oxidise. Ti has the highest oxidation potential of all elements. Among three elements Si, Mn and Cr, Si has highest oxidation potential, then Mn followed by Cr. In other words, Si can be oxidised at lower oxygen partial pressure than Mn and Cr. The free energy for formation of Si oxides is more negative than Mn and Cr. Aluminium appears to be slightly more ready to oxidise then does titanium. Kozlovskii et al did not calculate the oxidation potential of Al but Fairbank and Palethorpe (1966) took the calculation, as shown in Fig. 2-5.

Results in this work show that three elements Si, Cr and Mn, were enriched in the internal oxidation zone (Fig. 4-1), in agreement with expect theory. The oxidation potential of the different elements determined the oxidation reaction and resultant oxide structure composition. Therefore, different oxide phases were observed in this work, such as complex Cr-Mn oxides, Mn-Si oxides and Si oxides (Fig. 6-2 to 6-5). Al oxides were also observed (Fig. 6-6) as individual oxides or combined with Si, Mn and Cr to form complex oxides. This is in agreement with thermodynamic data (Fig. 8-1, Fairbank and Palethorpe 1966), the free energy for formation of Al oxides being more negative than Si.

8.2.2 Oxygen Diffusion Paths

Iron has a low solubility for oxygen and the diffusion of oxygen through the iron matrix is relatively slow (10^{-9} cm^2/s) (Parrish 1999). This explains the observation that the oxygen penetration in present work was only approximately 50μm. The oxygen was strongly enriched at the top surface of specimen, as shown in Fig. 5-1. It was observed that the penetration depth of oxygen was deeper than the depth of internal oxides, this probably being due that the low oxygen activity in this region within the materials.

Philibert (1999) has indicated that the diffusion path for oxygen in an alloy during oxidation can be controlled in number ways. It may be controlled by atomic transport of chemical species, including point defects; by diffusion through the reaction products, such as intermetallic compounds and oxides; by diffusion through the lattice as well as along grain boundaries; by diffusion on surfaces and at metal/oxide interface. In the case of the internal oxidation, oxygen diffusion is affected not only by the matrix lattice and grain boundaries but also by the oxide/matrix interface. Previous research (Stott 1984) indicated that the presence of the oxides particles may enhance or block the oxygen diffusion depending on shape and location of oxides. In other words, the effective flux of oxygen is influenced by the size, shape and orientation of the internal oxides. In the present study, diffusion paths of oxygen can be described as Fig. 8-2. The oxygen may diffuse along the grain boundary (path 1); through existing globular oxides/matrix interface (path 2); through the existing intergranular oxide/matrix interface (path 3); the oxygen diffusion may be limited by oxygen through the continuous oxides layer which is parallel to the surface of specimen (path 4).

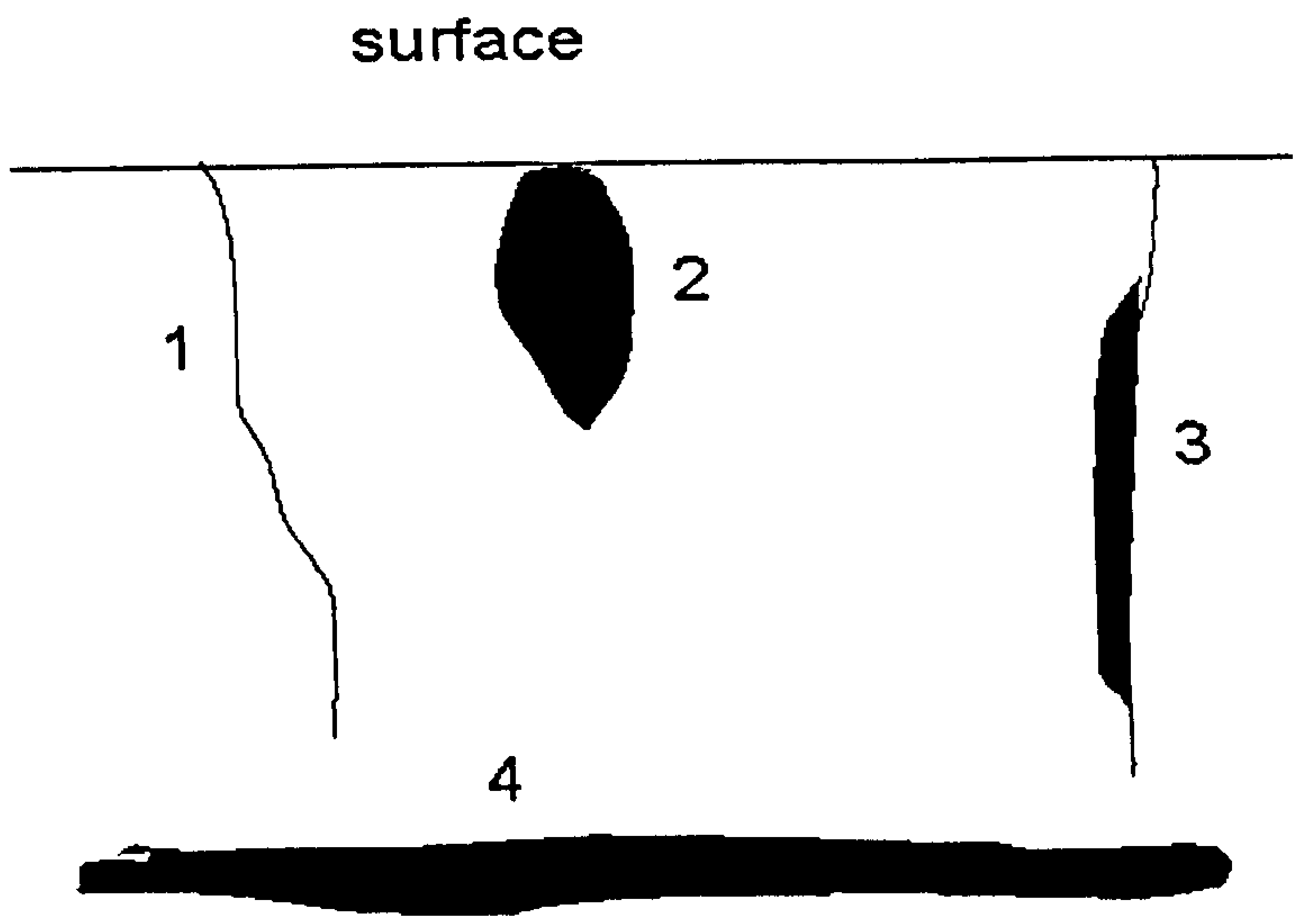

Fig. 8-2 The schematic diagram of diffusion paths of oxygen in internal oxidation of carburised steel. Path 1. grain boundary diffusion of [O]; Path 2, globular oxides/matrix interface diffusion of [O]; Path 3, intergranular oxides/matrix interface diffusion of [O]; Path 4, diffusion limit by [O] through the continuous oxides layer which is parallel to the surface

During the early heating stages uniform intergranular oxidation was observed in all the specimens. Oxygen diffusion was observed mainly along the grain boundaries (Fig. 8-2, path 1), the intergranular oxides were formed as thin films on grain boundaries which may in itself enhance the diffusion rate of oxygen into the materials as a sigle diffusion path is in replaced by two (Fig.8-2, path 3). Consequently, the higher oxygen flux region was introduced through the matrix lattices and grain boundaries. Larger global oxides were formed within grains as cubic and ellipsoid morphologies normal to the surface of specimen. In addition, small dispersed oxide particles grew around the larger oxides (Fig. 6-16) or adjacent to the larger oxide (Fig. 6-2). The presence of discrete small oxides particles around the larger oxides particles is evidence that suggests that the globular oxides provide easier diffusion paths for oxygen (Fig. 8-2, path 2) than the bulk metal lattice. Hence, this suggests that oxygen diffused not only through the matrix lattice but also along the metal/oxide interface.

The situation however, may be complicated since in some cases the existing oxides can block oxygen diffusion if internal oxides are continuous and parallel to the surface, because the low transport rate within the oxides enables them to act as an effective diffusion barrier. As was observed for the higher Si containing specimen, severe intergranular oxidation developed as a thick, continuous oxide layer in the internal oxidation zone (Fig. 7- 8). This arrested the inward diffusion of oxygen (Fig. 8-2, path 4) and as a result the penetration depth of internal oxides decreased whilst the density of the internal oxides in the near surface internal oxidation zone increased. The results in this work are in agreement with Stott's observation (1988). When the oxides grow as a continuous oxide layer parallel to the surface, the matrix/ oxides interfaces will block the oxygen diffusion. When the oxides grow in a rod-like morphology normal to the surface, the matrix/oxides interfaces will enhance the oxygen diffusion rate.

8.2.3 Growth Process of Internal Oxides

The schematic diagram of internal oxidation zone of carburised steel studied in this work is shown in Fig. 8-3, a porous surface continuous oxides layer and an internal oxidation zone. The internal oxidation zone divided into two-zones, an outer zone close to the surface which contained globular complex oxides elongated normal to the surface; an inner zone which contained intergranular oxides present as thin film on grain boundaries. Small dispersed oxide particles precipitated in both zones. The typical plan view schematic diagram of globular oxides and intergranular oxides are shown in Fig. 8-4.

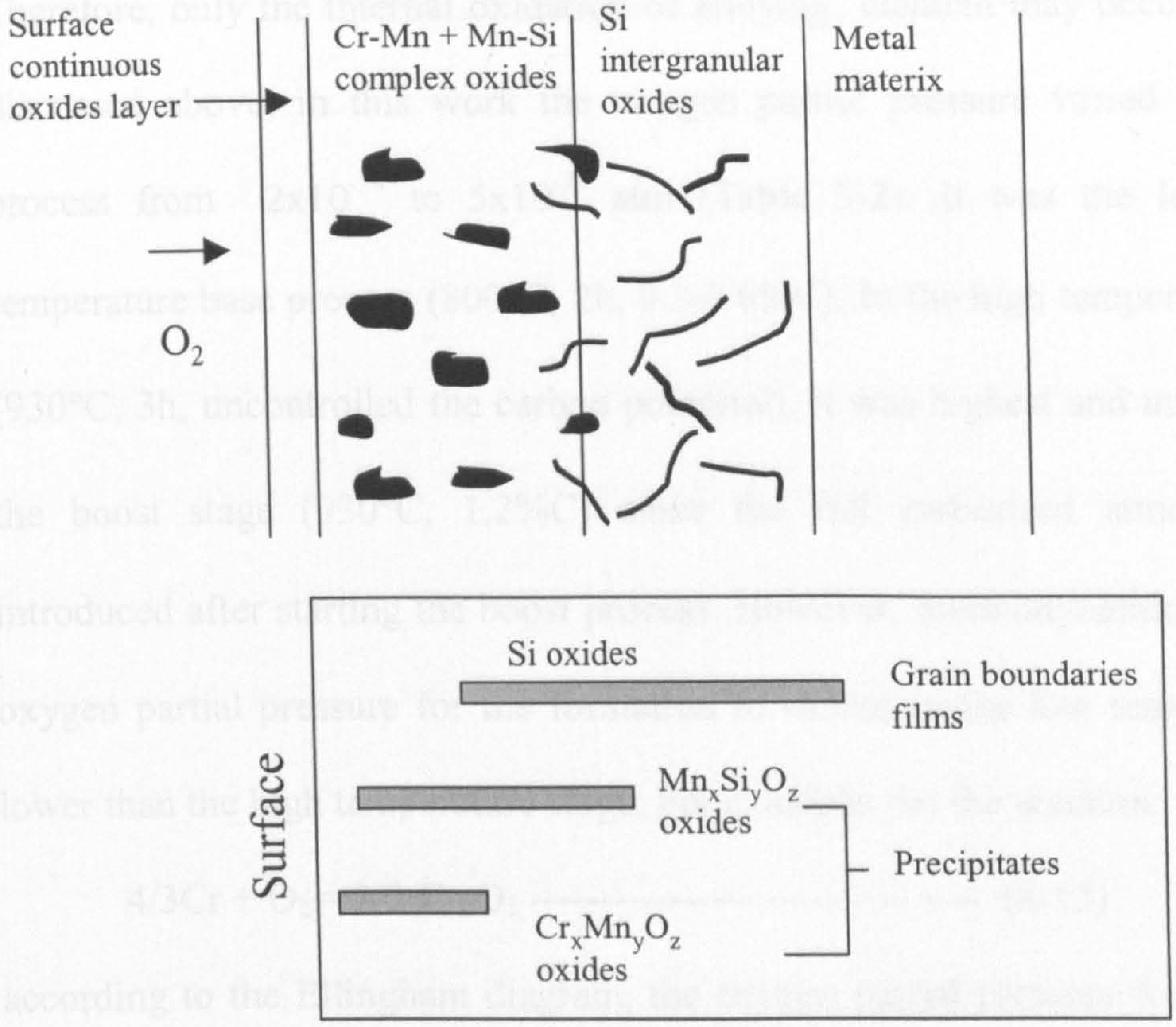

Fig. 8-3 Schematic diagram of internal oxidation of Cr-Mn-Ni Carburised steel.
a) Morphology of the internal oxidation zone; b) Distribution of internal oxides.

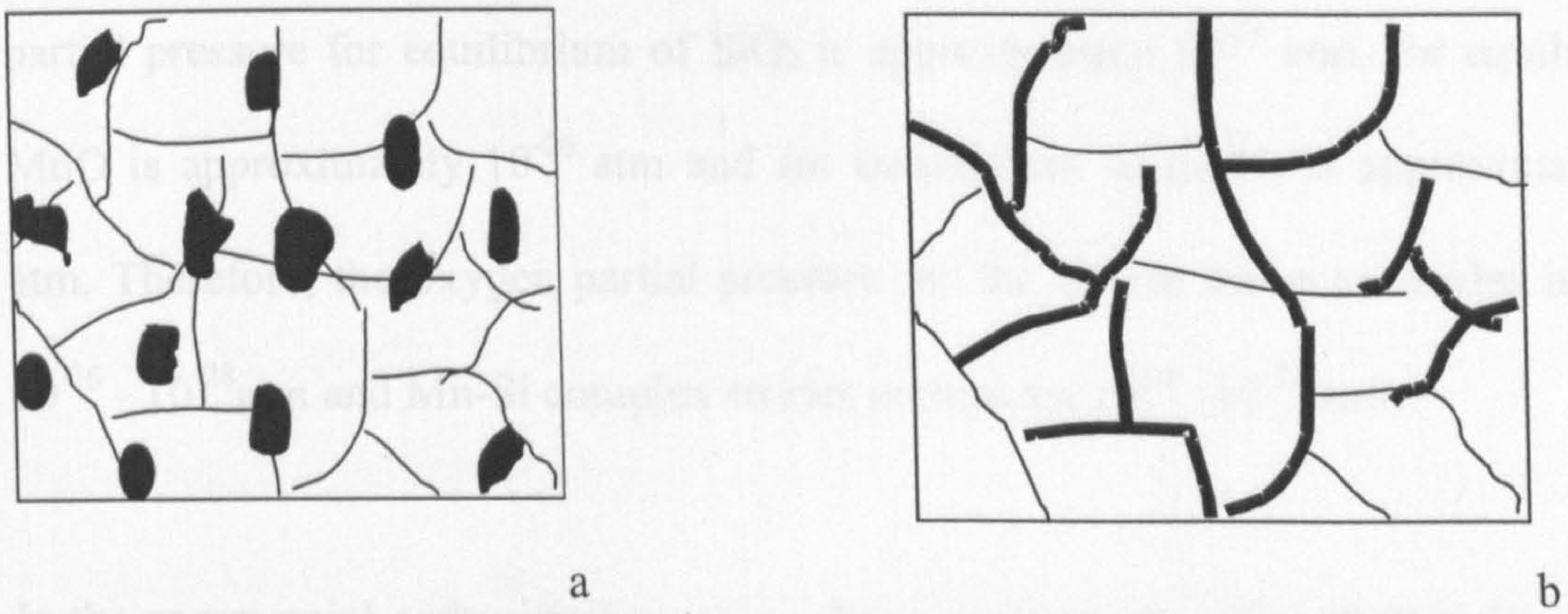

Fig.8-4 Morphology of two sort of the internal oxide precipitates.
a) Globular oxides
b) Intergranualr oxides

While the internal oxidation is driven by oxygen in the furnace atmosphere, the oxygen partial pressure differs with time during the process, making interpretation difficult, particularly in studies that simply examine the end result. Usually, the equilibrium O_2 pressure in the carburised atmosphere is approximately 10^{-19} to 10^{-25} atm (Stickels 1991). This is much lower than the oxygen level necessary to form any iron oxides.

Therefore, only the internal oxidation of alloying element may occur at this stage. As discussed above, in this work the oxygen partial pressure varied during the whole process from $2x10^{-19}$ to $5x10^{-21}$ atm (Table 3-2). It was the lowest in the low temperature base process (800°C, 2h, 0.3-0.6%C). In the high temperature base process (930°C, 3h, uncontrolled the carbon potential), it was highest and much higher than in the boost stage (930°C, 1.2%C) since the full carburised atmosphere was only introduced after starting the boost process. However, thermodynamically, the necessary oxygen partial pressure for the formation of oxides in the low temperature stage was lower than the high temperature stage. For example, for the reaction:

$$4/3Cr + O_2 = 2/3\, Cr_2O_3 \text{ ------------------------------ } (8\text{-}13)$$

according to the Ellingham diagram, the oxygen partial pressure for formation of a Cr oxide, such as for formation of $2/3Cr_2O_3$, is approximately 10^{-32} atm at 930°C but 10^{-23} atm at 800°C. The Ellingham diagram (Fig. 8-1) also shows that at 930°C, oxygen partial pressure for equilibrium of SiO_2 is approximately 10^{-28} atm, for equilibrium of MnO is approximately 10^{-26} atm and for equilibrium of Cr_2O_3 is approximately 10^{-22} atm. Therefore, the oxygen partial pressure for the Cr-Mn complex oxides is between 10^{-26} - 10^{-28}atm and Mn-Si complex oxides is between 10^{-26} -10^{-22} atm.

In the commercial carburising process, after a short heating time (0.25-0.5h) in the low temperature base process, a porous continuous oxide layer with a polycrystalline structure was formed on the metal surface by the reaction of the iron and outward diffusion of Mn, Si with O. High concentrations of Si were present at the interface of the surface/surface oxides layer, and, Mn was rich in the whole surface continuous oxides layer. Since the surface continuous oxide layer was not sufficiently dense to stop the diffusion of CO to the metal matrix, the dissolved C and O diffused into the alloy matrix. Specimens with high bulk content of the alloy elements Cr and Mn formed visible internal oxides soon. Si oxide was not visible at short treatment time in specimens B1-1 due to the low concentration of Si in the bulk content, while Si diffused to the surface layer. However, in the higher Si containing specimens D and E, X-ray mapping showed that Si was rich at the internal oxidation front (Fig.4-15). The internal oxides precipitated firstly along the grain boundaries where higher concentrations of oxygen existed than the bulk matrix, and nucleation of the internal oxides at grain boundaries occurred at a lower supersaturation than in the grain, hence grain boundaries were preferential sites for nucleation. Therefore, it is concluded that as soon as oxygen diffuses into the matrix and produced a supersaturation, Si, Cr and Mn internal oxides were formed close to the interface of matrix/scale. The internal oxidation process was controlled by oxygen diffusion along the grain boundaries.

Higher concentrations of oxygen at the interface of surface/surface oxide built up a steep oxygen gradient from the surface to the matrix and rapid oxygen diffusion would quickly produce supersaturation, favouring a homogeneously distributed nucleation process. The velocity of the internal oxidation front was higher (the rate at which a critical supersaturation may build up) at this stage than at later stages in the process. It was clear that at this stage there was a high degree of nucleation but slow growth. Therefore, uniform intergranular oxidation producing oxides containing Cr, Si and Mn was formed at the internal oxidation zone at this stage (1.0-2.0h). The plan view and X-ray mapping of the internal oxidation zone showed this situation (Fig.4- 8a, 4-9a, 4-12). In this way, volume diffusion of oxygen through the metal matrix may be relatively slow whilst interfacial diffusion may be more rapid. This is in agreement with diffusion theory by Reed-Hill (1973) that at low temperatures, grain boundaries diffusion is more important in determining the total diffusion.

Increasing temperature to 930°C in the base process and raising the oxygen partial pressure to 2×10^{-19}atm, increased the oxygen diffusion rate through the lattice. Substantial internal oxides formed as a result of the higher oxygen flux. More rod-like complex oxides (Cr-Mn and Mn-Si) nucleated with an orientation parallel to the direction of the oxygen flux. Since Cr-Mn complex oxides grew much more rapidly than Mn-Si or Si oxides, and significant Cr-Mn complex oxides were formed. It was observed in specimens B1-5 and E1-5 that the population density of the internal oxides was highest at this stage, consistent with the oxygen flux through the matrix and along grain boundaries.

As numerous internal oxides formed, the alloy elements were depleted in the matrix ahead of the advancing internal oxidation front (Figs. 5-14 to 5-16). The velocity of the internal oxidation front decreased with time, and as such, the nucleation rate decreased, a consequence of this was an increase in the oxide growth rate. However, an important factor was that the supply of Si to the grain boundaries was rapid since the diffusion coefficient for Si is higher than Mn, followed by Cr in Fe-Cr-Mn-Si alloy (Krishtal 1970). Si had a higher affinity for oxygen than Mn and Cr and as such formed oxides even at low oxygen partial pressure. Si intergranular oxide nucleated and grew along grain boundaries as a thin, relatively continuous film which contributed the oxide at great depth. In contrast, complex oxides of Cr-Mn and Mn-Si required a higher oxygen partial pressure for nucleation, and its oxides were less stable than Si oxides. Therefore, existing complex oxides tended to grow and subsequently, growth and coarsening occurred. Complex oxides became larger close to the surface within the grains and on the grain boundaries.

In summary, for the early stage of the base process, Cr, Mn and Si were oxidised and precipitated on the grain boundaries. The internal oxides developed as a uniform, continuous, intergranular oxide during this early oxidation reaction. After further heating, the less stable complex oxides grew to a larger size, whilst the stable Si oxides continued to nucleate as small oxide particles and penetrated to deeper grain boundary regions as intergranular oxides. Consequently, the internal oxidation front developed deeper within the matrix. This was the initial stage of the formation of two-zone morphology of internal oxidation.

At the boost stage, a higher carbon potential was introduced (1.2%C) and the oxygen partial pressure dropped to a lower level (2 x 10^{-20} atm). This lower level of O in solid solution reduced the rate at which nucleation of oxide could occur but it was still available for growth. Given the more nagative free energy of formation of SiO_2 when compared with Cr and Mn oxides, this lower O region favoured the nucleation of SiO_2. The results from this work showed that the internal oxidation zone mainly contained Si oxides as intergranular oxides on the grain boundaries and small dispersed oxide particles within grains for samples that only experimental with the boost process (Fig. 4-20, 4-22). The result was in good agreement with theoretical predictions. It was further shown that heating samples in a high carbon potential carburising atmosphere enhanced nucleation of Si oxides thereby enhancing penetration depth and oxide density. This work showed that the penetration depth of the larger internal oxides remained approximately constant after 5.8h heating. The intergranular oxidation (Si oxides) contributed to the greatest depth of penetration of internal oxides. Cr-Mn and Mn-Si complex oxides grew initially as rod-shaped particles but developed into roughly spherical shapes and were also observed to form large agglomerated oxide phases (Fig. 6-12 and 6-13). Finally, two internal oxidation zones were formed that were the generally characteristic of internal oxidation of carburised steel (Fig. 4-1g-h). The outer layer zone close to the surface consisted of globular oxides, which contained both the large Cr-Mn complex oxides, Mn-Si complex oxides, and agglomerated oxide phases (Fig. 4-8c, 4-9b, 4-16). The inner layer zone contained mainly intergranular oxidation (Si oxide), that precipitated along grain boundaries as thin films (Fig. 4-8d, 4-9c, 4-17). Small dispersed oxide particles were always observed in both zones around the larger oxides and intergranular oxidation.

The globular oxides, as shown in Fig. 8-4a, were approximately 1-1.5μm and were mainly elongated in a direction normal to the surface that within grain and grain boundaries, typically to a depth of 2.0-5.0μm, which is less than in previous work, e.g. 8.0μm reported by Kalner and Yurasov (1970). Intergranular oxides were observed typically at a depth of 7-20μm, as shown in Fig. 8-4b. As the Cr and Mn content increased in the matrix, more globular oxides formed. Conversely, as Si increased in the bulk metal, more intergranular oxides formed instead of globular oxides. The existing intergraular oxides grew continuously to become thick films and agglomerated to become a continuous layer. In cross sectional view, this continuous internal oxide film appeared as layers parallel to the surface (Fig. 7-7). In plan view, these oxides appeared as thick films (Fig. 4-9c). The growth of this continuous thick film increased the volume of internal oxidation zone generating local stresses eventually leading to spalllation of the layer. The internal oxidation region may have spalled off from this continuous oxides layer.

The grain size within the surface region of the steel is thought to influence oxide formation, in that as the grain size decreases, the probability of formation oxides within the grains increases. No quantitative analysis on the influence of grain size on the internal oxidation was performed in this work. However, Parrish (1999), suggested that the relationship between temperature and penetration depth might also be affected by grain size, as illustrated in Fig. 8-5. It is a logical that for a given oxidising potential, the greater the grain boundary area, the more rapid the oxygen diffusion into the sample, the greater the density of internal oxides and the less penetration depth of internal oxides will be. While the effect of grain size was not systematically investigated in the current study, a comparison with Fig. 7-4a-e shows that the density of internal oxides does indeed increase with a decrease in grain size.

Fig. 8-5 Relationship between temperature, grain size and internal oxidation zone (ref. Garrish 1999)

In summary:

Considering the commercial carburising process used in this research.

- The formation and growth of the internal oxidation was greater during the base process due to high oxygen partial pressure.

- During the boost process, the temperature increased along with a rise in carbon potential and a reduction in oxygen partial pressure. As a result, the formation and growth of the internal oxide was less.

This two stage process led to rapid nucleation during the base process and rapid growth during the boost process.

8.2.4 Depth Profile of Elements

The metal–oxygen reaction that leads to the precipitation of internal oxides will produce local composition gradients of the participating elements between the oxidised and unoxidised layers. The equilibrium driving force will result in diffusion of alloying elements from the matrix to the depleted zones. The concentration gradient of alloying elements within the internal oxidation region and matrix has been evaluated by the combined results of GDOES and EPMA. A schematicdiagram showing element concentration depth profile is given in Fig. 8-6. It was clearly shown by GDOES that Si was enriched at surface for the first 100nm, below which it was depleted in concordance with a higher concentration of Mn, following Cr. The appearance of a strong peak of the alloy elements concentration in depth profile was in order Si, Mn and Cr. It revealed that at the first heating stage, the Si diffused to the surface and reacted with oxygen, which depleted the bulk Si content of the underlying layers, thus the diffusion of Si to the surface was reduced. Mn diffused to the reaction front and reacted with oxygen. The elemental distribution in the surface region examined by EDS in the TEM (Fig. 6- 18),

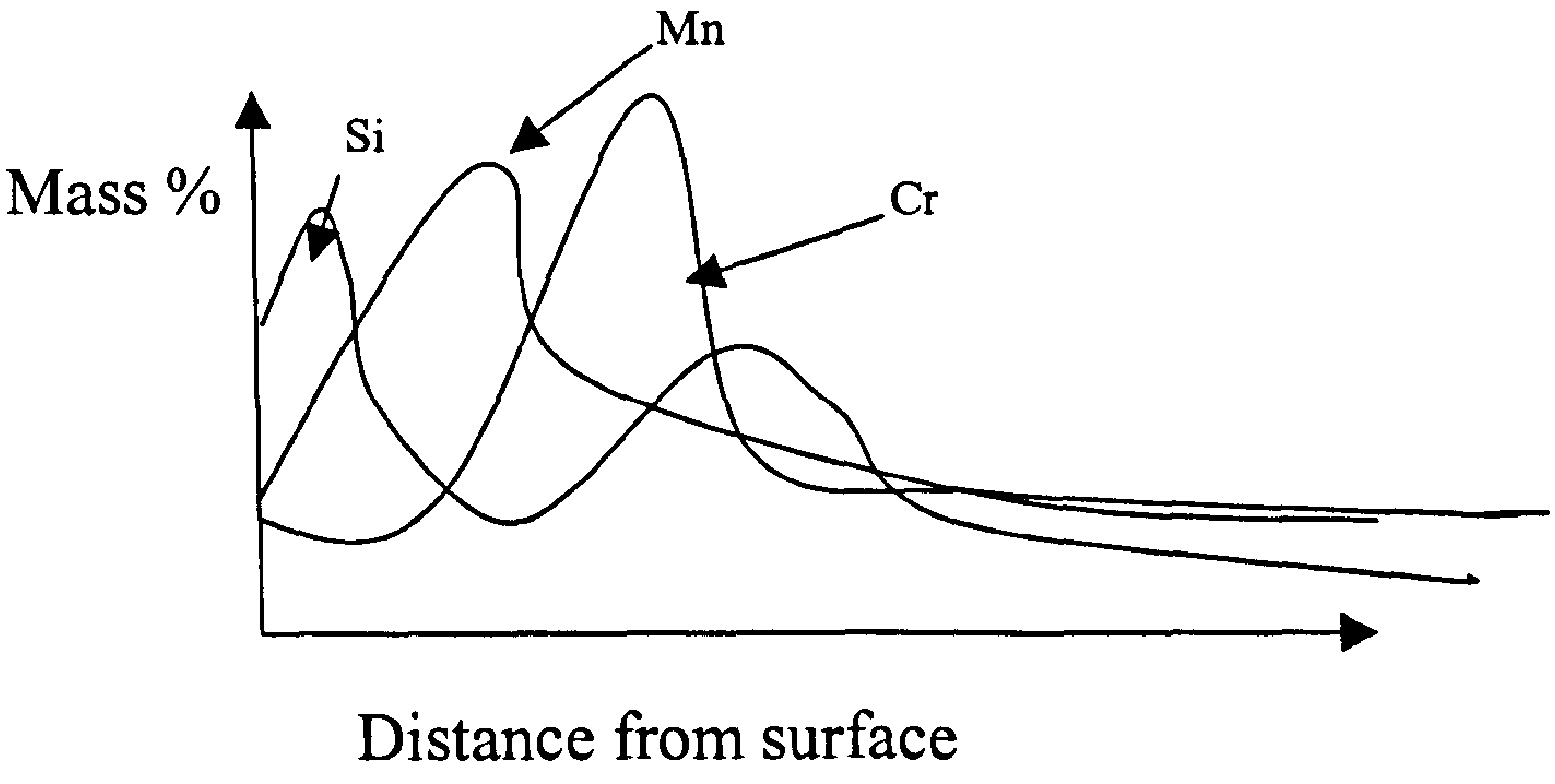

Fig. 8-6 Schematic diagram of the elements depth profile in the internal Oxidation region

also confirmed this result. The results are agreement with Lohermanin's (2000) work, who reported that Si was just concentrated at the top of the surface oxide layer and Mn was rich at the surface oxide layer. It agreed with theory that would expect Si has a higher affinity for oxygen, followed by Mn and then Cr. The results of alloy concentration in the internal oxidation region were approximately four times the bulk concentration for Cr and approximately three times for Mn after 8.0h heating for specimen E1-6. Such high local alloy content introduced a steep composition gradient in the surface region of the steel. Cr and Mn were rich close to the surface whilst Si enrichment was at a greater depth. This was consistent with the oxide morphology observed in that complex oxides (Cr-Mn and to be lesser extent Mn-Si) formed close to the surface where a higher oxygen content was present in solid solution. Intergranular Si oxides formed at greater depth on grain boundaries. This result was also in agreement with prediction from the free energy and oxygen partial pressure for formation of internal oxides. This distribution of the alloy elements was observed for all the specimens studied.

Elements migrating to the surface that form oxides, leave the adjacent matrix depleted in these elements. In the current study, enrichment of alloying elements was observed in the internal oxidation region, but was depleted in the matrix where internal oxidation had not occurred (Fig. 5–13 to 5–16). For example, in specimen C1-8, the maximum depletion of the alloy elements in the matrix close to the surface was 38.7%Si, 57%Mn and 40.6%Cr. The consequence of the composition gradient that developed during the internal oxidation process was that the matrix adjacent to the oxides would have its transformation behaviour modified. Thus, instead of the expected martensitic structure, higher temperature transformation products were observed, such as pearlite, as shown in Fig. 6-7. This observation agrees with that of Dowling et al (1995) who reported a pearlite microstructure in ASE 8620 with internal oxidation with a depth of approximately 5 μm. The depth of non-martensitic microstructure layer was in substantially deeper than the penetration depth of the internal oxides. Dowling et al confirmed that the main reason for the poor fatigue strength in this steel was the non-martensitic transformation products in the surface.

8.2.5 Penetration Depth and Population Density of Internal Oxides

Wagner (1959) indicated that the diffusion process in internal oxidation is the rate controlling process. The current study showed that the oxidation reaction rate was quite different for different carburised conditions. As expected, the higher the oxygen partial pressure in the atmosphere and more negative free energy for formation of the particular internal oxides during the base process, the more rapid the internal oxidation reaction, and therefore the greater the penetration depth of internal oxides. The oxidation rate might be considered controlled and supported by first, the interfacial diffusion of oxygen and then volume diffusion of oxygen. In the boost process, oxidation rate decreased when comparing with the base process, resulting in the rate of penetration depth of internal oxides increased more slower. Another reason which may affect increased rate of the penetration depth of internal oxides for long cycle heating was spallation of the internal oxidation zone. After long cycle heating, internal stresses generated due to the extensive internal oxidation, particularly intergranular oxidation, led to spalling. As a result, the measured penetration depth of internal oxides exhibited a slower increase than expected. It can be concluded the rapid nucleation of internal oxide in the base process quickly determined the penetration depth of the internal oxides in the internal oxidation zone.

The population density of the internal oxide precipitates in the internal oxidation zone (area fraction) was changed with time. Generally, as the carburising time increased, the population density increased with regard to the increasing area fraction of the internal oxides. However, the area fraction increased sharply between 2.0-5.8h where increased nucleation and later growth of the internal oxides was observed. The reason for the reduction of the internal oxides at 8.0h treatment was not understood. A possible reason for this phenomenon was spallation of the internal oxidation layer. As discussed above, the stress produced by massive internal oxides may induce spalling of the substrate. As observed in this study, severe intergranular oxidation may result in a denuded internal oxidation surface layer, especial for higher Si containing steels, as shown in Fig. 7-7. This denuded internal oxidation layer spalled off during further heating, as observed in specimen D1-7 (Fig. 4-7). This spallation denuded surface was responsible for the decrease in oxide population density. Another possible explanation was the low flux of oxygen at this stage, continued nucleation of the Si oxides consumed oxygen on the deeper grain boundaries making nucleation and growth of Cr and Mn oxides more difficult. Some of the existing complex oxides may have dissociated due to change furnace atmosphere condition. After further heating, the oxygen in solid solution was still high enough for Si to form more small dispersed oxides, which further increased the density of internal oxide in the internal oxidation zone.

8.2.6 Internal Oxide Phase

The morphologies of the internal oxides were quite different with different process conditions. As discussed above, the susceptibility of different elements to oxidation was determined to be in the order Si >Mn >Cr. The oxygen concentration in solid solution for the formation of Si oxides is lowest, then, Mn and following Cr (Fig. 8-1). The oxygen concentration in solid solution for formation of Cr-Mn and Mn-Si complex oxides must be somewhere between Cr oxides and Mn oxides, Mn oxides and Si oxides. Therefore, Cr-Mn, Mn-Si complex oxides, Si intergranular oxides and Si oxides were observed at a different carburised stage as a different morphology and structure. The results were consistent with other studies (Chatterijee-Fischer 1978 and Murai 1999).

There is generally a dearth of detailed analysis of the structure of internal oxides, and very little information on the exact oxides that form, several different structures were observed in the present work. Complex oxides appeared as $Cr_xMn_yO_z$ or $Mn_xSi_yO_z$, examples identified in this work were cubic $Cr_{1.5}Mn_{1.5}O_4$; cubic Mn_2CrO_4; orthorhombic $CrMnO_4$; orthorhombic Mn_2SiO_4; monoclinic or triclinic $MnSiO_3$. Intergranular oxides appeared usually as Si_xO_y, such as hexagonal SiO_2. Some of phases identified in this current work are consistent with the previous work of Dowling et al (1995), who found Mn_2SiO_4 in carburised 8624 steel after gas carburisation at 845°C for 4.5h. EDS analysis indicated that some of complex Cr/Mn oxide shown Cr/Mn signal rate 2/1 which agrees with Murai et al (1999). However, some internal oxides, such as

$FeOCr_2O_3$, which was identified in 20CrMnTi steel by X-ray diffraction technology in previous research (Sun 1989), were not found in the present research.

The formation of complex oxides followed that expected from the Ellingham diagram. It appeared that Cr-Mn complex oxides were formed directly at the base process because high oxygen partial pressure in the atmosphere and no MnO was observed. Therefore the Cr-Mn complex oxides probably formed directly rather than from transformation from MnO. This was considered to be because of higher oxygen partial pressure in the base process oxide in the specimen studied. Some of the Mn-Si complex oxide arose from transformation of the simple oxide. For complex Mn-Si oxides, SiO_2 may form as small particles at the internal oxidation front where the concentration of dissolved oxygen is high. It was observed in this work that small Si oxides formed in the internal oxidation zone, which therefore created a Si depleted zone around the Si oxide particles. This depletion of Si around the SiO_2 increased the equilibrium oxygen concentration in solid solution of SiO_2. As the equilibrium oxygen partial pressure at the SiO_2/matrix interface exceeded the equilibrium oxygen pressure for formation of $MnSiO_3$ or Mn_2SiO_4, then, these reactions took place to form $MnSiO_3$ or Mn2SiO4 as spherical particles. Similar observations were reported by Liu et al (1997) who believed that the $MnAl_2O_4$ complex oxide transformed from the simple Al_2O_3 in carburised Fe-Mn-Al alloy.

The oxide particle size was determined by a competition between the rate of nucleation as the internal oxidation front passes and the growth and coarsening rate of the particles. The longer time that a nucleated particle has to grow between the arrival of oxygen and solute at this point, the larger will be the particles. Si oxides were more stable than Mn and Cr oxides. Therefore, it was observed in this study that Si oxides were smaller than other oxide precipitates, followed by Mn-Si complex oxide precipitates, whilst the Cr-Mn complex oxide precipitates were the largest. The TEM observation in this work revealed that the internal oxide phases were classed as: Cr-Mn complex oxide phases with a cubic or ellipsoid shape; Mn-Si complex oxide phases which were ellipsoid or spherical; Si-oxides present as thin films on the prior austenite grain boundaries and also as spherical small oxide precipitates. The reason for the difference in precipitate morphology was not certain, but must depend on such factors as the interfacial energy, misfit strain effect or coherency of precipitates with matrix. Cubic shape oxides usually have an abrupt clear boundary with matrix (Fig. 6-2). If the incoherent edges grow rapidly, the cubic precipitates became rectangle or ellipsoidal shape (Fig. 6-3). Polyhedral shaped oxides were also observed in this studied (Fig. 6-4).

All the complex oxides observed in this work were crystalline, however, both crystalline and amorphous Si oxides were also observed (Fig. 6-10). This is in agreement with previously observations by Wood and Stott (1987) and Lanteri et al (1997). It was observed that some Si oxides were part amorphous and part crystalline, especially for the intergranular oxidation close to the surface, as shown in Fig. 6-13. The growth process was not well understood. It may nucleate first as an amorphous phase and then crystallise on further growth. However, amorphous phases may have resulted by specimen preparation process, as found by Stephenson (1988). The ion bombardment on the specimen may cause the Si-oxides to become amorphous during ion polishing process, or during examined it the TEM the action of the electron beam.

Different contrast features were observed in the TEM of the larger oxide precipitates. That may be due to some defect structure, some of which may accommodate composition variations within the particle, e.g. second phases formed on primary particles. The small or second phases may favour formation on the edges of the larger oxide precipitates (Fig. 6-2) in this case the interface may have a higher oxygen concentration. A high concentration stress zone was observed around the complex oxides due to the volume change on the formation of the oxide precipitates. The small dispersed oxide particles combined with carbides were also observed in this study.

Interestingly, this present work indicated that the complex oxides often contained a sheath of Si bearing oxides or Mn-Si oxides (Fig. 6-12 and 6-13) resulting in agglomerated oxide phases. This strongly suggested that Cr-Mn oxides formed first, and then acted as nucleation sites for Mn-Si complex oxides or Si oxides. At first sight, this appeared to be contrary to the behaviour expected with the thermodynamics favouring the formation of Si oxides rather than Cr and Mn. However, these agglomerated oxides almost certainly formed as a result of the change of oxygen concentration in solid solution during the carburising process. As discussed previously, this demonstrated that the oxygen partial pressure would vary during the gas carburising process. In the heat-up stage of the base process, the oxygen partial pressure was high, allowing Cr-Mn based, Mn-Si based oxides and Si oxides to form. However, the oxygen partial pressure will have fallen, greatly reducing the driving force for Cr-Mn based oxides to form, but still allowing the formation of Si based oxides or Mn-Si oxides. At this stage, the majority of prior austenite grain boundaries were already covered in Si based oxides, depleting the adjacent matrix regions of Si. This left the intragranular regions as the only major source of further Si oxidation, with the prior Cr-Mn complex oxides acting as heterogeneous nucleation sites and more rapid diffusion path for oxygen due to existing interface/matrix enhancing the diffusion path.

8.3. Effect of Si on Internal Oxidation

Si has been identified as the most significant element in terms of internal oxidation. The results showed that there was a critical Si content in which the deepest penetration depth of internal oxides was reached and morphology of the internal oxidation zone changed. Before this critical value, the penetration depth of internal oxides was increased with increasing Si content. The morphology of internal oxidation zone consisted mainly of globular oxide particles in the outer zone and intergranular oxidation in the inner zone. After this critical value, the penetration depth of internal oxides decreased as further increasing of Si content. The morphology of the internal oxidation zone consisted mainly of intergranular oxidation as network and fewer globular oxides particle close to the surface. This critical Si content varied in the range of (0.19-0.3) % Si in current study depending on different carburising conditions. This is in agreement with previous works by Kazuo (1995) and Williams (1997) who reported that the critical point was in range of 0.3-0.5 %. This critical value is related to the oxygen diffusion in the matrix. For the specimens with a low Si in the bulk content, oxygen diffused both through the matrix and oxide/matrix interface, as Si bulk content was increased, large size internal oxides, elongated normal to the surface were formed, which will have provided enhanced oxygen diffusion path, and therefore greater oxygen penetration. Therefore, the penetration depth of internal oxides increases. When Si bulk content exceeds the critical value, the high solute concentration led to greater internal oxide formation. The existing oxides tended to grow as thick films and agglomerated together to become a continuous internal oxide layer which was usually parallel to the surface. This blocked the inward oxygen diffusion, as a result oxygen penetration was reduced and the penetration depth of internal oxides decreased further. When the Si concentration was large enough to give selective oxidation, the outward diffusion of Si will form an external scale and stop internal oxidation. Combined with the penetration depth of the internal oxides and population density in the internal oxidation zone, it is obvious that although the high Si reduced the penetration depth of the internal oxides, the increase in area fraction of the internal oxides in the internal oxidation zone may bring more serious problem for the materials, for example, low surface hardness and spallation of internal oxidised region. It was observed in current study that high Si specimens had lower microhardness than low Si specimens for a constant depth from surface. It may be possible to reduce internal oxidation by using a higher Si bulk content in the steel. When the Si content exceed the critical value, for example, at least Si > 1% or even more, the protective oxidation film was formed by selective oxidation occurs in the steel which stop the internal oxidation. Further study is need by choosing high Si content steel (at least Si>1.0%).

The spallation phenomenon was frequently observed in the specimens with high Si bulk content after long cycle heat treatment. It may occur by the internal stress (growth stresses and thermal stresses) which is generated due to the formation of massive internal oxides. The growth stresses are generated mainly by volume change that occurred during oxidation, for example, typical volume increased would be 92% for Al_2O_3 from aluminium (Stott and Wood 1988). Compositional change in the matrix or internal oxides may also bring growth stresses. The thermal stresses are generated mainly due to the difference in thermal expansion coefficients of the matrix and oxides. As consequence of the stresses relief, the spalling of the internal oxidised subsurface region happens.

8.4 Influence of Process Parameters on the Internal Oxidation

8.4.1 Carbon Potential

The carbon potential of a furnace atmosphere at a specific temperature is defined as the carbon content of pure iron that is in thermodynamic equilibrium with the atmosphere. It is know that carbon can be added or removed rapidly from steel by an overall reversible reaction:

$$2CO \leftrightarrow C\ (\text{in Fe}) + CO_2 \text{ ---------------------------------- } (8\text{-}14)$$

and

$$CO + H_2 \leftrightarrow C\ (\text{in Fe}) + H_2O \text{ ---------------------------- } (8\text{-}15)$$

The methane enrichment of endothermic gas provides carbon for the process by slow reactions such as:

$$CH_4 + CO_2 \rightarrow 2CO + 2H_2 \text{ ------------------------------- } (8\text{-}16)$$

$$CH_4 + H_2O \rightarrow CO + 3H_2 \text{ -------------------------------- } (8\text{-}17)$$

that reduces the concentration of CO_2 and H_2O in the atmosphere, respectively. These reactions regenerate CO and H_2, thereby driving reactions eq. 8-14 and 8-15 to the right. Because the methane content of carburising atmosphere is usually far above the concentration that is expected at equilibrium, given the CO_2 and H_2O contents present, the sum of the reaction in Eq. 8-14 and 8-16 and in Eq. 8-15 and 8-17 reduces to:

$$CH_4 \rightarrow C + 2H_2 \text{ -- } (8\text{-}18)$$

Therefore, the carbon content during carburising is achieved by varying the flow rate of hydrocarbon- enriching gas while maintaining a steady flow of endothermic carrier gas.

The relationship between carbon potential for endothermic gas atmosphere and CO_2 is shown in Fig. 8-7. It shows that as the carbon potential increased in the process, flow rate of methane increased, to maintain a certain equilibrium condition, it must decrease

CO_2 and so the oxygen concentration decreased resulting in a decrease in internal oxidation. Table 3-2 gives the oxygen partial pressure related to the different carbon potentials for the experimental carburising process. For 1.2%C in 930°C, the oxygen partial pressure was $2x10^{-20}$atm, but at 0.4 %C in 930°C, the oxygen partial pressure was $2x10^{-19}$atm. The experimental results in this work agreed with this theory, as expected. It was observed that at 1.2% carbon potential and 930°C, only a few Si intergranular oxides were observed in the internal oxidation zone, the penetration depth of internal oxides was only 2.52μm whilst the area fraction of internal oxides in the internal oxidation zone was 10.2%. Comparing this result with 0.4 % carbon potential at 930°C, a substantial internal oxidation zone was formed that contained oxides of all three elements (Si, Mn and Cr). The penetration depth of the internal oxides was 5.28 μm that is more than twice that at 1.2% carbon potential. The area fraction of internal oxides was 19.6 % that again about twice that at 1.2% carbon potential.

Fig 8-7. Relationship between CO_2 content and carbon potential for endothermic gas (ref. Stickel 1991)

8.4.2. Carburised Temperature and Time

The influence of the carburising temperature on internal oxidation has been discussed by Chatterijee-Fischer (1978) and summarised, as shown in Fig. 8-8. The higher the carburising temperature, the greater the penetration depth of internal oxides. However, from the present work, comparing the low temperature base process (800°C) with the high temperature base process (930°C) (Fig. 3-2), the oxygen partial pressure was much higher in the high temperature base process, therefore, the later led to greater internal oxidation rather than the former. This was evidence that the degree of internal oxidation increased with carburising time, especially on the penetration depth of internal oxidation, and was observed in all the specimens studied. The longer the carburised time, the greater the chance for oxidation, the more internal oxides formed.

Fig.8-8 Depth of the oxidation zone with carburising time at different carburising temperature (ref. Chatterijee-Fischer 1978)

8.5 Proposed Model of the Internal Oxidation in Carburised Steel

Given the results obtained within the body of this work and a critical understanding of the literature a model to explain the formation of internal oxidation is proposed. Oxygen is a contaminant within the furnace atmosphere and even at very low levels is sufficient to diffuse into the alloy at high temperature and to react with the alloying elements in this case Si, Cr, and Mn. The reason why oxidation occurs in the morphology observed is a combination of the various concentration of alloying elements, different rates of diffusion of the alloy spices in iron and the free energy of formation an oxide types.

STAGE 1

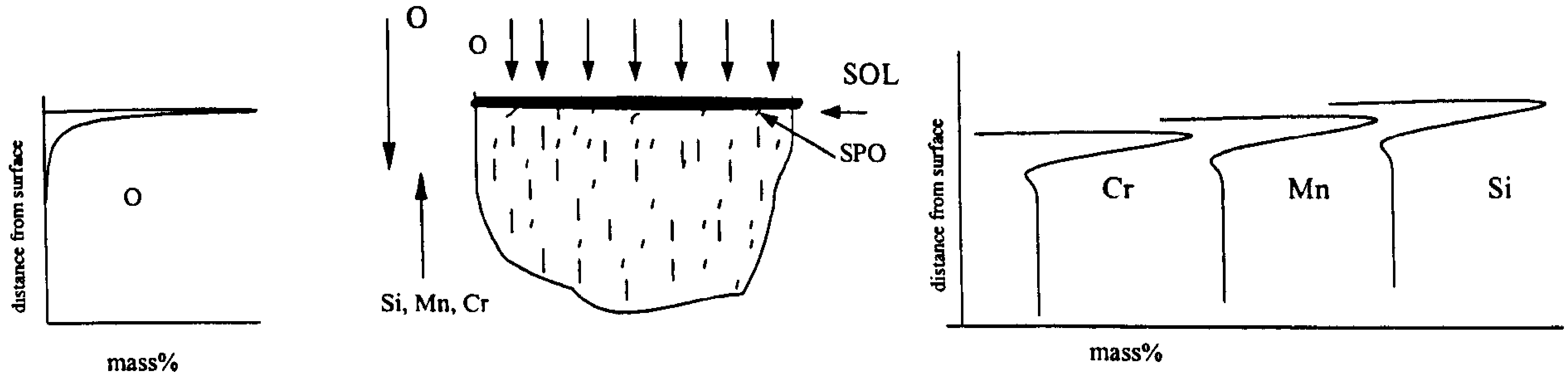

** SOL: Surface continuous oxide layer*
SPO: Small oxide precipitates

The following stages are proposed to account for the microstructures observed:

***Stage 1- Early heating stage*:**

As soon as the base process starts, there will be a relatively high concentration of oxygen at the surface. A continuous surface oxide layer is formed by the outward diffusion of alloy elements that forms mainly Fe base oxides along with Mn oxide and Si oxide. Whilst the Si content is low its diffusion in Fe is high and has the more negative free energy of formation of all the oxides considered. The alloy content of Mn is much higher and therefore Mn oxides were also observed in the outer layer. Cr has the slowest diffusion rate and less negative free energy of formation that accounts for its lack of presence in the surface layer.

A further consequence is that the Si level below the surface became depleted and whilst this occurred to some extent for the Mn there was much more Mn present than Si.

STAGE 2

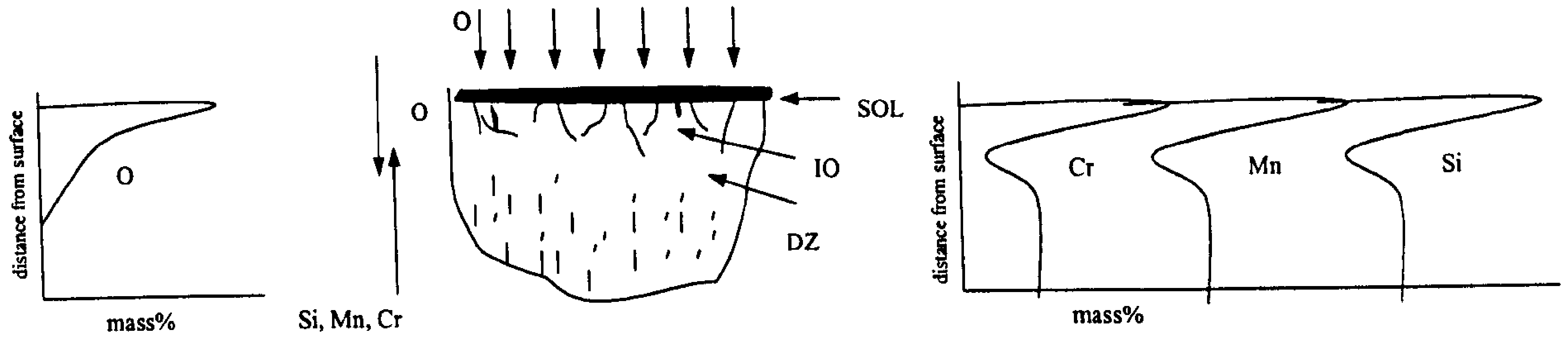

* *SOL: Surface continuous oxide layer.*
IO: Intergranular oxides.
DZ: Alloy elements depleted zone.

***Stage 2- The low temperature base process (800°C, uncontrolled carbon potential)*:**

Because of process conditions the oxygen partial pressure in the atmosphere at this stage was lower than the first stage, but still relatively high, typically 5E-21. Oxygen diffuses first along grain boundaries and then into the matrix substrate and precipitated uniform Cr, Mn and Si oxides on the grain boundaries as thin film intergranular oxides close to the surface which grow with time and further supply of oxygen. The internal oxidation process is controlled by the interfacial diffusion of oxygen. This type of morphology is found just below the surface.

STAGE 3

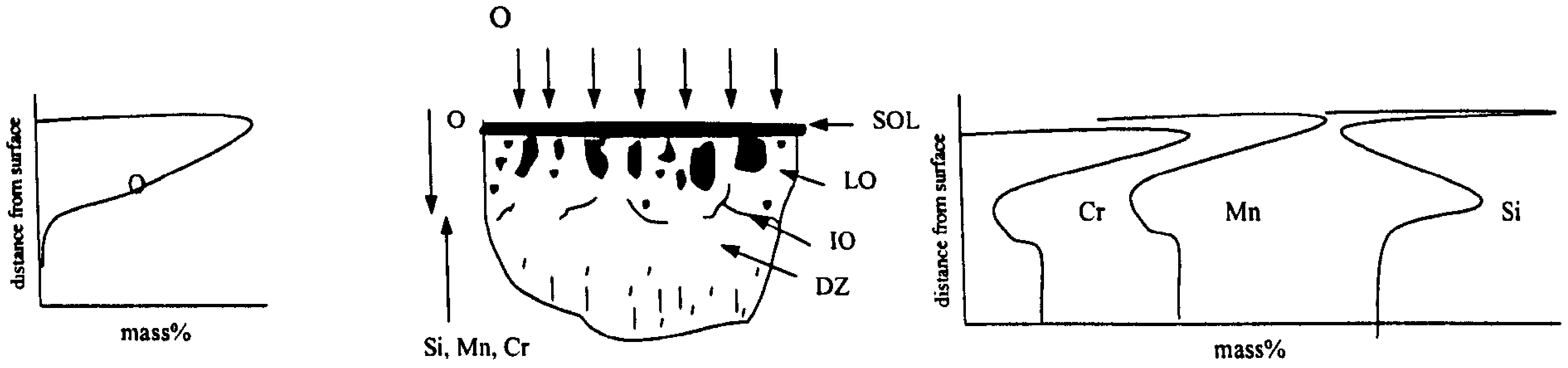

* *SOL: Surface continuous oxide layer*
LO: Complex Cr-Mn or Mn-Si oxides
IO: Intergranular oxides.
DZ: Alloy elements depleted zone.

- ***Stage 3- The high temperature base process (930°C, uncontrolled carbon potential).***

At this stage the oxygen potential is at its highest, typically 2E-19, and diffuses rapidly through the lattice and grain boundaries and existing oxide/matrix interfaces as well. Rod-like complex oxides (Cr-Mn and Mn-Si) nucleate rapidly within grains and are elongated normal to the surface and on the grain boundaries. Once the large internal oxides form, the alloy elements are depleted in the bulk matrix. In this layer, less stable complex oxides (Cr-Mn or Mn-Si) tend to grow and coarsen whilst new particles will nucleate at the internal oxidation front where alloy elements are available. Meanwhile, at greater depths within the material the concentration of the alloying elements is approximately that of the bulk composition. Oxygen will penetrate first along grain boundaries and given that Si has a much higher diffusion coefficient and higher affinity for oxygen forms the characteristic Si oxide network observed in the inner oxidation zone. The penetration depth of internal oxides increases with increasing content of intergranular Si oxides. The internal oxides nucleate and grow, building up a large internal oxidation zone at this stage. The internal oxidation process is controlled by the volume diffusion of oxygen.

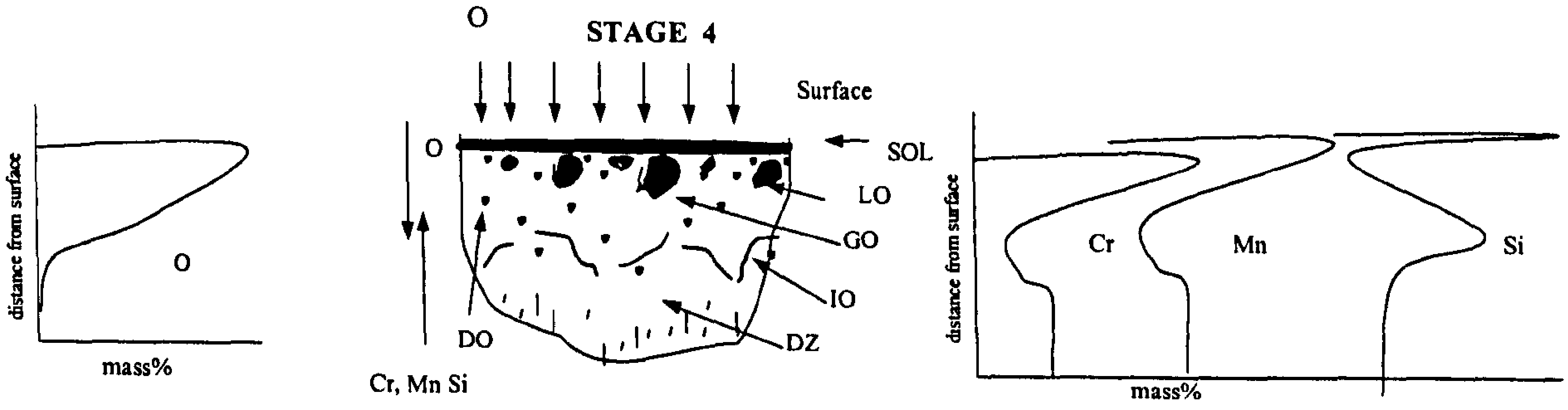

** SOL: Surface continuous oxide layer.*
GO: Agglomerated oxide phase.
DZ: Alloy elements depleted zone.
LO: Complex Cr-Mn or Mn-Si oxides.
IO: Intergranular oxides.

- ***Stage 4- The boost process (930°C, 1.2%C):***

At this stage there will be a low oxygen partial pressure in the atmosphere that does not reach equilibrium conditions for complex oxide nucleation whilst the equilibrium condition for the formation of Si oxides is still possible. Therefore, Si oxides continue to form as small dispersed oxide particles in the internal oxidation zone and as intergranular oxides on the deeper grain boundaries. Meanwhile, some Si or Mn-Si oxides grow around the larger Cr-Mn complex oxides to form a large agglomerated oxide phase. Existing complex oxides grow from rod-like to roughly spherical shape. The internal oxidation front passes to the deeper matrix due to the contribution of the Si intergranular oxides. The internal oxidation process is controlled by the interfacial diffusion of oxygen.

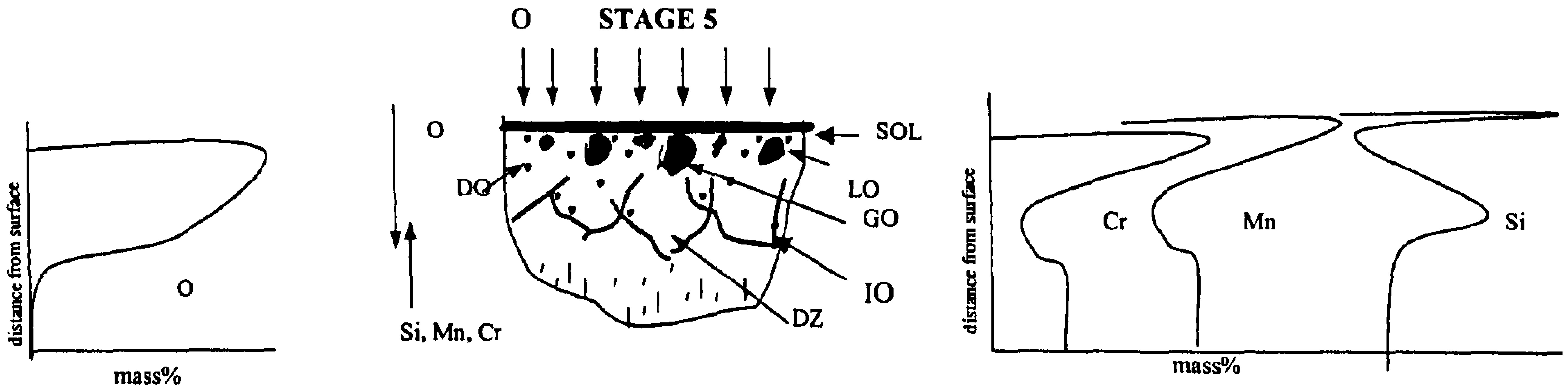

** SOL: Surface continuous oxide layer. LO: Complex Cr-Mn or Mn-Si oxides.*
GO: Agglomerated oxide phase. IO: Intergranular oxides.
DZ: Alloy elements depleted zone. DO: Dispersed small oxide particles.

- ***Stage 5. Equilibration Phase:***

After long cycle carburising, two zone morphology of the internal oxidation in the carburised steel is formed. An outer zone: larger size complex oxides (Cr-Mn and Mn-Si) within grains and on grain boundaries close to the surface; Inner zone: Si oxides as intergranular oxides thin films close to the internal oxidation front and remote from the surface. Dispersed small Si oxide particles are distributed in both internal oxidation zones. For samples with high Si content, severe intergranular oxides form together as a thick continuous oxide layer, parallel to the surface. During heating, this continuous film may cause spallation of the internal oxidation layer at the sub-surface. The internal oxidation process is controlled by the interfacial diffusion of oxygen.

8.6 Proposed Methods to Reduce or Eliminate Internal Oxidation

As discussed above, the internal oxidation phenomenon that occurs during the carburisation heat treatment is strongly influenced by alloying elements in the steel, which have a high affinity for oxygen. Therefore, possible ways to reduce or eliminate the internal oxidation can be considered in:

- Steel composition
- Carburisation condition
- Surface protective coating

8.6.1 Steel Composition

Steel design is an important path to reduce internal oxidation. The formation of internal oxidation is related to the presence of certain alloying elements, such as Si, Mn and Cr, and their quantities in solid solution within the steel. Cr and Mn are elements required to ensure the hardenability of the steel, but are also the elements that cause internal oxidation. The replacement, or partial replacement, of these oxide- forming elements with elements that have atomic numbers greater than that of iron would contribute to reducing internal oxidation, but at a cost. Such elements are Ni and Mo. Ni is an element that improves not only the hardenability of the steel but also the toughness of both the case and the core. Mo is an element which improves the hardenability of the steel, like Ni and more importantly, it can help suppress any non-martensitic transformation products arising from internal oxidation. The present work indicates that a 1.18 % Ni, 0.20% Mo steel did not effectively inhibited the formation of the internal oxidation if Si, Mn and Cr were still present with sufficient quantity in the steel. That is in agreement with previous research by Nakamura et al (1993) who reported that the introduction of 0.5% or more of Mo was considered to be beneficial in reducing internal oxidation. Hence, new carburising steel that contained 0.2%C, 0.09%Si, 0.8%Mn, 0.02%Ni, 1.06%Cr and 0.86%Mo was developed for high strength gears. This steel was designed from the view point of eliminating internal oxidation and non-martensitic phases, as well as containing the retained austenite content of 30% in the surface layer when the carbon potential of the atmosphere was about 0.80%. Therefore, for this composition, lowering the Si content decreased the penetration depth of the internal oxides and raising the Mo content inhibited the formation of a non-martensitic microstructure.

As discussed above, Si is the most important element that causes intergranular oxidation of steel. The present work found that although for high Si content (>0.5%), the penetration depth of the internal oxides reduced, the population density of internal oxides increased strongly which may led to more serious problems, such as reducing case hardness and lowering fatigue strength. The patent technology given by Sakamoto et al (1995), believed that high Si content was effective in arresting internal oxidation. They developed new steel based on the fact that penetration depth of internal oxides decreased with further increases in Si content. The test data (Si 0.77% in test steel) showed that the new steel improved the pitting fatigue strength. Further research would be necessary to compare fatigue strength with different Si contents. However, most recent research believes that low Si contents are the effective way to reduce internal oxidation. Previous research by Williams (1998) that studied the same base steel as studied here but with a different Si content (0.065-0.77) %, found that penetration depth of the internal oxides in the steel with 0.065% Si was 10μm but it rose to 20μm when the Si content increased to 0.11%. It was suggested that Si content in steel should be less than 0.065%. Burris'(1996) patent gave a low silicon steel that contained 0-0.05%Si and normal content for Cr and Mn (1.0%Cr, 0.6%Mn). Intergranular oxides were virtually eliminated from the as carburised surface and the case depth was significantly enhanced.

8.6.2 Carburisation Condition

It is impossible to control the endothermic carburising atmosphere to eliminate the formation of internal oxidation at the surfaces of case-hardened parts. However, it is possible to adjust the carburising process to reduce the internal oxidation at the surface of case-hardened parts. Present work indicates that the internal oxidation develops rapidly during the heating stage 0-5h in the base process of carburising, and complex oxides (Cr-Mn and Mn-Si complex oxides) are formed mainly at this stage. It was even worst in the high temperature base process (930°C for 3.0-5.0h). During this period, the internal oxides grew and coarsened and the population density increased rapidly. In the boost process (930°C, 1.2%C) only Si oxides formed on the grain boundaries. The present work also indicated that control of the carbon potential for the low temperature base process effectively reduced the degree of internal oxidation. Hence, theoretically, there is a possible way to control the internal oxidation by reducing the heating time in the base process to as short as possible, and controlling the carbon potential during the base process, especially for the high temperature stage (930°C). Another possible way to reduce internal oxidation is by using a separate preheating method. In this case, a fully controlled atmosphere should be introduced to the furnace in the base process and components heated uniformly to the carburising temperature in a neutral furnace atmosphere. Then, the carburising atmosphere should be introduced to the furnace to complete the carburised cycle. The separate preheating can be done either by separate heating chamber in a continuous furnace or by introducing different atmosphere conditions in the same batch furnace. Of course, this will enhance the cost of production.

8.6.3 Surface Protective Coating

It is known that if the concentration of solute element (M) in matrix is high enough, the outward diffusion of solute will be fast enough to form a continuous blocking layer of MO_v and stop internal oxidation. This transition to external oxidation is the basis for the design of Fe-, Ni-, and Co base engineering alloys which contain a sufficiently high concentration of solute, e.g. Cr, Al or Si to produce an external layer of a stable, slow growing oxide, e.g. Cr_2O_3, Al_2O_3 or SiO_2, which prevents oxidation of the parent metal. The basis of this selective oxidation would be to reduce the internal oxidation in carburised steel. A possibility may be to build up a protective layer on the surface of the component before carbursing or during the carburising process to stop internal oxidation. This protective layer can be build up either by

- a metal thin film coating made before the carburising process in which the selective oxidation of the metal will occur during carburising process to form a protective oxide film, such as a Si coating

or

- A high concentration solute in the carburising steel where selective oxidation during the carburising process will form a protective oxidation film, such as stable SiO_2 continuous oxide layer.

Thermodynamically, Si has a high affinity for oxygen and the free energy for formation of Si oxides is lower than other elements, such as Mn and Cr. Therefore, hypothetically a thin Si coating was coated on the surface of the component. Inward diffusion of oxygen reacts first with the Si coating to form Si oxides on the surface. Si on the surface consumes the inward diffusion of oxygen continuously to form a continuous Si protective oxidation layer. This Si oxide protective layer is thermodynamically stable, slow growing and is reasonable effective in blocking the further inward diffusion of oxygen.

CHAPTER 9

CONCLUSIONS

1. A model is presented that explains the phenomena of internal oxidation, the main features of which are:

   the availability and diffusion rate of oxide forming elements

   the free energy of formation of alloy oxides

   the supply of oxygen available in the commercial carburising system.

2. Si is the most significant alloying element in that it possesses an oxide that has the lowest free energy of formation and also has the highest diffusion rate when compared with other alloying elements, in this case Cr and Mn. Si becomes depleted in the near surface region as it diffuses to the surface to form a Si rich continuous oxide scale. Mn and Cr also diffuse to the surface, although slower than Si, and forms a sub-surface continuous layer. O continues to diffuse into the bulk of the material both in an intra and an inter granular mode. Because Si is depleted in the near surface zone then the diffusing O forms complex oxides with Cr and Mn both on grain boundaries and within grains. Si oxides will be present in this zone but only to a limited amount. Further diffusion of O into the bulk material reaches a further zone where Si is not depleted or has diffused Si from the bulk materials. O diffuses most rapidly along grain boundaries and thus forms Si oxides as a grain-boundary network. This gives the characteristic morphology of internal oxidation.

3. For the steel studied deepest the penetration depth of internal oxides at approximately 0.19-0.31 mass % Si occurred. Si oxides were not observed to form for lower Si level. Higher Si levels provided enough Si to form a surface continuous

layer and also significant Si remaining in the near surface zone to form a greater density of Si oxides as a network, which inhibited the ingress of O.

4. The thermodynamic equilibrium condition and oxygen partial pressure determines that the morphology of the internal oxidation zone in commercial carburised steel has a two-zone morphology characteristic. The outer layer zone close to the surface consisted of the larger size complex oxides, that contained both the Cr-Mn complex oxides, Mn-Si complex oxides, and agglomerated oxide phases within the grains and on the grain boundaries and close to the surface. The inner layer zone close to the internal oxidation front mainly contains intergranular oxidation (Si oxides), that precipitated along the grain boundaries as a thin film. The small dispersed oxide particles were always observed in both zones around the larger oxides and the interngranular oxidation.

5 Quantitative analysis on the internal oxidation zone confirmed that the penetration depth of the internal oxides in the internal oxidation zone increases continuously with increased carburised (exposure) time. It increases sharply in the base process and increases in a stable manner during the boost process. The area fraction of the internal oxides in the internal oxidation zone increases first with increase in exposure time in the base process. In the high temperature base process, a massive internal oxidation zone forms. The area fraction is larger at the time just before the boost process starting. Then, the area fraction of the internal oxides in the internal oxidation zone drops but then increases again. It relates to the oxides dissolved at the reaction process and spallation phenomenon of the surface internal oxidation layer.

6 The complex oxide phases were identified as Mn_2CrO4, $Cr_{1.5}Mn_{1.5}O_4$, $CrMnO_4$ as cubical or ellipsoidal shape in dimension about (1.0-2.5) μm and Mn_2SiO_4 and $MnSiO_3$ as spheroids in dia. 400-900nm. The intergranular SiO_2 formed as thin

films about 100-400 nm or even more in the specimens with high bulk Si content. The agglomerated oxide phases were observed to be complex Cr and Mn oxides that formed first in the core and then Si or Si-Mn oxide surrounding them.

7 Si-oxides were more stable than Cr and Mn oxides, resulting in the formation of small dispersed oxide particles, with spherical or cubical shape with dimensions of approximately 50nm within the internal oxidation zone. The small dispersed particles usually precipitated around complex oxides and intergranular oxide phases.

8 The diffusion path of oxygen in the internal oxidation zone is not only effected by the matrix lattice but also by the matrix/oxides interface. In other words, the existing internal oxides themselves affect the diffusion path for oxygen in the internal oxidation zone. As the larger oxides form normal to the surface, it acts as enhance the diffusion path for oxygen. As the continuous oxide layer parallel to the surface grows, it further prevents the inward diffusion of oxygen to the matrix.

9 The depth of internal oxidation was related to the C potential in that with higher C potential the internal oxidation zone was smaller; this was attributed to the C reacting with O to reduce the free O potential.

10 Internal oxidation will reduce the hardenablity of the surface region of the carburised steel. The micro-hardness in the internal oxidation region was lower than the normal case layer value due to the formation of internal oxidation, and non-martenstic transformation products. A pearlitic microstructure was observed around the internal oxide precipitates close to the surface region of the specimen studied.

11 The results confirm that control the base process, sing higher carbon potentials for the gas carburising process, and Si content in bulk metal, will be beneficial to reducing the internal oxidation phenomena in carburised steel. GDOES has proved to be a valuable tool in investigating the zonal nature of the oxide layers.

FURTHER WORKS

The current research has, for the first time, revealed the growth process of internal oxidation during a commercial carburising process and showed the morphological, structure and composition of the internal oxides by means of cross-sectional TEM and 3D dimensional SEM observations. Future research is proposed in the following areas:

Firstly, an adjustment of the commercial carburising process should be considered by controlling the base process in the carburising process to prevent the formation of massive complex internal oxides thus reducing the degree of total internal oxidation.

Secondly, it is necessary to study the relationship between the different morphologies of the internal oxides since it is clear that different morphologies will have different responses to mechanical properties such as fatigue.

Thirdly, it is acknowledged that the depletion of Si during the initial stages of carburisation to form the continuous surface oxide is highly detrimental. Work could be carried out to study the effect of purposefully providing a source of Si at the surface such that depletion will be reduced. A sol-gel process may be appropriate.

REFERENCES

1. Akiniwa, Y. and Harada. S., Trans. Of The Japan Society of Mechanical Engineering Part A, Vol.**59**, No. 564, p1827-1833 (1993)
2. Arkhipov, I.Y. and Kanunnikova, V.A., Sci.Heat Treat., No.11, p909-913 (1970)
3. Arkhipov, I.Y., Politiskii, M.S., Novikova, A.Y., Yurasov, S.A. and Nikanov, V.F, Met.Sci.Heat Treat., No.10, p867-871 (1970)
4. Arkhipor, I.Y., Batyreva, V. A. and Polotskii, M.S., Metal Science and Heat Treatment, Vol. **14** , No 6, p505-512 (1972)
5. Ashby, M.F. and Centamore, R.M.A., Acta Met., Vol.**16**, p1081-1092 (1968)
6. Ban, H., Canadian Patent, 2,139,301 (1995)
7. Bohm, G and Kahlweit M., Acta Met., Vol.**12**, p641-648 (1964)
8. Bohnenkamp, B. and Engell, H.J., Arch. Eisenhuettebw, Vol. **35**, p1011 (1964)
9. Bosch, R.A., Lenel, F.V. and Ansell, G. S., Trans ASM, Vol. **57**, p960-971 (1964)
10. Burris, K.W., US patent, No: 5,536,335 (1996)
11. Blumenthal, R.N., Proc. of the second international conference on caburising and nitrifing with atmospheres, Ohio, USA, p17-22 (1995)
12. Chatterjee-Fischer, R., Matall. Trans., Vol. **9A**, p1553-1560 (1978)
13. Colombo, G.H., Fusani, F. and Lamberto, M., J. Heat Treat., Vol. **3**, No2 (Dec. 1983)
14. Daneliya, E.P.and Kandyba, G.I., Russian Metallurgy, Vol.4, p162-169 (1987)
15. Dawes, C and Cooksey, R.J., Special report 95: Heat Treatment of Meatls, Iron and Steel Institute, London, p77-92 (1966)
16. Dowling, W.E., Donlon,W.T., Copple, W.B. and Darragh, C.V., Proc. of the second international conference on carburizing and nitriding with atmospheres, ASM International, p55- 60, Ohio, USA (1995)
17. Ebeling, R. and Ashby, M.F., Phil Mag, Vol.**13**, p805-834 (1966)
18. Edenhofer, B., Proc. of the second international conference on carburising and nitriding with atmospheres, ASM International, p37-42 (1995)
19. Edenhofer, B., 5th ASM Heat Treatment and Surface Engineering Conference in Europe', Sweden (June 1999)

20. Evanson, K., Krauss, G. and Medlin,D., Proc. of the second international conference on carburising and nitriding with atmospheres, p61-69, Ohio, USA (1995)
21. Fairbank, L.H. and Palethorpe, L.G.W., Special report 95: Heat treatment of metals, iron and steel institute, London, p57-69 (1966)
22. Foryst, E.P., Stingeder, G., Grasserbauer, M. and Foryst, J., Archives of metallurgy, Vol. **34**, p42-56 (1989)
23. Gantois et al, 3th internaional conference on heat treatment with atmosphere, Gothenburg, Sweden, 7-9 June, 1999
24. Gesmundo, F., Viani, F. and Niu, Y., Oxidation of metals, Vol. **47**, No. ¾, P355-380 (1997)
25. Gunnerson, S., Metal treatment and Drop Forging, Vol.**30**, p219-229 (1963)
26. Hilldenwall, B and Ericsson, T., J. Heat Treat., Vol.**1**, No3, p3-13 (June 1980)
27. Hirai, M., Uno, M. and Nakasato, F., Sumitomo Metals, Vol. **41**, No. 4, P27-34 (1989)
28. Hoffmann, R., Harterei-Technische Mitteilungen., Vol. **39**, No. 3, p99-111 (1984)
29. Hultgren, J. A and Haggelund, M., Trans. Am. Soc. Metals, Vol.**39** (1947)
30. Huin, D., Lanterl, V.,Loison, D., Autesserre, P and Gaye, H., Microscopy of Oxidation-3, p573-586 (1997)
31. Kalinin, A.T. and Novikova, A. Ya, MiTOM, No. 10(1965)
32. Kalnel, V.D and. Yurasov, S. A, Metal Sci. Heat Treat., Vol.**6**, p 451-454 (1970)
33. Kanisawa, H. and Sato, H., J. Japan Soc. Heat Treat., Vol.**37** No.5 p 287-292 (1993)
34. Kanisawa, H., Ochi, T and Koyasu, Y., Nippon Steel Technical Report, No 64, p 50-54, (Jan. 1995)
35. Kanisawa, H. and Sato, H., J. Of the Japan Soc. For Heat Treatment (Japan), Vol. **37**, No.4, p225-230 (Aug.1997)
36. Kanisawa, H. and Sato, H., J. Of the Japan Soc. For Heat Treatment (Japan), Vol. **37**, No.5, p287-292 (Oct.1998)
37. Kary, R. Metal Prog., No. 2 (1948)
38. Kazuo,S., Tatsuo, F. and Hideo, U., Canadian patent No: 2,137,744 (1995)
39. Kikuchi,M., Komine, A. and Kibayashi, Y., J. Of The Soc. Of Mater. Sci., Japan, Vol.**38**, No.425, p 111-116-73 (1989)
40. Kikuchi, M., Ueda,H., Hanai, K. and Naito,T., ADV. IN. SUR. TEAT: TECHNOL-APPL-Z-FF (Japan), Vol.**3**, p 69-74 (1986)

41. Kikuchi,M., Ueda, H.and Natio T, , Metall. Trans. Vol.**18A** , p 156-158 (Jan. 1987)
42. Kim,H. and Kweon, Y., Matellurgical and Materials Transactions A, Vol. **27A,** p2557-2564 (1996)
43. Kim, Y.H. and Lee,S.W., J. Of the Korea Inst. Of Met. & Mater. Vol.**29**, No.11, p1131-1138 (1991)
44. Kimura,T., Tanaka,H. and Nakamura, S., Electric Furance Steel (Japan), Vol.**68**, PT.1, p7-15 (Jan. 1998)
45. Kizu, T., Nagaki, Y., Inazumi, T. and Hosoya, Y., ISIJ International, Vol.**42,** No.2, p206-214 (2002)
46. Kool, B.J. and DE Hosson, TH. M., Acta Mater., Vol.**46**, No 6, p1909-1922 (1998)
47. Koyasu, Y. and Kanisawa , H.,Ochi,T.,Yanase, M.,Takada, H.,Natio, K. and Ishikawa, H., Nippon Steel Technical Report,No, 53, p 35-43, (April 1992)
48. Kozlovskii, I.S., Kalinin,A.T., Novikova, A.Y., Lebedeva, E.A. and Feofanova, A.I., Metal Sci. Heat Treat., No3 p157-161 (1967)
49. Kozlovskii,I.S., Manevskii, S.E. and Kazachenko, Matallovedenie I Termicheskaya Obrabotka Metallow, p7-10 (June 1980)
50. Krauss,G., Advanced material and processes (USA), Vol.**148,** No 6, p36Z-36DD (Dec. 1995)
51. Krauss. G, 5th ASM heat reatment and surface engineering conference in Europe, June 7-9, Sweden (1999)
52. Krishtal, M.A. and Mokroua, A.M, Diffusion Process in Metal, p44- (1974)
53. Kurokasa, Y., Kamada, Y., Nishida,K. and Murai, N., Sumitomo Metals (Japan) , Vol. **48,** No4, p204-206 (Oct. 1996)
54. Lanterl,V., Huin, D., Drillet, P. and Gaye, H., Microscopy of Oxidation –2, Institute of materials, p535-550 (1993)
55. Lanterl, V., Huin, D.,Drillet, P., Bouleau, D., Henry, P. and Gaye, H., Microscopy of Oxidation-3, Institute of materials, p535-550 (1997)
56. Li, Y and morral, J.E, Acta Materials, Vol. **50,** p3683-3691 (2002)
57. Liu, J. Y. and Chang, S. C., Corrosion Science, Vol. **39**, No. 6, p1021-1035 (1997)
58. Lohrmann, M and Lerche, W., Heat Treatment of Metals, No4, p85-90 (2000)
59. Maak , F., Z.Metallk, Vol. **52,** p545-546 (1961)
60. Meijering, J.L. and Druyesteyn, M. J., Philips Res. Rep., Vol. **2,** p81 (1947)

61. Meijering, J.L. Advances in Materials Research, ed. by Herbert Herman, Vol.**5**, p1-80 (1977)
62. Michael, J.R and Stephenson, E.T., Metallurgical transactions A, Vol. **19A**, p 953-959 (1988)
63. Murai, N., Tsunura, T. and Hasebe, M., 10^{Th} international congress of the international federation for heat treatment and surface engineering', p55-70 (1999)
64. Murai, N. and Aihara, K., Kanbara, S., Tsumura, T. and Nishida, K., Sumitomo Metals (Japan), Vol **45**, PT 4 p11-21 (1993)
65. Nakamura, M and Matsushima, Y., Hasegawa, T. and Nakatani, Y., KOBELCO Technology Review, No. 16, p14-19 (1993)
66. Nakanish, E., Ueda, H. and Kajiura, T., Journal of the Society of Material Science, Japan, Vol.**26**, N250, P68-73 (1985)
67. Namiki, K. and Isokawa, K., Transactions ISIJ, Vol. **26** p642-648 (1986)
68. Namiki, K. and Sugiura, S., Umegaki, S., Okada, Y. and Tani, I., SAE paper 890531, p71-77 (1989)
69. Natio, T.,Ueda, H. and Kikuchi, M., Metall. Trans. Vol.**15A**, p1431-1436 (July 1984)
70. Naito,T.,Ueda, H. and Kikuchi,M., J. Of The Soc. Of Mater. Sci., Japan, Vol. **32**, No.361, p1162-1166 (1885)
71. Oda, S., Koide, T., Matsui, M. and Yamamoto, Y., JSME International Journal, Series3, Vol. **32**, No.3, P455-459 (1989)
72. Ono, H., Okamoto, K. and Nishiyama, Y, Paper 32, resented at heat treatment 1981, (Sept.1981)
73. Okasaki, K. et al., J.Jpn.Ins.Met.Sci.Heat Treat. (USSR), Vol. **15**, No.7, Plenum Publising, p622-624 (July 1973)
74. Pacheco.J.H. and Krauss. G, J.Heat Treatment, Vol.7, No. 2, p77-86 (1989)
75. Parrish, G., Heat treatment of metals, Vol.1, p 6-12 (1976)
76. Parrish, G and Harper, G. S., Production Gas Carburising, Pergamon Press (1985)
77. Parrish, G., Carburising : Microstructures and Proeries, ASM international, p11-36 (1999)
78. Philibert, J., Solid State Ionics, 117, p7-11 (1997)
79. Porter, D. A. and Easterling , K.E., 'Phase transformations in metals and alloys', T.J. Press Ltd. (1989)
80. Preson, S., Carburiasing: Processing and Performance, ASM International, p191-198 (1989)

81. Rapp, R.A., Acta Met, Vol.**9**, p730-741 (1961)
82. Rapp, R.A., Corrsion , Vol.**21**, p382 (1965)
83. Rapp, R A and H.D.Colson, Trans TMS-AIME, **236**, p1616-1618 (1966)
84. Rhines, F.N., Johnson, W.A. and Anderson, W.A., Trans. AIME, Institute of Materials, **147**, p205-220 (1942)
85. Sakamoto. K, Fukuzumi. T. and Ueno. H, Canada Patent 2,137,744 (1995)
86. Satoshi, O. and Koide T. et al, 'The effect of intergranular oxidation on the bending fatigue strength of case-hardened gears', JSME International Journal, Vol.**33**, No. 3 p455-459 (1989)
87. Scherbedinskii, G.V. and Shumakov, A.I., IZV. Akad. Nauk. SSSR. Met., No 3, p193-199 (May/June1979)
88. Sheehan J. P and Howles M. A. H, SAE paper, 720268, Society of Automotive Engineers, p16 (1972)
89. Shida, Y, and Stott, F.H., Bastow, B.D, Whitle, D.P and Wood, G.C, Oxidation of metals, Vol.**18**, No3/4, p 93-113 (1982)
90. Shinha, A. K., Ferrous physical metallurgy, Butterworth publishers, p379 (1989)
91. Smith, Y.E. and Eldis, G.T., Climax Molybdenum Co., Michgan (1975)
92. Stephenson, E.T., and Michael, J.R., Metallurgical Transactions A, Vol.**19A**, p1876-1878 (1988)
93. Stickels, ASM metal handbook, Vol. **4**, Heat treating, Chapter 3 Gas Carburising, ASM International, USA. p312-467 (1991)
94. Stott, F.H., Wood, G.C., Whittle, D.P., Bastow, B.D., Shida,Y. and Villafane,M., Solid State Ionics, Vol.**12**, p365-374 (1984)
95. Stott, F.H., and Wood, G.C., Materials Science and Technology, Vol.**4**, P1072-1078 (Dec. 1988)
96. Stratton, P.F. and Tsujimoto, Y., Heat Treatment of Metals, p29-32, No2 (2000)
97. Sun, Y., Xu, D. and Li, J., Heat treatment and Surface Engineering, ASM INTER., p 305-311 (1988)
98. Swisher, J.H., Oxidation of Metals and Alloys', ed. by Douglass, D.L., ASM, p253 (1971)
99. Takada. J. and Adachi, M., Journal of Materials Science, Vol.**21**, No.6, P2133-2137 (1986)
100. Takada. J and Yamamoto, S.,Kikuch, S. and Adachi, M., Mtallurgical Transactions A, Vol.**17A**, p221-229 (1986)
101. Tanaka, H., Kobayashi, S.,Nakasato, F. and Uno, M., J. of Iron and Steel Ins.

Japan, Vol. **79** No 1, p 90-97 (Jan. 1993)

102. Tarlock, G.L, Microscopy of Oxidation, p172-182 (1990)
103. Thyne, C.V. and Krauss, G., Carburising : Process and Performance, ASM International, p333-340 (1989)
104. Udyavar, M and Young, D.J., Corrosion Science, Vol.**42**, No. 5, P861- 883 (2000)
105. Van Valck, L.H., International Metal Reviews, P207-212 (1977)
106. Verhoeven, J.D., Chen, N., and Bevolo, A., J. Heat Treating, Vol. **9**, No. 2 p73-80 (1992)
107. Villafane, A. M. PhD thesis, University of Manchester, 1983
108. Wang, H., Metal Heat Treatment (Chinese), No. 3, p 24-29 (1991)
109. Wagner, C., Z Elektrochem. Vol.**63**, p772-790 (1959)
110. Williams, D.M., and Smiths, G.C., in 'oxide dispersion strengthening' edited by Antell, G.S., New York, p509-536 (1968)
111. Williams, R.G. and Cook, W.T, Reported No. SL/MA/TN/S2917/6/97/D, Swinden Technology Centre, Corus (1997)
112. Williams, R.G. and Cook, W.T, Reported No. SL/MA/R/S2917/6/98/D, Swinden Technology Centre, Corus (1998)
113. Wolf, J.S. and EVans, E.B., Corrosion, Vol.**18**, 129t (1962)
114. Wolf, J.S., Weeton, J.W. and Freche, J.C., NASA technical note NASA TN D -2813 (May 1965)
115. Wood, D.L., Trans TMS-AIME, **215**, p925-932 (1959)
116. Wood, G.C, and Stott, F.H., Materials Science and Technology, Vol.**3**, P519-530 (1987)
117. Wood, G.C, Stott, F.H., Whittle, D.P., Shida, Y. and Bastow, B. D., Corrosion Science Vol.**23**, No.1, p9-25 (1983)
118. Woolhouse, G.R. and Brown, L.M., J Inst. Metals, Vol. **98** , p106-110 (1970)
119. Yi, M. and Lin, J.S, Transactions of Metal Heat Treatment, Vol.**12** No. 2 , p14-20 (1990)
120. Young, D.J., Materials at High Temperature, Vol.17, No. 4, p465-470 (2000)

Generally Reference:

1. American Society for Metals, Oxidation Of Metals and Alloys, Metals Park Ohio, USA, 1970
2. Andrens, K. W., Dyson, D.J. and Keown, S. R., Interpretation of electron diffraction Patterns, ADAM Hilger, Ltd., London, UK, 1967
3. Birks, N. and Meier, G.H., Introduction High Temperature Oxidation of metals, Edward Arnold Ltd., 1983
4. Belk, J.A., Electron Microscopy and Microanalysis of Crstalline Materials, applied Science publishers, 1979
5. Gaskell, D.R., Introduction to Metallurgical Thermodynamics, Scripta Publishing Company, Washington, D.C., USA, 1973
6. Goldstein, J.I.and Yakowitz, H., Practical Scanning Electron Microscopy, Plenum Press, 1975
7. Krauss, G., Heat Treatment and Surface Engineering, ASM International, 1988
8. Krauss, G., Carburising: Processing and Performance, ASM International 1989
9. Lee, W.E. and Rainforth, W.M., Ceramic Microstructures, 3.4 Electron Microscopy, 1994
10. Loretto, M. H., Electron beam Analysis of Materials, Chapman & Hall, London,1994
11. Nencomb, S.B.and Bernett, M. J., Microscopy of Oxidation, Institute of Materials, 1993
12. Parrish, G., Carburising: Microstructures and Properties,ASM Inernational, Maerials park, OH, USA, 1999
13. Parker, R.H., An Introduction to Chemical Metallurgy, Pergamon Press Ltd.,1978
14. Porter, D.A. and Easterling, K.E., Phase Transformations in Metals and Alloys, Chapman & Hall, London, 1993
15. Read-Hill, R.E., Physical Metallurgy Principle, PWS Engineering, Boston, Massachusetls, USA, 1973
16. Shinha, A.K., Ferrous Physical Metallurgy, Butter Worths Publishs, USA, 1989
17. Watt, I.M., The Principles and Practice of Electron Microscopy, Cambridge University Press, UK, 1985
18. Willams, D.B. and Bary Cater, C., Transmission Electron Microscopy, 2. Diffraction; 3.Image; 4. Spectrometry. Plenum Publishing Corporation, New York, USA, 1996

THE RAW ANALYTICAL DATA RELEVANT THIS THESIS

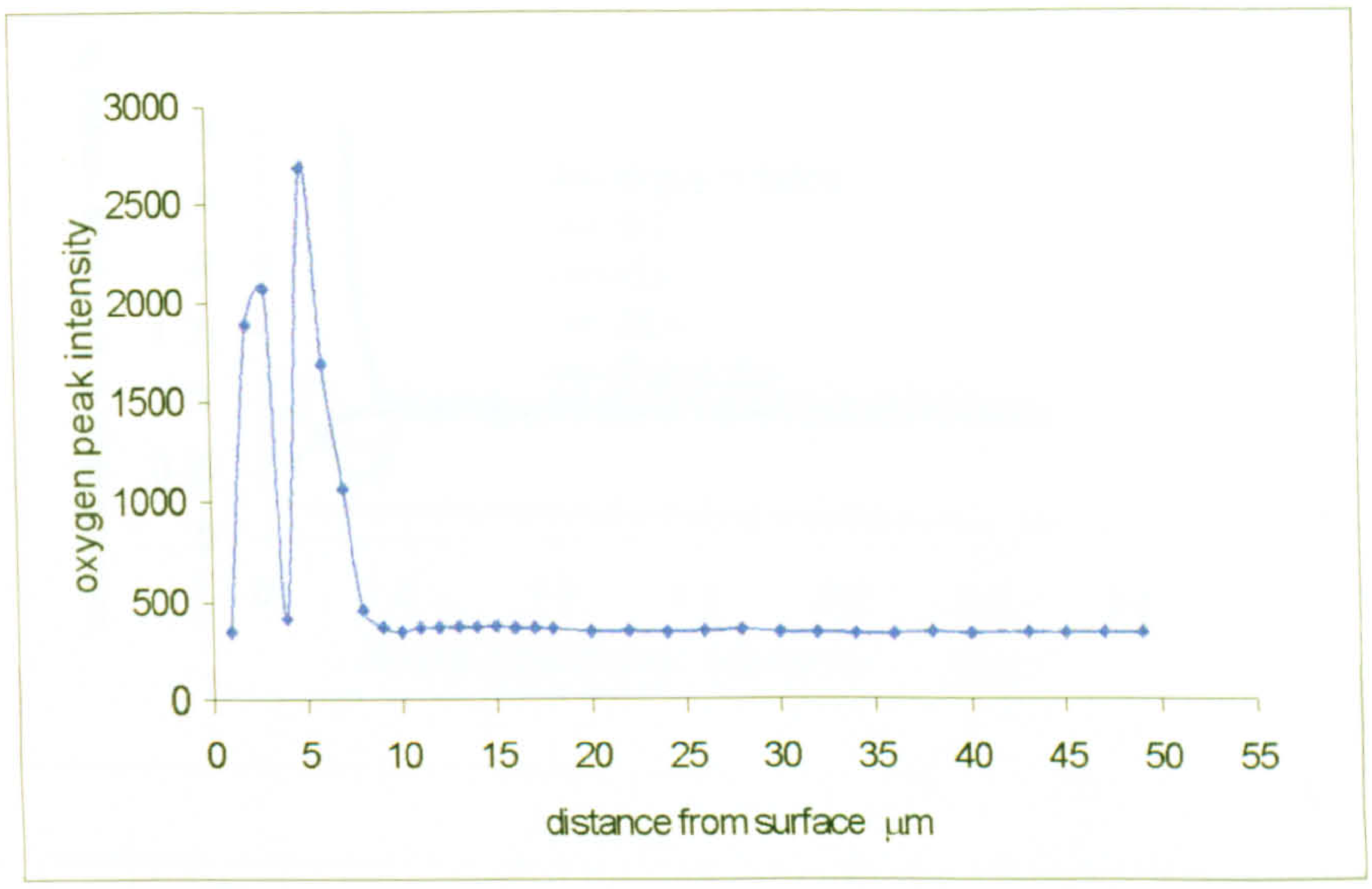

a. 1.0h

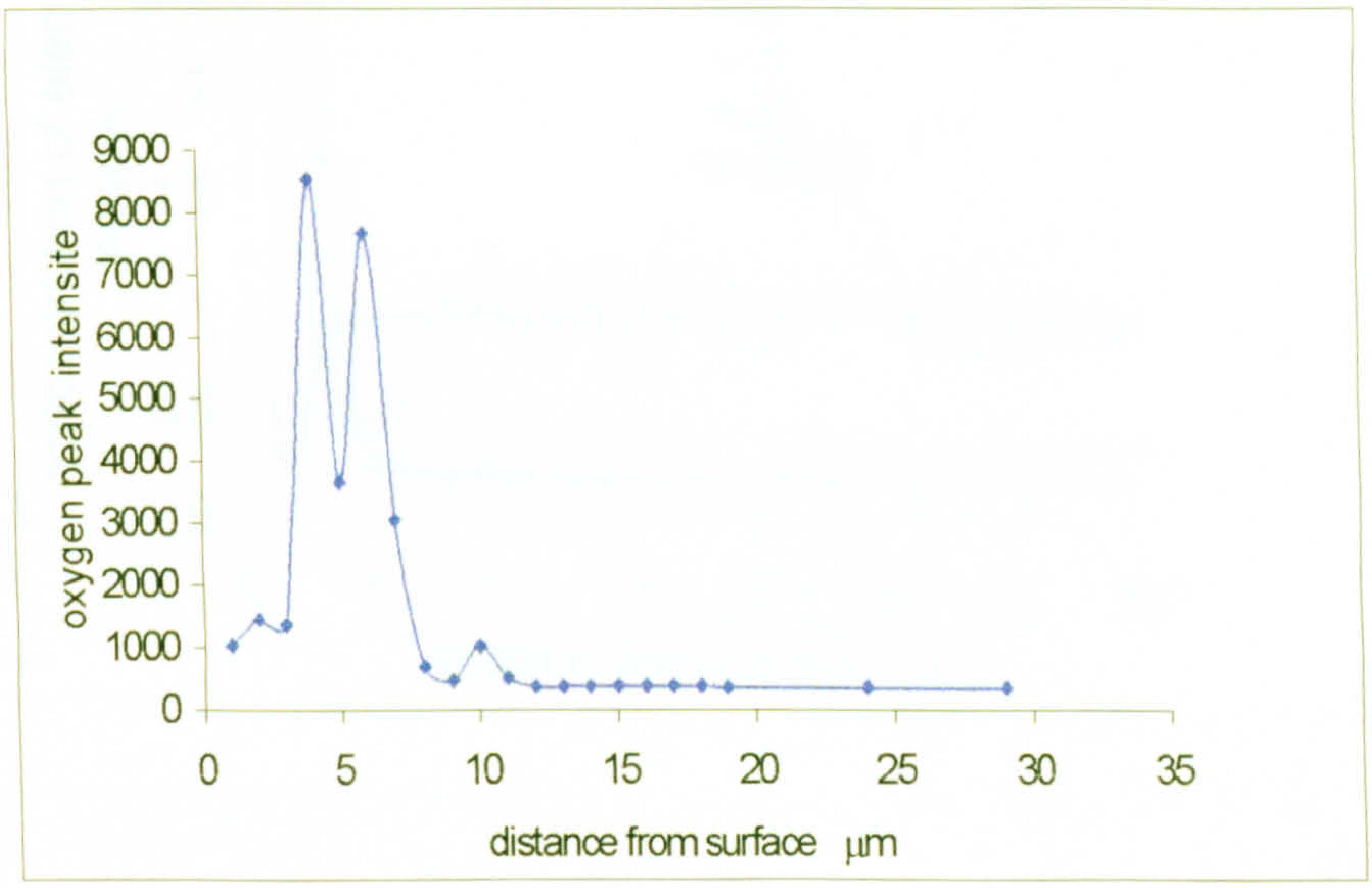

b.2.0h

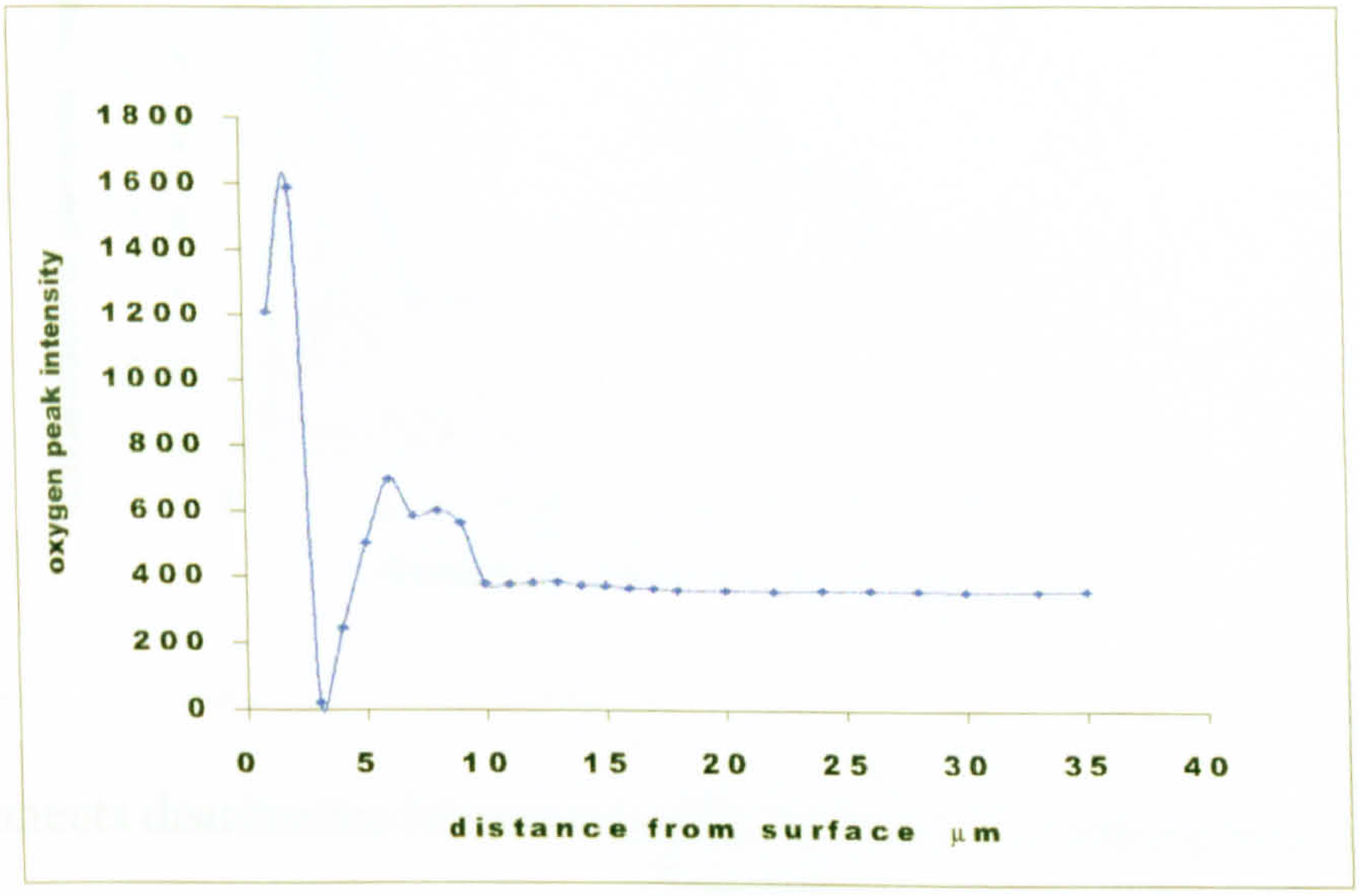

c. 5.8h

Fig. 1 Oxygen penetration in the specimens. a B1-3 b. B1-4, c B1-5

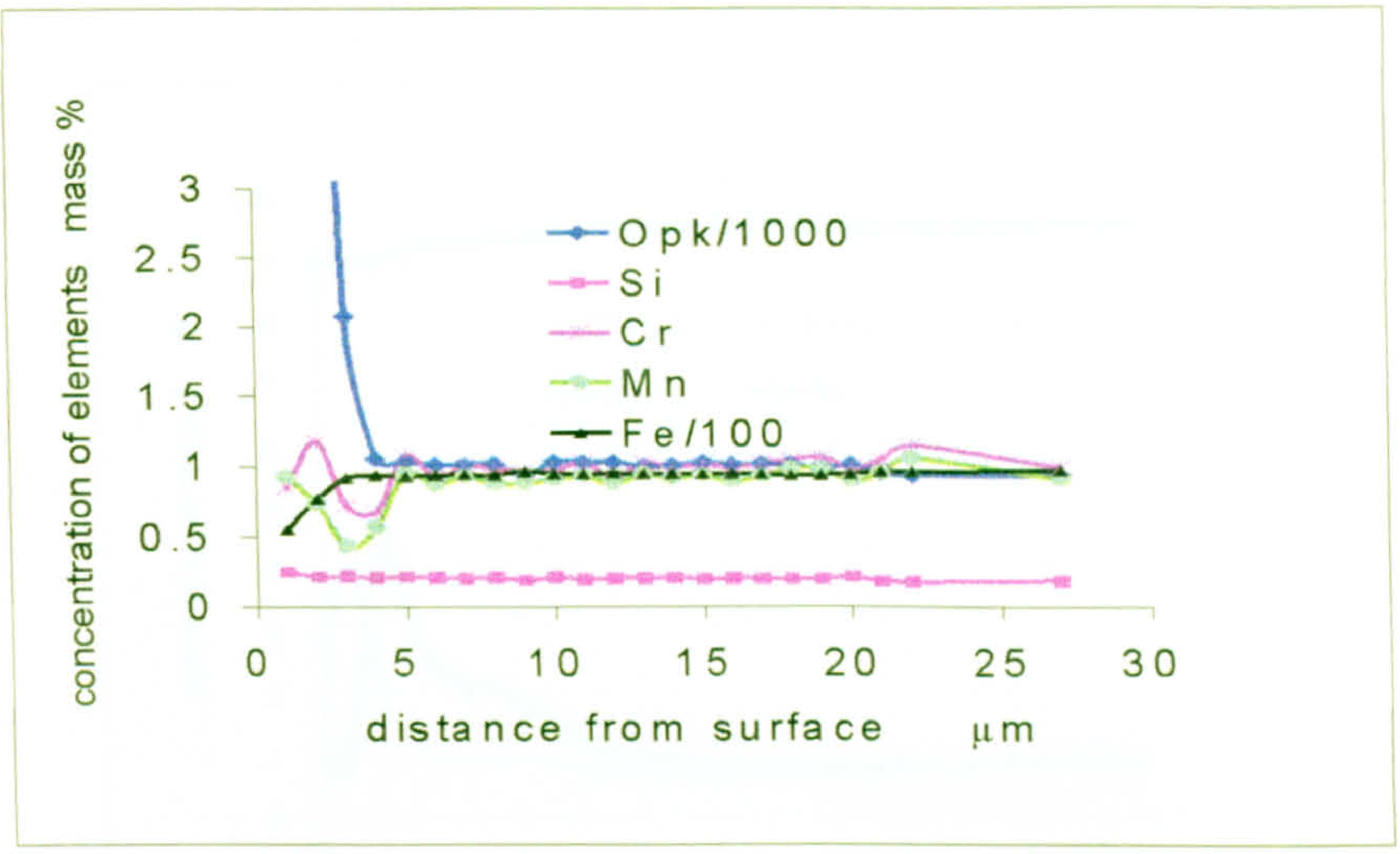

a.0.25h

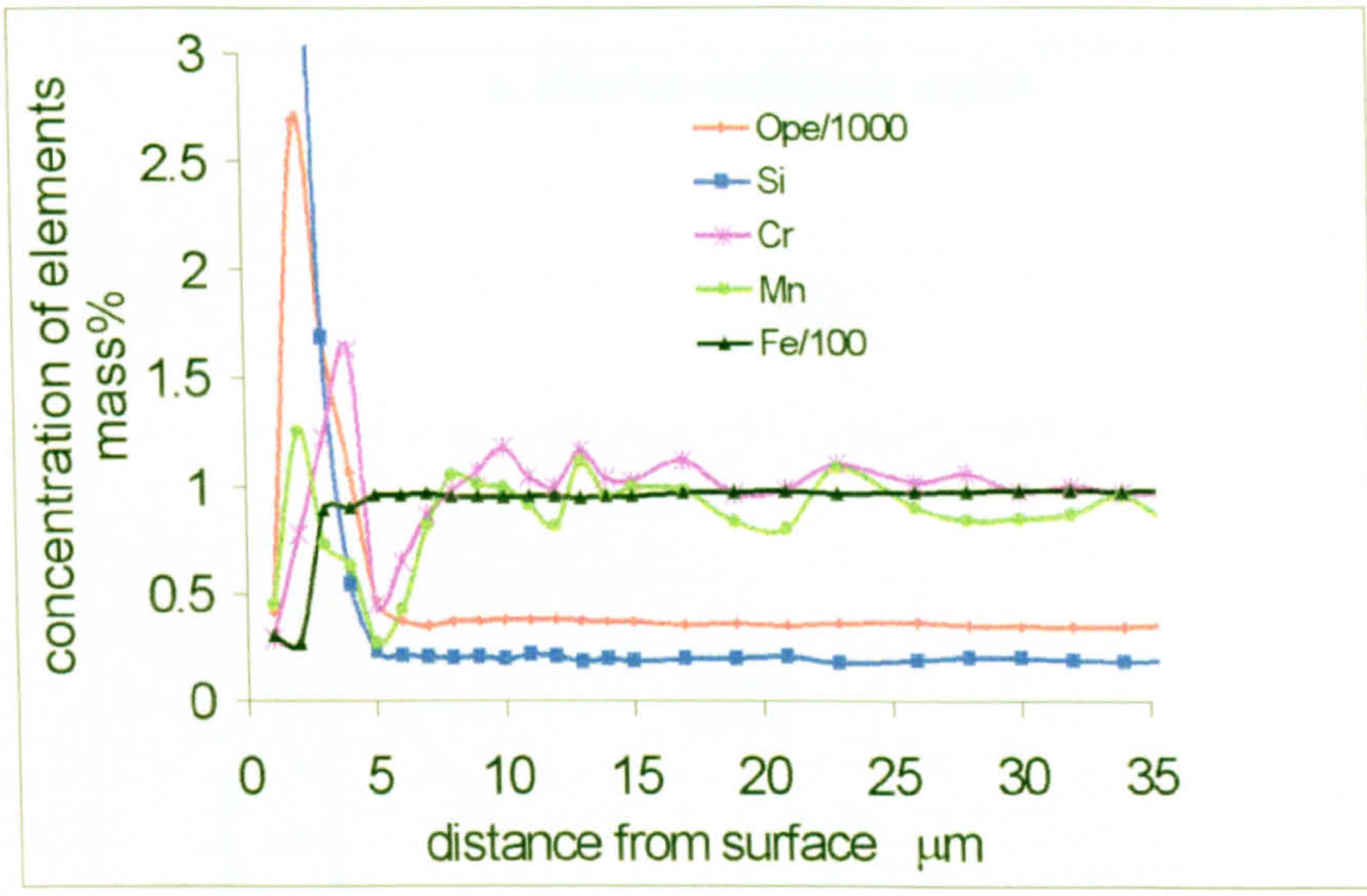

b.1.0h

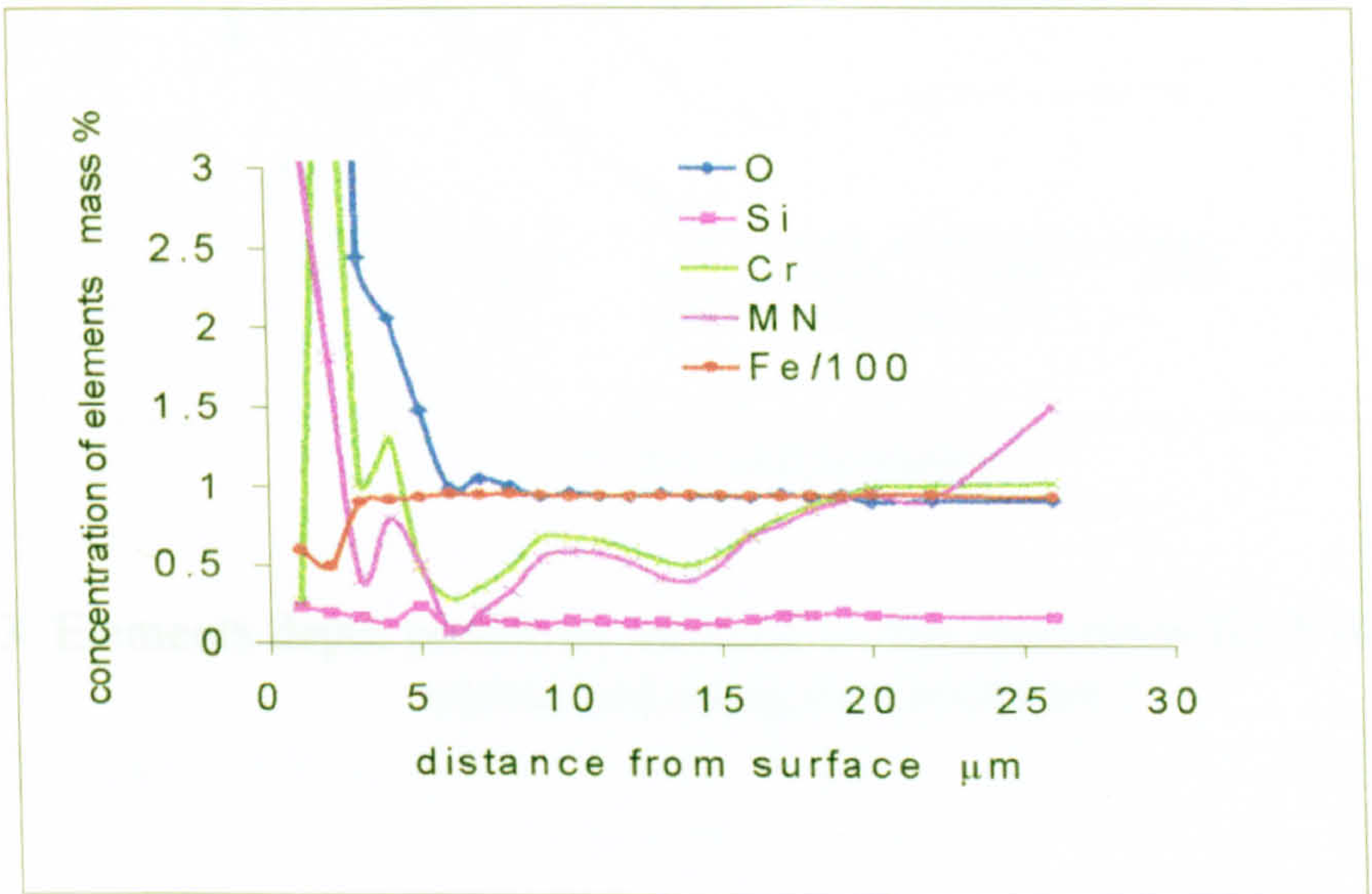

d. 11.0h

Fig. 2 Elements distribution in specimens B1 carburised using the procedure 1 by EPMA line scan

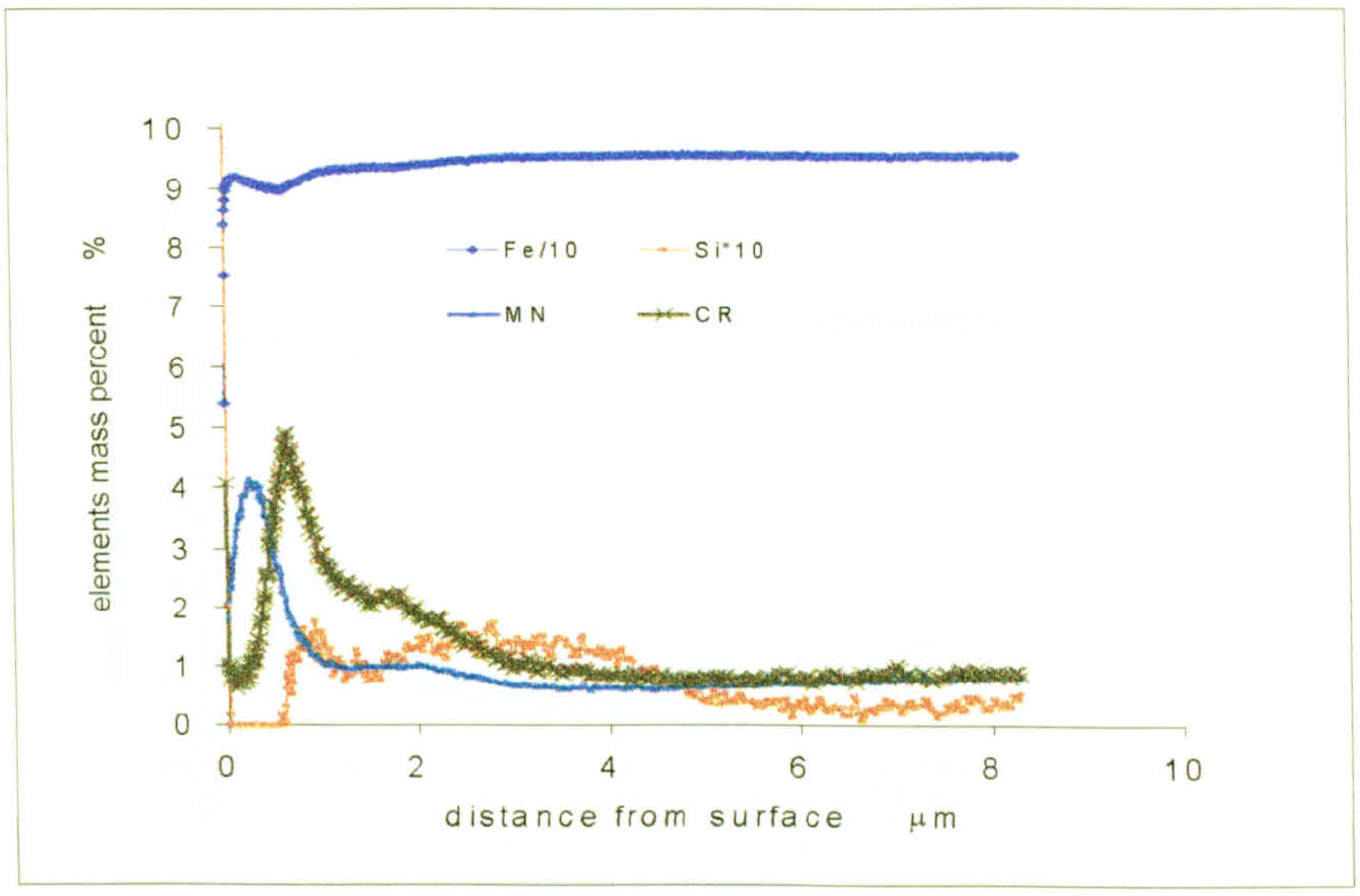

a. internal oxidation region

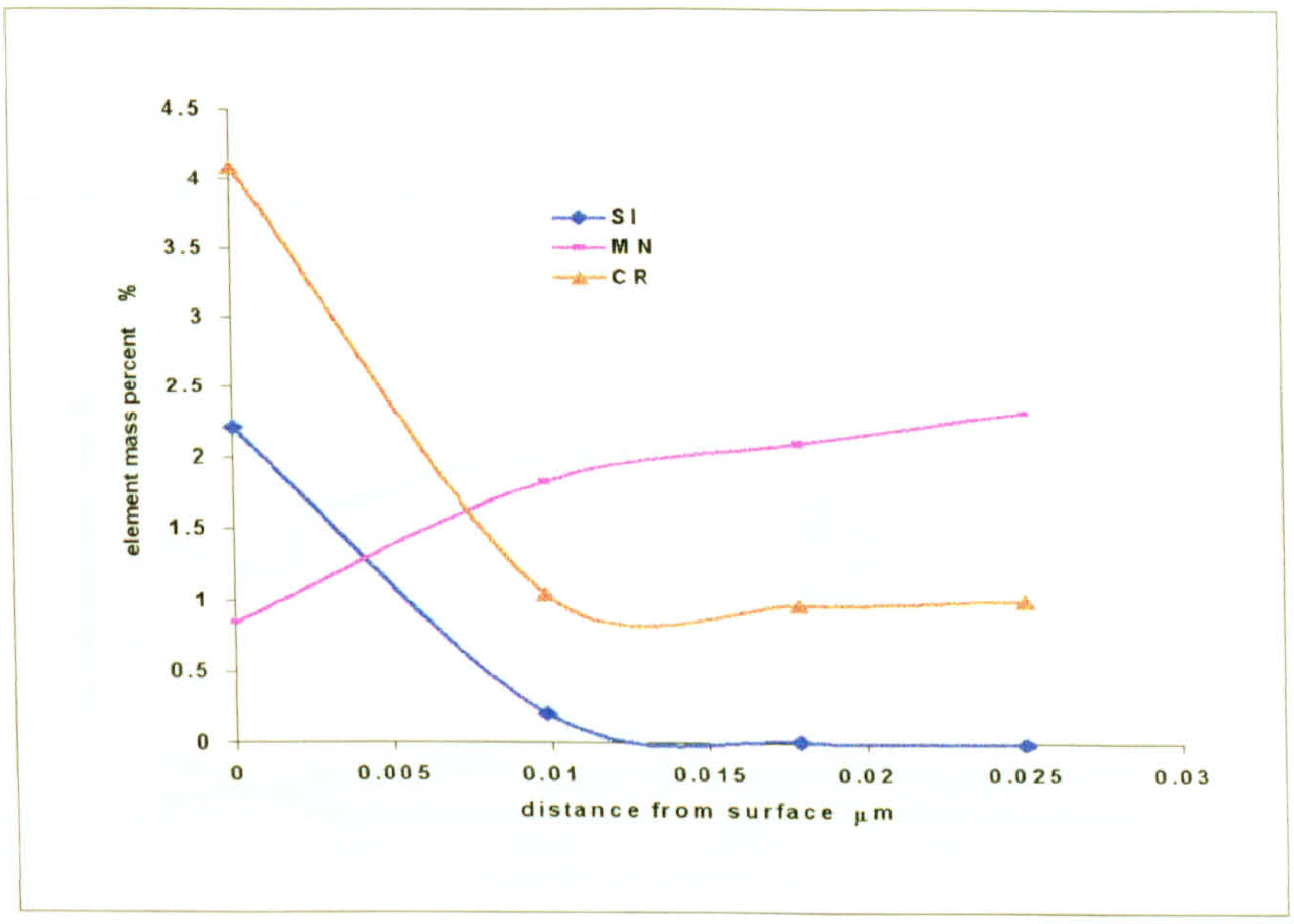

b. top surface region

Fig. 3 Elements depth profile by GDOES in the specimens B1-5 (0.19% Si, 5.8h) carburised using the procedure 1.

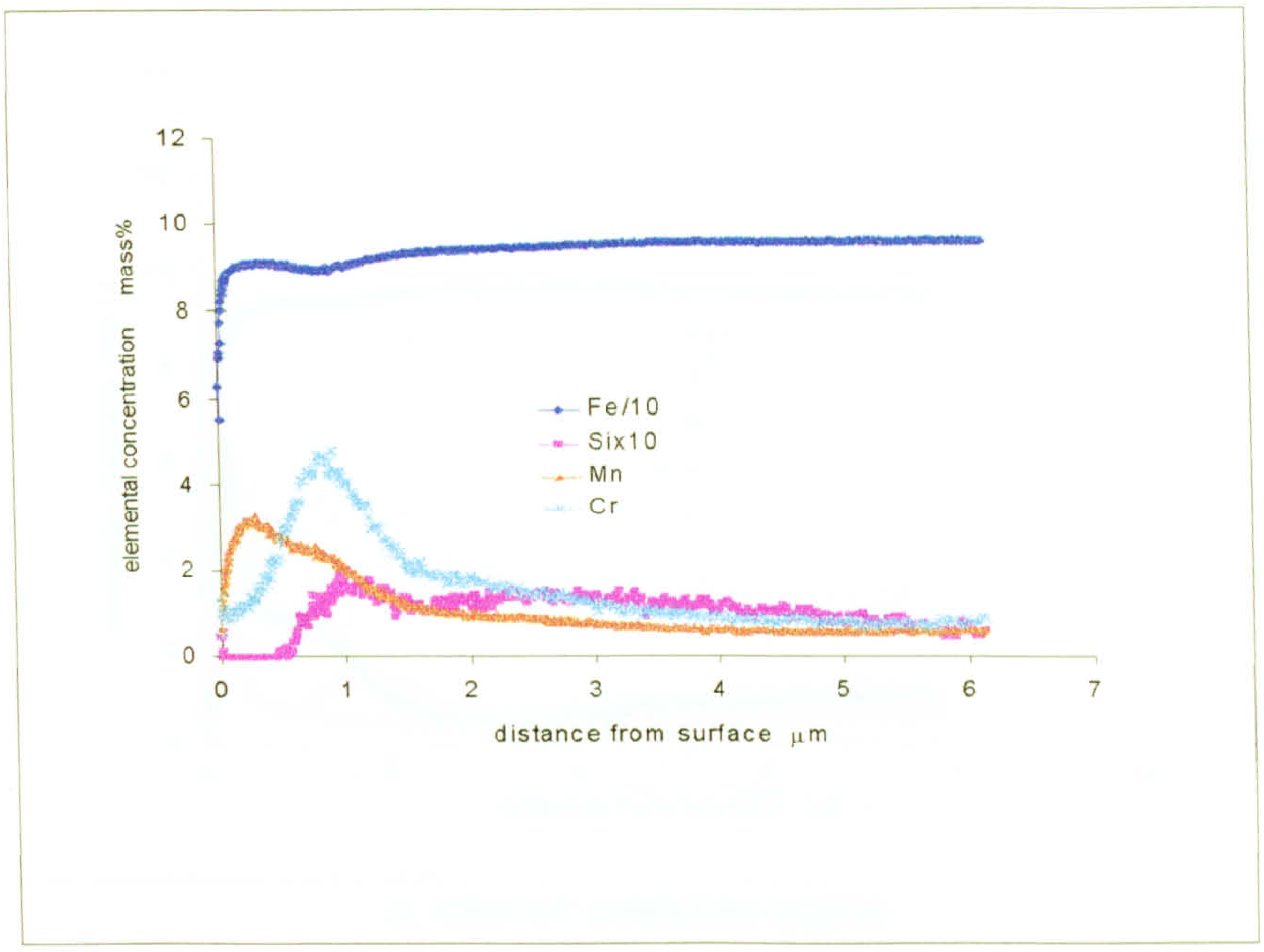

a. internal oxidation region

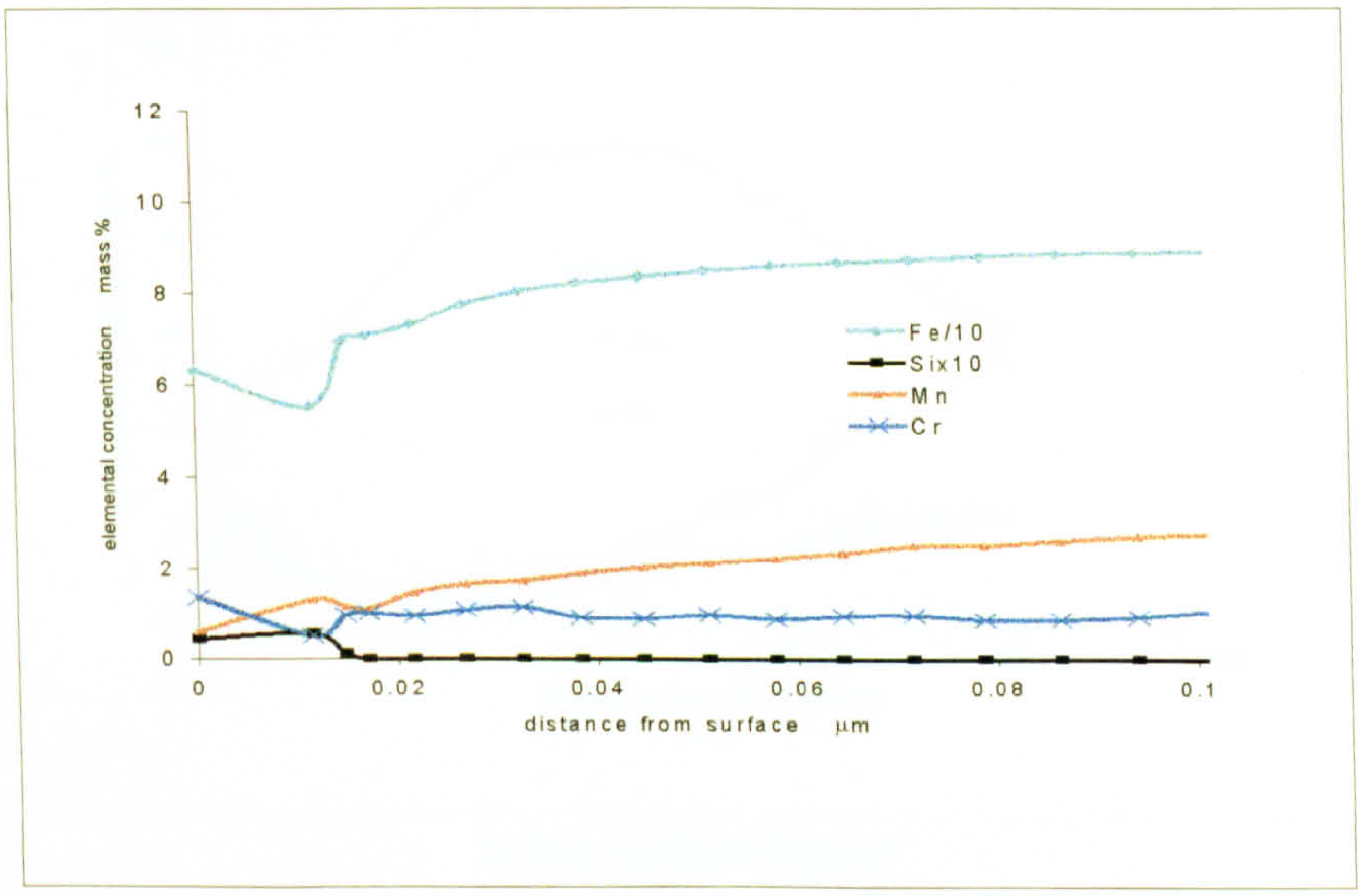

b. top surface region

Fig. 4 Elements depth profile in specimen B1-6 (0.19% Si, 8.0h) carburised using the procedure 1by GDOES.

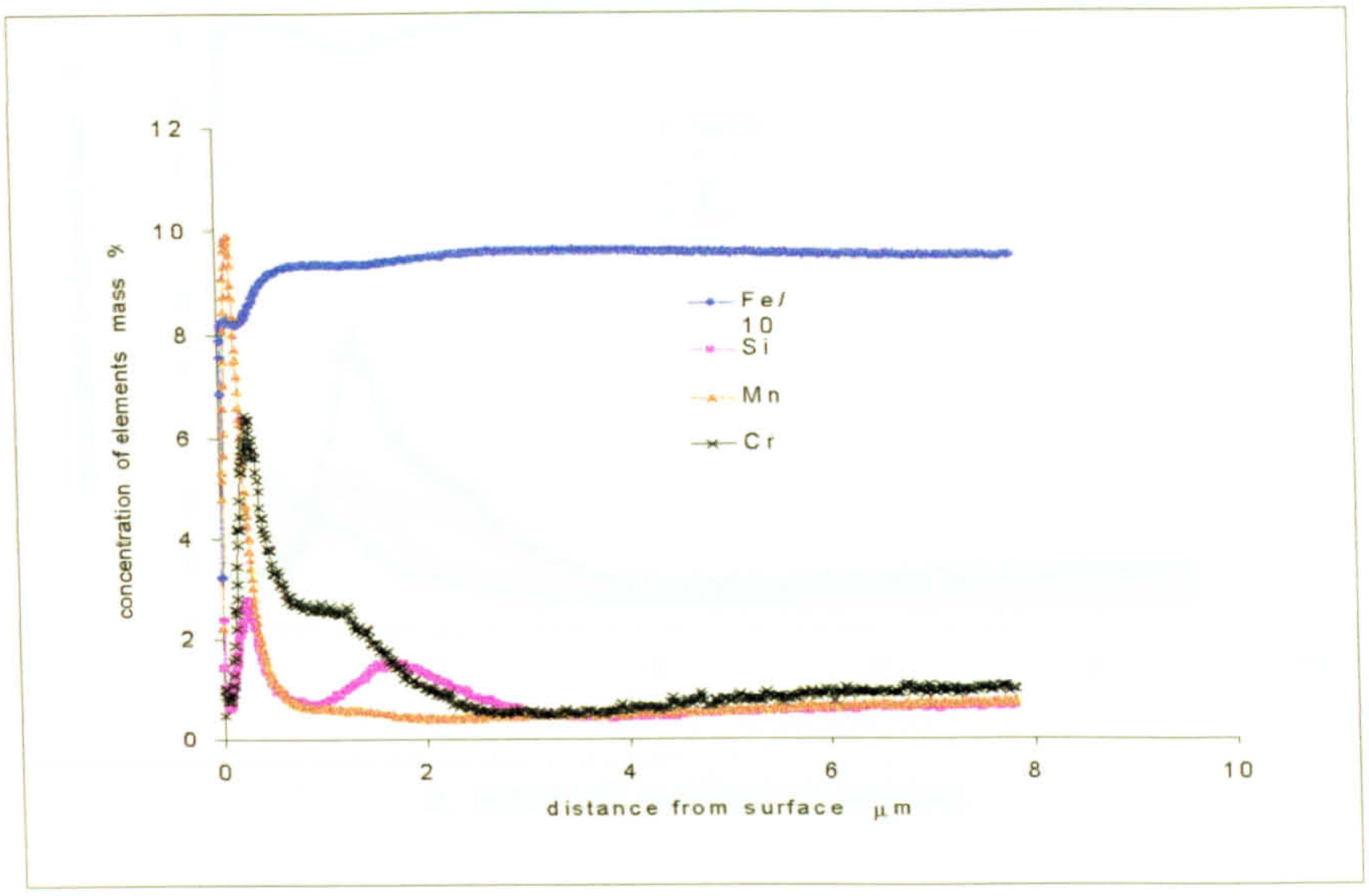

a. internal oxidation region

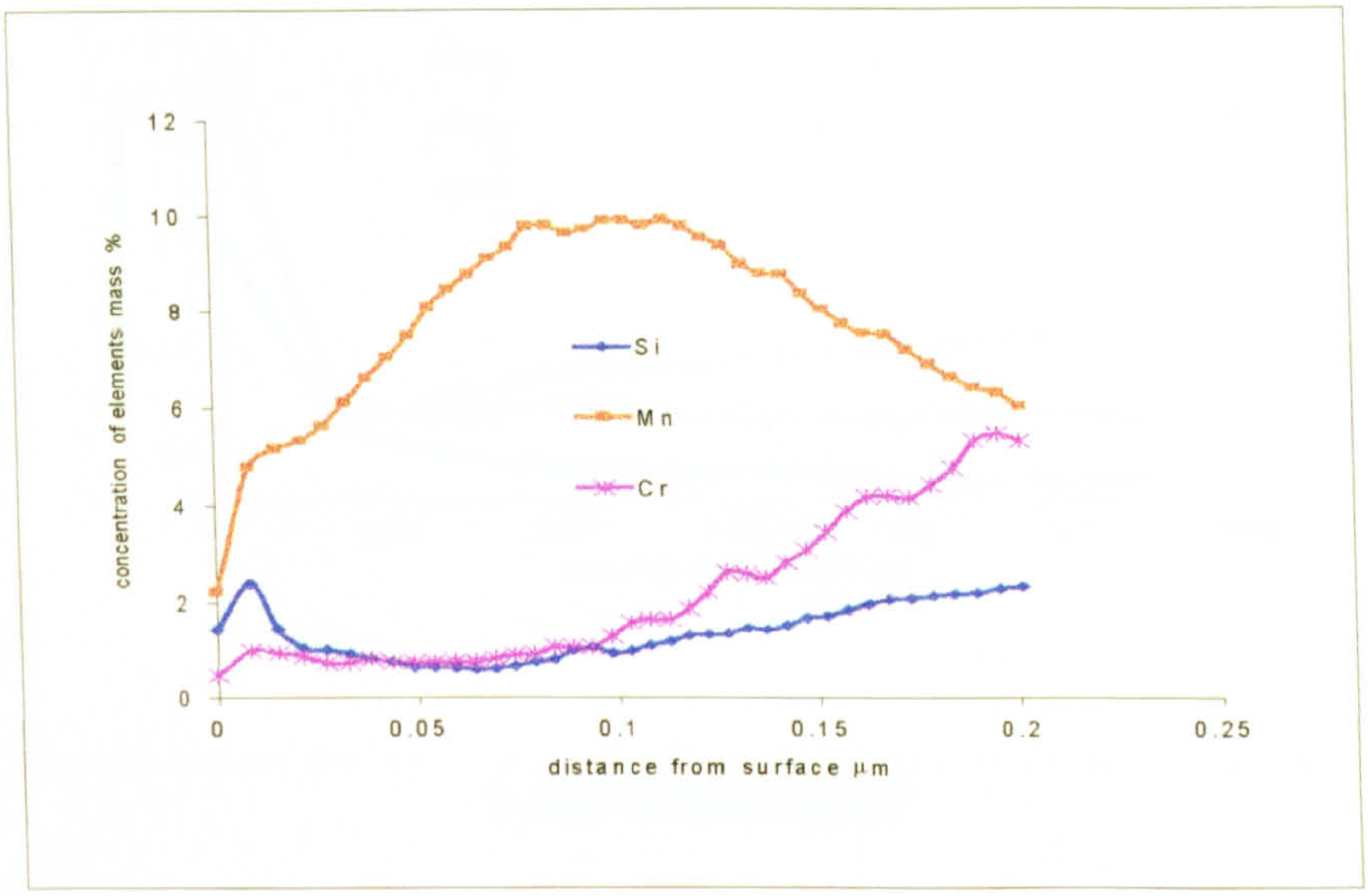

b. top surface region

Fig. 5 Elements depth profile in the specimen E1-4 (0.77%Si) carburised using the procedure 1 for 2.0h by GDOES.

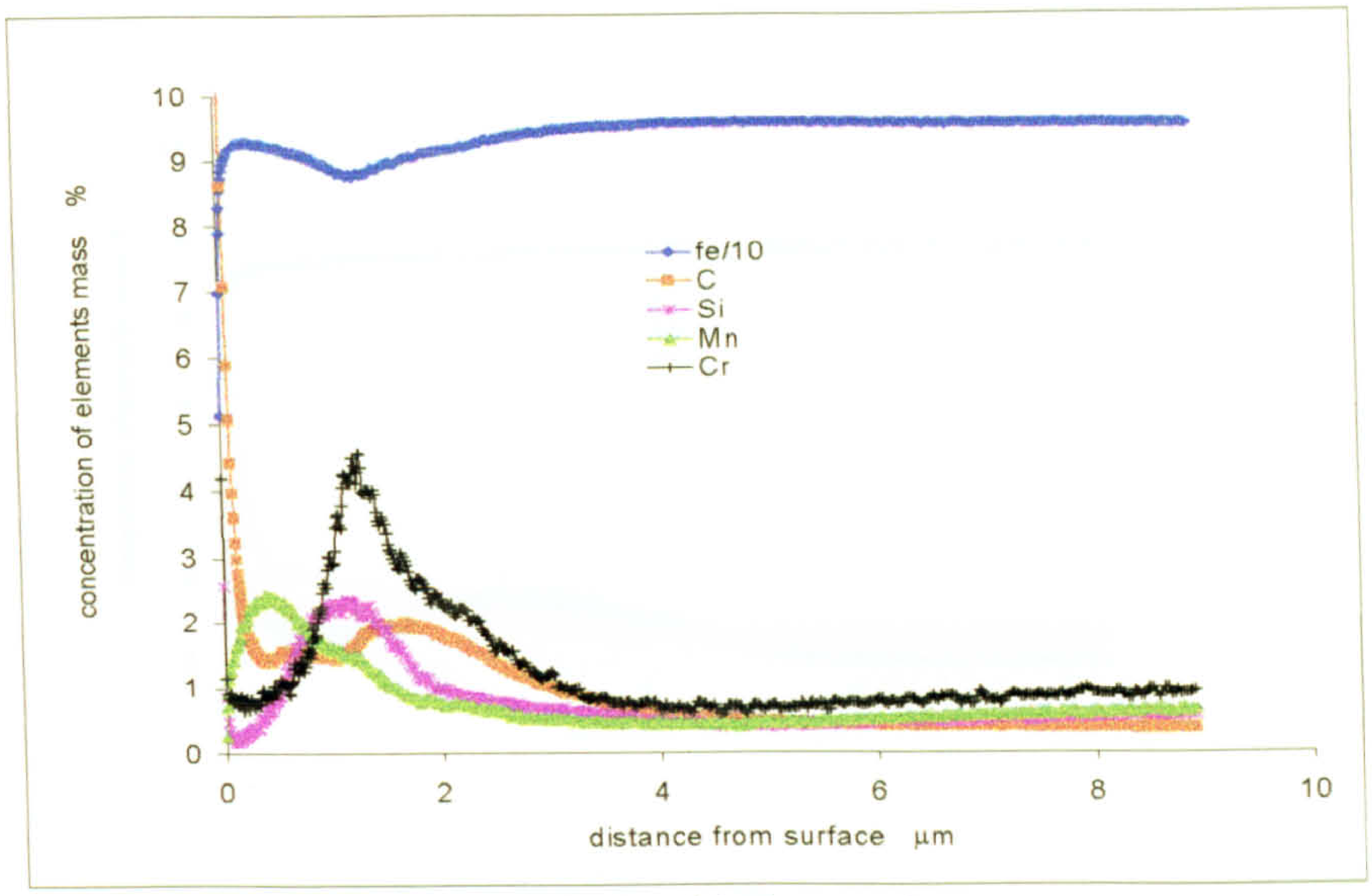

a. internal oxidation region

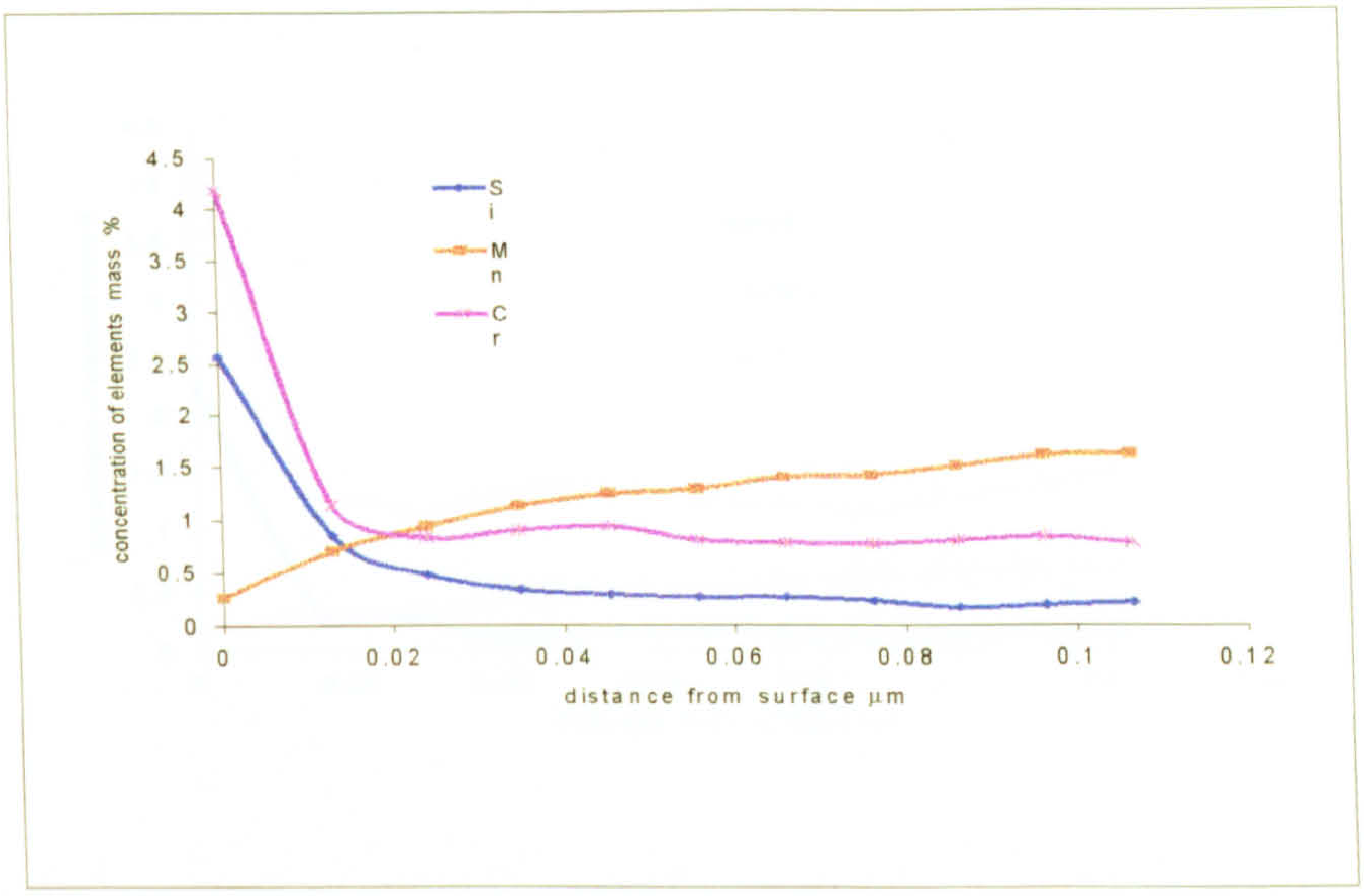

b. top surface region

Fig. 6 Elements depth profile in the specimen E1-5 (0.77%Si) carburised using the procedure 1 for 5.8h by GDOES.

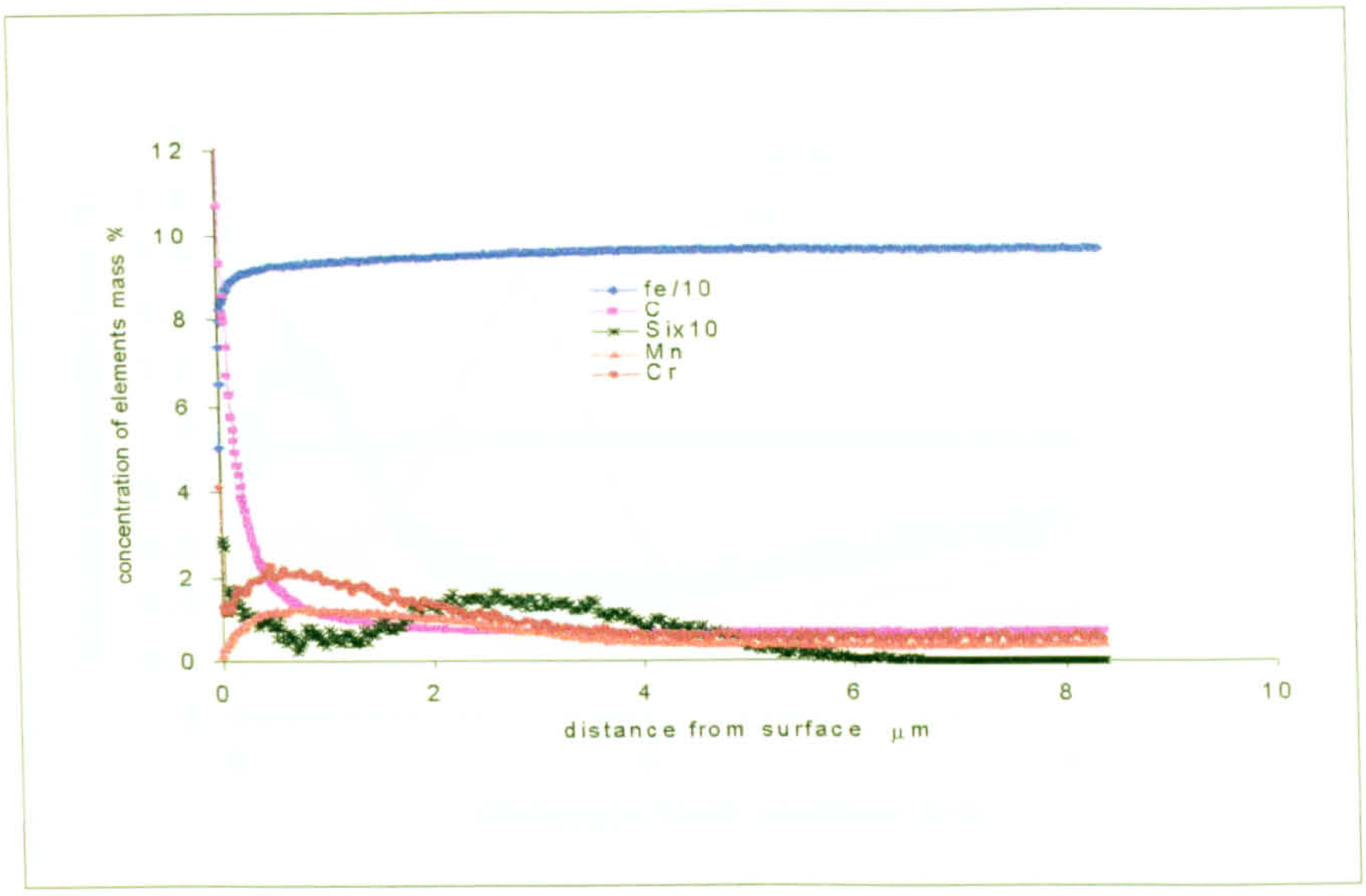

a. internal oxidation region

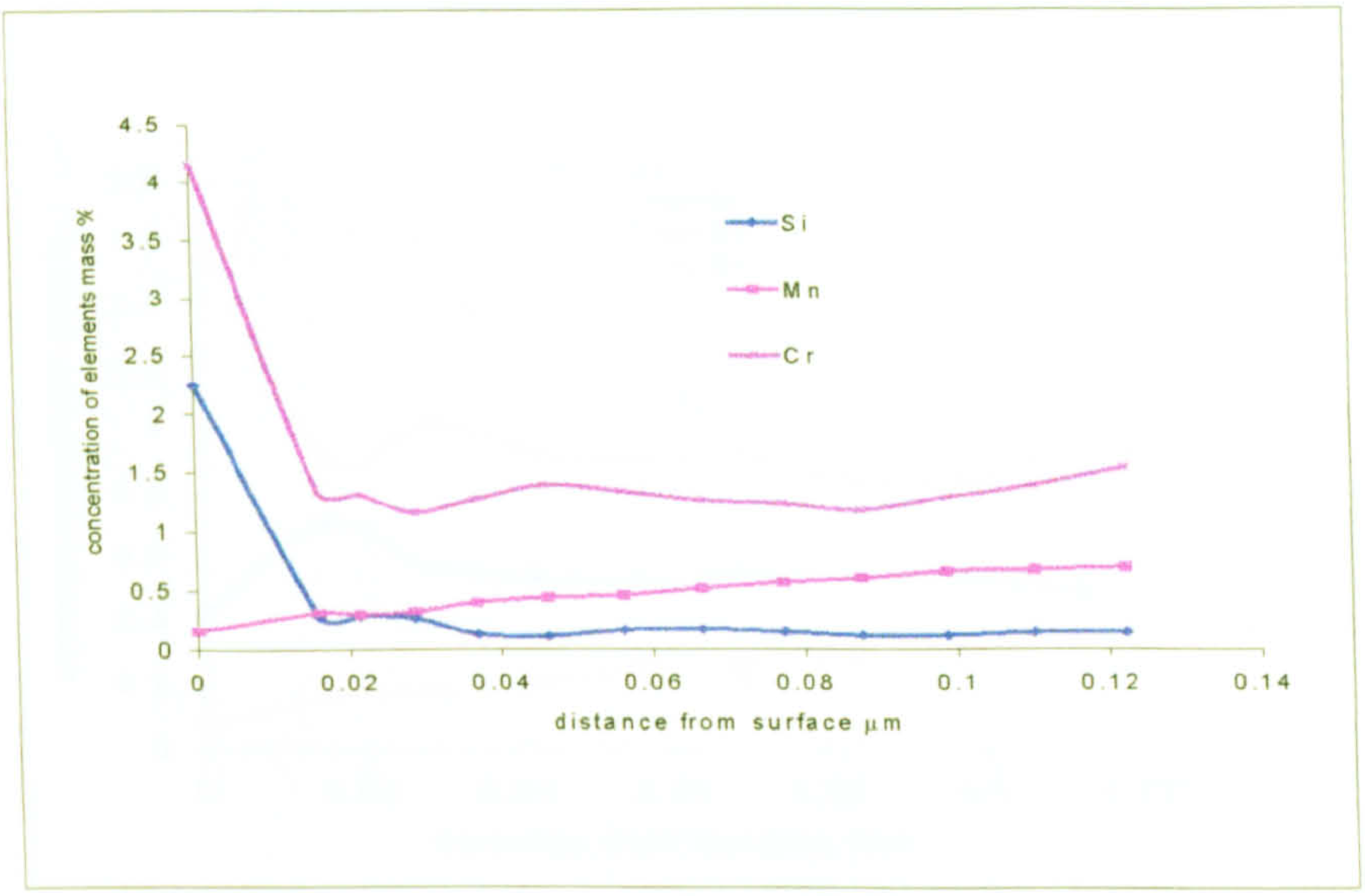

b. top surface region

Fig. 7 Elements depth profile in the specimens A1-8 (0.11%Si,) carbuirsed using the procedure 1 for 16.6h by GDOES.

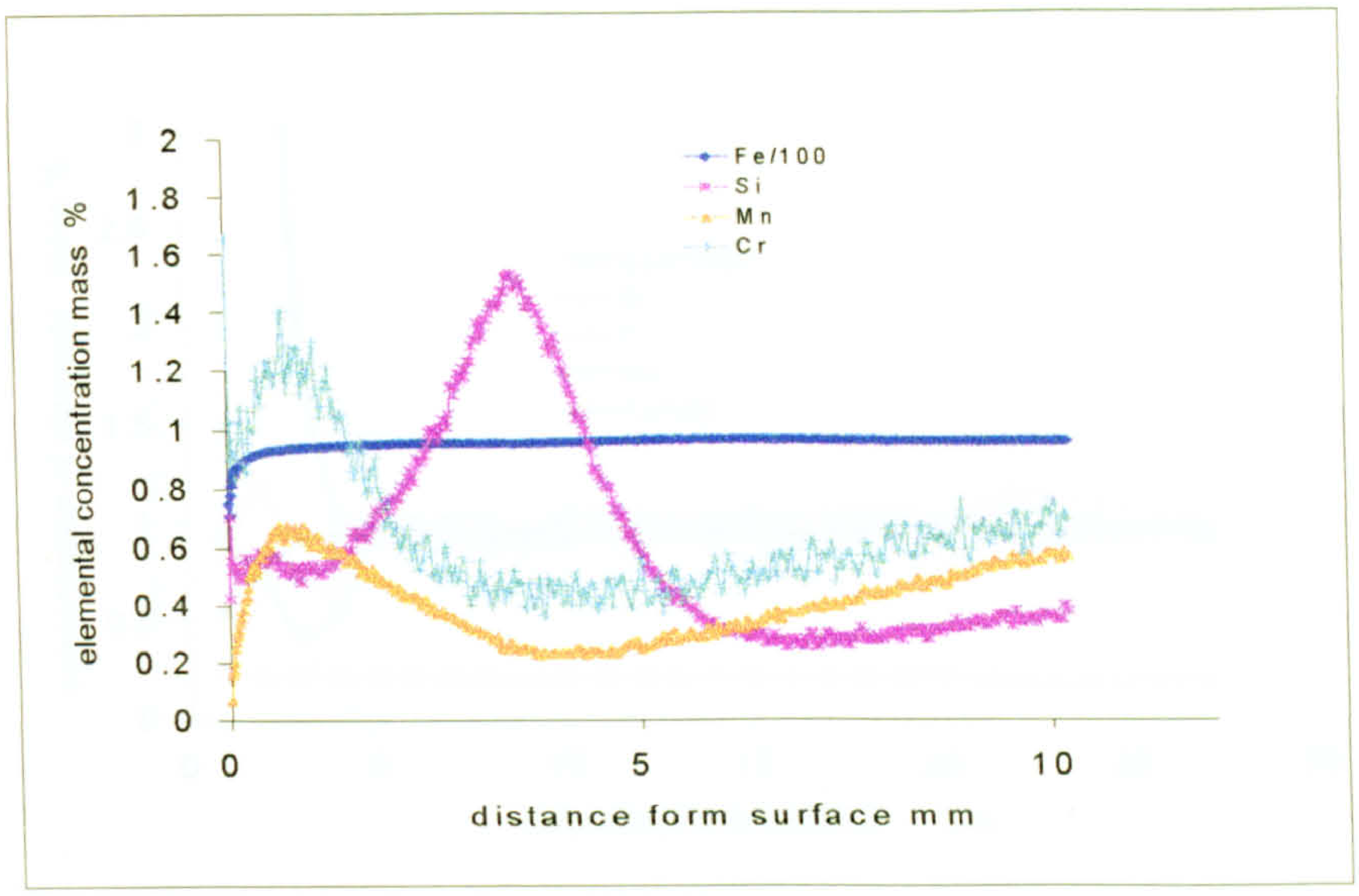

a. internal oxidation region

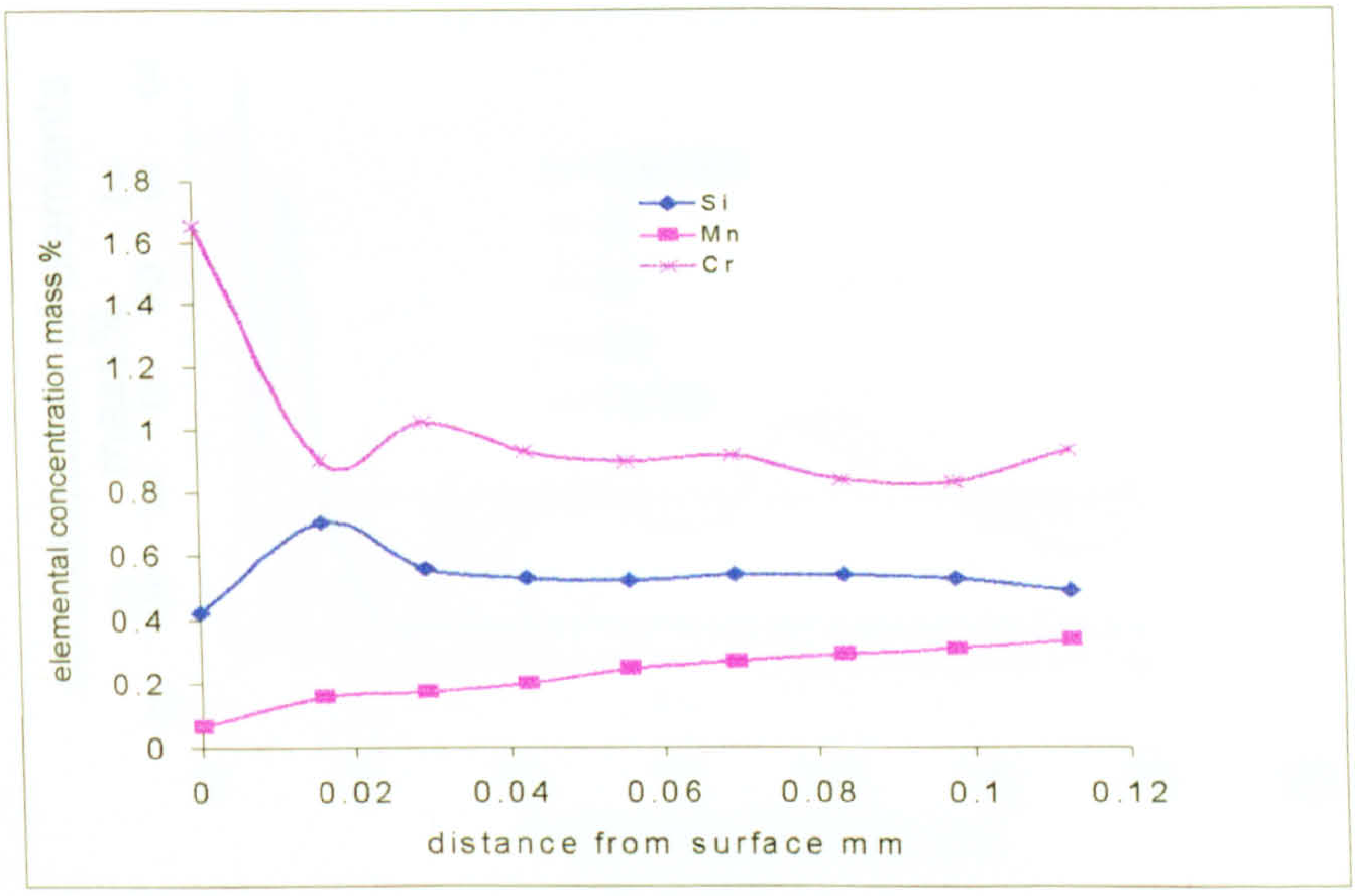

b. top surface region

Fig. 8 Elements depth profile in the specimen D1-8 (0.56%Si) carburised using the procedure 1 for 16.6h by GDOES.

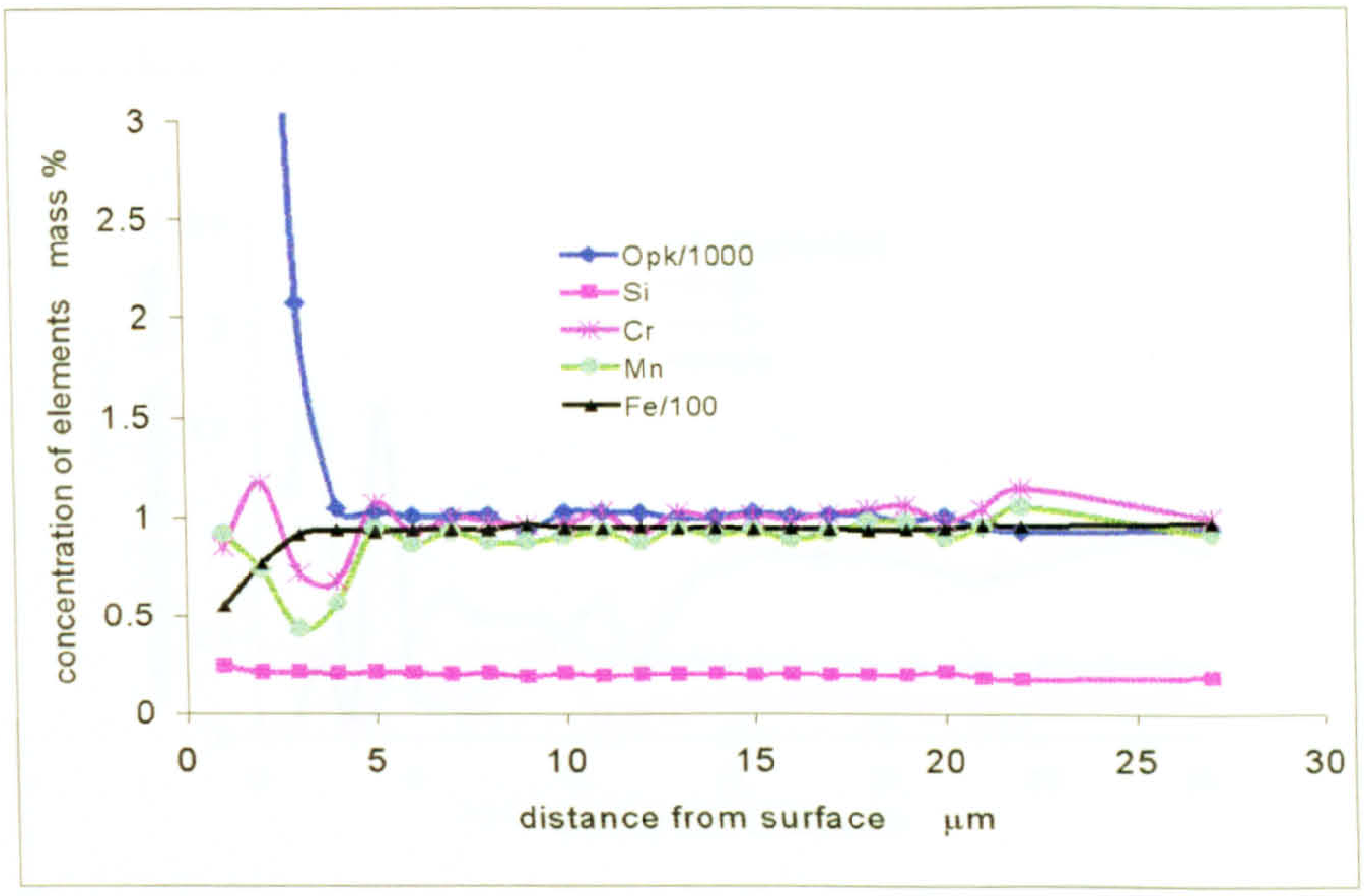

a.0.25hr

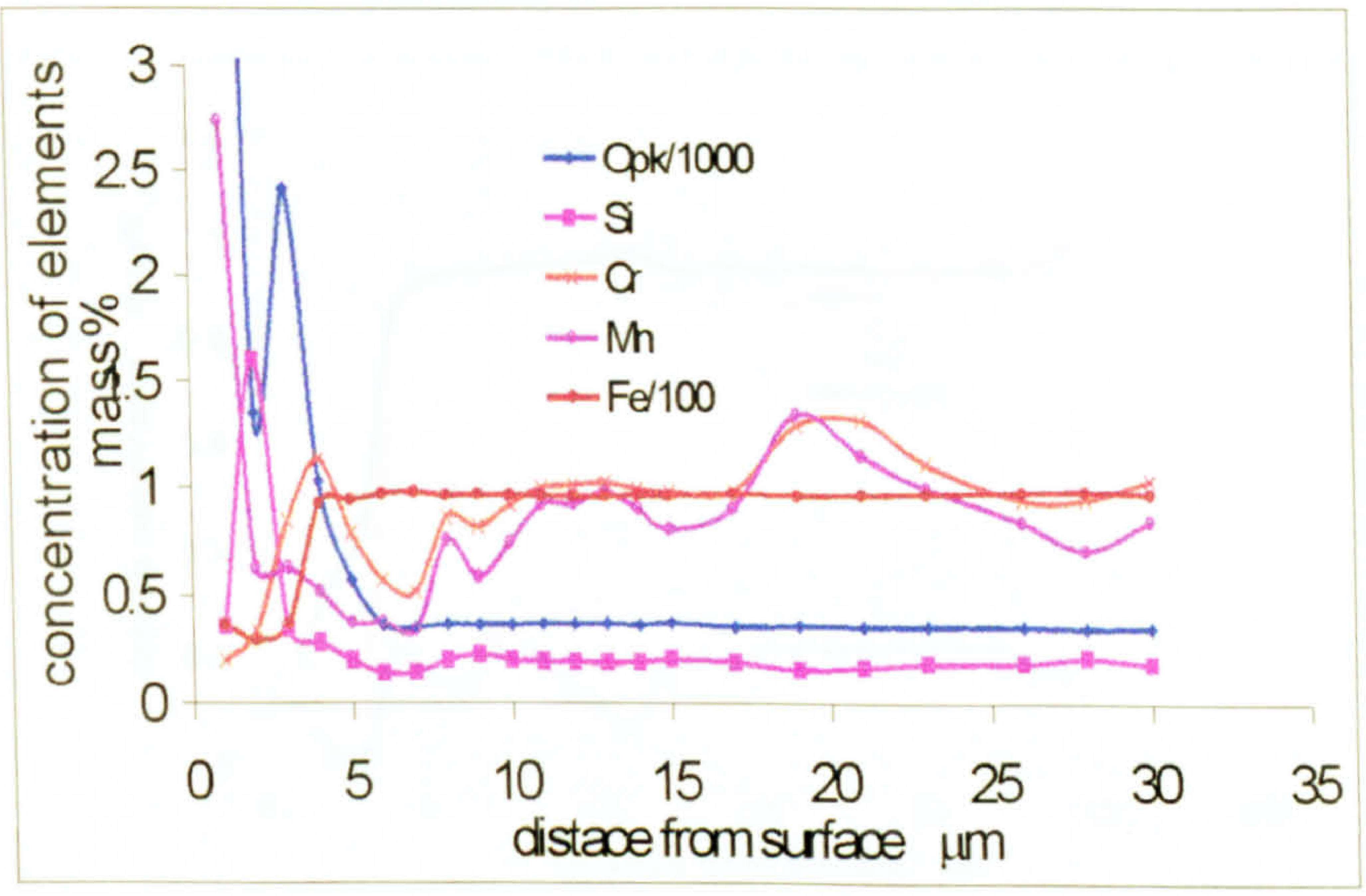

b. 1.0hr

Fig. 9 Depletion of alloy elements in matrix with different carburised time for specimens B1carburised at the procedure1.a. 0.25h; b. 1.0h; c. 5.8h; d.16.6h

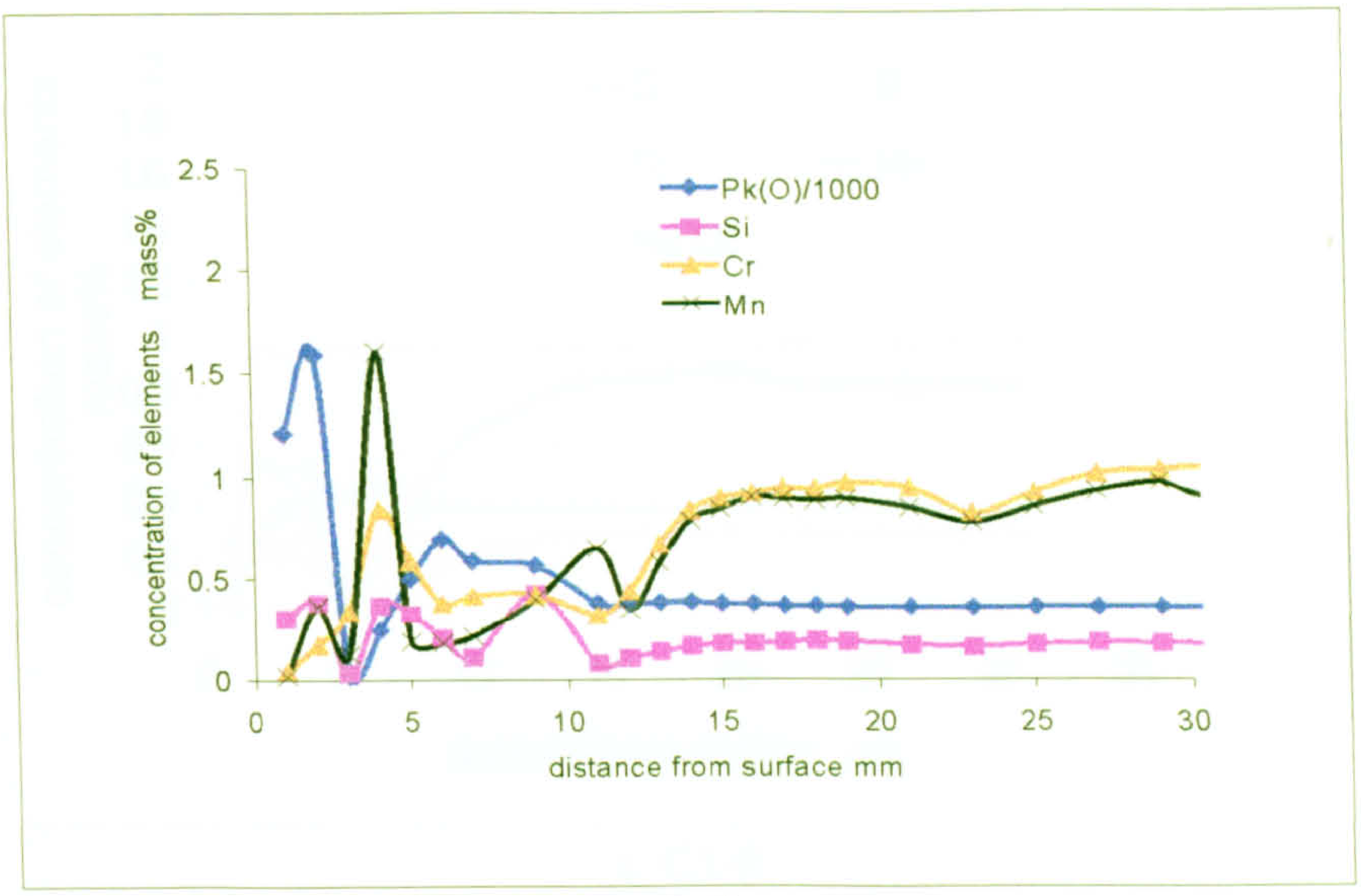

c.5.8h

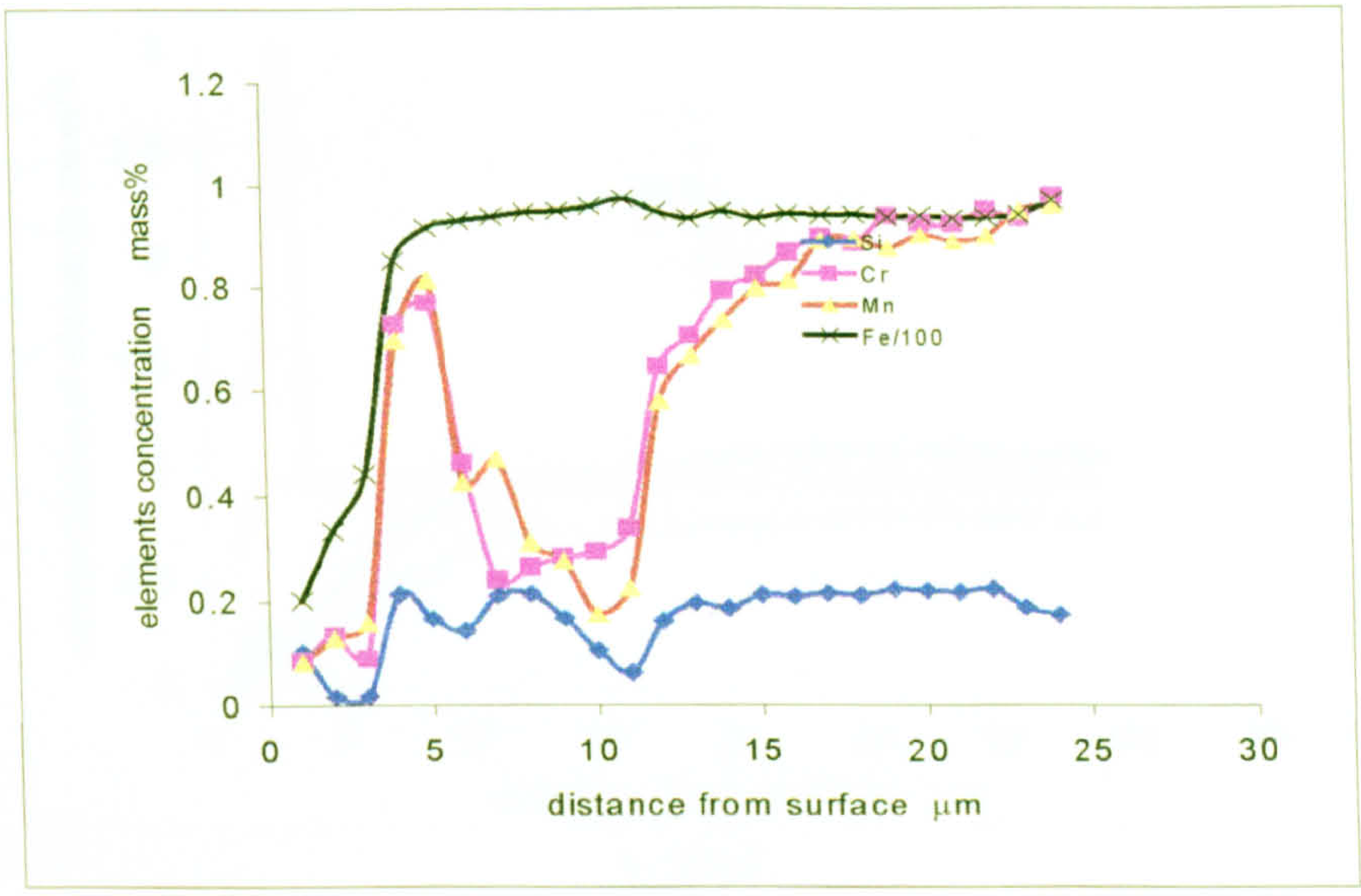

d.16.6h

Fig. 9 Depletion of alloy elements in matrix with different carburised time for specimens B1carburised at the procedure 1, a. 0.25h; b. 1.0h; c. 5.8h; d.16.6h

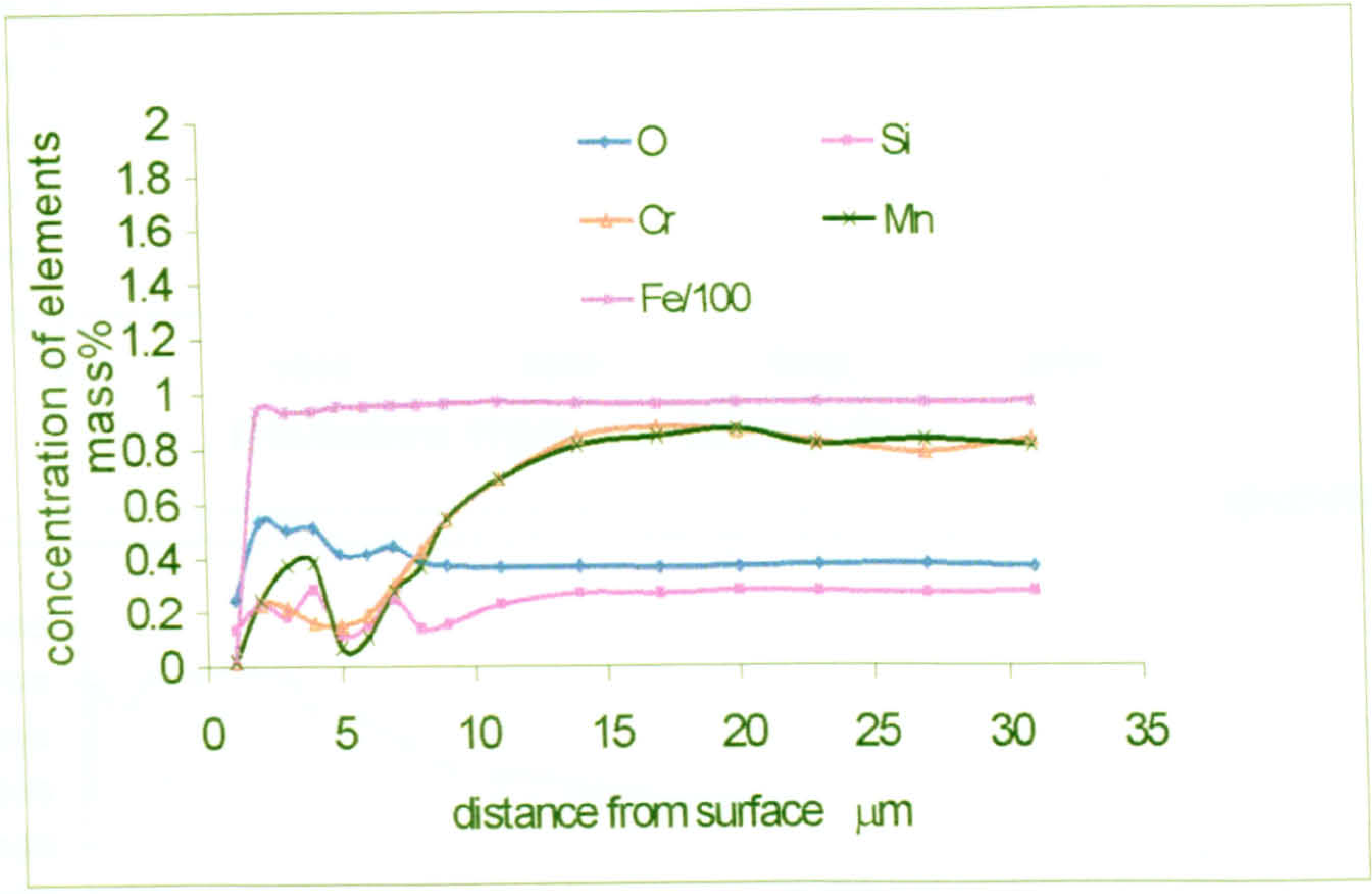

a. C1-8

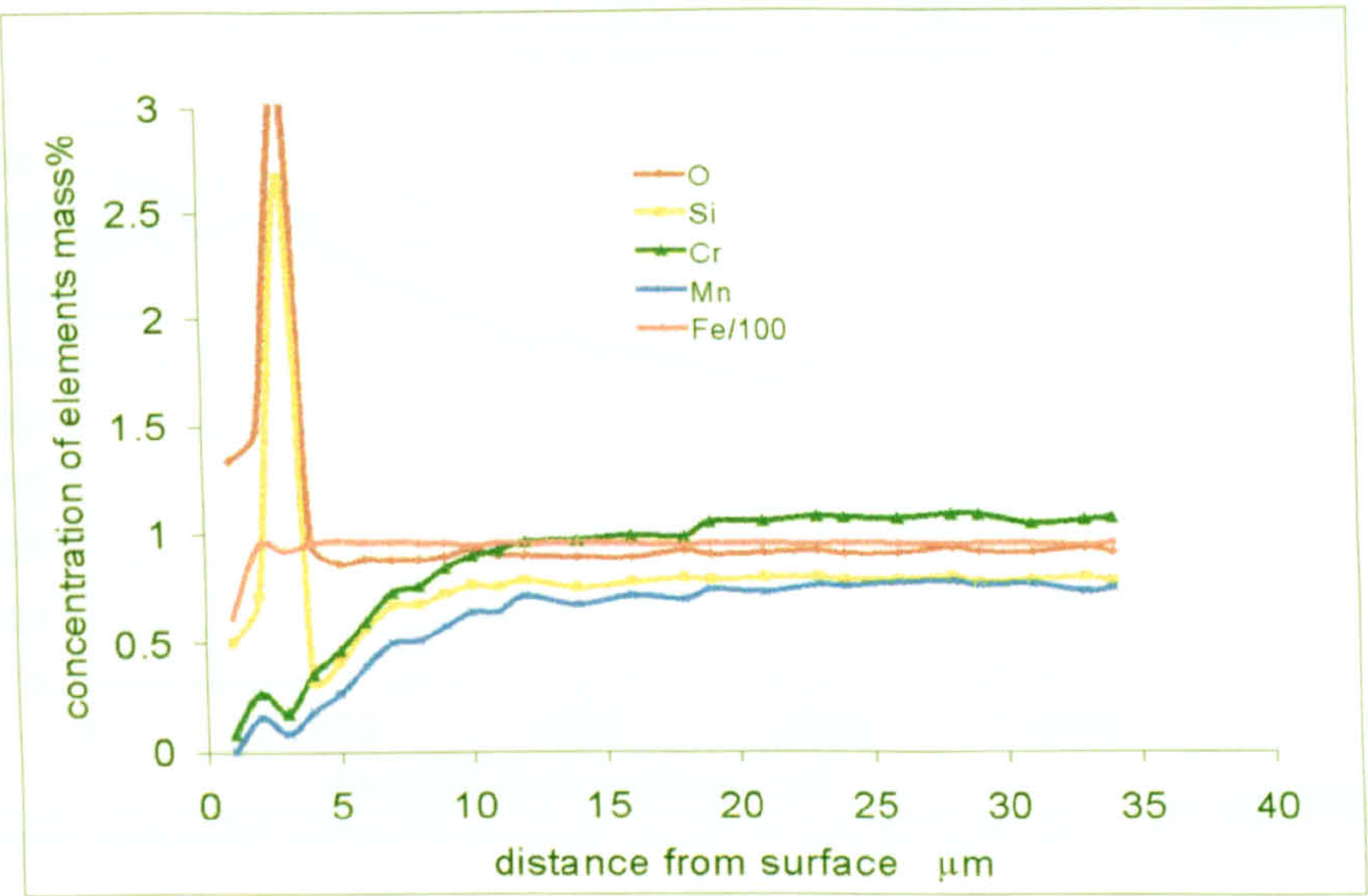

b. E1-8

Fig. 10 Depletion of alloying element in matrix with different carburised time for specimens carburised using the procedure 1 for 16.6h. a. C1-8 (0.31%Si); b. E1-8 (0.77%Si)

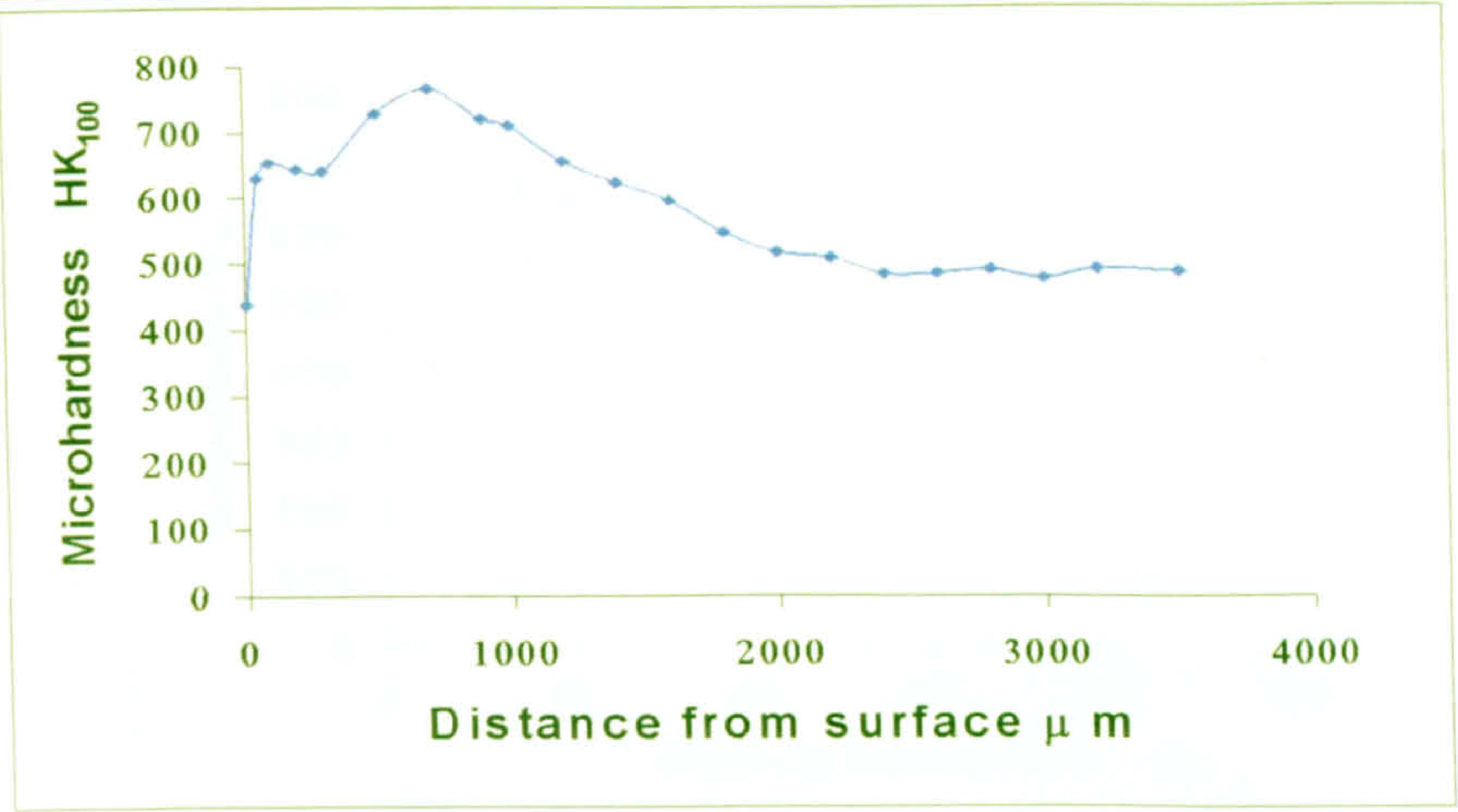

specimen A1-8

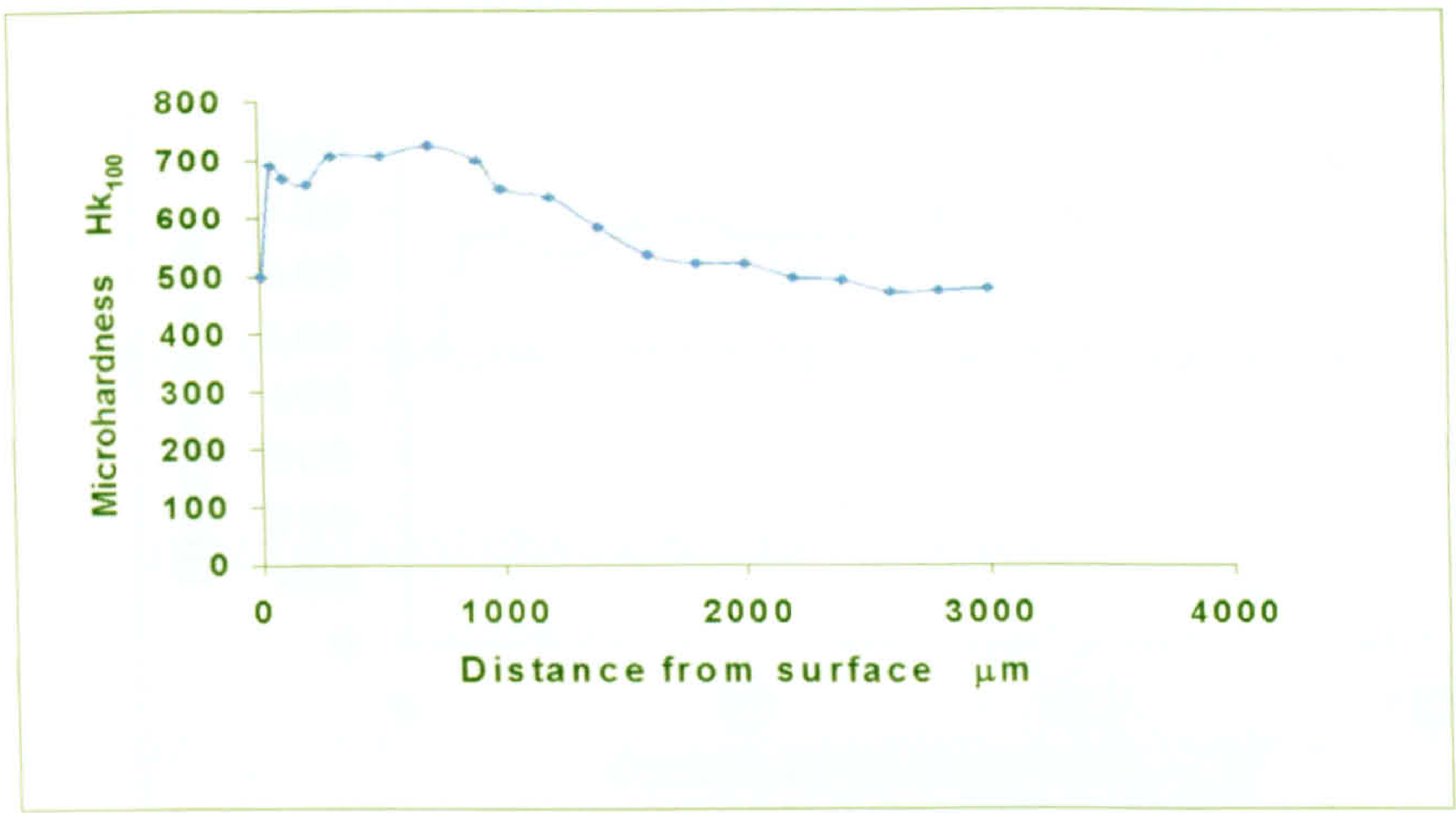

specimen C1-8

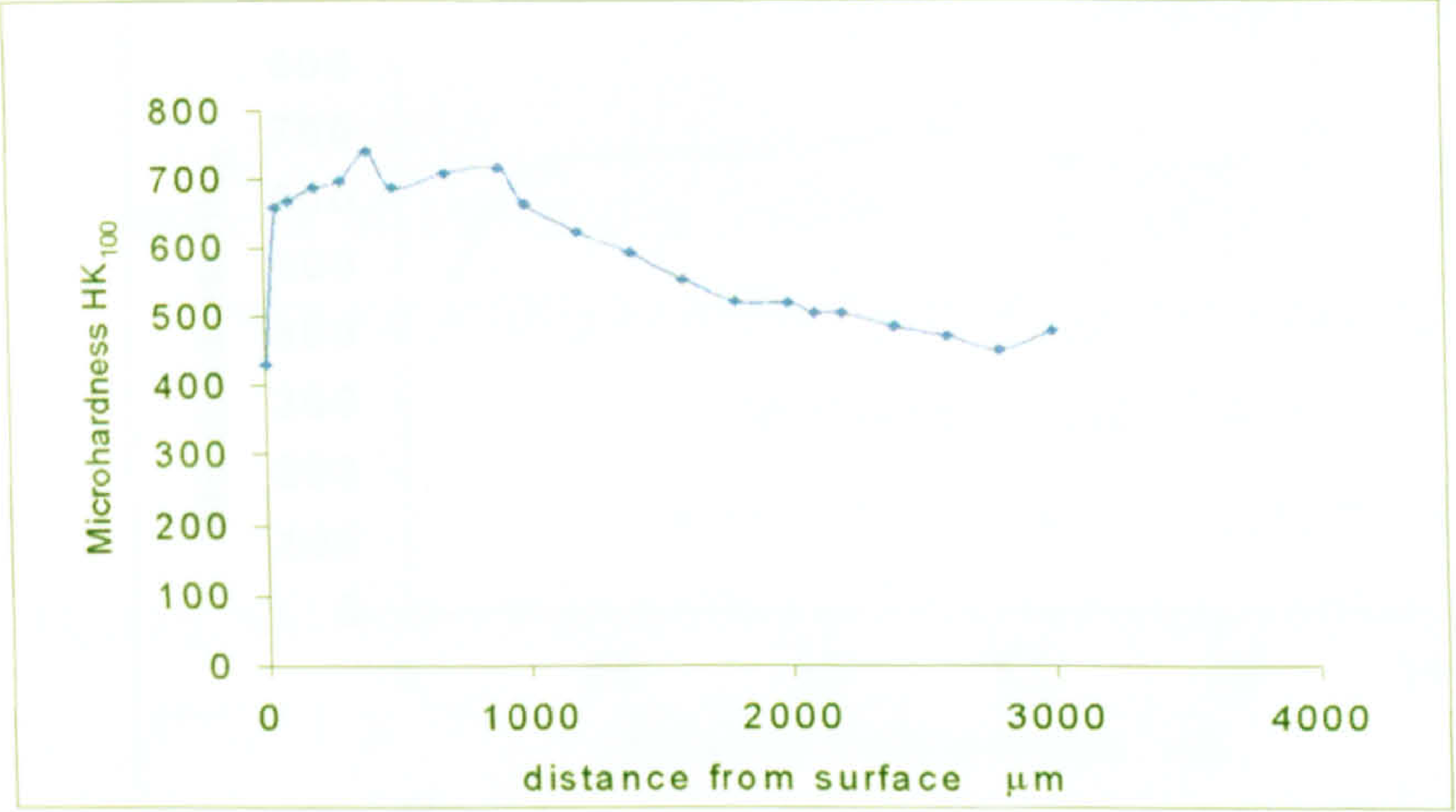

specimen D1-8

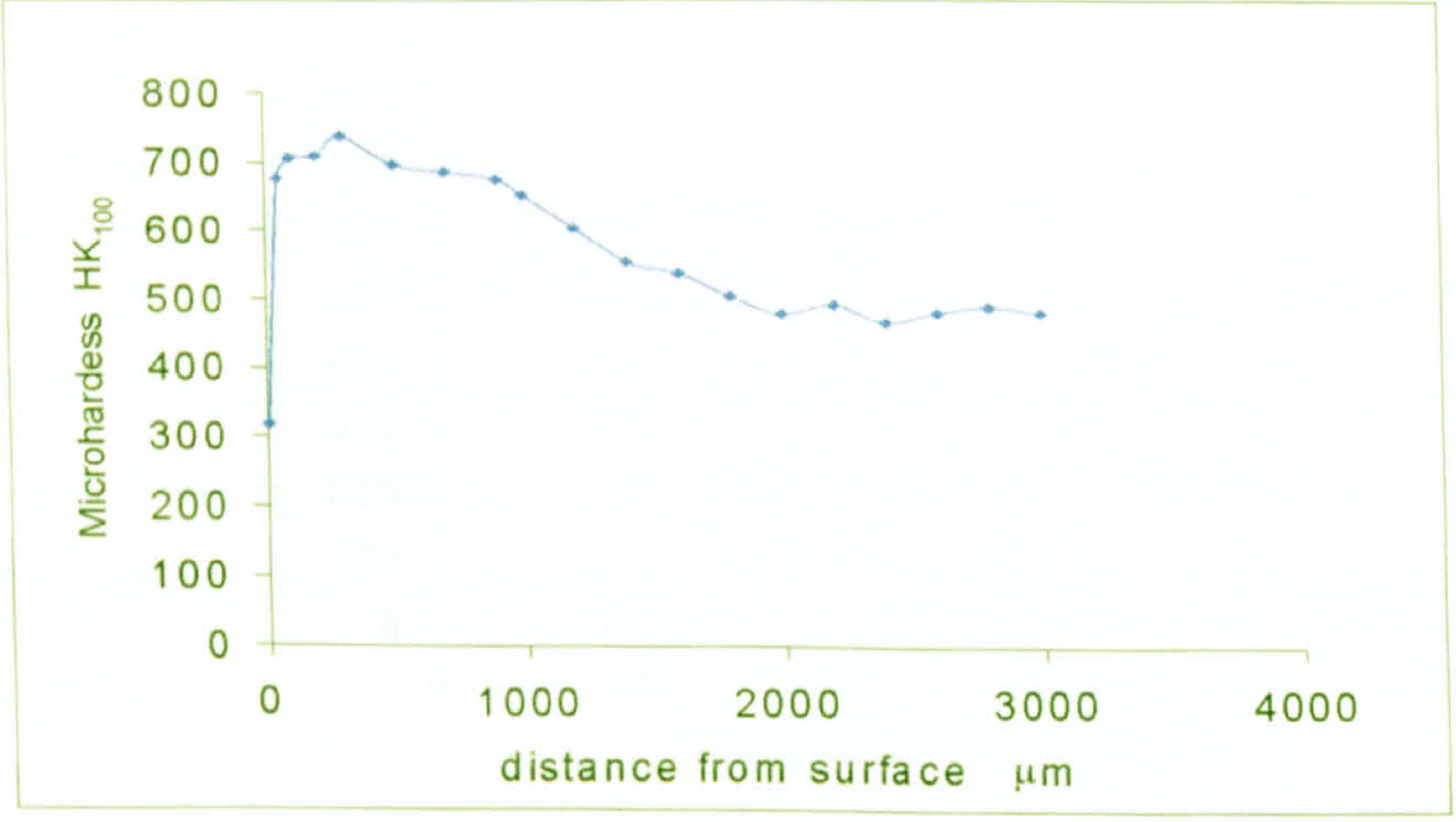

specimen E1-8

Fig . 11 Microhardness of case layer in specimens carburised using the procedure 1

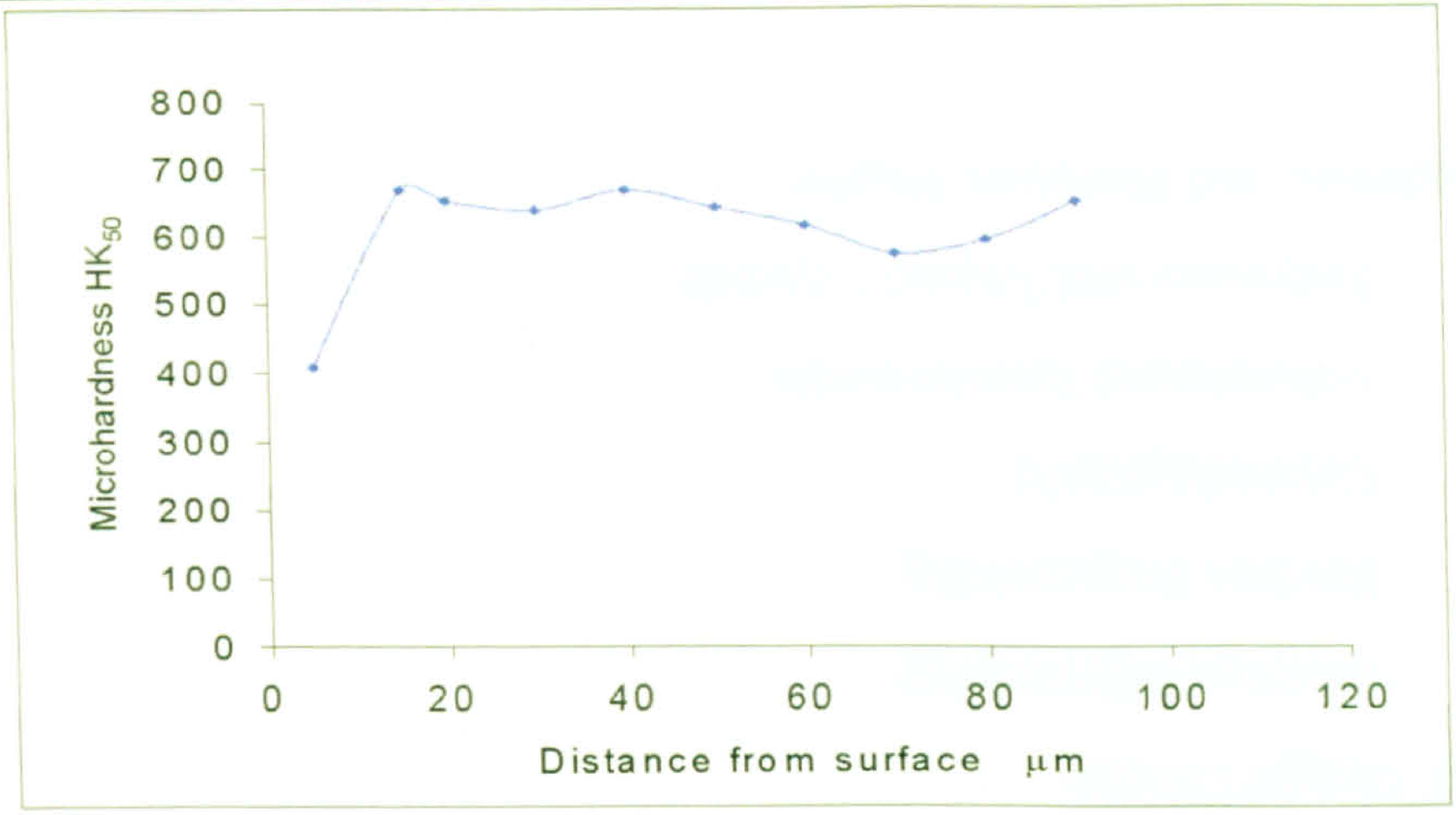

specimen A1-8

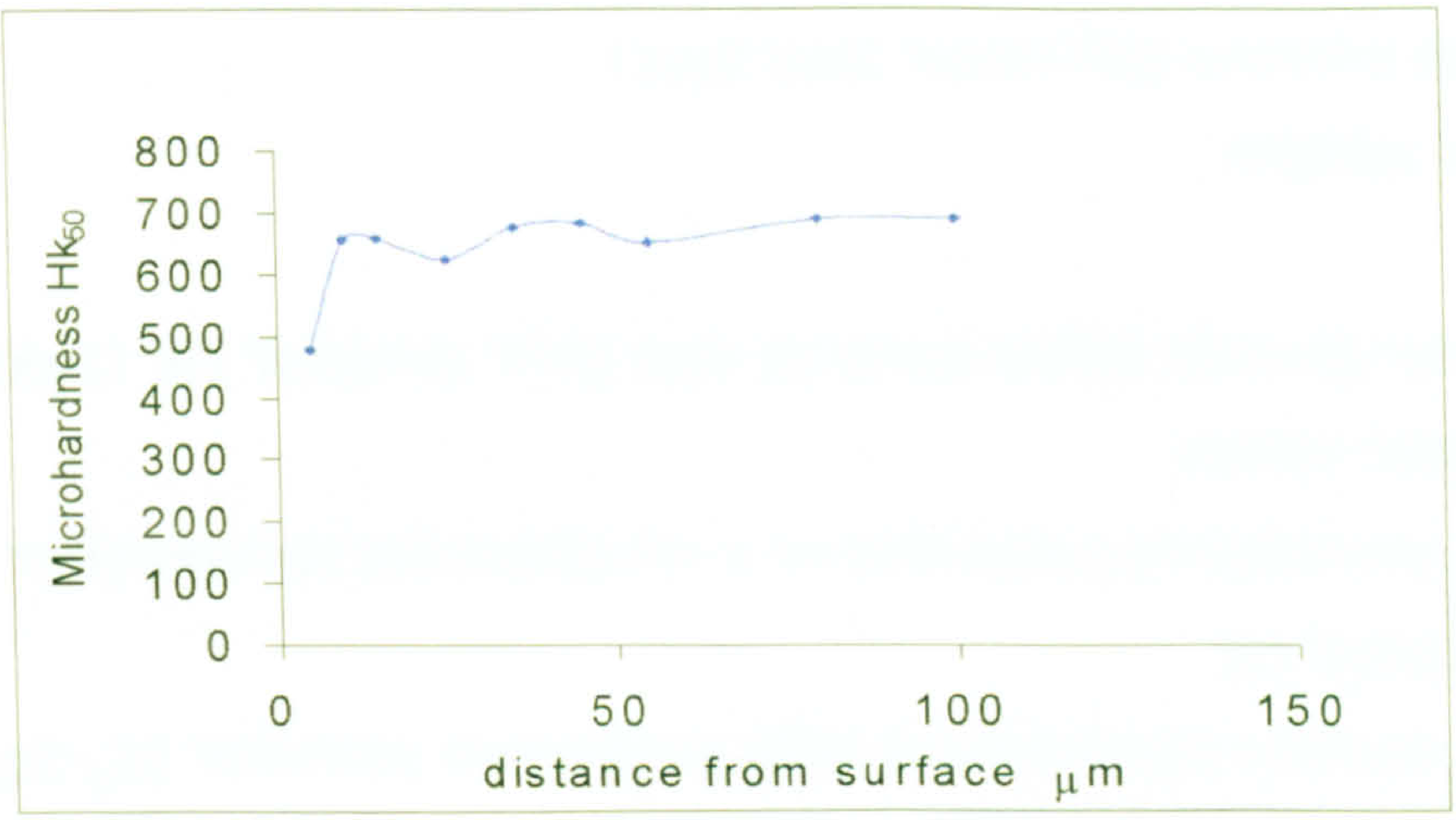

specimen C1-8

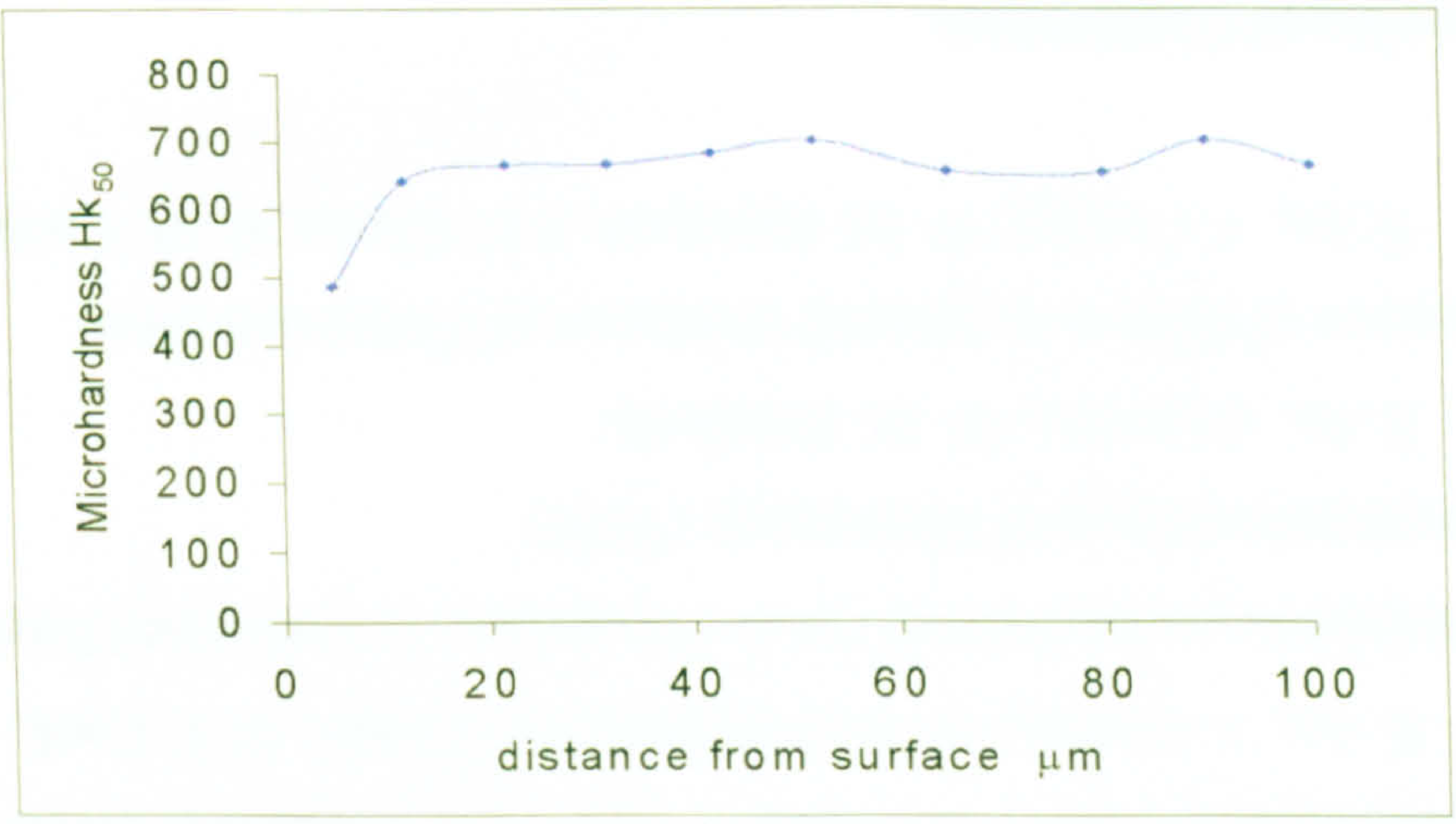

specimen D1-8

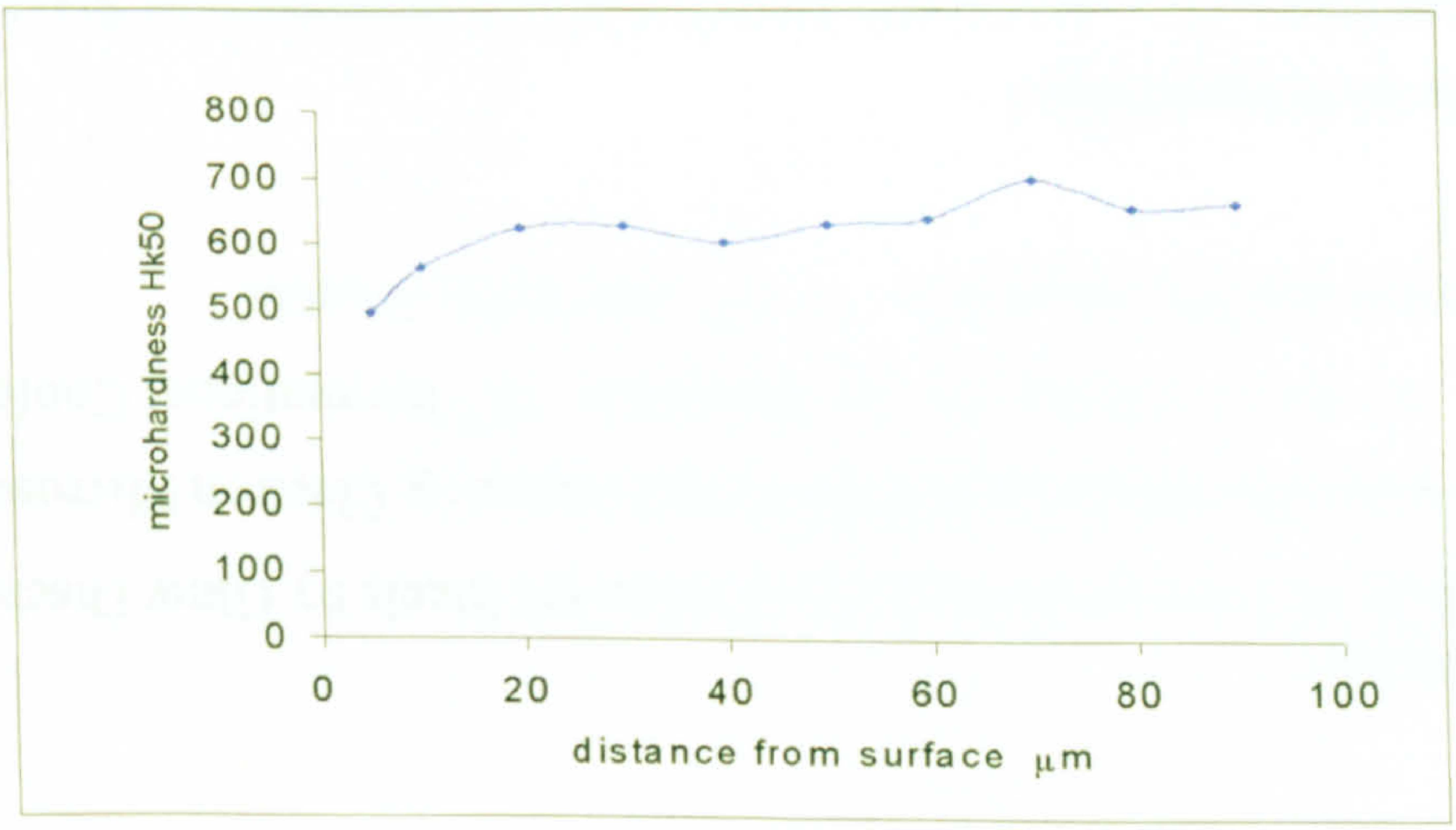

specimen E1-8

Fig. 12 Microhardness of internal oxidation layer in specimens carburised using the procedure1

PUBLICATION AND OTHERS

Publication:

1. A Study of Internal Oxidation in Carburised Steels by Glow Discharge Optical Emission Spectroscopy (GDOES) and Scanning Electron Microscopy (SEM)
   X. An, J. Cawley, W. M. Rainforth, 16th International Conference on X-ray Optics and Microanalysis, 2th- 6th July 2001, Vienna

Papers in Preparation:

1. A Microstructure Study of Internal Oxidation in Carburised Steels
   X. An, J. Cawley, W. M. Rainforth, P.C.Clarke, W.T. Cook,
2. Investigation on the Internal Oxide Precipitates in Carburised Steel by Transmission Electron Microscopy (TEM)
   X.An, J.Cawley, W. M. Rainforth,
3. Influence of Silicon on Internal Oxidation of Carburised Steel
   X.An, J. Cawley, W. M. Rainforth, P.C. Clarke, B. M. Cook

International Conference:

1. Quantitative Microscopy of High Temperature Materials, 22th-24th, Nov. 1999. Sheffield, UK
2. 16th International Conference on X-ray Optics and Microanalysis, 2th- 6th July 2001, Vienna, Austria
3. Sixth, Seventh, Eighth Sheffield ABS Days, Sheffield, UK (2000,2001,2002)

Other Studies:

1. MRI Research Day (1999, 2000, 2001)
2. MRI Taught Course
   - Electron Microscopy
   - Surface Engineering
   - Crystallography
   - Vibriational Spectroscopy
   - Polymers and Liquid Crystals
3. Academic and Business English